

- PROGRAMA DE DOCTORADO EN OCEANOGRAFÍA -
Departamento de Física
Bienio 2006 – 2008

Breeze-forced oscillations and strongly nonlinear tide-generated internal solitons

**Oscilaciones forzadas por las brisas y ondas internas solitarias de
origen mareal fuertemente no lineales**



**UNIVERSIDAD DE LAS PALMAS DE GRAN CANARIA
Departamento de Física**

Tesis Doctoral presentada por D. Borja Aguiar González para obtener el grado de Doctor por la Universidad de Las Palmas de Gran Canaria.

Dirigida por el Dr. Ángel Rodríguez Santana, el Dr. Theo Gerkema y el Dr. Jesús Cisneros Aguirre.

El Director

El Director

El Director

El Doctorando

Las Palmas de Gran Canaria a de Abril de 2013



UNIVERSIDAD DE LAS PALMAS DE GRAN CANARIA
Departamento de Física

ANEXO I

**D. Salvador Galván Herrera Secretario del Departamento de Física
de la Universidad de Las Palmas de Gran Canaria,**

CERTIFICA,

Que el Consejo de Doctores del Departamento en sesión extraordinaria tomó el acuerdo de dar el consentimiento para su tramitación a la tesis doctoral titulada ‘Breeze-forced oscillations and strongly nonlinear tide-generated internal solitons’ presentada por el doctorando D. Borja Aguiar González y dirigida por los Doctores Ángel Rodríguez Santana, Theo Gerkema y Jesús Cisneros Aguirre.

Y para que así conste, y a efectos de lo previsto en el Art. N° 6 del Reglamento para la Elaboración, Defensa, Tribunal y Evaluación de Tesis Doctorales de la Universidad de Las Palmas de Gran Canaria, firmo la presente en Las Palmas de Gran Canaria, a de Abril de 2013.

A mis padres Mappi e Ignacio

A mi hermano Jose

Thesis Preview

The present Thesis entitled ‘*Breeze-forced oscillations and strongly nonlinear tide-generated internal solitons*’ was developed at the Universidad de Las Palmas de Gran Canaria and the Royal Netherlands Institute for Sea Research. Financial support for this PhD study was provided by the Ministry of Science and Innovation (Spanish Government) through a FPU grant awarded to D. Borja Aguiar González, and the research project PROMECA (CTM2008-04057/MAR), whose Chief Investigator is Dr. Ángel Rodríguez Santana.

This PhD research has been co-supervised by Dr. Ángel Rodríguez Santana and Dr. Jesús Cisneros Aguirre from the Department of Physics at the Universidad de Las Palmas de Gran Canaria, and Dr. Theo Gerkema from the Department of Physical Oceanography at the Royal Netherlands Institute for Sea Research.

The structure of the Thesis is organized as follows. The first half of the document deals with breeze-forced oscillations. *Chapter 1* introduces the ‘state of the art’ on the study of this phenomenon. Next we present an observational study on breeze-forced oscillations poleward the critical latitude for diurnal-inertial resonance along *Chapters 2–3*. The second half of the document is devoted to modeling strongly nonlinear tide-generated internal solitons. Subsequently, *Chapter 4* provides the empirical and theoretical background on the phenomenon of study. *Chapter 5* presents the derivation of a theoretical model on strongly nonlinear tide-generated internal solitons; and, *Chapter 6* discusses on numerical experiments performed with the derived model. Conclusions and future research are presented in *Chapter 7*. Finally, a summary in Spanish is included in *Chapter 8* as required by the PhD Thesis Regulations from the Universidad de Las Palmas de Gran Canaria (BOULPGC. Art. 2,

Chap. 2, November 5th 2008). The references are listed at the end of the document.

Presentación de la Tesis

La presente Tesis Doctoral se titula ‘Oscilaciones forzadas por las brisas y ondas internas solitarias de origen mareal fuertemente no lineales’ y se ha desarrollado entre la Universidad de Las Palmas de Gran Canaria y el Royal Netherlands Institute for Sea Research. La financiación ha procedido del Ministerio de Ciencia e Innovación (Gobierno de España) a través de la concesión de una beca del Programa de Formación de Profesorado Universitario (FPU) al doctorando D. Borja Aguiar González, y del proyecto de investigación PROMECA (CTM2008-04057/MAR), del cual el Dr. Ángel Rodríguez Santana es Investigador Principal.

Esta Tesis Doctoral ha sido codirigida por el Dr. Ángel Rodríguez Santana y el Dr. Jesús Cisneros Aguirre, ambos del Departamento de Física de la Universidad de Las Palmas de Gran Canaria, y por el Dr. Theo Gerkema del Departamento de Oceanografía Física del Royal Netherlands Institute for Sea Research.

La estructura del documento se ha organizado de la siguiente manera. La primera parte de la Tesis Doctoral (*Capítulos 1-3*) investiga la respuesta del océano al forzamiento de las brisas. El *Capítulo 1* introduce el ‘estado del arte’ en el estudio de este fenómeno físico. Los *Capítulos 2-3* forman el núcleo de un estudio observacional sobre oscilaciones forzadas por las brisas en latitudes críticas para la resonancia diurno-inercial. La segunda parte de la Tesis Doctoral (*Capítulos 4-6*) desarrolla un modelo teórico para la simulación de ondas internas solitarias de origen mareal fuertemente no lineales. El *Capítulo 4* introduce el ‘estado del arte’ en el estudio de este fenómeno físico. El *Capítulo 5* describe el desarrollo del modelo teórico. El *Capítulo 6* presenta la discusión de diferentes simulaciones numéricas obtenidas con el modelo. Las conclusiones y trabajo futuro abarcan el contenido del *Capítulo 7*. Por último se incluye

un resumen en español de la Tesis Doctoral en el *Capítulo* 8 para cumplir con los requisitos establecidos por el Reglamento para la Elaboración, Tribunal, Defensa y Evaluación de Tesis Doctorales de la Universidad de Las Palmas de Gran Canaria (BOULPGC. Art. 2, Cap. 2, 5 de Noviembre de 2008). Las referencias citadas a lo largo del documento figuran al final del mismo.

Summary

The present thesis deals with observations of breeze-forced oscillations and modeling of strongly nonlinear tide-generated internal solitons. These two phenomena are of special interest owing to its periodic appearance, specially in shelf areas, with associated highly energetic motions. The contents of the seven chapters which compose this thesis are distributed as follows.

The first half of the thesis (*Chapters 1-3*) is devoted to the study of breeze-forced oscillations around the critical latitudes for diurnal-inertial resonance. *Chapter 1* contains an introduction to the various physical concepts surrounding a breeze-forced scenario, i.e. sea-land breezes, near-inertial oscillations, periodic forcing and near-inertial resonance. In *Chapter 2* we study the temporal evolution of resonant breeze-forced oscillations in coastal areas poleward of the critical latitude for diurnal-inertial resonance (30°N/S). The research is based on simultaneous and co-located meteorological and oceanographic data collected from three REDEXT (Red Exterior de Boyas) buoys deployed around the Iberian Peninsula: the Gulf of Cádiz, the Gulf of Valencia and the Cape Peñas area. With this aim, new applications of rotary wavelet analysis are performed. In *Chapter 3* we explore the role of breeze-forced-oscillations on promoting diapycnal mixing processes. The measurements we used here were taken during the Maritime Rapid Environmental Assessment 2004 (MREA04) sea trial off the west coast of the Iberian Peninsula and from a meteorological land station provided by the Instituto Hidrográfico - Portugal. This research provides observational results of breeze-forced oscillations in the stratified waters of the Bay of Setúbal, framed within the critical latitudes ($30^\circ \pm 10^\circ\text{N/S}$), for diurnal-inertial resonance where they can greatly contribute to triggering diapycnal mixing.

The second half of the thesis (*Chapters 4-6*) focuses on the modeling of strongly nonlinear tide-generated internal solitons. *Chapter 4* starts our re-

Summary

search with an introduction to a solitons scenario in the ocean. Thereof, in *Chapter 5* we derive a new two-fluid layer model consisting of a set of forced rotation-modified Boussinesq equations for studying the generation and evolution of strongly nonlinear weakly nonhydrostatic dispersive interfacial waves. Next we develop and describe the numerical scheme used to solve the model. In *Chapter 6*, a set of numerical experiments is presented and discussed. The results of this chapter validate the model as a useful tool for exploring and interpreting the conditions under which full nonlinearity effects become important for soliton generation.

Chapter 7 closes this PhD study presenting an overview of the main scientific contributions and conclusions which arise from results and discussion of this work.

Resumen

La presente Tesis Doctoral se centra en el estudio observacional de oscilaciones forzadas por las brisas y el modelaje de ondas internas solitarias de origen mareal fuertemente no lineales. El interés de estos fenómenos oceanográficos radica en su aparición periódica, especialmente en ambientes de plataforma continental, con corrientes asociadas altamente energéticas. La estructura de este trabajo de investigación se encuentra dividida de la siguiente manera.

La primera parte de esta Tesis Doctoral (*Capítulos 1 – 3*) abarca el estudio observacional de oscilaciones forzadas por las brisas en latitudes críticas para la resonancia diurno-inercial ($30^\circ \pm 10^\circ$ N/S). El *Capítulo 1* contiene una introducción al fenómeno de las oscilaciones forzadas por las brisas. El *Capítulo 2* se basa en medidas simultáneas de datos meteorológicos y oceanográficos procedentes de tres boyas REDEXT (Red Exterior de Boyas) localizadas en el Golfo de Cádiz, el Golfo de Valencia y en las proximidades del Cabo Peñas. Con estas medidas, y aplicando la metodología de wavelet rotatoria, analizamos la evolución temporal de oscilaciones forzadas por las brisas en latitudes que se encuentran por encima de la latitud crítica para la resonancia diurno-inercial (30° N/S). El *Capítulo 3* investiga el papel de las oscilaciones forzadas por las brisas en la generación de procesos de mezcla diapicna. Los datos proceden de la campaña oceanográfica Maritime Rapid Environmental Assessment 2004 (MREA04), que tuvo lugar en la costa oeste de la Península Ibérica en Abril de 2004, y de una estación meteorológica costera del Instituto Hidrográfico - Portugal.

La segunda parte de la Tesis (*Capítulos 4 – 6*) trabaja el modelaje de ondas internas solitarias de origen mareal fuertemente no lineales. El *Capítulo 4* contiene una introducción al fenómeno de ondas internas solitarias en el océano. El *Capítulo 5* describe el desarrollo teórico empleado para derivar un nuevo modelo de generación de ondas internas solitarias fuertemente no lineales y

Resumen

débilmente no hidrostáticas. Se detalla además el esquema numérico aplicado para resolver el modelo. Por último, el *Capítulo 6* presenta una serie de experimentos numéricos que validan el modelo como una herramienta útil para explorar e interpretar las condiciones bajo la cuales los efectos fuertemente no lineales de las ondas internas solitarias se consideran determinantes para la adecuada simulación del fenómeno.

El *Capítulo 7* presenta las principales contribuciones y conclusiones del presente trabajo de investigación, así como futuras líneas de trabajo.

Contents

List of Figures	xv
1 Introduction to a Breeze-Forced Scenario	1
1.1 Sea-Land Breezes	1
1.2 Breeze-Forced Oscillations	7
1.2.1 Periodic Forcing and Near-Inertial Resonance	13
1.2.2 Stratification and Vertical Mixing	19
1.3 Scope of the Study	22
2 Breeze-Forced Oscillations Poleward of the Critical Latitude for Diurnal-Inertial Resonance	25
2.1 Outline	25
2.2 Data and Methodology	26
2.3 Results and Discussion	29
2.3.1 Characterization of Three Wind-Forced Scenarios	29
2.3.2 The Ocean Response to Diurnal Wind Forcing: A Rotary Analysis	38
2.4 Conclusions	46
3 Breeze-Forced Oscillations and Diapycnal Mixing	49
3.1 Outline	49
3.2 Data and Methodology	51
3.3 Results and Discussion	54
3.3.1 A Breeze-Forced Scenario	54
3.3.2 Breeze-Forced Oscillations	56
3.3.3 Diapycnal Mixing and Breeze-Forced Events	59
3.3.4 Impact of BFOs in the Bay of Setúbal	65
3.4 Conclusions	66

CONTENTS

4	Introduction to a Solitons Scenario	71
4.1	Solitary Waves in the Ocean	71
4.2	A Mathematical Approach to Solitons	78
4.3	Scope of the Study	85
5	A Model for the Generation of Strongly Nonlinear, Weakly Nonhydrostatic Interfacial Waves	87
5.1	Outline	87
5.2	Preliminaries	88
5.3	Scaling	89
5.4	Vertically Integrated Equations	91
5.4.1	Upper Fluid-Layer	91
5.4.2	Lower Fluid-Layer	92
5.5	Expansion in δ	94
5.5.1	Lowest Order	95
5.5.2	Next Order	96
5.5.2.1	Pressure in Upper Layer	97
5.5.2.2	Pressure in Lower Layer	99
5.6	The Generation Model	101
5.7	Numerical Modeling	105
5.7.1	Numerical Strategy	105
5.7.2	Preliminaries to Solve \bar{u}_1	111
5.7.3	Summary of Equations	120
6	Numerical Experiments Solitons	123
6.1	Outline	123
6.2	Configuration of the Numerical Experiments	124
6.2.1	The Two-Fluid Layer System	124
6.2.2	Setting the Space-Time Grid	126
6.2.3	Basic Tests	127
6.2.4	Set of Experiments	129
6.3	Generation of the Linear Hydrostatic Internal Tide	130
6.4	Generation of Strongly Nonlinear Solitons	134
6.4.1	'Table-Top' Solitons (Rotationless Test, $\mu = 0$)	134
6.4.2	Solitons with Two Layers of Equal Thickness (Rotation- less Test, $\mu = 0$)	136
6.4.3	Strongly Nonlinear Solitons dispersed by the Effects of the Earth's Rotation	137
6.5	Conclusions	139

7	Conclusions and Future Research	141
8	Summary of the Thesis in Spanish	143
8.1	Un Escenario Forzado por las Brisas	145
8.1.1	Brisas Tierra-Mar	145
8.1.2	Oscilaciones Forzadas por las Brisas	152
8.1.3	Marco del Estudio, Objetivos y Metodología	170
8.2	Ondas Internas Solitarias en el Océano	174
8.2.1	Estudios Observacionales	174
8.2.2	Descripción Matemática de los Solitones	183
8.2.3	Marco del estudio, Objetivos y Metodología	191
8.3	Conclusiones y Trabajo Futuro	195
A	Rotary Wavelet Method	197
A.1	Rotary Wavelet Power Spectrum	197
A.2	Rotary Coefficient	199
A.3	Statistical Significance Test	200
A.4	Cross-Rotary Wavelet Power Spectrum	201
A.5	Rotary Wavelet Coherence Squared Spectrum	201
A.6	Rotary Wavelet Phase Spectrum	202
B	Theorem for Derivatives of Integrals with Variable Boundaries	205
C	Derivation of Function $G_i(x, t)$	207
C.1	Upper Layer	207
C.2	Lower Layer Over an Oscillating Topography	209
D	Derivation of $\overline{\left(\frac{\partial p_2^{(1)}}{\partial x}\right)}$	213
E	Substituting \bar{u}_2 in terms of \bar{u}_1	215
	References	219
	Data Acknowledgements	233
	Agradecimientos	235
	Curriculum Vitae	239

CONTENTS

List of Figures

1.1	Diagram of a Lake Breeze Regime	2
1.2	Diagram of a Land Breeze Regime	3
1.3	Seasonal Variability of Sea-land Breezes on the Texas-Louisiana shelf	5
1.4	The Effect of Coastlines on Sea Breezes	7
1.5	Seasonal Variability of Breeze-Forced Oscillations on the Texas-Louisiana shelf	9
1.6	Breeze-Forced Oscillations on the Namibian shelf	10
1.7	Phase Evolution of Breeze-Forced and Free Near-Inertial Oscillations	12
1.8	Slab Model of Forced Oscillations	14
1.9	A Continuous Model with Friction of Forced Oscillations	18
1.10	Effects of Breeze-Forced Oscillations on the Vertical Mixing	21
1.11	Regions for Diurnal/Semidiurnal Resonance	23
2.1	Oceanographic Buoys - Puertos del Estado	27
2.2	Rotary Wavelet Power Spectrum of Wind at the Buoy Gulf of Cádiz	31
2.3	Rotary Wavelet Power Spectrum of Wind at the Buoy Valencia II	32
2.4	Rotary Wavelet Power Spectrum of Wind at the Buoy Cape Peñas	33
2.5	Rotary Wavelet Power Spectrum of Currents at the Buoy Gulf of Cádiz	34
2.6	Rotary Wavelet Power Spectrum of Currents at the Buoy Valencia II	35
2.7	Rotary Wavelet Power Spectrum of Currents at the Buoy Cape Peñas	36

LIST OF FIGURES

2.8	Averaged Wavelet Variance of Wind and Currents from the Buoy at the Gulf of Cádiz	39
2.9	Averaged Wavelet Variance of Wind and Currents from the Buoy at the Gulf of Valencia	40
2.10	Averaged Wavelet Variance of Wind and Currents from the Buoy at the Cape Peñas area	41
2.11	Squared Wavelet Coherency and Phase Spectra between Wind and Currents (Clockwise Components) measured at the Buoy Gulf of Cádiz	43
2.12	Squared Wavelet Coherency and Phase Spectra between Wind and Current (Clockwise Components) measured at the Buoy Cape Peñas	45
3.1	MREA04 Data Set	51
3.2	Wind Time series for the Bay of Setúbal	55
3.3	Breeze-Forced Oscillations on the Portuguese shelf	57
3.4	Surface Contours for the Bay of Setúbal	60
3.5	Diapycnal Mixing Analysis	62
3.6	Rotary Wavelet Power Spectrum of Wind from a Meteorological Station at Sines	66
4.1	Schematic of Canonical Soliton Packets	72
4.2	Solitary Waves over the Oregon shelf	74
4.3	Evolution of a Solitons Packet in the Sulu Sea	75
4.4	Remote Sensing SAR (Synthetic Aperture Radar) images of Solitons in the Sulu Sea	77
4.5	Solitary wave solutions of the eKdV equation	82
4.6	Comparison of KdV and MCC theories	83
6.1	Configuration of the Numerical Experiments	125
6.2	Moving Topography vs. Tidal Motion	128
6.3	Generation of the Linear Hydrostatic Internal Tide (Rotationless case, $\mu = 0$)	131
6.4	Generation of the Linear Hydrostatic Internal Tide (at Mid Latitudes: $\phi = 45^\circ$, $\mu = 4.61$)	132
6.5	Generation of the Linear Hydrostatic Internal Tide (at High Latitudes: $\phi = 90^\circ$, $\mu = 6.52$)	133
6.6	Generation of ‘Table-Top’ Solitons	135
6.7	Time evolution of ‘Table-Top’ Solitons	136

6.8	Generation of Solitons between Two Layers of Equal Thickness	137
6.9	Time evolution of Solitons between Two Layers of Equal Thickness	137
6.10	Time evolution of Strongly Nonlinear Solitons dispersed by the Effects of the Earth's Rotation (at Mid Latitudes: $\phi = 45^\circ$, $\mu = 4.61$)	138
8.1	Diagrama de un régimen de brisas de lagos	146
8.2	Diagrama de un régimen de brisa de tierra	147
8.3	Variabilidad estacional de las brisas mar-tierra en la plataforma de Texas-Louisiana	149
8.4	El efecto de la costa sobre las brisas	151
8.5	Variabilidad estacional de las oscilaciones forzadas por la brisa en la plataforma de Texas-Louisiana	154
8.6	Oscilaciones forzadas por la brisa en la plataforma de Namibia	156
8.7	Evolución de la fase de oscilaciones forzadas por brisa y casi-inercial 'libres'	157
8.8	Modelo de oscilaciones forzadas	160
8.9	Modelo Continuo con fricción de oscilaciones forzadas	166
8.10	Efectos de las oscilaciones forzadas por brisa en la mezcla vertical	169
8.11	Regiones para resonancia diurna/semidiurna	171
8.12	Esquema de paquetes de solitón canónico	176
8.13	Ondas solitarias sobre la plataforma de Oregon	178
8.14	Evolución de un paquete de solitones en el Mar de Sulu	180
8.15	Imágenes de teledetección SAR (Synthetic Aperture Radar) de solitones en el Mar de Sulu	181
8.16	Soluciones de ondas solitarias de la ecuación eKdV	188
8.17	Comparación de las teorías KdV y MCC	189

LIST OF FIGURES

Chapter 1

Introduction to a Breeze-Forced Scenario

This chapter presents a review on observations, theoretical and modeling works from the existing literature on the topic ‘breeze-forced oscillations within the critical latitudes for diurnal-inertial resonance’, which for short we may refer in future chapters as ‘resonant breeze-forced oscillations’. In Section 1.1 we start the introduction to a breeze-forced scenario with a brief description of the fundamental aspects of sea-land breezes as a forcing to the coastal ocean. Therein, we focus on the physics of resonant breeze-forced oscillations in Section 1.2. We discuss the scope of this PhD study within the described context in Section 1.3.

1.1 Sea-Land Breezes

Sea-land breezes are thermally-induced winds caused by the differential heating and cooling of sea and land at diurnal cycles. This phenomenon is supported due to the ocean has a higher specific heat capacity than land, what entails that during daytime land warms up more than the ocean and so the air above it. The process reverses at night time, when land cools more than the ocean. This results in land-water air pressure differences driving systems of breezes, generally onshore-offshore, along about two thirds of the earth’s coasts (Simpson, 1994). Thus we have the scenario where sea-land breezes can

1. INTRODUCTION TO A BREEZE-FORCED SCENARIO

occur, i.e. along coastlines adjacent to large bodies of water: oceans, seas, lakes, rivers,...

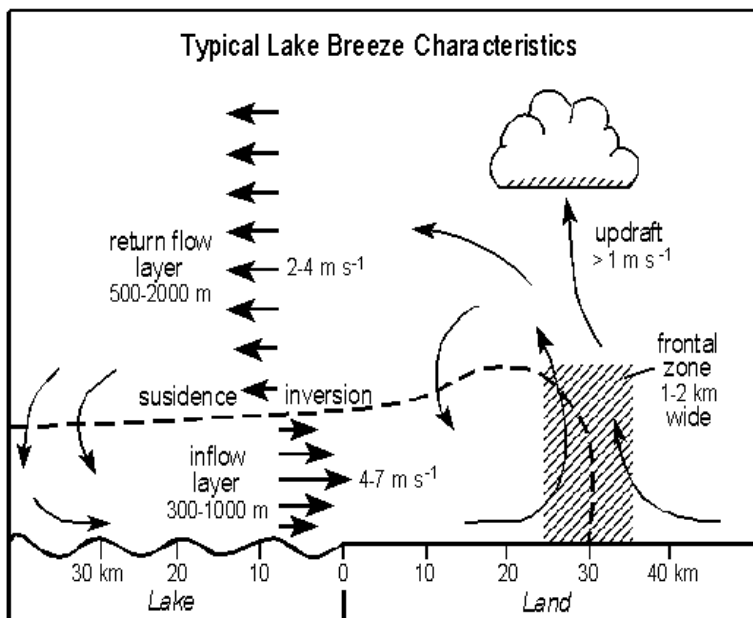


Figure 1.1: Diagram of a Lake Breeze Regime - Idealized illustration of a typical lake breeze circulation and its associated front. The dashed line represents the outer boundary of the inflow layer. The frontal zone is not shown to scale. [From Sills (1998)].

A general description of a sea-land breeze event may start with calm weather conditions where surface pressures over land and sea are initially the same along a straight coastline. After daytime insolation, air over land is heated and starts to expand. Then, a fall of the pressure at low levels in the atmosphere inland leads to a pressure gradient between air over land and air over sea. Once the pressure gradient is acting, one can say the onset of the breeze system has taken place. This pressure gradient working during daytime is the driving force of the onshore surface winds known as 'sea breezes'.

Figures 1.1 and 1.2 show two idealized schemes for a breeze system. These schemes detail lake-land breezes acting in the Great Lakes (North America)

based on previous literature values (Moroz, 1967; Lyons, 1972; Lyons and Olson, 1973; Keen and Lyons, 1978) and allow us to explain the main dynamics of sea-land breezes. However, though thickness layer and velocity values maintain rather similar numbers, it should be noticed that horizontal scales have been observed to be longer in oceanic areas in comparison with those in lake-land breeze systems (Simpson, 1994; Hyder et al., 2002; Rippeth et al., 2002; Simpson et al., 2002; Gille et al., 2003; Zhang et al., 2009; Hyder et al., 2011). Oceanic horizontal scales may extend from several tens to a few hundreds of kilometres alongshore, and more than 100 km offshore from the coast (Simpson, 1994; Gille et al., 2003; Aparna et al., 2005; Gille et al., 2005; Zhang et al., 2009).

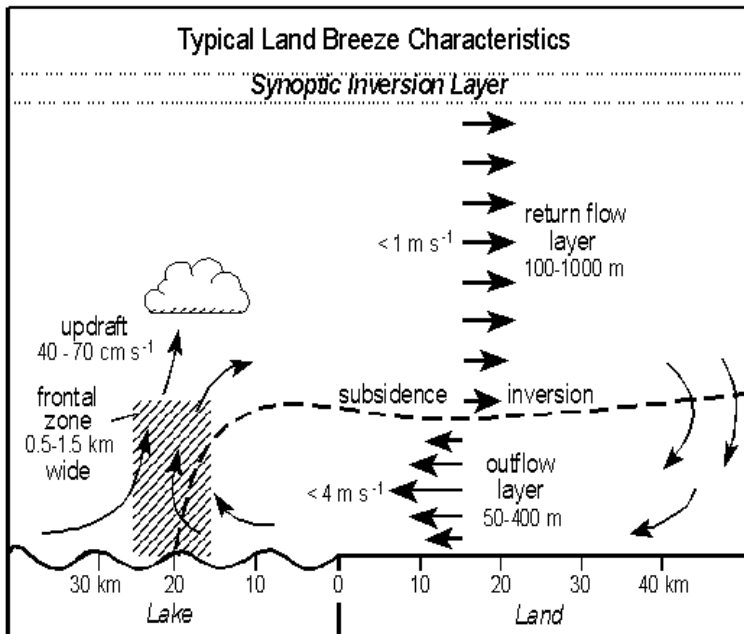


Figure 1.2: Diagram of a Land Breeze Regime - Idealized illustration of a typical land breeze circulation and its associated front. The dashed line represents the outer boundary of the outflow layer. The frontal zone is not shown to scale. [From Sills (1998)].

The thickness of the sea breeze layer may reach a height from the surface between 300 – 1000 m, depending on the site, with typical wind speeds about

1. INTRODUCTION TO A BREEZE-FORCED SCENARIO

$4 - 7 \text{ m s}^{-1}$ (Figure 1.1). Nonetheless, it has been also found that it can even exceed 10 m s^{-1} in some cases (Pattiaratchi et al., 1997). This cool and wet air flowing inland converges to the warm and dry air ascending from the heated land. The result is a frontal zone (1-2 km wide) parallel to the coast where a line of cumulus clouds tends to arise. This cloud formation is an evidence of the so called ‘sea-breeze front’. Above the sea breezes flowing inland, a weaker return flow of $2 - 4 \text{ m s}^{-1}$ balances the system at a height of $\sim 500 - 2000 \text{ m}$, and sinks over inshore waters closing the sea breeze cell.

During the night time and the early morning, land becomes cooler than the ocean and the process reverses (Figure 1.2). Thereof, the air contracts inland and descends creating a zone of relatively high pressure. The consequent pressure gradient between land and sea drives the onset of the seaward winds known as ‘land breezes’ (Figure 1.2). The cooling of the atmosphere over land is restricted to a shallower layer at night than the layer of heating of the air during the day time. This makes land breezes to be typically shallower and weaker than sea breezes. Therefore, the thickness of the land breeze layer presents a lower height varying between $50 - 400 \text{ m}$ with typical wind speeds $< 4 \text{ m s}^{-1}$. These offshore breezes are balanced by a return flow ($< 1 \text{ m s}^{-1}$) over sea moving landward at a height of $100 - 1000 \text{ m}$ and descending over the coast. In this case, the convergence zone tends to form cumulus clouds over the sea, where the air flows upward. This boundary is known as the ‘land-breeze front’.

As expected from thermally-induced winds, the strength of sea-land breeze systems is directly proportional to the temperature gradient between air over land and air over the ocean (Pielke and Segal, 1986). Hence, frequency and intensity of sea-land breeze events are higher during periods of strong daytime heating and night time cooling in the absence of large scale wind systems. In tropical and subtropical climates, where the atmospheric pressure gradient between land and sea tends to be steady throughout the year, sea-land breeze events are expected to occur at any season. On the contrary, in temperate climates, sea-land breezes have often to overcome winds from different directions driven by the passage of cyclones and anticyclones which affects its appearance (Simpson, 1994). At these latitudes, the breeze system needs a temperature difference between land and sea which must be large enough to promote breezes getting over large scale wind systems. Therefore, they are most frequently observed during spring and summer months when large sea-land temperature differences are accompanied by favourable synoptic conditions. A nice exam-

ple of seasonal variability for sea-land breezes is shown in Zhang et al. (2009) for the Texas-Louisiana shelf (Figure 1.3). They use a wavelet power spectrum of the eastwest wind component to evaluate the temporal evolution of the wind variance at a location on the shelf from December 1997 to April 2004. As it can be seen from the spectrum, the magnitude of diurnal wind variance, mainly associated with sea breeze, peaks in summer months (June-August) and is weaker during the nonsummer months (September-May) (Zhang et al., 2009).

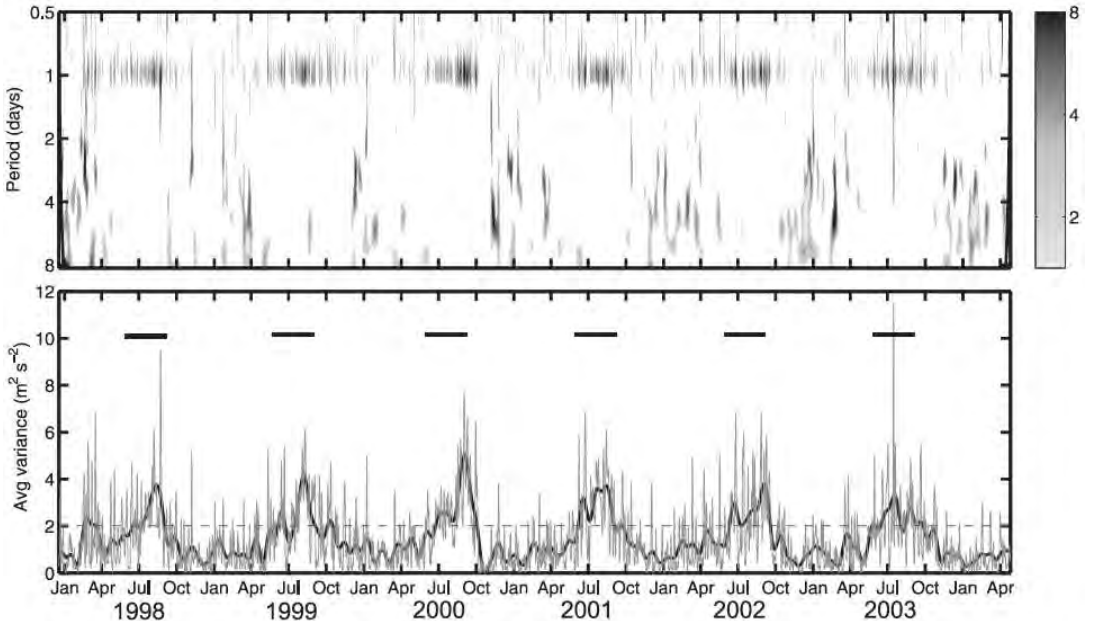


Figure 1.3: Seasonal Variability of Sea-land Breezes on the Texas-Louisiana shelf - (top) Wavelet power spectrum (unitless) of the normalized 10-m eastwest wind component (mean value was subtracted from the time series and then normalized by the standard deviation) at NDBC buoy station PTAT2 (27.838°N, 97.058°W). Only significant values are plotted, which are >95% confidence for a red-noise process with a lag-1 coefficient of 0.72 (Torrence and Compo 1998). (bottom) The gray solid curve is the frequency- (period) averaged wavelet variance time series ($\text{m}^2 \text{s}^{-2}$) over the 0.831.17 cpd band during the observation period. The black solid curve is the 3-month low-passed values of the gray curve. The horizontal gray dashed line is the 95% confidence level. The black bars indicate summer periods. [From Zhang et al. (2009) - Fig. 2].

1. INTRODUCTION TO A BREEZE-FORCED SCENARIO

Along a straight coastline and over a flat terrain, the sea breeze initially extends out to sea as well as inland at right angles to the coast. Along the day-time, the breeze direction shifts a few degrees anticyclonically due to Earth's rotation and, after a period of time, may approach geostrophic balance flowing approximately parallel to the coastline if the circulation is long lived (Lyons, 1972), particularly at offshore locations. The period of time the breeze direction would take for this shift is related with the Coriolis parameter and so depends on the latitude. Land breezes, in contrast, are usually less shifted, no more than 20-30°.

Nevertheless, most coastlines are irregular what induces areas of breeze convergence and divergence. Hence, wherever the coast is not straight, the shape of the shoreline makes the result more complicate and the breezes flow will not be uniform. Simpson (1994) showed in a simple diagram (Figure 1.4) how the sea breezes converges (the land breezes diverges) at convex coasts; and, inversely, the sea breezes diverges (the land breezes converges) when the coast is concave. Accordingly, convergences zones which promotes strong sea breezes during daytime (and weaker divergent land breezes at night) can be found in capes, peninsulas, etc. And divergent sea breezes (convergent land breezes) occur more frequently in bays, gulfs, etc.

Wind shifts, in addition to those produced by Earth's rotation and irregularities along the coastline, may be also produced by the presence of coastal topography. This effect tends to shift the sea-breeze direction later in the day towards the main heated land mass further inland. All these factors together make the behaviour of a sea-land breeze event to be not straightforward. The result can be as surprising as we may find breezes rotating at different senses over relatively close areas, oscillating even against Earth's rotation (Simpson, 1994).

The fact of sea-land breeze systems are not determined by solely one aspect, but depend on the interaction of several local factors, presents important consequences on forcing the coastal ocean. As one can imagine, a clockwise rotating wind system will not produce the same ocean response at a given latitude than a counterclockwise rotating wind. Thus, an appropriate methodology which allow us to characterize in time-frequency space both the amplitude and rotating properties of sea-land breezes is crucial to further explore dynamics of breeze-forced oscillations in the ocean. On the basis of these arguments, we find rotary wavelet method (*Appendix A*) a suitable option to this kind of studies, though to our knowledge it has no been yet applied in the literature.

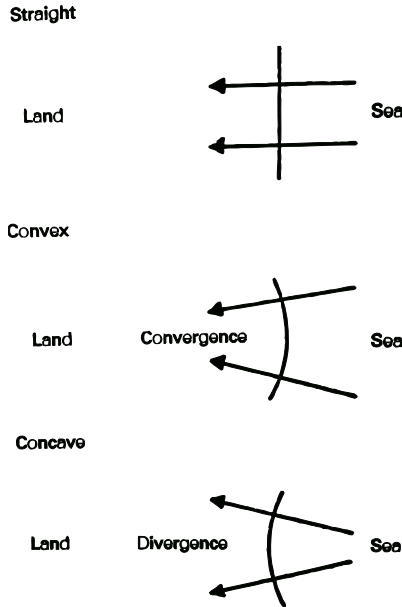


Figure 1.4: The Effect of Coastlines on Sea Breezes - The effect of curved coastlines on the strength of the sea breeze. It is strengthened by convex coasts and weakened by concave ones. [From Simpson (1994) - Fig. 7.1].

1.2 Breeze-Forced Oscillations

In coastal areas where dominant wind is driven by a pressure gradient between air over land and over sea at diurnal cycles ('sea-land breezes'), the ocean may be forced in response to this periodic transfer of momentum. The motion which results from this forcing is known as 'breeze-forced oscillations' (BFOs).

These forced-motions are characterized by anticyclonic rotation at the diurnal frequency and a 180° out of phase configuration between currents flowing above and below the pycnocline. To the reader's eyes this description could perfectly match to that attributed to 'free' near-inertial motions acting near 30°N/S , where inertial and diurnal periods are close to each other. However, although breeze-forced oscillations are a type of near-inertial motions, and so the similarity, the former presents some features which makes them different.

In general terms, near-inertial oscillations (NIOs) arise in response to impulsive injections of momentum, which may be caused by changes in the

1. INTRODUCTION TO A BREEZE-FORCED SCENARIO

wind stress vector (Pollard and Millard, 1970) or by the transient response in a geostrophic adjustment process (Gill, 1984). The resulting motions are driven by a dynamic balance between the geostrophic and radial accelerations, which makes them rotate anticyclonically at the local inertial frequency f . The surface-generated oscillations are consequently more energetic in the surface layers, and propagates downwards through the water column via internal friction (Qi et al., 1995). Consequently, there is an increasing phase delay and decreasing energy with depth relative to near-inertial currents rotating at shallower layers. The vertical structure is thus characterized by a first baroclinic mode with a phase shift of $\sim 180^\circ$ between surface and bottom layers (Millot and Crepon, 1981; Orlić, 1987; Salat et al., 1992; Knight et al., 2002). These ‘free’ motions may last for many oscillatory cycles, especially in regions where the frictional damping is weak.

On the contrary, breeze-forced oscillations are ‘periodic’ inertial motions in response to a more regular forcing close to the inertial frequency (Hyder et al., 2011). At first, the ocean response seems analogous to that exhibited by ‘free’ near-inertial oscillations, anticyclonic currents rotating phase-shifted above and below the pycnocline. Nevertheless, these wind-generated oscillations near coastal areas differ from purely near-inertial oscillations in several aspects that we describe now, and which respond to the nature of its driving force: the sea-land breezes.

Regarding to its time variability, breeze-forced oscillations are of higher appearance and intensity during summer months, according to its forcing variability. Throughout this seasonal period, atmospheric pressure gradient due to enhanced diurnal heating and cooling cycles promotes stronger breezes with uninterrupted phase, and subsequently the transfer of energy to the ocean results in a diurnal band which is highly enriched within the kinetic spectrum. For instance, Zhang et al. (2009) examine the breeze-forced oscillation variability on the Texas-Louisiana shelf (TLS) using wavelet analysis. Thus, they presented the wavelet power spectrum of the north-south current time series at 14 m in order to highlight how the diurnal-inertial band (DIB) peaks in summer compared to nonsummer seasons (Figure 1.5). In their analysis they also found that, while stratification helps the enhancement of the DIB current variance, the deepening of the mixed layer depth appears to weaken it (Zhang et al., 2009).

1.2 Breeze-Forced Oscillations

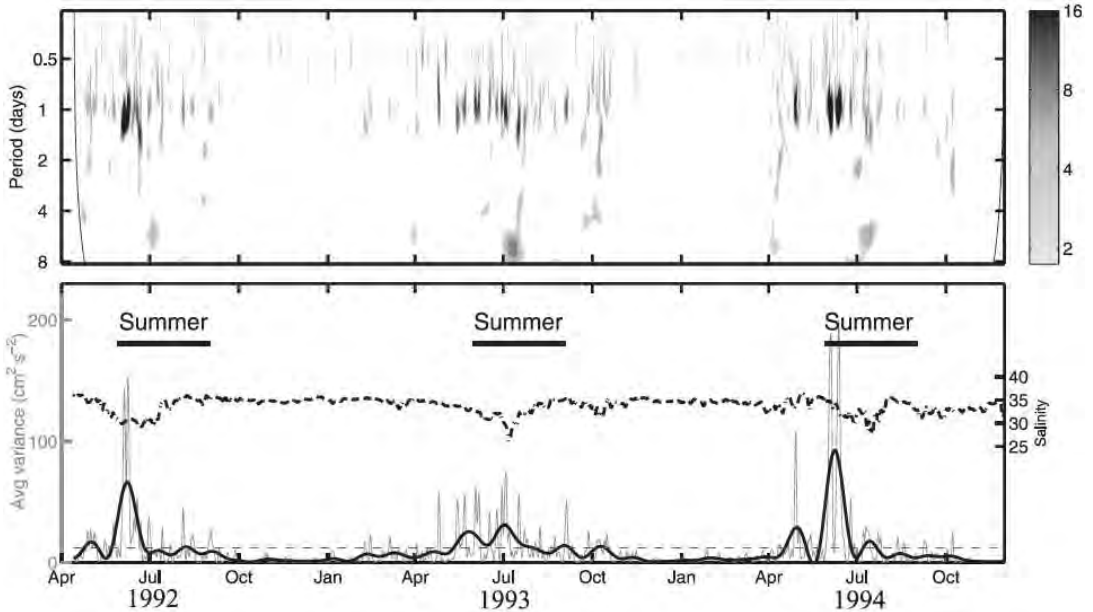


Figure 1.5: Seasonal Variability of Breeze-Forced Oscillations on the Texas-Louisiana shelf - (top) Wavelet power spectrum (unitless) for the hourly northsouth current time series at the upper meter (14 m) of mooring 21. Only significant values are plotted, which are those $>95\%$ confidence for a red-noise process with a lag-1 coefficient of 0.72 (Torrence and Compo 1998). The two gray lines on either end indicate the cone of influence, where edge effects become important. (bottom) The gray solid curve is the frequency- (period) averaged wavelet variance time series ($\text{cm}^2 \text{s}^{-2}$) over the 0.831-17-cpd band during the observation period. The black curve is the 1-month low-passed values of the gray curve. The horizontal gray dashed line is the 95% confidence level. The black dashed-dotted curve is the 2-day running averaged salinity time series at the top meter of mooring 21. [From Zhang et al. (2009) - Fig. 4].

It is also remarkable, that rotating currents from breeze-forced oscillations are of similar magnitude at all depths across the shelf and to the shelf edge (e.g. Figure 1.6), with apparently no phase propagation effects downwards, as it happens for inertial oscillations. Craig (1989b) proposed that flow reversal at depth is forced through a barotropic surface slope driven by the breezes, and as a result of the no-normal-flow condition at the coastal boundary (see also Webster (1968); Chen and Xie (1997)). Thus, breezes would be able to transfer energy to the near bed through a pressure gradient which is of comparable magnitude to the surface forcing but opposite in phase. This

1. INTRODUCTION TO A BREEZE-FORCED SCENARIO

mechanism (which is further detailed in *Section 1.2.1-1.2.2*) has been modeled with success to account the observed energetic phase-shifted currents in the lower layers (Rippeth et al., 2002; Simpson et al., 2002).

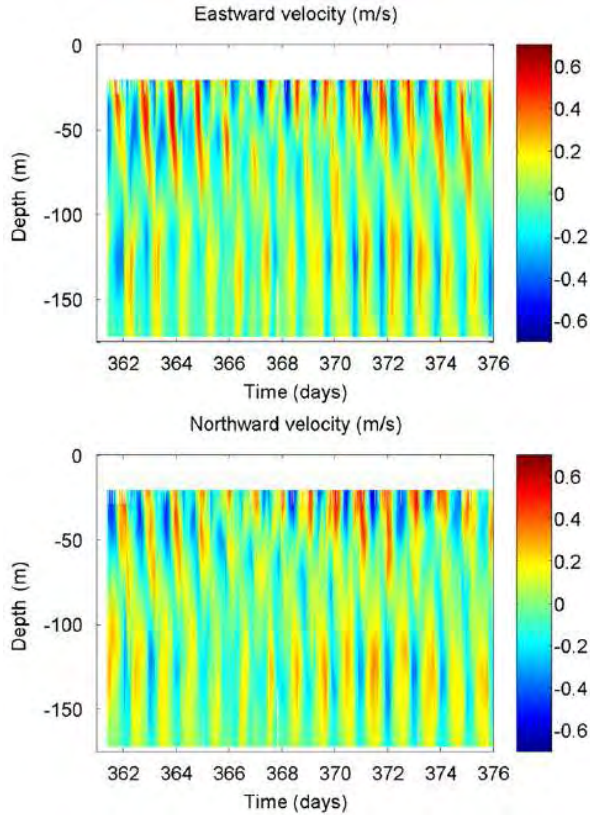


Figure 1.6: Breeze-Forced Oscillations on the Namibian shelf - The observed vertical structure of eastward and northward currents over a fifteen day period from 28 December 1998 00:00 GMT to 12 January 1999 00:00 GMT. Note these are observed total current with the mean over the 15-day period removed from both current components (i.e. no filtering has been applied). [From Hyder et al. (2011) - Fig. 6].

Unlike ‘free’ inertial motions, which present a random phase evolution as a result to impulsive injections of momentum, breeze-forced oscillations exhibit an almost constant phase evolution in time while being forced at a specific frequency (that from the sea-land breezes). In this regard Simpson et al.

(2002) show an illustrative example for a breeze forcing which is interrupted (after day 31 in Figure 1.7) and the resultant motion switches to the inertial frequency so that, when viewed as a diurnal-forced motion, there is a regular increase in the phase lag with time (Figure 1.7). Thus the alternation of diurnal-forced and transient-inertial oscillations is an expected feature of wind-forced motions. Additionally, some authors Hyder et al. (2002); Rippeth et al. (2002); Sobarzo et al. (2007); Hyder et al. (2011) have also observed in time series data that there is a beat period of $\sim (2\pi/(\omega - f))$ in which the strength of the periodic diurnal current components (ω) oscillates in combination with free phase inertial current components (f).

Geographically, near-inertial motions are a widespread feature in deep and coastal oceans which brings into play an important source of energy available for mixing (Webster, 1968; Millot and Crepon, 1981; Salat et al., 1992; Font et al., 1995; van Haren et al., 1999; Knight et al., 2002; van Aken et al., 2005; Sobarzo et al., 2007; Chaigneau et al., 2008). However, near-inertial energy level is not uniform worldwide and is more variable than the rest of the spectrum (Fu, 1981; Garret, 2001; Gerkema and Shrira, 2005). Breeze-forced oscillations contribute (among other phenomena not addressed here) to those geographical differences on the near-inertial energy levels. This is based on the fact that depending on the latitude in which the breeze forcing is acting, the ocean response may be resonant. Thus, near 30° N/S, inertial and diurnal periods are close to each other and the transfer of momentum and energy from breeze forcing to inertial motions can be significantly increased (Hyder et al., 2002; Rippeth et al., 2002; Simpson et al., 2002; Sobarzo et al., 2007).

On the basis of all mentioned differences between breeze-forced oscillations and ‘free’ near-inertial oscillations, valuable efforts have been done in the last decades to develop theory and model breeze-forced oscillations (Craig, 1989b; Chen and Xie, 1997; Rippeth et al., 2002; Simpson et al., 2002; Hyder et al., 2002, 2011). In the following, we review theoretical and modeling works which focus on the observed behaviour of the ocean to breeze forcing. Additionally, we point out those modeling results which predict interesting features not yet confirmed with observations and thus needed of further research. This review provides a deeper insight into the physics behind the generation and evolution of breeze-forced oscillations.

1. INTRODUCTION TO A BREEZE-FORCED SCENARIO

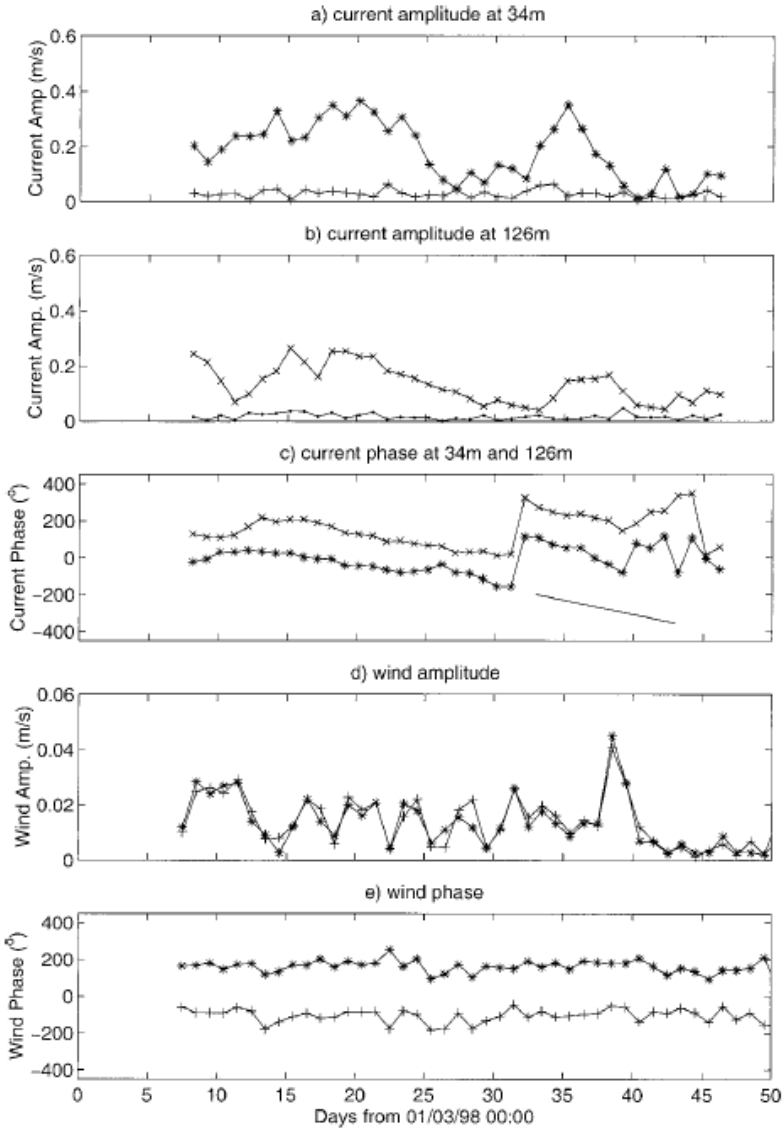


Figure 1.7: Phase Evolution of Breeze-Forced and Free Near-Inertial Oscillations - Amplitude and phase of the diurnal motion over the full recording period. (a) Current at 34-m anticlockwise (*) and clockwise (+), (b) current at 126 m anticlockwise (x) and clockwise (●), (c) phase of anticlockwise component at 34 m (*) and 126 m (x), (d) wind amplitude as anticlockwise (*) and clockwise (+) components, and (e) phase of the wind components (*) anticlockwise and clockwise (+). The straight sloping line in (c) indicates the rate of phase change of a pure inertial oscillation ($15.5^\circ \text{ d}^{-1}$). [From Simpson et al. (2002) - Fig. 7].

1.2.1 Periodic Forcing and Near-Inertial Resonance

Theoretical and modeling advances on the ocean response produced by periodic forcing (tidal and wind forcing) at a particular frequency have been greatly benefited from the studies of Battisti and Clarke (1982) and Craig (1989a,b). In the following we describe the dynamics of breeze-forced oscillations by introducing some recent illuminating works.

Critical Latitudes for Resonance

The essential mechanism and latitudinal variation of diurnal wind-forced motions are clearly illustrated in Simpson et al. (2002) with a simple slab model for a water column of depth H vertically uniform in velocity forced by an oscillating wind stress τ_s with no horizontal pressure gradients (Figure 1.8). Frictional damping is introduced linearly via $(-ru, -rv)$, leaving the dynamical equations for the complex velocity $w = u + iv$ as

$$\frac{\partial w}{\partial t} + if\omega = \frac{-rw + \tau_s}{\rho H} \quad (1.1)$$

Then, the complex amplitudes for clockwise (W_-) and anticlockwise (W_+) forcing at frequency ω are

$$W_- = \frac{A_-}{i(f - \omega) + r'}; \quad W_+ = \frac{A_+}{i(f + \omega) + r'} \quad (1.2)$$

where $\tau_s/(\rho H) = A_{\pm}e^{\pm\omega t}$ and $r' = r/(\rho H)$. As it can be seen in Figure 1.8 (top), the ocean response is resonant ($W \rightarrow A/r'$) for the clockwise case at the critical latitude of 30°N where $f = \omega$, and for the anticlockwise case at the critical latitude of 30°S where $f = -\omega$. In other words, the ocean response is resonant when diurnal and inertial periods are close to each other. Under these circumstances, current and forcing are in phase and the transfer of momentum and energy is significantly enhanced. It is also shown that the phase of the current changes rapidly between limiting values of $+\pi/2$ and $-\pi/2$ farther than 30°N/S , and that this effect is sharper when using a higher coefficient for frictional damping.

1. INTRODUCTION TO A BREEZE-FORCED SCENARIO

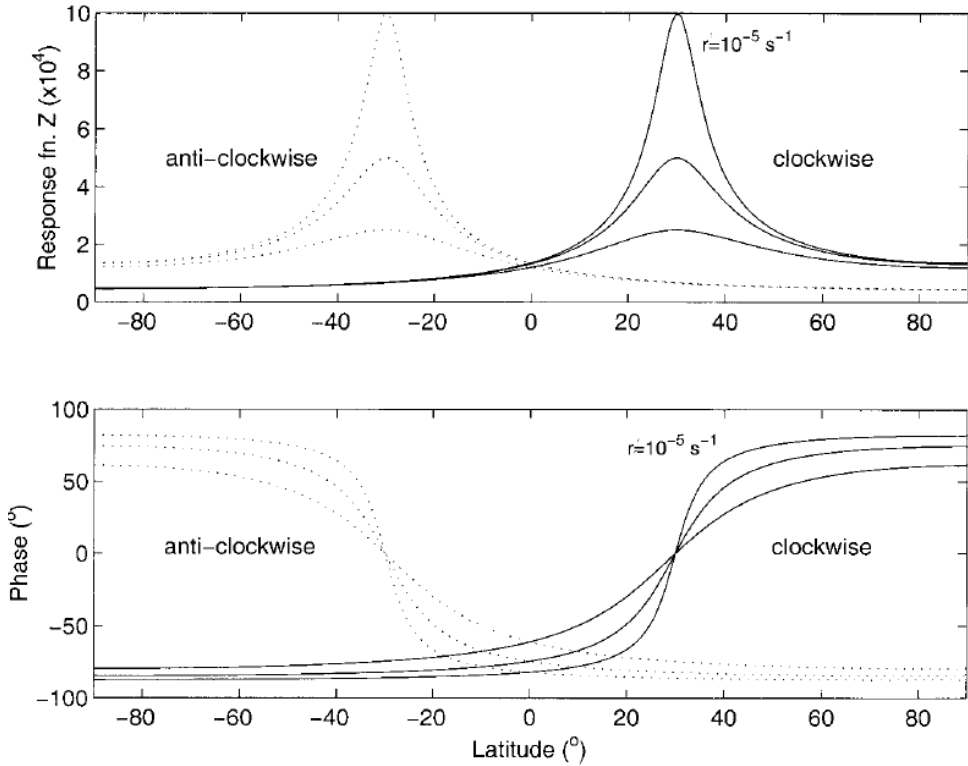


Figure 1.8: Slab Model of Forced Oscillations - Variation of the response function $Z = W/A$ with latitude for a simple slab model of forced oscillations with $r' = 10^{-5}, 2 \cdot 10^{-5}, 4 \cdot 10^{-5} \text{ s}^{-1}$. The amplitude (a) and phase (b) are shown for clockwise (solid line) and anticlockwise (dotted line). [From Simpson et al. (2002) - Figure 1].

Dynamics of Rotary Breeze-Forced Oscillations

If we now move a step forward, we find the two-layer model developed by Simpson et al. (2002), which allows us to introduce the physics behind breeze-forced oscillations in coastal areas. They hypothesised an oscillatory diurnal wind stress acting directly at the ocean surface and in the presence of a coast. This condition produces a coast-normal surface slope variation which drives the transfer of momentum to the whole water column through a pressure gradient of comparable magnitude but opposite in phase to the surface forcing.

From this starting point, Simpson et al. (2002) use a frictionless two-layer

analytical model with the upper layer being forced by a diurnal wind stress and the opposing surface slope resulting from this wind forcing; and, the lower layer being forced solely by the surface slope. This external pressure gradient forces the lower layer leading to phase-shifted motions with relatively the same amplitude as in the upper layer. The model successes on reproducing the key features of reported breeze-forced oscillations in the literature: anticyclonic currents rotating $\sim 180^\circ$ out of phase above and below the pycnocline with energetic amplitudes of similar magnitud and almost constant phase within every layer (Chen et al., 1996; Rippeth et al., 2002; Simpson et al., 2002; Zhang et al., 2009; Hyder et al., 2011). In contrast to what is observed with free near-inertial motions (Millot and Crepon, 1981; Orlić, 1987), which exhibit an increasing phase delay and less energetic currents in deeper waters due to momentum is transferred downward through the shear stress described by classical Ekman theory.

Simpson et al. (2002) set their simple two-layer model to account the diurnal wind-forced ocean response as follows. They consider the flow in a shelf region bounded by a coastline extending in the y direction at $x = 0$ and with a depth profile $H(x)$. The layers are assumed to be uniform in density (ρ) and velocity (u, v) but decoupled from each other by a frictionless interface. Depth of each layer is given by h_1 and h_2 , the upper and lower layers, respectively. The motion is forced by an oscillatory wind stress (τ_x, τ_y) at the diurnal frequency ω , which acts directly only at the surface layer. Hence, they derive the following momentum equations for the upper (subscript 1) and lower (subscript 2) layers

$$\begin{aligned} \frac{\partial u_1}{\partial t} - f v_1 &= \frac{\tau_x}{\rho h_1} - g \frac{\partial \eta}{\partial x}, \\ \frac{\partial v_1}{\partial t} + f u_1 &= \frac{\tau_y}{\rho h_1}; \end{aligned} \tag{1.3}$$

$$\begin{aligned} \frac{\partial u_2}{\partial t} - f v_2 &= -g \frac{\partial \eta}{\partial x}, \\ \frac{\partial v_2}{\partial t} + f u_2 &= 0; \end{aligned} \tag{1.4}$$

where η is the surface elevation, g is gravitational accelaration, and f is the Corilis frequency. The key component of this model enters into play through

1. INTRODUCTION TO A BREEZE-FORCED SCENARIO

the ‘Craig approximation’ (Craig, 1989b) (eq. 1.5), which sets up the role of the coastal boundary inducing a pressure gradient in response to surface stress forcing. The approximation derives from the lowest order vertically integrated solution, after assuming that the ratio of the shelf width L to the barotropic wavelength $2\pi(gH)^{1/2}/\omega$ is small. This requirement of the ‘Craig approximation’ implies that the time of transit of a barotropic wave across the shelf is small in comparison to the inertial period. Then, the surface slope induced by the applied wind stress can be defined as

$$\frac{\partial\eta}{\partial x} = \frac{\tau_x + i(f/\omega)\tau_y}{\rho g H}. \quad (1.5)$$

Because of the no-normal-flow condition at the coast, the diurnal cross-slope wind stress τ_x generates an opposing surface slope component. In accordance, the diurnal alongshore wind stress τ_y induces a coast-parallel, depth uniform current $V = i\pi/(\omega g H)$ that, in geostrophic balance, requires a surface slope component of amplitude $(f/\omega)\tau_y/(\rho g H)$.

As the system is derived, it is clear that the wind stress forcing and the opposing surface slope govern the upper layer, while in the lower layer only operates the induced surface slope variation (the pressure gradient associated with the surface slope acts throughout the entire water column).

Defining the complex velocity as $w = u + iv = We^{i\omega t}$, and introducing the ‘Craig approximation’ into the momentum equations, eq. (1.3) and eq. (1.4), Simpson et al. (2002) describe the diurnal-inertial resonance in the Southern Hemisphere through the regular oscillatory solutions for anticlockwise motion

$$W_1 = \frac{\gamma T_x + i(\gamma + f/\omega + 1)T_y}{i\rho H(f + \omega)}; \quad (1.6)$$

$$W_2 = \frac{-(T_x - if/\omega T_y)}{i\rho H(f + \omega)}. \quad (1.7)$$

with $\gamma = h_2/h_1$, positive ω corresponding to anticlockwise motion; T_x and T_y being the complex amplitudes of the wind stress; and W_1 and W_2

the complex amplitudes of the motion in upper and lower layer, respectively. Thus, the ocean response, eq. (1.6) and eq. (1.7), for the anticyclonic motion will be enhanced at latitudes close to 30° S where it enters in resonance with $f \rightarrow -\omega$ so that $f/\omega \rightarrow -1$ leading to

$$W_1 \approx \frac{\gamma T_x + i(\gamma + iT_y)}{\rho H(f + \omega)} \approx W_2. \quad (1.8)$$

This particular solution for the steady state response of the ocean near critical latitudes reproduces the main features of observed wind-forced diurnal-inertial oscillations that may be influenced by land boundaries (Chen et al. (1996); Rippeth et al. (2002); Simpson et al. (2002); Zhang et al. (2009); Hyder et al. (2011)). The phase of the forced-motion oscillating within the diurnal-inertial band is shifted by 180° between upper and lower layers, and the velocity amplitude is of comparable magnitude in the two layers when the factor γ , which is a function of the depth of the pycnocline, is of order unity as it occurs in the study area of Simpson et al. (2002). Analogous effects are obtained from the regular oscillatory solutions for clockwise motion in the Northern Hemisphere (see Rippeth et al. (2002)). The ocean response is then enhanced at latitudes close to 30° N where $f \rightarrow \omega$ (Northern Hemisphere) and the motion is resonant. In both hemispheres, the ocean response to cyclonic forcing at the diurnal frequency is remarkably weaker in the ratio $| (f + \omega) | / | (f - \omega) |$.

It should be noted that the previous model (Simpson et al., 2002) ignores internal and frictional effects in the mechanism. However, these effects of frictional coupling between layers have been further explored by Rippeth et al. (2002) using a continuous model with friction based on the same dynamics as the model of Simpson et al. (2002). Hence, the new model includes many more layers and shear stresses specified in terms of an eddy viscosity. This modeling work was tested for four different cases (Figure 1.9): run A including a pycnocline and the coastal boundary condition; run B including a pycnocline but not a coastal boundary condition; run C not including a pycnocline, but the coastal boundary condition; and, run D not including neither a pycnocline nor the coastal boundary condition. The aim was to evaluate whether the coastal boundary condition or an existing pycnocline determines the vertical structure of wind-forced motions.

1. INTRODUCTION TO A BREEZE-FORCED SCENARIO

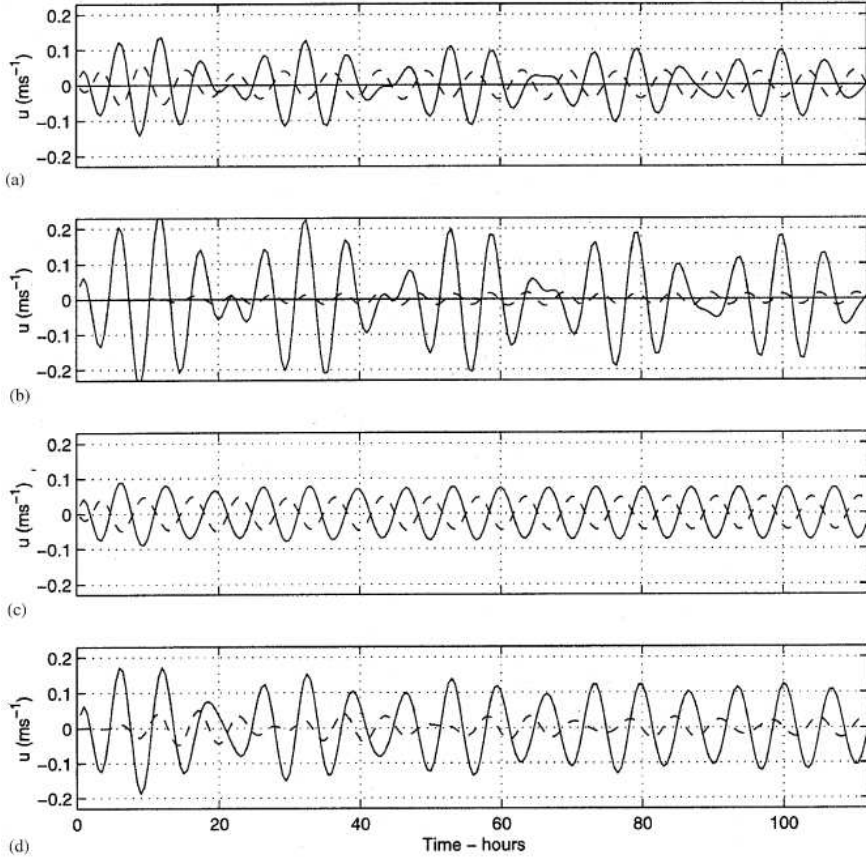


Figure 1.9: A Continuous Model with Friction of Forced Oscillations - Results from the continuous model. The predicted near surface (solid line) and near bed (dotted line) along-shore current components. (a) Run A: results from the model run which includes a pycnocline and the coastal boundary condition. (b) Run B: results from the model run which includes a pycnocline but does not include a coastal boundary. (c) Run C: results from the model run which includes the coastal boundary but no pycnocline. (d) Run D: results from the model run with no coastal boundary or pycnocline. [From Rippeth et al. (2002) - Fig. 9].

Run results only reproduced the characteristic phase shift and the penetration of energy to near the bed in the cases where the coastal boundary condition was included (run A and run C in Figure 1.9), whereas in its absence (run B and run D) forced motions did not exhibit these features. The authors also found that internal shear stresses did not greatly modify the frictionless

response to forcing (run A and run C), and confirmed that the reverse flow in the lower layers primarily results from a barotropic pressure gradient ('Craig approximation') set up by the applied wind stress and the no-normal-flow condition at the coastal boundary, which is the basis of the model. Consequently, these results point out that the upper and lower layers of breeze-forced motions behave differently than those in purely inertial motions, where the out of phase layers are not driven by a constant forcing but by phase propagation effects and the pycnocline has as well a main role in the propagation.

Modeling results from Rippeth et al. (2002) also find a beating cycle between diurnal and inertial periods, despite using a diurnal forcing. In the case of runs without a pycnocline (runs C-D), the beating dies after 4 days as the transient signal is damped out, leaving a steady state diurnal period solution. This behaviour appear to be consistent with previously mentioned beat periods found in observational data (Hyder et al., 2002; Sobarzo et al., 2007; Hyder et al., 2011).

1.2.2 Stratification and Vertical Mixing

Near-inertial oscillations close to the critical latitude for diurnal-inertial resonance play an important role on vertical mixing processes, specially in coastal stratified areas with low tidal energy (Rippeth et al., 2002; Simpson et al., 2002; Hyder et al., 2011). As highlighted in Hyder et al. (2011), earlier suggestions that NIOs brings into play around half the kinetic energy in the worlds oceans (Pollard and Millard, 1970; Pollard, 1980, 1970) are now confirmed with new observations. Thus, an estimated energy flux of $\sim 0.5-0.7$ TW can be found in the literature, a value comparable with that from the internal tides of 0.9TW (Park et al., 2005; Watanabe and Hibiya, 2002; Alford, 2003a,b; Munk and Wunsch, 1998).

The first baroclinic mode of NIOs, with antiphase motions between layers above and below the pycnocline, carries along high vertical shears which promote dissipation and vertical mixing in stratified areas. Previous works about strong inertial oscillations (Knight et al., 2002; van Haren, 2000) estimated the gradient Richardson number, Ri , to assess mixing conditions promoted by NIOs. This nondimensional number is calculated by

$$Ri = \frac{N^2}{S^2} , \tag{1.9}$$

1. INTRODUCTION TO A BREEZE-FORCED SCENARIO

where N^2 is the squared Brunt-Väisälä frequency (squared buoyancy frequency), and S^2 is the squared vertical current shear applied to a fluid parcel. The squared Brunt-Väisälä frequency is given by

$$N^2 = -\frac{g}{\rho_0} \frac{\Delta\rho}{\Delta z}, \quad (1.10)$$

where ρ is the potential density calculated from temperature and conductivity data; g is the gravity constant; ρ_0 is the averaged potential density; and Δz is the vertical distance between the top and the bottom of the fluid parcel. Finally, the vertical squared shear is given by

$$S^2 = \left(\frac{\Delta u}{\Delta z}\right)^2 + \left(\frac{\Delta v}{\Delta z}\right)^2, \quad (1.11)$$

where Δu and Δv are the east-west and north-south current differences between the top and bottom of the fluid parcel, respectively. Then, typical values for $Ri < 1$ indicate the generation of Kelvin-Helmholtz instabilities caused by the vertical shear that triggers mixing in a stratified fluid (Miles, 1986; Van Gastel and Pelegrí, 2004). On the contrary, if $Ri \gg 1$, buoyancy is dominant since there is insufficient kinetic energy to homogenize the water column.

Knight et al. (2002) estimated Ri using ADCP and CTD data in the North Sea and found values less than 1 when strong inertial currents carried large vertical shears across the thermocline, although never approached to critical values of 0.25. Dissipation measurements were also made and indicated that mixing within the thermocline layer was more intense and was associated to high mean thermocline diffusion coefficients when large inertial current shears were acting. Modeling results and observations in the North Sea (van Haren, 2000) also support the importance of tidal and inertial shear across stratification for vertical exchange likely due to internal shear-driven turbulence.

If we now consider inertial motions acting around the critical latitudes for diurnal-inertial resonance, one finds that the near-resonant response to diurnal wind forcing involves an efficient transfer of momentum and energy to the ocean with diurnal-inertial motions dominating the kinetic energy spectrum (Simpson et al., 2002). Under these conditions, it is reasonable to expect that breeze-forced oscillations represent the major source of turbulent kinetic energy driving vertical mixing, specially in the absence of friction resulting

from strong tidal motion (Rippeth et al., 2002; Simpson et al., 2002; Hyder et al., 2011). Nevertheless, observations of vertically sheared flows are not in themselves evidence of mixing as rightly pointed out by Zhang et al. (2009). To our knowledge, they published for the first time a time series analysis of the effects of observed breeze-forced oscillations on the vertical mixing.

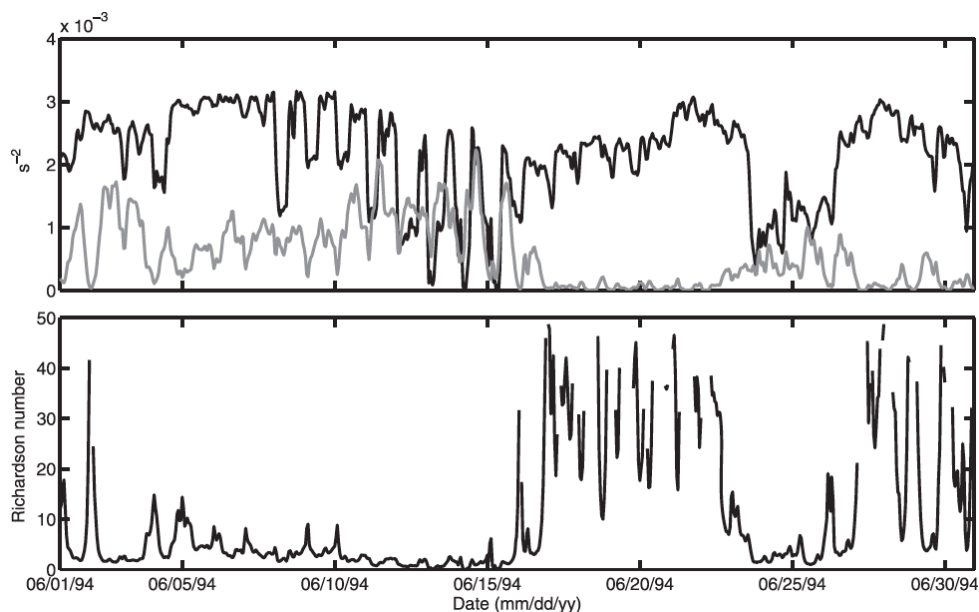


Figure 1.10: Effects of Breeze-Forced Oscillations on the Vertical Mixing - (top) The black and grey curves are the Brunt-Väisälä frequency and squared shear time series calculated from the temperature, conductivity and current measurements at mooring 22, respectively. (bottom) Bulk Richardson number time series calculated from the Brunt-Väisälä frequency and squared shear time series (Ri_b). For clarity, the bulk Richardson number is potted only when it is less than 50. [From Zhang et al. (2009) - Fig. 10].

Zhang et al. (2009) estimated the bulk Richardson number on the Texas-Louisiana shelf (TLS) with measurements at two depths (3 and 23 m) at mooring 22 (28.35°N, 93.96°W, ~ 50 m depth), what allowed them to explore the stability of the water column during breeze-forced current events as a part of the LATEX project (Figure 1.10). Thereof, they found that during strong events of breeze-forced currents (~ 12 and 21-24 June 1994) the bulk Richardson number was suppressed. The velocity shear increased significantly during these periods and the stratification decreased, making the bulk Richardson

1. INTRODUCTION TO A BREEZE-FORCED SCENARIO

number small (on the order of 1 on ~ 12 June 1994). And, on the contrary, they observed the bulk Richardson number became larger because of the increase of the stratification and the significant decrease of the velocity shear when breeze-forced currents were suppressed after a meteorological front passed by mooring 22 on 16 June 1994. This analysis supports that strong breeze-forced current events could significantly enhance the vertical mixing through the water column during summer periods of the TLS.

Although sea-breezes have been widely described and reported, further research is needed to better understand breeze-forced current dynamics around the critical latitudes for diurnal-inertial resonance; and, subsequently, to assess the real impact of this atmosphere-ocean interaction on the vertical mixing of stratified waters.

1.3 Scope of the Study

Hyder et al. (2011) made a valuable effort representing on a world map (Figure 1.11) the locations where surface rotary diurnal currents have been reported. They indicate observations attributed to wind-forced diurnal currents with \ast 's; whereas \bullet 's indicate those candidates they suggest that could be wind-forced motions or re-analysis may help to determine whether they are indeed wind-forced motions. However, the authors are cautious and point out that this database is not comprehensive, and also that some missing cases might be masked by, or have been attributed to, tidal forcing.

Figure 1.11 is also used by Hyder et al. (2011) to present expected regions of diurnal-inertial resonance based on the poleward limit of known observations for wind-forced rotary diurnal surface currents in the Aegean at 40° N (Hyder et al., 2002), where $\omega/f \sim 0.77$ (inertial period 18.7 h). Thus, the authors induced from theory that an estimated equatorward limit might be 23° S, where we find again that $\omega/f \sim 0.77$ (inertial period 30.9 h).

Resonant regions for tidal forcing are expected to act similarly (Maas and Van Haren, 1987; Furevik and Foldvik, 1996), and are shown in Figure 1.11 assuming the same ω/f limits for diurnal tidal periods. The result spans broadly the same latitudes as those for wind-forced motions. Analogously, semidiurnal tidal resonance with the inertial period (Furevik and Foldvik, 1996; Middleton and Denniss, 1993) is expected to be found between 48° - 90° N/S for M_2 (period 12.42 h) with resonance at $\sim 75^\circ$ N/S, and between

50°-90° N/S for S_2 (period 12 h) with resonance at the pole.

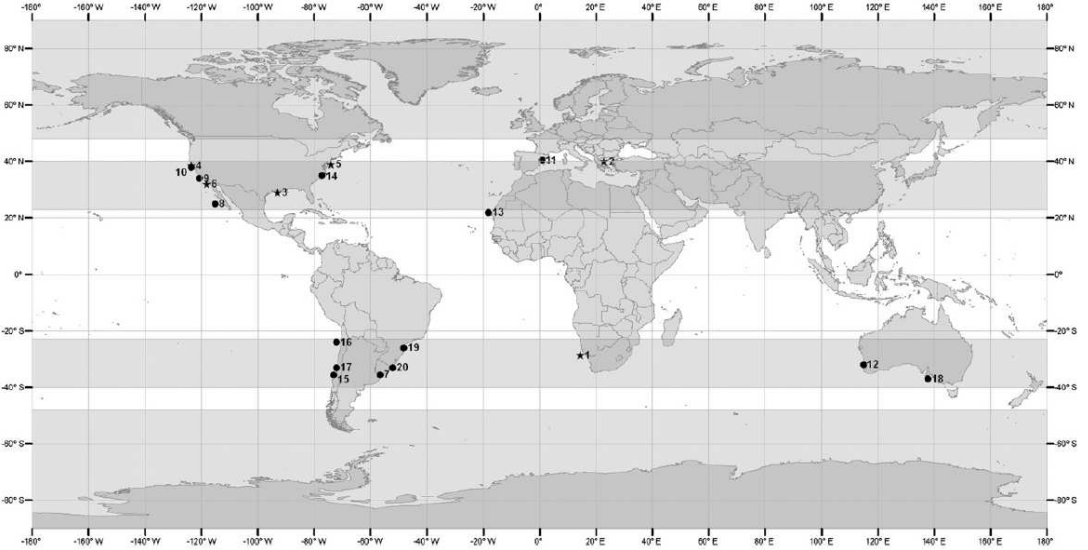


Figure 1.11: Regions for Diurnal/Semidiurnal Resonance¹ - The equatorward regions where diurnal winds or tidal forcing would be expected to force energetic rotary diurnal currents between 23 and 40 N/S are shaded in grey. The corresponding poleward regions of inertial resonance for semi-diurnal M2 tidal forcing, between 48 and 90 N/S, are also shaded. [From Hyder et al. (2002) - Fig. 2].

From the picture of critical latitud mechanisms which enhance the near-inertial energy band, it is also interesting to mention the parametric subharmonic instability (PSI) (Simmons et al., 2004; MacKinnon and Winters, 2005; Van Haren, 2005; van Haren, 2007), which involves the energy transfer from semidiurnal tides to higher-frequency near-inertial motions at latitudes near 28.8° N/S.

However, although the dynamic response to wind-forced periodic surface slope is similar to that for the tidal forcing, it is important to recall that the latter acts through the entire water column and, hence, frictional damping and bottom layer effects may be expected to be more relevant. This condition need to be considered since it may reduce the extent of the tidal resonant regions (Hyder et al., 2011).

This PhD study contributes to the described context for ‘breeze-forced os-

1. INTRODUCTION TO A BREEZE-FORCED SCENARIO

cillations' providing observational results and analysis from four new locations on this topic around the Iberian Peninsula and hence framed poleward of the critical latitude (30° N/S) for diurnal-inertial resonance.

Firstly, in *Chapter 2* we use time series data from two regions which may act as a proxy of resonant breeze-forced oscillations poleward of the critical latitude for diurnal-inertial resonance: the Gulf of Cádiz and the Gulf of Valencia. Concurrently we also present time series data from a third region in which resonance is not expected to occur. This last region is placed nearby, but out of the critical latitudes, and serves as a 'blank test' for our study: the Cape Peñas area. The research focused in this case on the characterization of the temporal evolution of observed breeze-forced oscillations. Special attention is given to the effects of the phase correlation between the breeze forcing and the subsequent ocean response giving rise to resonant breeze-forced oscillations and, therefore, enhancing the diurnal-inertial energy budget.

Secondly, in *Chapter 3* we explore the role of breeze-forced-oscillations on promoting diapycnal mixing processes. This research provides a new data set of breeze-forced oscillations in the stratified waters of the Bay of Setúbal, framed within the critical latitudes ($30^\circ \pm 10^\circ$ N/S) for diurnal-inertial resonance where they can greatly contribute to triggering diapycnal mixing.

Chapter 2

Breeze-Forced Oscillations Poleward of the Critical Latitude for Diurnal-Inertial Resonance¹

2.1 Outline

The present chapter focuses on the temporal evolution and variability of breeze-forced oscillations (BFOs) poleward of 30° N and near the limit for diurnal-inertial resonance. Observations were collected from three different regions around the Iberian Peninsula (from south to north): the Gulf of Cádiz and the Gulf of Valencia (both regions being within the critical latitudes for resonance); and, the Cape Peñas area (out of the critical latitudes for resonance). The time series data belong to the REDEXT (Red Exterior de Boyas) network of oceanographic and meteorological buoys, and were provided by Puertos del Estado (Spain).

Due to the rotary nature of the process, we find rotary wavelet analysis (Torrence and Compo, 1998; Hormazábal et al., 2002) an obvious and suitable

¹Aguilar-González B., Hormazábal S., Rodríguez-Santana A., Cisneros-Aguirre J., Martínez-Marrero. Breeze-Forced Oscillations around The Poleward Limit for Diurnal-Inertial Resonance. *In Preparation to be Submitted to an International refereed Journal*

methodology to study the temporal evolution of breeze-forced oscillations. However, to our knowledge this is the first time that it is applied with this aim in the literature. Thus, we use rotary wavelet power spectra to characterize and quantify breeze-forced oscillation variance and variability according to its driving force, the sea-land breezes.

Additionally, we use rotary wavelet coherency and phase spectra to further explore how breeze-forced oscillations arise and evolve in time according to the onset of sea-land breezes; therefore, enhancing the diurnal-inertial energy budget.

This research is based on time series data of surface current velocity and wind velocity over annual cycles from three REDEXT buoys. Data and methodology are described in *Section 3.2*. In *Section 3.3* we present and discuss the main results. Special attention is given to observed differences between wind-forced diurnal-inertial oscillations within out of the critical latitudes for resonance. We summarize the main conclusions in *Section 3.4*. *Appendix A* describes the rotary wavelet method used in this study.

2.2 Data and Methodology

Time series data of surface current and wind velocity were provided by Puerros del Estado (Spain) from the REDEXT (Red Exterior de Boyas) network of buoys. This network is composed of Wavescan and SeaWatch moorings measuring oceanographic and meteorological variables all along the spanish coastline. Locations of these moorings were originally chosen to be representative of the surrounding ocean dynamics. Data are transmitted in real time via satellite. After transmission, a control test is applied to guarantee quality of measurements.

In this work we use REDEXT buoys from two different regions which may act as a proxy of resonant breeze-forced oscillations poleward of 30° N and near the limit for diurnal-inertial resonance: the Gulf of Cádiz and the Gulf of Valencia. The third region of study was intentionally selected nearby but out of the critical latitudes for diurnal-inertial resonance: the Cape Peñas area. This configuration allow us to count with a ‘blank area’ in which resonance is not expected to happen in comparison with other two areas where resonance is expected. Thus, we can better elucidate how important can be a situation where resonant breeze-forced oscillations occur as well as how different the

forced mechanism evolves in both situations. The locations of the three buoys are represented in Figure 2.1 and their corresponding inertial periods, offshore distances and depths are listed in Table 2.1.

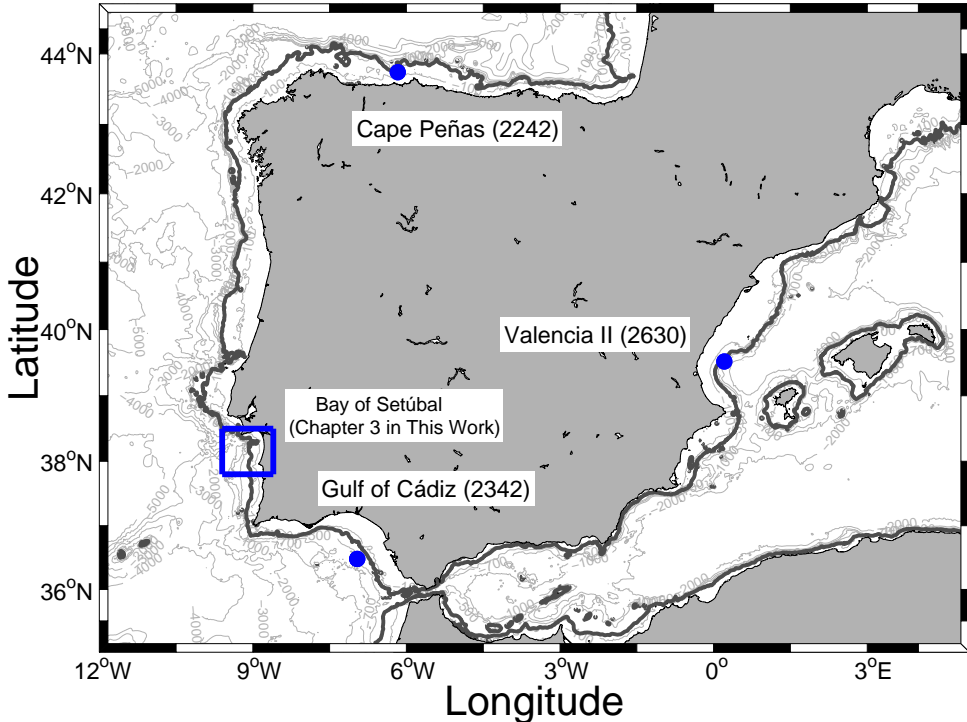


Figure 2.1: Oceanographic Buoys - Puertos del Estado - Map of the Iberian Peninsula showing the oceanographic buoys used in this study and provided by Puertos del Estado from the REDEXT network (Red Exterior de Boyas). Isobath of 200 m is highlighted in black.

In the Gulf of Cadiz, Gulf of Valencia and Cape Peñas area, time series of surface current velocity are collected from a UCM-60 current meter settled in Seawatch REDEXT buoys, which have been providing oceanographic and meteorological data since August 1996, September 2005 and March 1998, respectively. The current meter measures velocity at 3 m depth (range: 0 to 3 m s⁻¹ 1% accuracy and current direction within $\pm 1^\circ$). Meteorological sensors (Aandera 2740 and Aandera 3590) measure wind velocity (up to 70 m s⁻¹) and direction at 3 m over the surface with an accuracy of 1.5% and 1%, respectively (Criado-Aldeanueva et al., 2009). Both surface current and

2. BREEZE-FORCED OSC. AROUND THE POLEWARD LIMIT

wind velocity data are obtained by averaging the measurements of the first 10 min of each hour, providing hourly data to the user. All data marked as of dubious quality by Puertos del Estado during control tests were discarded from our analysis. Gaps in time series, usually due to maintenance or failure of the instruments, have been linearly interpolated when its duration was less than 8 hours. Longer gaps have been left blank. Years with high recurrence of long period gaps were not considered in our study for clarity on the data representation over annual cycles. Additionally, prior to any further analysis, principal tidal constituents were removed from the current measurements using the T_Tide Harmonic Analysis Toolbox of Pawlowicz et al. (2002) to eliminate the influence of principal tidal energy (Zhang et al., 2009).

Buoy (Code)	Position (Lat./Long.)	Offshore Dist. (km)/ Depth (m)	Inertial Period (hr)
Gulf of Cádiz (2342)	36.48°/-6.96°	80 / 450	20.13
Valencia II (2630)	39.52°/0.21°	59 / 260	18.81
Cape Peñas (2242)	43.74°/-6.17°	19 / 450	17.31

Table 2.1: Oceanographic Buoys from Puertos del Estado - Oceanographic buoys used in this study and provided by Puertos del Estado from the REDEXT network (Red Exterior de Boyas).

This chapter attempts to provide a basis for the analysis of resonant breeze-forced oscillations where rotary wavelet method (Torrence and Compo, 1998; Hormazábal et al., 2002) is applied to vector time-series of current and wind velocity (see *Appendix A*). This method separates vector time-series into clockwise (CW) and counterclockwise (CCW) components within time-frequency space (rotary wavelet power spectrum). Further application of the rotary wavelet method on two complex time-series leads to cross-rotary wavelet power spectrum, which provides an estimate of the joint power content of two time-series for rotary components rotating in the same sense. And finally, the rotary wavelet coherency and phase spectrum which, respectively, find significant time-frequency regions where the two time series covary and detects any lag between corotating components of both series, although not necessarily have high power content in common (Hormazábal et al., 2002).

To conclude it is important to note that none time series data were filtered in order to preserve low- and high-frequency variability in our wavelet results. The entire picture provided by rotary wavelet analysis results allow us to explore within the same figure all frequency bands interacting simultaneously in

time and frequency domains for both the atmosphere and the ocean. However, characterization of the general atmosphere/ocean circulation in the areas of study is beyond the scope of this research¹ and, hence, dominant long-period processes will be addressed here only when they play a role on the dynamics of the analyzed breeze-forced scenario.

2.3 Results and Discussion

2.3.1 Characterization of Three Wind-Forced Scenarios

We present a wavelet rotary analysis of meteorological and oceanographic time series data from three different regions around the Iberian Peninsula to characterize the temporal evolution and variability of sea-land breezes and the ocean response to this wind forcing.

Hence, we explore qualitatively simultaneous and co-located measurements of wind at 3 m above the sea surface and ocean currents at 3 m depth. In the next section we use the rotary wavelet method to quantify current variance in response to breeze forcing as well as to investigate the effects of the phase correlation between the forcing and the ocean response in the enhancement of breeze-forced oscillations.

Geographically, the Gulf of Cádiz and the Gulf of Valencia are framed within the critical latitudes for diurnal-inertial resonance ($30^\circ \pm 10^\circ$ N/S). The Cape Peñas area bounds the poleward limit though being out of this range of latitudes (Figure 2.1; see also Table 2.1 for details on local inertial periods). The three areas present a wide continental shelf for the development of the coastal breeze-forced oscillations subject of this study.

A) Temporal Evolution of Sea-land Breezes

Sea-land breezes are thermally-induced winds and so their strength is directly proportional to the temperature gradient between air over land and air over the ocean (Pielke and Segal, 1986). Consequently, one may expect to find higher recurrence and intensity of sea-land breeze events during periods

¹Details on the main currents and tidal components for REDEXT buoys can be found in <http://www.puertos.es>.

2. BREEZE-FORCED OSC. AROUND THE POLEWARD LIMIT

of strong daytime heating and night time cooling in the absence of large scale wind systems.

These conditions can be found specially during summer months when large sea-land temperature differences are accompanied by favourable synoptic conditions and sea-land breezes do not need to overcome winds from different directions driven by the passage of cyclones and anticyclones.

On the contrary, during winter months breezes need a larger temperature difference between land and sea than in summer to promote breezes getting over large scale wind systems¹. As a consequence, sea-land breezes are less probable to occur under this scenario. Spring and autumn months represent the transitional periods between both situations. This pattern responds to the climatology of a sea-land breeze system (Hunter et al., 2007; Zhang et al., 2009).

Figures 2.2-2.4 show the rotary wavelet power spectra of wind at the buoys located in the Gulf of Cádiz, the Gulf of Valencia and the Cape Peñas area, respectively.

Firstly, in Figure 2.2, we observe that the temporal evolution of the wind variance at the Gulf of Cádiz shows a clear seasonal pattern within the diurnal band, the weather band (2-8 days) and the intraseasonal band (16-64 days), for both the clockwise and counterclockwise senses.

The diurnal wind variance appears as a well-defined packet which is visibly enhanced from the early spring to the early autumn (April-October) in comparison to the lately autumn and winter months (November-March). On the contrary, the weather band and the intraseasonal band involve broader phenomena in the frequency domain and are specially enhanced during winter months, when large scale wind systems are more active. The weakening of these low-frequency bands occur from the early spring to the early autumn, what greatly benefits the onset and enhancement of diurnal-sea land breezes which do not have to overcome winds from large scale scale systems.

¹It has been tested with time series data of atmospheric pressure (not shown here) from the three REDEXT buoys that the three areas of study present regularly calm weather conditions during summer months and a more intense large scale activity during winter months.

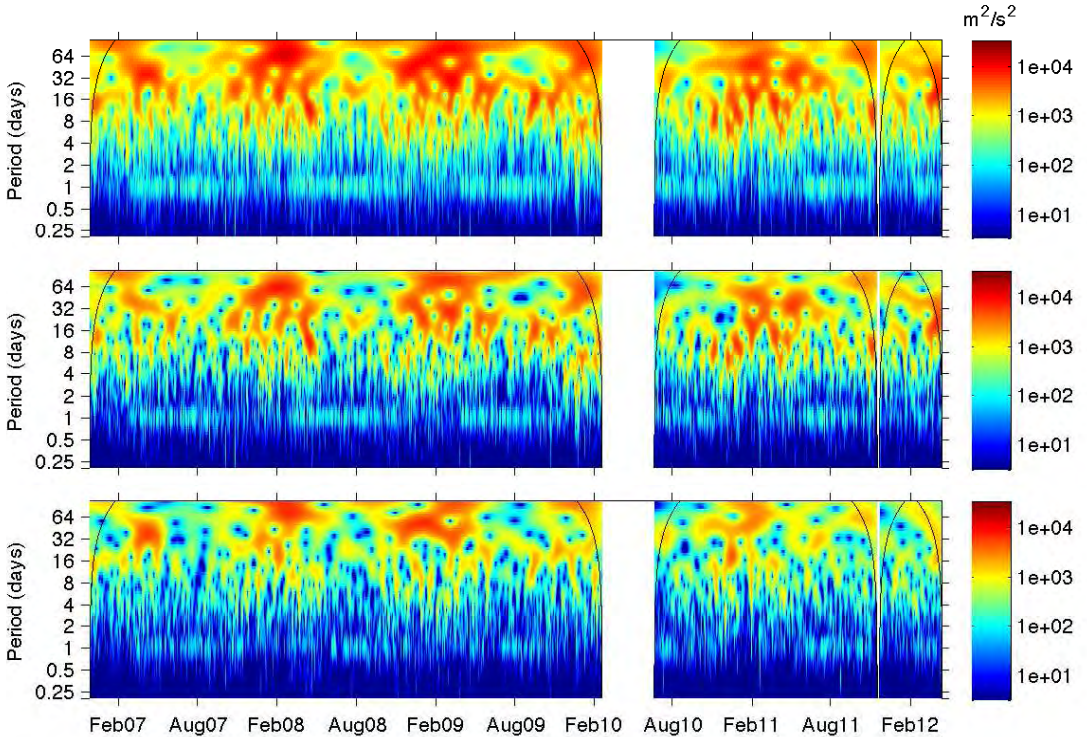


Figure 2.2: Rotary Wavelet Power Spectrum of Wind at the Buoy Gulf of Cádiz - Rotary wavelet power spectrum of surface winds (3 m above sea surface) measured at the Buoy Gulf of Cádiz. (upper panel) Total rotary wavelet power spectrum. (intermediate panel) Rotary wavelet power spectrum of clockwise component. (lower panel) Rotary wavelet power spectrum of counterclockwise component. The two black lines on either end indicate the ‘cone of influence’ where edge effects become important.

The pattern described above is consistent with that indicated for the climatology of a sea-land breeze system (Hunter et al., 2007; Zhang et al., 2009). The diurnal wind variance observed during nonsummer seasons may be forced by mechanisms other than sea-land breezes, such as synoptic wind events. The same cause has been pointed out for diurnal wind variance observed during non-breezes periods on the Texas-Louisiana shelf (Chen et al., 1996; Zhang et al., 2009). For this reason in *Section 2.3.2* we will use only data from spring-summer months for our analysis on the effects of the phase correlation between the breeze forcing and the subsequent ocean response giving rise to resonant breeze-forced oscillations.

2. BREEZE-FORCED OSC. AROUND THE POLEWARD LIMIT

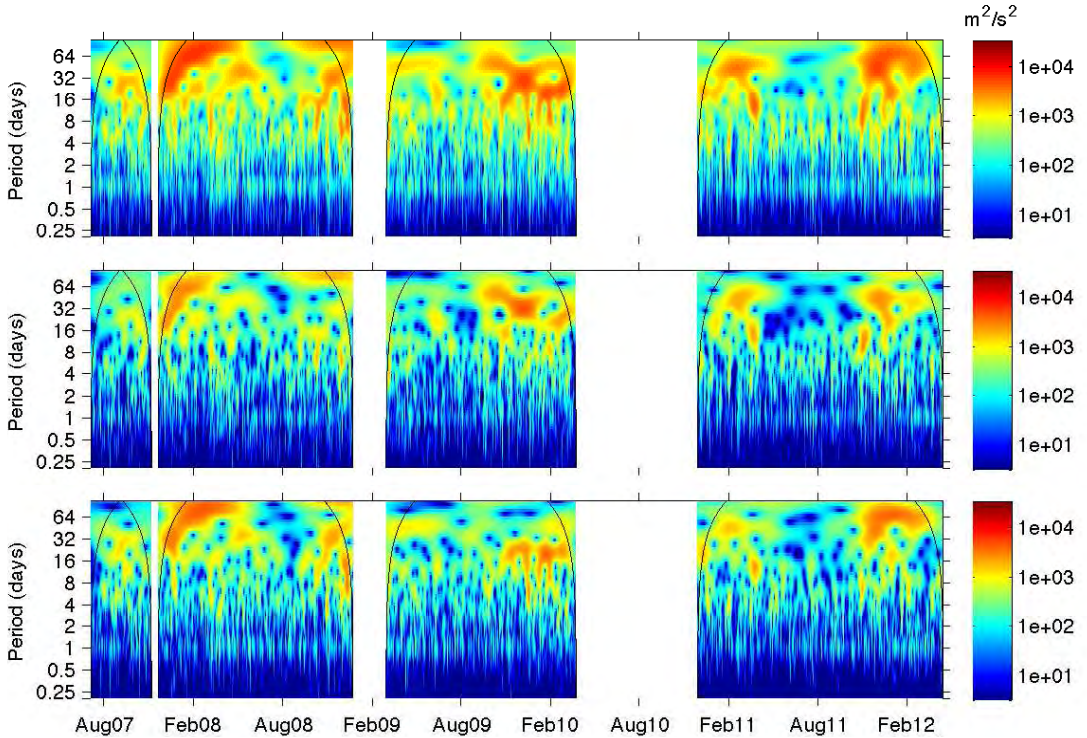


Figure 2.3: Rotary Wavelet Power Spectrum of Wind at the Buoy Valencia II - Rotary wavelet power spectrum of surface winds (3 m above sea surface) measured at the Buoy Valencia II. (upper panel) Total rotary wavelet power spectrum. (intermediate panel) Rotary wavelet power spectrum of clockwise component. (lower panel) Rotary wavelet power spectrum of counterclockwise component. The two black lines on either end indicate the ‘cone of influence’ where edge effects become important.

Figure 2.3 presents the rotary wavelet power spectrum of wind for the buoy deployed at the Gulf of Valencia. The temporal evolution of the wind variance exhibits in this area a slightly different pattern to that observed in the Gulf of Cádiz. The weather and intraseasonal bands show also an enhancement of variance during the winter months; however, in general terms, large scale wind systems are weaker than those observed in the Gulf of Cádiz for the same months. This may explain that the diurnal wind variance appears as a more continued packet of activity throughout the year since there may exist more days with favourable synoptic conditions for the development of sea-land breezes even during winter months.

As it occurs at the buoy of the Gulf of Cádiz, both senses of rotation (Figure 2.3 - intermediate, lower pannels) are noticeable in the signal of the sea-land breeze system.

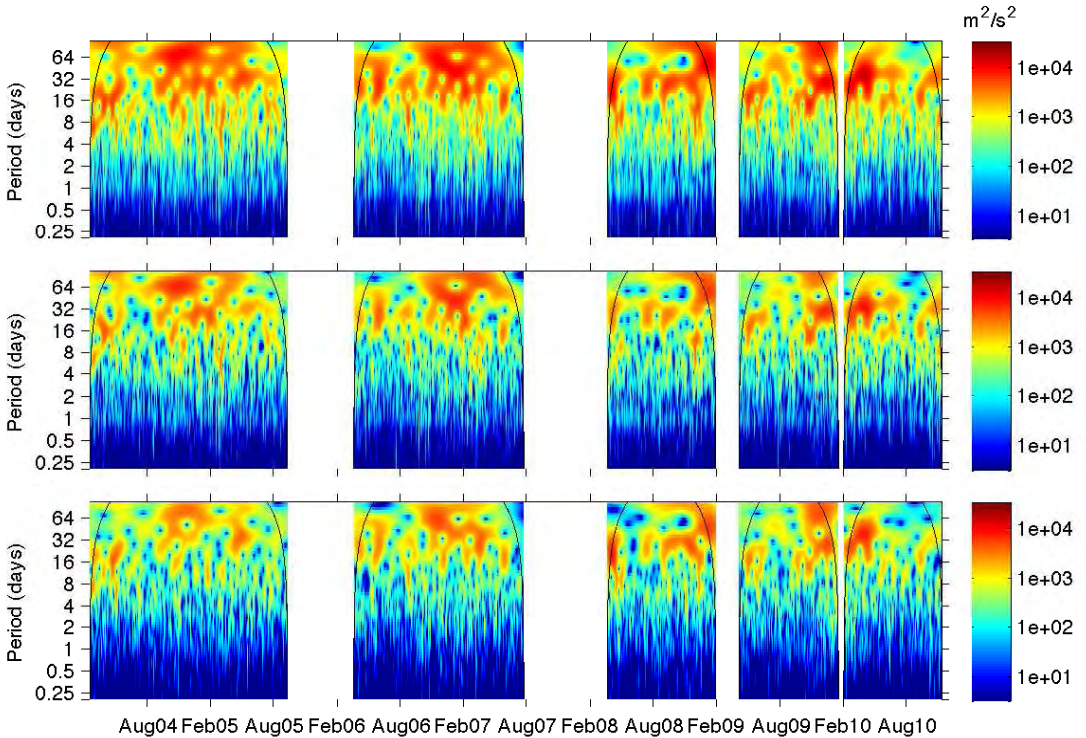


Figure 2.4: Rotary Wavelet Power Spectrum of Wind at the Buoy Cape Peñas - Rotary wavelet power spectrum of surface winds (3 m above sea surface) measured at the Buoy Cape Peñas. (upper pannel) Total rotary wavelet power spectrum. (intermediate pannel) Rotary wavelet power spectrum of clockwise component. (lower pannel) Rotary wavelet power spectrum of counterclockwise component. The two black lines on either end indicate the ‘cone of influence’ where edge effects become important.

Finally, Figure 2.4 shows the rotary wavelet power spectrum of wind measured from the buoy deployed at the Cape Peñas area. In this case, the diurnal wind variance does not present a clear seasonal pattern, neither the continued presence of well-packaged signal. On the contrary, sporadic and continuous events dominate the diurnal band, specially in the clockwise sense of rotation (Figure 2.4 - intermediate pannel). This might be the response to a more in-

2. BREEZE-FORCED OSC. AROUND THE POLEWARD LIMIT

tense weather and intraseasonal bands in comparison with the other two areas of study, what difficulties here the development of a sea-land breeze system. It is also worth mentioning that the diurnal wind variance vanishes for the counterclockwise sense during summer months, while it is relatively more active during winter months (Figure 2.4 - lower panel).

B) Temporal Evolution of Wind-Forced Oscillations

Now, surface ocean currents measured from the three REDEXT buoys subject of this research are similarly analyzed with the rotary wavelet method. Thus, Figures 2.5-2.7 present the rotary wavelet power spectra of currents at the Gulf of Cádiz, the Gulf of Valencia and the Cape Peñas, respectively.

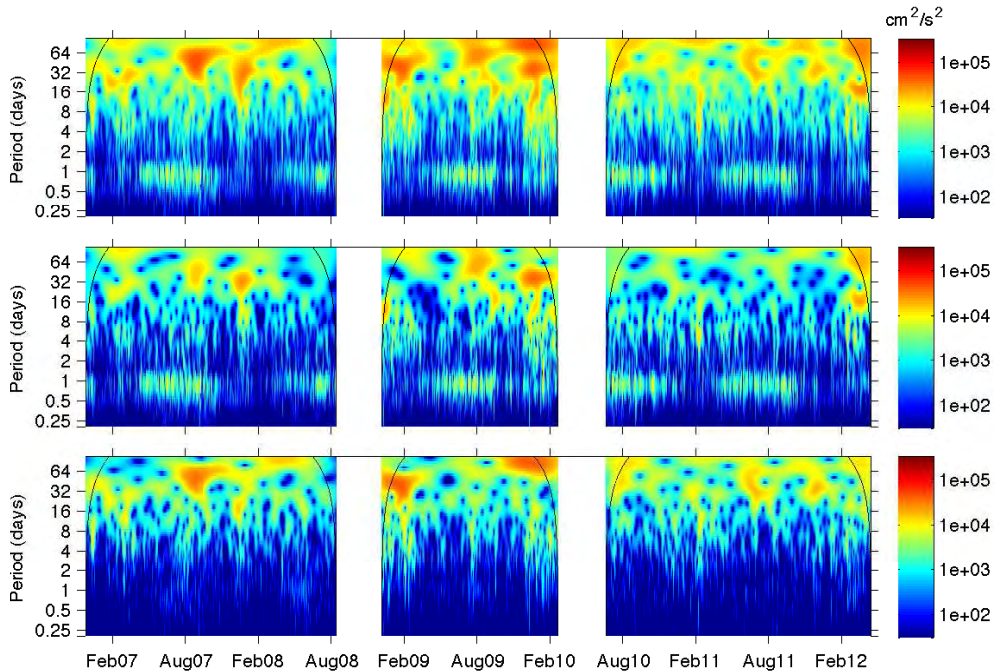


Figure 2.5: Rotary Wavelet Power Spectrum of Currents at the Buoy Gulf of Cádiz - Rotary wavelet power spectrum of surface currents (at 3 m depth) measured at the Buoy Gulf of Cádiz. (upper panel) Total rotary wavelet power spectrum. (intermediate panel) Rotary wavelet power spectrum of clockwise component. (lower panel) Rotary wavelet power spectrum of counterclockwise component. The two black lines on either end indicate the ‘cone of influence’ where edge effects become important.

At this point we focus our attention on the temporal evolution of the diurnal-inertial variance, which is the band of the main concern for the study of breeze-forced oscillations in the Northern Hemisphere. Thus, from Figures 2.5-2.6 it becomes evident that the diurnal-inertial signal exhibits a well-defined packet of enhanced variance in the clockwise sense of rotation (Figure 2.5 and 2.6, intermediate panels) from the early spring to late autumn months. These observations, made from measurements taken in the Gulf of Cádiz and the Gulf of Valencia, are in good agreement with the seasonal pattern described for sea-land breeze systems in other regions (e.g. the Texas-Louisiana shelf (Zhang et al., 2009)).

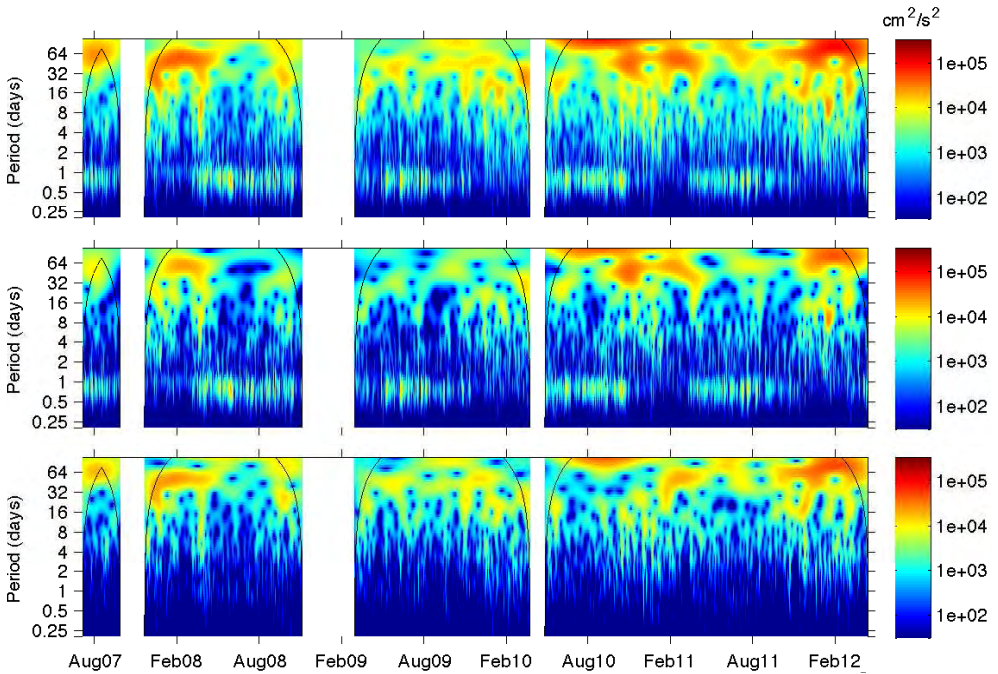


Figure 2.6: Rotary Wavelet Power Spectrum of Currents at the Buoy Valencia II - Rotary wavelet power spectrum of surface currents (at 3 m depth) measured at the Buoy Valencia II. (upper panel) Total rotary wavelet power spectrum. (intermediate panel). Rotary wavelet power spectrum of clockwise component. (lower panel) Rotary wavelet power spectrum of counterclockwise component. The two black lines on either end indicate the ‘cone of influence’ where edge effects become important.

In this regard, it is interesting to highlight that, in spite of a noticeable

2. BREEZE-FORCED OSC. AROUND THE POLEWARD LIMIT

signal of diurnal wind forcing all along the year in the Gulf of Valencia (Figure 2.3), breeze-forced oscillation variance is enhanced only from the early spring to the late autumn months (Figure 2.6 - intermediate panel). This scenario responds to previous description given in *Chapter 1*, where the vertical structure of breeze-forced oscillations was shown to be partially supported by a first baroclinic mode marked by the depth of the pycnocline in stratified waters (Simpson et al., 2002; Rippeth et al., 2002; Zhang et al., 2009; Hyder et al., 2011). This explains that during winter months in the Gulf of Valencia, even in presence of breeze-forcing, the ocean response does not develop an effective transfer of momentum from wind to the interior of the water column.

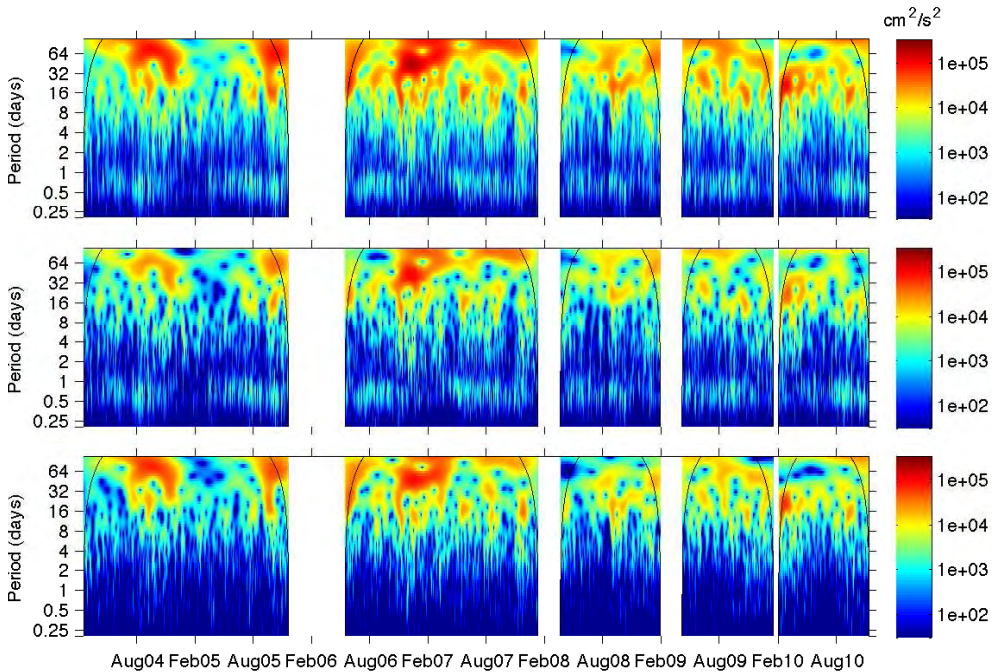


Figure 2.7: Rotary Wavelet Power Spectrum of Currents at the Buoy Cape Peñas - Rotary wavelet power spectrum of surface currents (at 3 m depth) measured at the Buoy Cape Peñas. (upper panel) Total rotary wavelet power spectrum. (intermediate panel) Rotary wavelet power spectrum of clockwise component. (lower panel) Rotary wavelet power spectrum of counterclockwise component. The two black lines on either end indicate the ‘cone of influence’ where edge effects become important.

The previous two areas of study, the Guf of Cádiz and the Gulf of Valen-

cia, are both within the critical latitudes for diurnal-inertial resonance ($30^\circ \pm 10^\circ$ N/S); unlike the buoy placed at the Cape Peñas area which is located out of this range of latitudes (Table 2.1). Consequently, it is not surprising that Figure 2.7 shows in the clockwise sense of rotation (intermediate panel) a broader and less defined packet of diurnal-inertial variance within the frequency space (y -axis). Also, this diurnal-inertial band appears now more centred around the local inertial period, which is closer to semidiurnal band (17.31 hours). However, there is a remarkable increase of inertial current variance during summer months, what is in accordance with the enhancement of surface inertial oscillations in stratified waters whenever there is an injection of wind energy to the ocean¹. During these months, the signal is weaker than in previous resonant regions and occasionally broadens the inertial band to diurnal periods. It is clear that diurnal-inertial resonance hardly takes place over these latitudes where both periods starts to become too far from each other (Simpson et al., 2002).

In regions poleward of 30° N, like the Cape Penhñas area, large/mesoscale activity with negative vertical relative vorticity ($\zeta < 0$) takes special interest as it may induce an effective Coriolis ($f_{eff} = f + \zeta/2$) which broadens the inertial frequency domain allowing near-inertial motions with intrinsic frequencies below f (Kunze, 1985; Young and Ben Jelloul, 1997; Kunze and Boss, 1998), and hence closer to diurnal periods. Under these conditions, regions with $\zeta < 0$ would help to generate a near-resonance response with diurnal wind forcing. This situation may explain the observed enhancement of near-inertial oscillations approaching the diurnal frequency sporadically in the Cape Peñas area (Figure 2.7 - intermediate panel) when the transfer of momentum and energy from diurnal wind forcing to inertial motions can be significantly increased (Lerczak et al., 2001; Hyder et al., 2002; Rippeth et al., 2002; Simpson et al., 2002).

On a whole, the Cape Peñas area exhibits a more recurrent appearance of ‘free’ inertial currents (Figure 2.7 - intermediate panel) which appear to be enhanced in the stratified waters of the summer months and may be caused by impulsive wind pulses in absence of a clear presence of breeze forcing (Figure 2.4 - intermediate panel). As we previously advanced, the buoy at the Cape Peñas will serve us here as a ‘blank test’ in our analysis of resonant

¹We do not see any evidence that indicates that the semidiurnal tides are larger during summer months to account the observed enhancement of the inertial band. Therefore, transfer of semidiurnal tidal energy to the inertial band does not seem to be a dominant mechanism in this area.

2. BREEZE-FORCED OSC. AROUND THE POLEWARD LIMIT

wind-forced oscillations in comparison with the buoys deployed at the Gulf of Cádiz and the Gulf of Valencia, where breeze-forced oscillations are expected to enter in resonance.

It is remarkable the fact that in all rotary wavelet power spectra shown above, currents in the counterclockwise sense of rotation (lower pannels) are of little variance within the diurnal-inertial band, highlighting the dominant role of clockwise diurnal-inertial motions (in the Northern Hemisphere).

2.3.2 The Ocean Response to Diurnal Wind Forcing: A Rotary Analysis

In this section we firstly use the rotary wavelet method to quantify results and discuss observed differences among the three regions of study. Later we use a cross-rotary wavelet analysis to explore the onset of wind-forced diurnal-inertial motions focusing on the phase correlation between the wind forcing and the ocean response. In this regard, special attention will be given to those main aspects which distinguish the generation of resonant breeze-forced oscillations and ‘free’ inertial motions caused by impulsive injections of momentum from wind.

Thus, Figures 2.8-2.10 present the 3-month smoothed wind and current variance time series derived from the rotary wavelet power spectra shown in Figures 2.2-2.7. In all cases the total (black line), clockwise (red line) and counterclockwise (blue line) rotary components are indicated. Additionally, we also show the 95% confidence level (dashed line in grey).

As can be observed in Figure 2.8, the Gulf of Cádiz presents a regular wind (top pannel) and current (bottom pannel) seasonal pattern corresponding the description of a breeze-forced system (see Figures 1.3 and 1.5). The magnitude of the diurnal wind variance exhibits here a wide signal which spans in time from February to October and which can be as large as $8 \text{ m}^2 \text{ s}^{-2}$ for both senses of rotation, though with a predominance of the clockwise sense (Figure 2.8 - top pannel). During winter months (December-January), the diurnal wind variance decreases to values less than $4 \text{ m}^2 \text{ s}^{-2}$. Accordingly, the diurnal-inertial current variance peaks for the clockwise sense of rotation during summer months (June-August) with values up to $200 \text{ cm}^2 \text{ s}^{-2}$, an order of magnitude greater than those observed during winter months when they are less than $10 \text{ cm}^2 \text{ s}^{-2}$. These values highlight the importance of breeze-

forced oscillations within the diurnal-inertial band when the enhancement of energy in summer may be available to promote mixing in coastal stratified areas (Zhang et al., 2009; Aguiar-González et al., 2011)¹.

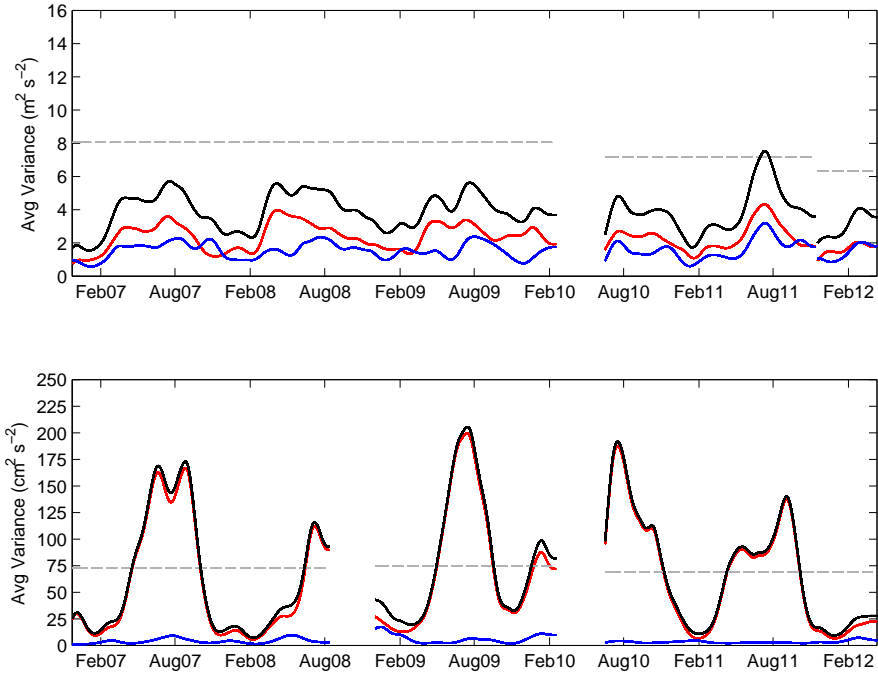


Figure 2.8: Averaged Wavelet Variance of Wind and Currents from the Buoy at the Gulf of Cádiz - (top) The black line is the frequency (period) averaged total wavelet variance of wind time series ($\text{m}^2 \text{s}^{-2}$) over the diurnal band. Analogously, the red (blue) line represents the frequency (period) averaged clockwise (counterclockwise) wavelet variance. The horizontal dashed line is the 95% confidence level. (bottom) Same as previously but for current time series ($\text{cm}^2 \text{s}^{-2}$) over the diurnal-inertial band. All time curves represent 3-month low-passed values.

The diurnal variance of wind at the Gulf of Valencia does not show a regular seasonal pattern (Figure 2.8 - top pannel) and its values oscillate all along the year between $3 \text{ m}^2 \text{ s}^{-2}$ and $7 \text{ m}^2 \text{ s}^{-2}$. At this location, clockwise and counterclockwise components are of similar strength and hence the wind

¹Also *Chapter 3* in this thesis.

2. BREEZE-FORCED OSC. AROUND THE POLEWARD LIMIT

forcing exhibits a rectilinear behaviour.

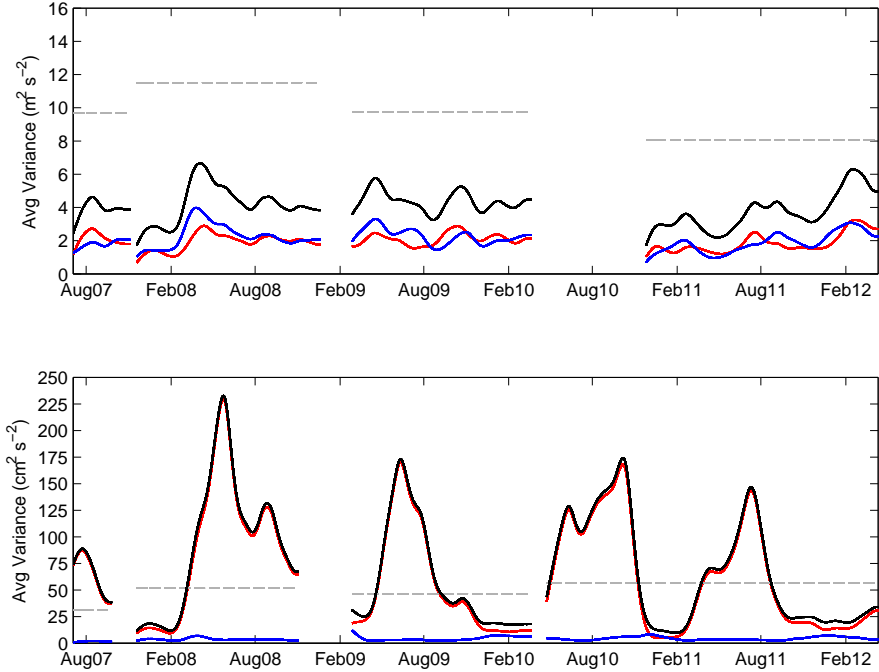


Figure 2.9: Averaged Wavelet Variance of Wind and Currents from the Buoy at the Gulf of Valencia - (top) The black line is the frequency (period) averaged total wavelet variance of wind time series ($\text{m}^2 \text{s}^{-2}$) over the diurnal band. Analogously, the red (blue) line represents the frequency (period) averaged clockwise (counterclockwise) wavelet variance. The horizontal dashed line is the 95% confidence level. (bottom) Same as previously but for current time series ($\text{cm}^2 \text{s}^{-2}$) over the diurnal-inertial band. All time curves represent 3-month low-passed values.

In this regard it is worth while to recall modeling results for observations made in the Thermaikos Gulf (Hyder et al., 2002). Those results predicted that maximum current amplitudes occurred when the breeze forcing was purely clockwise but that rectilinear diurnal winds also forced strong clockwise currents. This is in good agreement with the observed increase of diurnal-inertial current variance in the clockwise sense forced with rectilinear diurnal winds during summer months (Figure 2.9 - bottom panel), when stratification in the Gulf of Valencia contributes to the development of the first baroclinic

mode that supports the vertical structure of breeze-forced oscillations. During these months the diurnal-inertial current variance reaches values as large as $225 \text{ cm}^2 \text{ s}^{-2}$, an order of magnitude greater than during winter months (less than $10 \text{ cm}^2 \text{ s}^{-2}$).

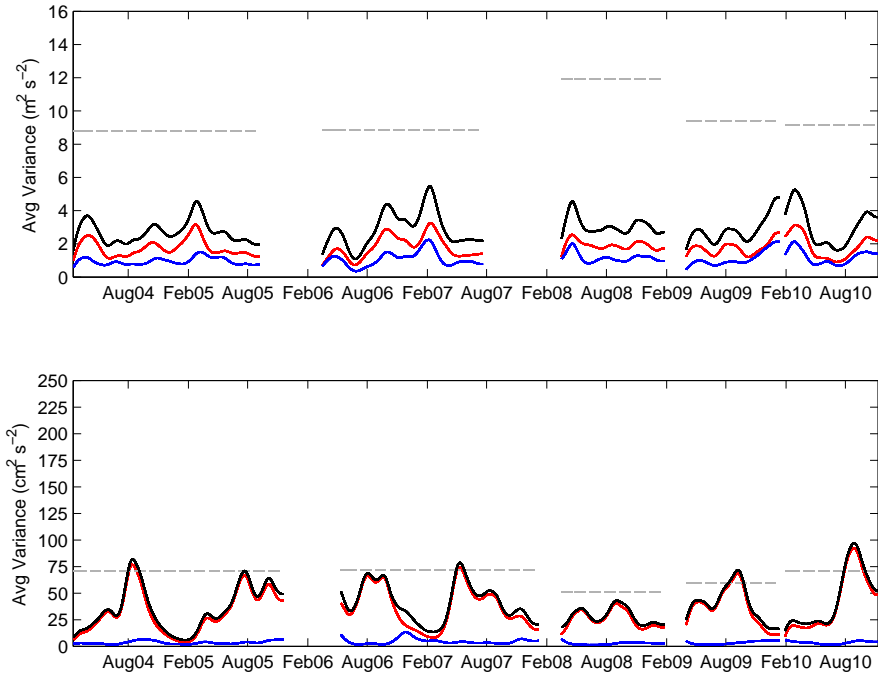


Figure 2.10: Averaged Wavelet Variance of Wind and Currents from the Buoy at the Cape Peñas area - (top) The black line is the frequency (period) averaged total wavelet variance of wind time series ($\text{m}^2 \text{ s}^{-2}$) over the diurnal band. Analogously, the red (blue) line represents the frequency (period) averaged clockwise (counterclockwise) wavelet variance. The horizontal dashed line is the 95% confidence level. (bottom) Same as previously but for current time series ($\text{cm}^2 \text{ s}^{-2}$) over the diurnal-inertial band. All time curves represent 3-month low-passed values.

Lastly, Figure 2.8 (top panel) presents the diurnal wind variance time series at the Cape Peñas area, which does not show either a regular seasonal pattern and values oscillate all along the year between $2 \text{ m}^2 \text{ s}^{-2}$ and $5 \text{ m}^2 \text{ s}^{-2}$. Here the diurnal-inertial current variance also increases its values from winter months (less than $10 \text{ cm}^2 \text{ s}^{-2}$) to summer months (up to $75 \text{ cm}^2 \text{ s}^{-2}$). However

2. BREEZE-FORCED OSC. AROUND THE POLEWARD LIMIT

it is clear that the enhancement of the inertial variance is not as large as in the Gulf of Cádiz and the Gulf of Valencia, where resonance between diurnal wind forcing and inertial motions from the ocean response may occur.

After quantifying observed differences between resonant breeze-forced oscillations within critical latitudes and wind-forced inertial oscillations out of this range of latitudes, now we proceed to explore the wavelet coherency and phase spectra between wind and currents to characterize the onset of both types of inertial motions.

With this aim, we use two time series data (of two months each one) corresponding to spring-summer periods as representative of a situation in which both resonant breeze-forced oscillations in the Gulf of Cádiz and wind-forced inertial oscillations in the Cape Peñas area are present¹.

Thus Figures 2.11 and 2.12 show the wavelet coherency and phase spectra between wind and current clockwise components, which are of the main concern for the study of diurnal-inertial motions in the Northern Hemisphere. The top and intermediate panels present rotary wavelet power spectrum of wind and currents (clockwise components), respectively, in order to account the diurnal-inertial variance in relation with the wavelet coherency and phase spectra between wind and currents. The red color in the squared wavelet coherency spectra (bottom panel) means that coherency (γ^2) is high, while the blue means it is low. The vectors indicate the phase difference between wind and current at different frequencies and at each time (bottom panel). For clarity only one vector is plotted for each day. Positive phase angles between wind and current indicate that current leads wind. Accordingly, vectors are in phase pointing straight up, out of phase pointing straight down, and current leads wind by 90° pointing right. Only phase angles (vectors) for $\gamma^2 > 0.7$ are plotted.

As can be observed in Figure 2.11 (Gulf of Cádiz), the wind and current show high coherency ($\gamma^2 > 0.7$) in the diurnal-inertial band for most of April-May 2007 with large associated diurnal-inertial current variance. These results support that the near-resonant condition in this area promotes the generation

¹Time series data from the Gulf of Valencia exhibit an analogous pattern (not shown here) to that described for the onset of resonant breeze-forced oscillations during spring-summer months in the Gulf of Cádiz and, hence, we assume the latter may be representative of the onset of resonant BFOs poleward of the critical latitude for diurnal-inertial resonance (30° N/S).

and accumulation of diurnal-inertial current energy via breeze-forced oscillations as we describe in the following.

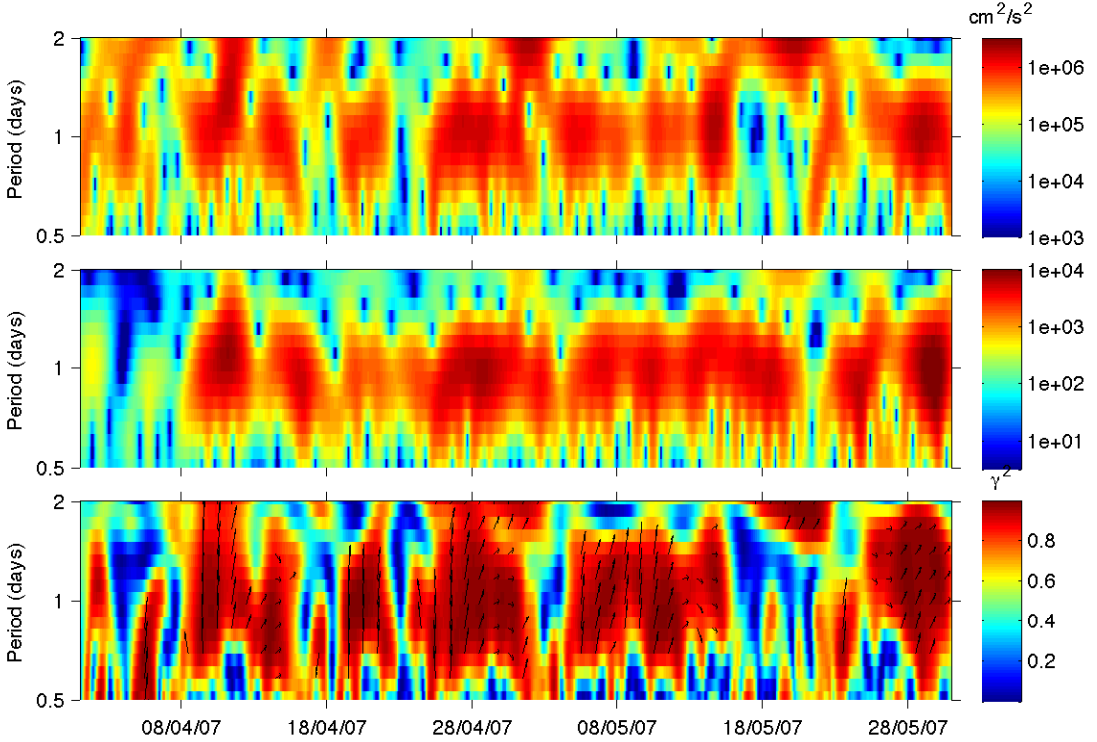


Figure 2.11: Squared Wavelet Coherency and Phase Spectra between Wind and Current (Clockwise Components) measured at the Buoy Gulf of Cádiz - (top panel) Rotary wavelet power spectrum of surface winds. (intermediate panel) Rotary wavelet power spectrum of surface currents. (lower panel) Squared Wavelet Coherency (γ^2) and Phase Spectra between Wind and Current (Clockwise Components). The vectors indicate the phase difference between the wind and current at different frequencies. Positive phase angles between wind and current indicates that current leads wind. Accordingly, vectors are in phase pointing straight up, out of phase pointing straight down, and current leads wind by 90° pointing right. For clarity only one vector is plotted for each day. Only phase angles (vectors) for $\gamma^2 > 0.7$ are plotted.

The four patches of very high coherency within the diurnal-inertial band (bottom panel) are of special interest owing to its associated high diurnal wind (top panel) and current (intermediate panel) variance. These patches

2. BREEZE-FORCED OSC. AROUND THE POLEWARD LIMIT

are representative of breeze-forced events and are observed during 8-13 April, 19-23 April, 28 April - 2 May and 3-17 May. All these events start with the same pattern, diurnal wind (breezes) variance arises preceding the increase of diurnal-inertial current variance (breeze-forced oscillations), which is in phase with vectors pointing straight up.

At times after the onset of the phenomenon, the phase difference between wind forcing and forced-currents slightly increases to positive phase angles (vectors deviate pointing to the right), and therefore currents leads wind forcing. This pattern may be consistent with an alternation of cycles of forced oscillations, when current motions are in phase with wind forcing, and cycles of decreased forcing when the currents tend to revert to ‘free’ inertial oscillations (Simpson et al., 2002). This would explain that in Figure 2.11, whenever the forcing decreases, the observed phase difference between wind and currents increases and tends to show inertial current phase leading diurnal wind phase since at latitudes poleward of 30° N/S ‘free’ inertial motions are of higher frequency than diurnal motions.

If the wind forcing vanishes completely after several days being active, the situation could be similar to that observed for the breeze-forced event starting on 3 May (Figure 2.11 - bottom panel). After more than 10 days of constant wind forcing, diurnal wind variance drops on 17 May; however diurnal-inertial current variance is still high and from then ‘free’ inertial oscillations dominate (see in intermediate panel the decreasing tendency from diurnal to inertial period). As expected, low coherency values between wind and currents are found for days after 17 May, when the breeze forcing has disappeared (top panel).

The enhancement of diurnal-inertial current variance observed in Figure 2.11, and related to a high coherency between forcing and forced-motions, suggests that energetic breeze-forced events are promoted when the relationship between wind and currents lasts for several cycles. These results are in good agreement with previous observations reported by Zhang et al. (2009) on the Texas-Louisiana shelf (equatorward of 30° N). They suggested that the longer this in phase relationship persists, the larger the magnitude of the diurnal-inertial current becomes until a steady state is reached.

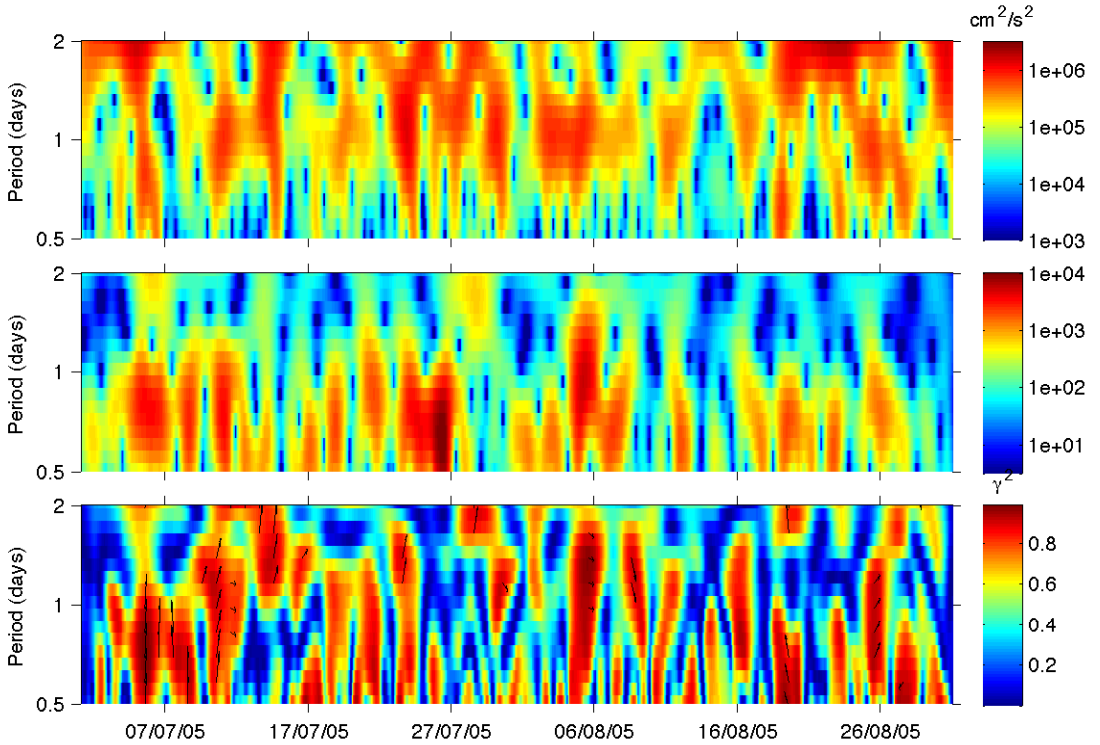


Figure 2.12: Squared Wavelet Coherency and Phase Spectra between Wind and Current (Clockwise Components) measured at the Buoy Cape Peñas - top pannel) Rotary wavelet power spectrum of surface winds. (intermediate pannel) Rotary wavelet power spectrum of surface currents. (lower pannel) Squared Wavelet Coherency (γ^2) and Phase Spectra between Wind and Current (Clockwise Components). The vectors indicate the phase difference between the wind and current at different frequencies. Positive phase angles between wind and current indicates that current leads wind. Accordingly, vectors are in phase pointing straight up, out of phase pointing straight down, and current leads wind by 90° pointing right. For clarity only one vector is plotted for each day. Only phase angles (vectors) for $\gamma^2 > 0.7$ are plotted.

Finally, Figure 2.12 (Cape Peñas) shows an analogous analysis to that developed in Figure 2.11 for the Gulf of Cádiz. However, as we previously advanced, the Cape peñas area is out of the range of diurnal-inertial resonance and serve us here as a ‘blank test’ of a situation in which resonant diurnal-inertial oscillations are not expected to occur. Thus, in comparison with results from the Gulf of Cádiz time series data, here the wind and current show very

low coherency and the diurnal-inertial phase difference (bottom panel) is highly variable for most of the analysed period (July-August 2005)¹. It is clear that there exists diurnal wind forcing acting during this period (top panel); however, there is no evidence of this wind forces periodic diurnal-inertial currents. The inertial current variance (intermediate panel) seems to respond to impulsive injections of momentum from diurnal wind (top panel) although beyond that initial pulse, near-inertial currents may oscillate ‘freely’. Therefore, the dominant ocean response appears to be in the form of transient oscillations which do not accumulate efficiently near-inertial energy in time as it occurs in regions of diurnal-inertial resonance where forced currents may last for several cycles.

2.4 Conclusions

We use time series data of surface current velocity and wind velocity over annual cycles from three different regions around the Iberian Peninsula: the Gulf of Cádiz and the Gulf of Valencia (both regions within the critical latitudes for resonance); and, the Cape Peñas area (out of the critical latitudes for resonance).

Rotary wavelet analysis results provide evidence that sea-land breeze forcing enhances clockwise rotary current motions (breeze-forced oscillations) which greatly contribute to near-inertial energy budget and its variability in the Gulf of Cádiz and the Gulf of Valencia (Northern Hemisphere). These results also support that the near-resonant condition in these areas promotes the generation and accumulation of diurnal-inertial current energy via breeze-forced oscillations. Squared wavelet coherency and phase spectra suggest that energetic breeze-forced events are enhanced when the relationship between wind and currents lasts for several cycles and present a high coherency between the forcing and forced-motions being in phase.

We find that the diurnal-inertial current variance attributed to breeze-forced oscillations exhibits a clear seasonal pattern which peaks during spring-summer months, presumably due to observed strong breeze events take place

¹This analysis has been performed with other periods of time in the area of study and analogous results were found.

when coastal waters are sufficiently stratified¹. This enhancement of diurnal-inertial current variance due to breeze-forced oscillations in the Gulf of Cádiz and the Gulf of Valencia has been estimated to be as large as an order of magnitude higher during summer months (reaching values of up to $225 \text{ cm}^2 \text{ s}^{-2}$) than in winter months (values are less than $10 \text{ cm}^2 \text{ s}^{-2}$).

Despite the fact that this research focuses on time series data from the Gulf of Cádiz and the Gulf of Valencia, we find that these results and methodology may have applications to the study of breeze-forced oscillations over other coastal areas poleward of the critical latitude for diurnal-inertial resonance (30°N/S).

The inertial current variance in the Cape Peñas area also exhibits a seasonal pattern and increases its values from winter months (less than $10 \text{ cm}^2 \text{ s}^{-2}$) to summer months (up to $75 \text{ cm}^2 \text{ s}^{-2}$). However, this enhancement is not as large as in the Gulf of Cádiz and the Gulf of Valencia, where resonance between diurnal wind forcing and inertial motions from the ocean response may occur. The inertial current variance in the Cape Peñas area seems to respond to impulsive injections of momentum from diurnal wind. The dominant ocean response appears to be in the form of transient ‘free’ oscillations which do not efficiently accumulate near-inertial energy in time as it occurs in regions of diurnal-inertial resonance where forced currents may last for several cycles.

These results support the role of resonant breeze-forced oscillations on the generation and accumulation of near-inertial energy which may be available for promoting vertical mixing with important consequences on coastal dynamics as we will explore in the following chapter.

¹We explore the effects of breeze-forced oscillations in stratified waters, and associated diapycnal mixing process, in *Chapter 3*.

2. BREEZE-FORCED OSC. AROUND THE POLEWARD LIMIT

Chapter 3

Breeze-Forced Oscillations and Diapycnal Mixing¹

3.1 Outline

This chapter presents an analysis of diapycnal mixing processes triggered by breeze-forced oscillations (BFOs) with observational data. Our interest focused on the relative importance of this phenomenon overcoming the vertical stability of the water column. The goal is to highlight breeze-forced oscillation dynamics in areas where the coast exhibits a well-developed sea-land breeze regime; and, hence, the ocean response is strongly controlled by breeze-forced dynamics. Our research is based on previous literature and new observations of BFOs taken during the Maritime Rapid Environmental Assessment 2004 (MREA04) sea trial off the west coast of the Iberian Peninsula, within the critical latitudes for diurnal-inertial resonance. Additionally, we also count with wind data from a meteorological land station provided by the Instituto Hidrográfico - Portugal

Analysis of the measurements shows evidence of dominant circular anticyclonic oscillations forced by sea-land breezes acting during the MREA exercise into the Bay of Setúbal (Portugal). Furthermore, currents were distributed

¹Aguiar-González B., Rodríguez-Santana A., Cisneros-Aguirre J., Martínez-Marrero. 2011. Diurnal-inertial motions and diapycnal mixing on the Portuguese shelf. *Cont. Shelf. Res.* 31, 1193–1201.

3. BREEZE-FORCED OSC. AND DIAPYCNAL MIXING

into two main layers with highly stratified and vertically sheared flows. Surface stratification entered into the system through the Sado Estuary (freshwater input). As it will be discussed, breeze-forced currents were found to promote mixing in stratified shallow waters of the shelf area over the scale of a few days. The period of observation counts with days of breeze and relaxed-wind events, what allowed us to track the evolution of the water column at different stages.

Wind conditions were determined with an Aanderaa meteorological buoy placed in the Bay of Setúbal during the MREA04 experiment. Currents data were recorded from two Barny ADCP (Acoustic Doppler Current Profiler) deployments located on the north and south sides of the bay, respectively. Both ADCP's covered almost the full depth of water (~ 112 m) with 24 bins of 4 m size at both sites. Simultaneous CTD (Conductivity, Temperature, Depth) and data were used to analyse the strength of observed breeze-forced oscillations in promoting diapycnal mixing through the squared vertical shear (S^2), squared buoyancy frequency (N^2) and gradient Richardson Number (Ri) of the water column.

The potential role that breeze-forced oscillations may play in shelf areas with low tidal energy has been recurrently highlighted in the literature. Vertically sheared flows in stratified waters may lead to diapycnal mixing and, correspondingly, one could expect that breeze-forced oscillations in stratified waters may promote mixing throughout the water column. Nevertheless, to the best of our knowledge only one paper previous to this study (Zhang et al., 2009) has addressed an analysis which explicitly supports observational evidence of this role.

The present research provides a new data set of breeze-forced oscillations in stratified waters near the critical latitudes ($30^\circ \pm 10^\circ$ N/S) for diurnal-inertial resonance, where they can greatly contribute to triggering diapycnal mixing. The results of our analysis show that the ocean response to breeze forcing may be enhancing vertical mixing between surface and deeper waters in the Bay of Setúbal through breeze-forced diurnal-inertial currents. A detailed description of the data and methodology used in this chapter is given in *Section 3.2*. In *Section 3.3* we combine data from two ADCP deployments, available CTD casts, a meteorological buoy and a meteorological land station to draw the scenario where the evolution of the water column is analyzed and discussed in terms of breeze-forced oscillation events promoting diapycnal mixing. The chapter ends with conclusions in *Section 3.4*.

3.2 Data and Methodology

The MREA04 experiment was performed by the NATO Undersea Research Centre (NURC) from 29 March-19 April 2004 to test the reliability and quality of several real-time coastal oceanic prediction systems (e.g., Rixen and Ferreira-Coelho (2007); Allard et al. (2008); Ko et al. (2008); Leslie et al. (2008); Lam et al. (2009)). The operational area extended off the west coast of Portugal from 40°N - 36°N and from 11°W - 8°W . This study uses observational data taken over the continental shelf off Portugal, into the Bay of Setúbal (Figure 3.1).

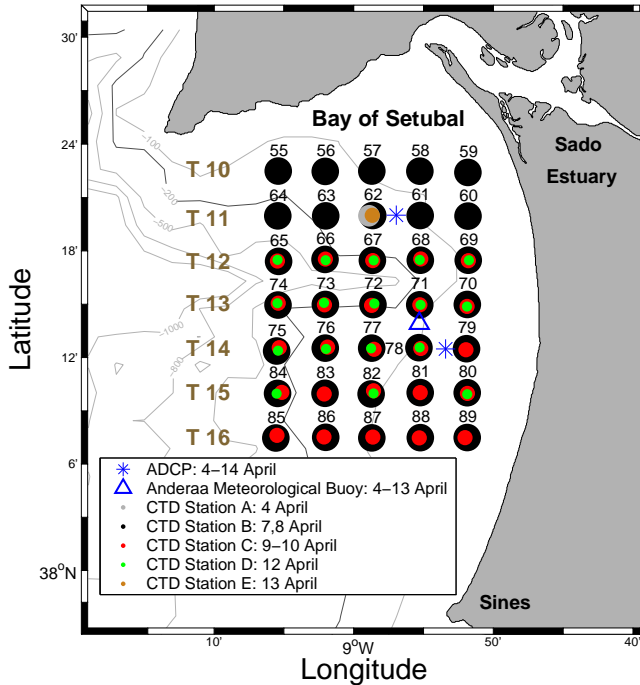


Figure 3.1: MREA04 Data Set - Operational area over the continental shelf off Portugal (Bay of Setúbal) during the MREA04 sea trial. CTD stations were sampled several times, represented by coloured circles for each sampling day. Locations of Barny North and Barny South ADCP deployments (close to CTD station 62 and CTD station 78, respectively), an Anderaa meteorological buoy and bottom topography are also shown. The Sado estuary influences the area from the north side of the bay.

3. BREEZE-FORCED OSC. AND DIAPYCNAL MIXING

This region is characterised by a steep bathymetry because of the Setúbal Canyon, and by fluvial inputs coming from the Sado estuary on the northern side of the bay. Related to tides, the Bay of Setúbal is mainly dominated by lunar (M2) and solar (S2) semidiurnal components (Martins et al., 2002).

Vertical temperature and salinity profiles were obtained using Seabird 911 Plus CTD real-time pumped systems. The CTD stations were sampled several times to get incoming temperature and salinity data in real-time to run, correct and compare the forecasts made by the coastal oceanic prediction models tested during the MREA04 trial. A total of 195 CTD casts were distributed among 95 different sites over the continental shelf and open ocean area from 31 March-16 April 2004. In this chapter, we present the 35 different sites that were analysed to get an overview of the coastal ocean conditions involving the observed breeze-forced oscillations, and study the associated diapycnal mixing processes into the Bay of Setúbal. These sites spanned a regular CTD grid with a spatial resolution of 5 km between CTD stations and transects (Figure 3.1).

Currents data were obtained from two RDI Workhorse ADCP's deployed on Barny-type trawl safe platforms and situated on the north (Barny North ADCP) and south (Barny South ADCP) sides of the bay at 106,6 m and 118 m depth, respectively (Figure 3.1). Both deployments of Barny Sentinel ADCP's recorded vertical profiles of horizontal velocity (u, v) with a broadband of 307.2 kHz and 24 bins of 4 m size. The ADCP heads were about 6 m from the bottom. Both profilers sampled data once every minute for the period of 4 – 14 April 2004.

The rotary spectral method (Hayashi, 1979; van Aken et al., 2005) was applied to examine the variance in the current oscillations for each frequency band as clockwise and counterclockwise rotating variances. Because breeze-forced oscillations involve currents rotating in a clockwise (counterclockwise) direction in the Northern (Southern) Hemisphere, this technique contributes to determining its presence.

Next the diurnal-inertial band, in which breeze-forced oscillation peak, was isolated from the rest of the frequencies to characterise its properties. Previously, to filter this band, the original current records were decimated to 1 datum per hour after lowpass filtering. Then frequency-band of interest was isolated via band-pass filtering with a fourth-order Butterworth filter with zero-phase response and quarter-power points at $\{c^{-1}\omega_c, c\omega_c\}$ around

a centre frequency, ω_c . The bandwidth parameter, $c = 1.25$, was chosen to be narrow enough to maximally isolate the frequency band while being wide enough to avoid filter ‘ringing’, as described in Alford (2003b). The centred frequencies for Barny North (Barny South) ADCP records were taken from the largest peaks of the diurnal-inertial band in the rotary spectral analysis ($\omega_c = 1.054$ cpd for Barny North ADCP, and $\omega_c = 1.142$ cpd for Barny South ADCP).

The meteorological conditions of the area were analysed using an Aanderaa Coastal Monitoring Buoy CMB-3280 (Figure 3.1), located between both ADCP Sentinel deployments for the period 4 – 13 April 2004. Wind speed, wind direction, wave height and period, air temperature, air pressure and relative humidity data transmitted ashore in real-time by VHF/UHF radio were measured. Horizontal wind time series along and off the Portuguese coast were obtained after decomposing the speed and direction of the winds into north-south (v) and east-west (u) components. These data were recorded at a rate of ~ 1 datum every 10 minutes, so that horizontal wind time series were linearly interpolated. This interpolation provided a regular sampling time of 1 datum every 10 minutes and filled some gaps in data records of less than 30 minutes. Afterwards, wind data were decimated to 1 datum per hour after lowpass filtering, as was done for the ADCP’s records. Then the rotary spectral method was also applied to the wind data to assess the presence of sea-land breezes (O’Brien and Pillsbury, 1974; Simpson et al., 2002) as forcing for diurnal-inertial motions in this area.

Diurnal variability in the cross-shore wind component was isolated after band-pass filtering, following the same procedure as used previously for the diurnal-inertial current variability. Here the centre frequency for the Butterworth filter was 1.1 cpd, where the largest peak of spectral density energy was found for the sea-land breeze regime. This technique was used to compare the evolution of the sea-land breeze regime and diurnal-inertial oscillation events.

The role of the observed diurnal-inertial motions in triggering diapycnal mixing was approached by analysing the CTD casts collected next to the ADCP deployments (Figure 3.1). With this aim, we estimated the squared vertical shear (S^2), squared buoyancy frequency (N^2) and gradient Richardson Number (Ri) for the Barny North ADCP and CTD station 62 (Figure 3.5a-d), and the Barny South ADCP and CTD station 78 (Figure 3.5e-h). In the recent years, a combination of CTD and ADCP data of different sizes (4, 8 and 16 m) has been expanded to assess mixing processes induced by vertical shear flows

3. BREEZE-FORCED OSC. AND DIAPYCNAL MIXING

(Muench et al., 2002; Martínez-Marrero et al., 2008). However, it is important to use an appropriate parameterization for the estimation of the diapycnal diffusivity. Here, we present estimations made with the diapycnal diffusivity parameterisation of k_v , Eq. (3.1) in $\text{m}^2 \text{s}^{-1}$, (Pacanowski and Philander, 1981) based on the gradient Richardson number, Ri , following:

$$k_v = \frac{5 \cdot 10^{-3} + 10^{-4} \cdot (1 + 5 \cdot Ri)^2}{(1 + 5 \cdot Ri)^3} + 10^{-5} \quad (3.1)$$

where Ri was calculated through N^2 from CTD profiles (temperature and salinity) in combination with S^2 from the ADCP time series (horizontal velocity profiles).

We close the study attempting to give a more general character to the observations made on breeze-forced oscillations for the area surrounding the Bay of Setúbal. With this aim we present the rotary wavelet spectrum (Torrence and Compo, 1998; Hormazábal et al., 2002)¹ of a wind velocity time series measured at Sines (37.95°N; 8.88°W) during the 2004. Wind data were provided by the Instituto Hidrográfico - Portugal and recorded with an Aanderaa meteorological station at 35.1 m above the mean sea level. Data were measured at 10 m above the ground with a sampling interval of 10 minutes.

3.3 Results and Discussion

3.3.1 A Breeze-Forced Scenario

To study the role of the local wind cycle in generating wind-forced motions on the Portuguese shelf we used an Aanderaa meteorological buoy placed in the interior of the Bay of Setúbal, between the Barny North and Barny South ADCP deployments for the period 4 – 13 April 2004 (Figure 3.1).

For this purpose, the rotary spectral method was applied to the horizontal wind time series obtained along and off the coast (Figure 3.2a,b). The largest area of energy density was found centred at 1 cpd (Figure 3.2c) for both the clockwise and counterclockwise directions. This revealed the presence of a dominant sea-land breeze regime (O'Brien and Pillsbury, 1974; Simpson et al.,

¹For further details on the wavelet methodology the reader is referred to *Appendix A*.

2002) into the Bay of Setúbal. Subsequently, the diurnal band of the cross-shore wind component was isolated via band-pass filtering (Figure 3.2d) to explore episodes of intense sea-land breezes during the MREA04 trial.

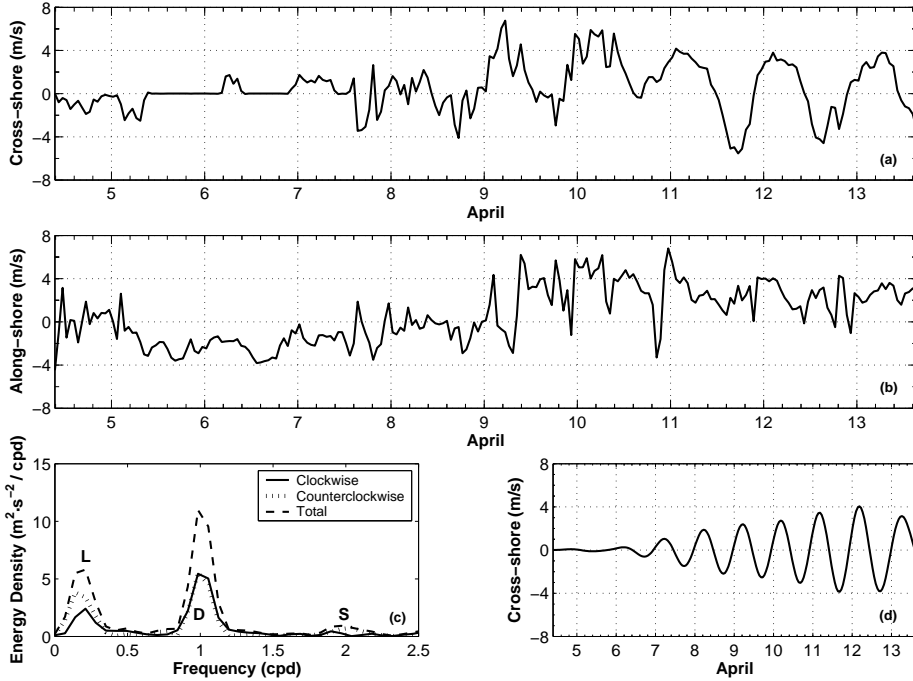


Figure 3.2: Wind Time series for the Bay of Setúbal - Time series of horizontal wind components, cross-shore (a) and along-shore (b), from an Aanderaa meteorological buoy (see Figure 3.1). The time record extended from 4-13 April 2004. The sea-land breezes are evident in the cross-shore component after 7 April. (c) Rotary power spectral density of Setúbal winds. Capital letters indicate low (L), diurnal (D) and semidiurnal (S) frequency bands. The large peaks at 1 cycle day⁻¹, for both the clockwise and counterclockwise directions, are due to a dominant sea-land breeze regime. (d) Time series of cross-shore wind component after band-pass filtering to isolate diurnal variability and show evidence of the sea-land breeze regime.

A pattern of onshore winds during the day, followed by offshore winds at night, became more evident on 7 – 8 April and thereafter. This episode of an increasing force of sea-land breezes started before diurnal-inertial motions were clearly present at both ADCP sites (Figure 3.3e,f) on 9 – 10 April, as expected for the setting of the ocean response. The diurnal-inertial events observed at

3. BREEZE-FORCED OSC. AND DIAPYCNAL MIXING

the beginning of the Barny North record, on 4 – 6 April (Figure 3.3e), might also be the consequence of a sea-land breeze regime forcing the bay a few days before initiation of the meteorological buoy record. During the MREA04 sea trial, we found values for this wind cycle with a maximum speed of about 4 m s^{-1} , within the typical range of $2 - 5 \text{ m s}^{-1}$ reported for sea-land breeze regimes (Simpson et al., 2002).

3.3.2 Breeze-Forced Oscillations

During the MREA04 sea trial, diurnal-inertial events were recorded in the Bay of Setúbal (Figure 3.1) at the Barny North and Barny South ADCP sites ($\sim 38^\circ \text{ N}$), where diurnal and inertial frequencies approach each other and breeze-forced oscillations may be enhanced. Decimated time series from these current profilers are shown in Figure 3.3a,b.

The depth-averaged rotary power spectral density for both ADCP locations (Figure 3.3c,d) shows that currents within the diurnal-inertial band were dominated by circular, clockwise motions. Here we define the diurnal-inertial band as approximately between 0.88 cpd and 1.38 cpd and involving both the diurnal ($\omega_d = 1 \text{ cpd}$) and inertial frequencies ($f \sim 1.24 \text{ cpd}$ about 38° N). The central peak of this band ($\omega_c \sim 1.1 \text{ cpd}$) was found at both sites in between ω_d and f . The proximity between these two frequencies, together with the length of the ADCP records, prevent us from distinguishing dominant peaks around ω_d and f .

For the most part, the diurnal-inertial band showed higher energy densities than did the semidiurnal band at both locations. Nevertheless, a strong variation in energy distribution was observed between the Barny North and Barny South records for this frequency-band that was more energetic at the Barny North ADCP site. Semidiurnal currents also exhibited different features, depending on the location. Elliptical clockwise gyres, 1 order of magnitude smaller than the diurnal-inertial band, were found to dominate at the Barny North ADCP site (Figure 3.3c), whereas elliptical counterclockwise gyres with the same order of magnitude as the diurnal-inertial band were found at the Barny South ADCP site (Figure 3.3d).

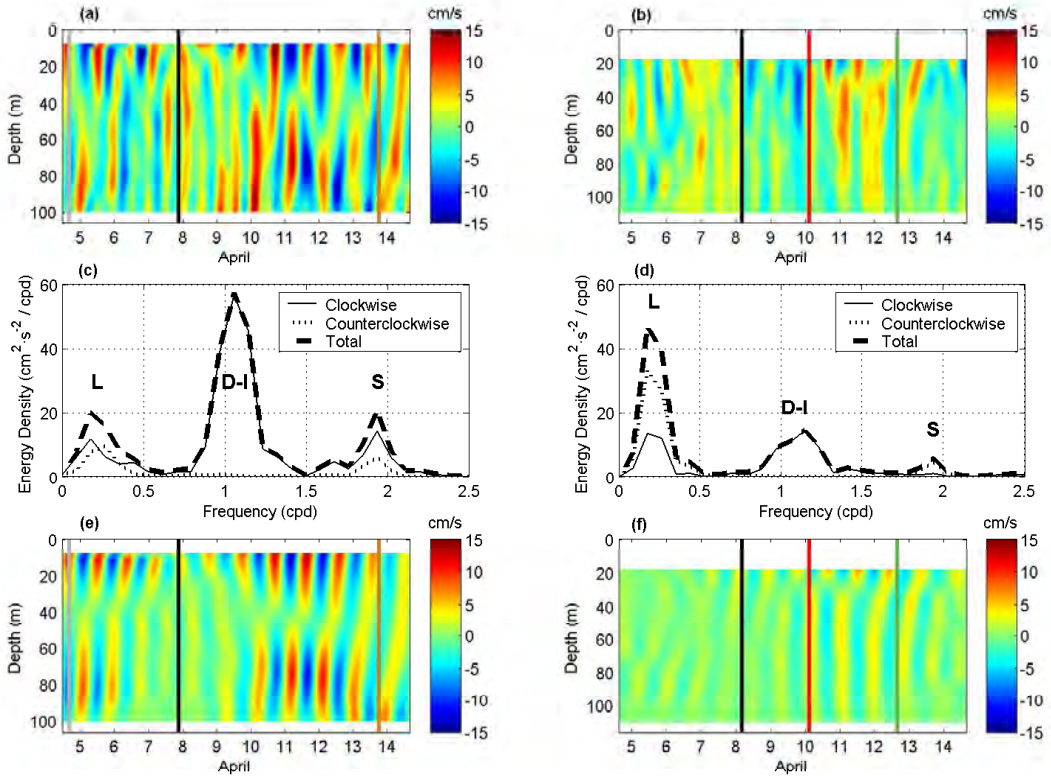


Figure 3.3: Breeze-Forced Oscillations on the Portuguese shelf - (a-b) Cross-shore currents (u) recorded at Barny North (Barny South) ADCP location as a function of time and depth during 4-14 April 2004. Time series have been decimated to 1 data point per hour after low-pass filtering oscillations shorter than 9 hours. Along-shore currents (v) showed an analogous pattern. (c-d) Depth-averaged rotary power spectral density of currents measured by the Barny North (Barny South) ADCP. The capital letters indicate low (L), diurnal-inertial (D-I), and semidiurnal (S) frequency bands. (e-f) Cross-shore currents (u) computed from (a-b) after band-pass filtering to isolate diurnal-inertial motions. The vertical colour lines represent the sampling times for the CTD casts used in Figure 3.5 to estimate the gradient Richardson number, Ri , concerning the Barny North (Barny South) ADCP.

Hereafter, we focus on the observation that the diurnal-inertial band was predominantly more energetic at both ADCP locations. To this end, the diurnal-inertial band was isolated (Figure 3.3e,f) via band-pass filtering (Alford, 2003b). Then circular clockwise currents oscillating within this band

3. BREEZE-FORCED OSC. AND DIAPYCNAL MIXING

(Figure 3.3c,d) were characterised in a two-layer configuration with a phase shift of $\sim 180^\circ$ between the upper and lower layers at both ADCP locations. Thereof, maximum current amplitudes of approximately 15 cm s^{-1} were found at the upper and lower layers for the Barny North ADCP location (Figure 3.3e) when diurnal wind forcing increased during 10–13 April (Figure 3.2d), whereas the maximum values were weaker, at approximately 5 cm s^{-1} , for the same period at the Barny South ADCP location. This period of increasing diurnal wind forcing appeared after 3 days of wind relaxation on 4–7 April. However, we also found evidence of diurnal-inertial oscillations with amplitudes of approximately 10 cm s^{-1} on those days at the Barny North site (Figure 3.3e). As we previously pointed out, these oscillations might be the transient response to a sea-land breeze regime that was acting a few days before the initiation of the meteorological buoy record and vanished later, what lead to wind-forced diurnal-inertial oscillations evolving into free near-inertial oscillations (Rippeth et al., 2002; Simpson et al., 2002). This situation would support the central peak (ω_c) of the diurnal-inertial band being band between ω_d and f as a combination of breeze-forced diurnal oscillations and transient near-inertial oscillations that come into play when wind forcing diminishes (Figure 3.3c,d).

According to the barotropic pressure gradient set up by breeze forcing at surface and its response in antiphase at the lower layer (Hyder et al., 2002; Rippeth et al., 2002; Simpson et al., 2002), the resultant breeze-forced oscillations showed, within every layer, very small variations in phase with depth. Additionally, the interface related to this 180° phase shift seemed to be fixed at a certain depth at both ADCP locations ($\sim 40 \text{ m}$ at Barny North and $\sim 30 \text{ m}$ at Barny South), except for the period 10 – 14 April when the depth of the phase shift moved downward along the Barny North ADCP record from 40 m to 70 m (Figure 3.3e). This deepening of the interface might have been a consequence to increasing diurnal wind intensities during those days (Figure 3.2d), in combination with a deepening of the pycnocline also from 40 m to 70 m (7-13 April in Figure 3.5a) owing to diapycnal mixing processes (as it will be analysed in Section 3.3.4). This observation agrees with previous works of modeling (Rippeth et al., 2002) in which the vertical structure of breeze-forced oscillatitons is driven by the above mentioned pressure gradient forcing, but the pycnocline marks the depth at which the phase shift is set up. Because of this behaviour, it was not rare to find a weakening of the diurnal-inertial vertical structure at the Barny North ADCP after 13 April, when the support of the interface had been strongly eroded and motions related to inertial contribution were damped out in the absence of a sharpened pycnocline

(as also shown in Rippeth et al. (2002)).

In modeling these energetic oscillations for MREA exercises, it is important to highlight that these are essentially wind-forced motions. Therefore, accurate meteorological forcing represents a critical target to get realistic predictions in real-time, similar to previous suggestions for near-inertial motions observed during the Maritime Rapid Environmental Assessment 2003 (MREA03) exercise, which was performed off of the west coast of Italy near the Elba Island (Coelho and Robinson, 2003). It has been attempted (*research not shown here*) to forecast the observed breeze-forced oscillations with a coastal oceanic prediction model around the ADCP's sites during the MREA04 sea trial. Tests were capable of reproducing the essential physics of these oscillations, although the forecasted oscillations are weaker and phase lagged in comparison with the observations. Recent efforts and improvements have been done in modeling for MREA exercises with adaptive sampling on short-time scales (Wang et al., 2009; Haley and Lermusiaux, 2010; Lermusiaux et al., 2010; Ueckermann and Lermusiaux, 2010).

3.3.3 Diapycnal Mixing and Breeze-Forced Events

The role that observed breeze-forced oscillations could be playing in the interior of the Bay of Setúbal responds to its associated high vertical shear within stratified layers (Pelegrí and Sangrà, 1998; Rodríguez-Santana et al., 1999, 2001) and is discussed here in terms of diapycnal mixing processes.

The entire Bay of Setúbal exhibited different stages of stratification during the MRE04 sea trial that involved breeze-forced oscillations and intrusions of fluvial waters coming from the Sado estuary. As is shown by the surface salinity and potential density fields in Figure 3.4a,d, this estuarine signal strongly affected the northern and western sides of the bay on 7-8 April, enlarging the area influenced on 9-10 April (Figure 3.4b,e). After a few days, this lighter and freshwater signal had already disappeared (12 April; Figure 3.4c,f). In the following we assess breeze-forced currents triggering diapycnal vertical mixing between oceanic and estuarine waters in the interior of the bay. We focus on that scenario accounting for the interaction between diurnal-inertial oscillation current events and stratification due to freshwater inputs.

3. BREEZE-FORCED OSC. AND DIAPYCNAL MIXING

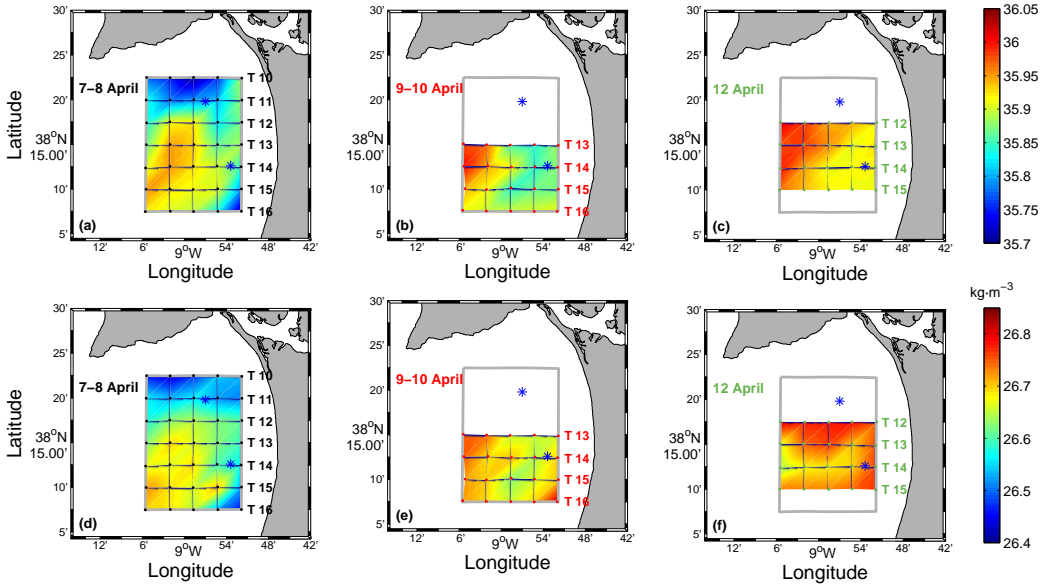


Figure 3.4: Surface Contours for the Bay of Setúbal - (a-c) Surface salinity and (d-f) surface potential density contours computed from CTD stations B, CTD stations C and CTD stations D, respectively. Blue stars correspond to the locations of Barny North and Barny South ADCP deployments. An input of fluvial waters (less salty and less dense than oceanic waters) coming from the Sado estuary is clear in surface contours (a) and (d).

To this end, the squared vertical shear (S^2), squared buoyancy frequency (N^2) and the gradient Richardson Number (Ri) were studied for the Barny North ADCP and CTD station 62 (Figure 3.5a-d), and the Barny South ADCP and CTD station 78 (Figure 3.5e-h). Critical values of $N < 0.7$ cph were not considered in this analysis to make a reliable estimate of Ri (Muench et al., 2002).

Barny North site

Figure 3.5a shows the vertical distribution of potential density at CTD station 62 on three different days: 4 April (grey line) and 13 April (brown line), when breeze-forced events were detected (Figure 3.3e); and 7 April (black line), corresponding to a relaxation of current oscillations. These captured ‘scenes’ allowed us to analyse the strength of breeze-forced diurnal-inertial motions in triggering diapycnal mixing processes according to its evolution over time.

Based on these profiles, the water column was found to be highly stratified on 7 April from 10 – 20 m depth, when breeze-forced currents vanished, reaching a maximum N^2 of approximately $2 \times 10^{-4} \text{ s}^{-2}$ (Figure 3.5b). This maximum responded to the intrusion of estuarine waters (warmer and lighter than oceanic waters) into the bay (Figure 3.4a,d).

On the contrary, profiles on 4 and 13 April exhibited lower levels of stratification near the surface and all along the water column until a depth of approximately 60 m, where N^2 started to increase for next 20 m, approaching values of $2 \times 10^{-5} \text{ s}^{-2}$. For these two sampled days in which breeze-forced oscillations were stronger (Figure 3.3e), the squared vertical shear S^2 (Figure 3.5c) showed two pairs of maximum values. These two peaks concern the depths where the maximum currents were acting within the described out-of-phase layer configuration for diurnal-inertial oscillations. The largest peaks were both over $3 \times 10^{-5} \text{ s}^{-2}$ at 80 – 90 m on 4 April and occupied a broader range of depths on 13 April (60 – 80 m). The secondary peaks placed around 30 – 60 m on 4 April, and 20 – 50 m on 13 April, with values of $1.3 \times 10^{-5} \text{ s}^{-2}$ and $2.1 \times 10^{-5} \text{ s}^{-2}$, respectively.

With regards to the profile sampled when there was a period of relaxed-winds (7 April in Figure 3.5c), two maxima of S^2 were also observed at similar depths to the previous ones, but with inverted positions. The largest peak was located between 30 – 40 m with $S^2 \sim 3.3 \times 10^{-5} \text{ s}^{-2}$, and the second largest peak was located over 80 m with $S^2 \sim 1.6 \times 10^{-5} \text{ s}^{-2}$. These peaks might be the response to attenuated diurnal-inertial currents during 7 – 8 April, which decayed in a transitional state, disturbed by the intrusion of estuarine waters into the bay. The break in the vertical structure of the water column caused by this intrusion is evident by comparison of the potential density profiles taken on 4 April and 7 April (Figure 3.5a).

From the combination of previous data (N^2 and S^2), the vertical distribution of the gradient Richardson number was estimated (Figure 3.5d) to locate the depths at which the generation of Kelvin-Helmholtz instabilities caused by vertical shears in a stratified fluid could be suitable to trigger mixing and account for the observed changes in the vertical distribution of the potential density.

3. BREEZE-FORCED OSC. AND DIAPYCNAL MIXING

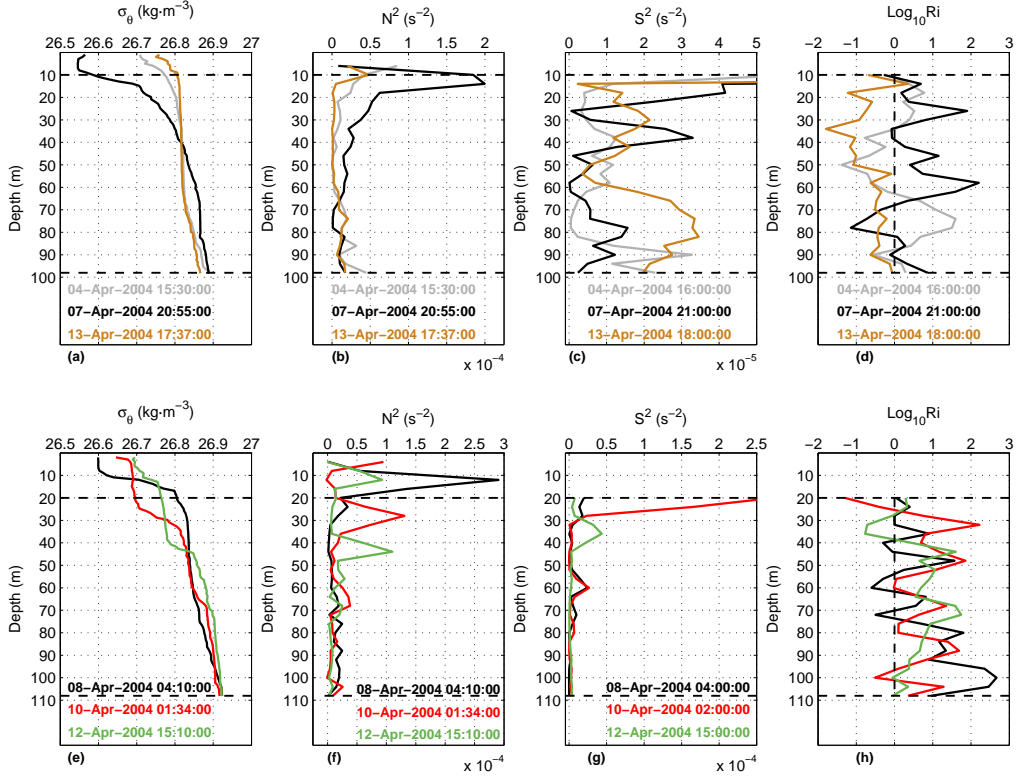


Figure 3.5: Diapycnal Mixing Analysis - Vertical time-profiles of (a,e) potential density, σ_θ ; (b,f) squared buoyancy frequency, N^2 ; (c,g) squared vertical shear, S^2 and (d,h) logarithm of the gradient Richardson number, Ri . These plots combine data from CTD station 62 together with Barny North ADCP (a-d) and data from CTD station 78 together with Barny South ADCP (e-h) after low-pass filtering oscillations shorter than 9 hours. Horizontal dashed lines represent the range of depths sampled with the Barny North (South) ADCP.

Subcritical values ($Ri < 0.25$) were found at several depths during breeze-forced events. On 4 April, the two maximum peaks of S^2 corresponded with values lower and close to subcritical Ri , respectively. The first peak, $Ri \sim 0.04$, was found at 50 m and was associated with high vertical diapycnal diffusivities coefficients, k_v , of approximately $3 \times 10^{-3} \text{ m}^2 \text{ s}^{-1}$. The second peak, $Ri \sim 0.27$, was also associated with high values, $k_v \sim 4 \times 10^{-4} \text{ m}^2 \text{ s}^{-1}$, around 90 m depth. Analogously, the two peaks of high S^2 on 13 April coincided approximately with low Ri values of 0.02 over 30 m and 0.23 at 90 m, which were associ-

ated with an enhanced k_v of $\sim 4 \times 10^{-3}$ and $\sim 5 \times 10^{-4} \text{ m}^2 \text{ s}^{-1}$, respectively. Overall, on 13 April, the whole profile supported values of $Ri < 1$, giving rise to high diapycnal diffusivities, especially in the range of the upper layer (20-50 m depth) observed for breeze-forced oscillations during 10 – 14 April (Figure 3.3e).

It is worth noting that, during the breeze-relaxed period on 7 – 8 April, Ri values larger than 1 were obtained with high levels of high stratification near the surface and attributable to strong inputs of fluvial waters on these days. Nevertheless, at deeper levels (around 80 m), Ri values close to 0.1 were also found with $k_v \sim 2 \times 10^{-3} \text{ m}^2 \text{ s}^{-1}$.

The common pattern observed on 4 and 13 April during breeze-forced current events was a two-layer vertical structure with high values of S^2 embedding stratified waters. As a result, the pycnocline that partially contributed to supporting this two-layer configuration was significantly eroded. In such a way, this triggered a vertical displacement of the interface with high stratification, now smoothed, towards deeper waters. These results suggest that the displacement was promoted by the high vertical shear of the upper and lower layers acting over the depths of the highest stratification.

If we now recall the theoretical works of Rippeth et al. (2002) and Simpson et al. (2002), one can understand why in presence of a noticeable breeze-forcing over 8-13 April (Figure 3.2d) there is, on the contrary, a weakening of the breeze-forced current system. These studies predict that breeze-forced currents at the lower layer, in relation to those in the upper layer, vanish by a factor γ which is dependent of the depth of the pycnocline following $\gamma = h_2/h_1$ (being h_1 (h_2) the thickness of the upper (lower layer)). Thus, the deepening and smoothing of the interface observed along 8-13 April (Figure 3.5a-d) could have driven the self erosion of the baroclinic mode which supported the breeze-forced current system (Figure 3.3e) owing to its associated vertical diapycnal mixing. A similar finding was reported by Zhang et al. (2009) in the Gulf of Mexico, where they observed that the deepening of the mixed layer depth driven by freshwater inputs and vertical mixing weakened the diurnal-inertial ocean response to breeze-forcing.

Barny South site

Regarding the Barny South ADCP deployment and CTD station 78, Figure 3.5e presents the vertical profiles of potential density on three different

3. BREEZE-FORCED OSC. AND DIAPYCNAL MIXING

days: 8 April (black line), characterised by the absence of breeze-forced events; and 10 April (red line) and 12 April (green line), which involved increasing breeze-forced oscillations (Figure 3.3e).

As can be observed in Figure 3.5f, the maximum values of N^2 that partially supported the baroclinic mode of these diurnal-inertial motions increased their depth from 8 April (10 m) to 12 April (45 m) while decreasing their values from approximately $3 \times 10^{-4} \text{ s}^{-2}$ to $1 \times 10^{-4} \text{ s}^{-2}$. This deepening of the pycnocline likely occurred according to the mechanism previously explained for breeze-forced currents oscillating around the Barny North ADCP site.

On 10 April, the distribution of vertical shear (Figure 3.5g) exhibited a maximum at 20 m, which was above the interface of high stratification, with an S^2 of approximately $2.7 \times 10^{-4} \text{ s}^{-2}$. A secondary peak of $S^2 \sim 3 \times 10^{-5} \text{ s}^{-2}$ was found on the same day for the lower layers, which is similar to the situation described for the Barny North ADCP. Likewise, on 12 April, a maximum of S^2 was also found above the interface of high stratification with values of $\sim 4.3 \times 10^{-5} \text{ s}^{-2}$ at approximately 35 m.

For days when breeze-forced diurnal-inertial oscillations were acting, the main peaks of S^2 coincided with low Ri values of 0.05 at 20 m depth on 10 April and 0.17 at 35 m depth on 12 April (Figure 3.5h). The values of k_v associated with these Ri values were also relatively high, approximately $2.6 \times 10^{-3} \text{ m}^2 \text{ s}^{-1}$ on 10 April and $8 \times 10^{-4} \text{ m}^2 \text{ s}^{-1}$ on 12 April. As a consequence, the combination of strong vertical shears and surface inputs of stratification from the estuary produced the same effects as illustrated for the area sampled by the Barny North ADCP and CTD station 62. Thus, a noticeable modification of the density vertical distribution at relatively short-time scales was also found in response to diapycnal mixing processes enhanced by breeze-forced motions. Additionally, it was also found that again the well-defined baroclinic mode structure which supported the breeze-forced currents (Figure 3.5e-h on 10 April) broke up due to vertical mixing (Figure 3.5e-h on 12 April), hence weakening the diurnal-inertial ocean response even in presence of breeze-forcing (Figure 3.3f).

CTD and ADCP observations reported here, although they were not planned during the MREA04 sea trial for the present research, successfully capture the critical moments and consequences of the interactions between breeze-forced current events and stratified waters in the interior of the bay. These results contribute to explaining the main vertical changes observed in the CTD casts

next to the ADCP deployments during observed breeze-forced events and support that these events may play an important role in promoting vertical mixing. This mechanism is of special interest in areas where the water column is stratified and strong vertical shears, as shown in this study, can be responsible for the diapycnal transport of nutrients. In these cases, breeze-forced oscillations may be able to promote regions of high biological productivity, as it has been observed for strong inertial currents in the North Sea (van Haren et al., 1999).

3.3.4 Impact of BFOs in the Bay of Setúbal

One may expect that breeze-forced oscillations reported here are not an isolated feature of the area of study but be part of the hydrodynamics of the bay. Counting with shelf conditions next to an estuary which supplies freshwater to the surface ocean, one has half of the required scenario for breeze-forced oscillations. However, the forcing to the system cannot be assumed to be a regular pattern of the area without analysing the local sea-land breeze system.

In this section we use wind time series data from a land meteorological station at Sines (Figure 3.1), which bounds the southern side of the Bay of Setúbal, in order to determine whether the area may be a suitable candidate for further research on the impact of breeze-forced oscillations in stratified waters.

With this aim the rotary wavelet spectrum is shown in Figure 3.6 for wind data during 2004. As it can be observed, the result of the wavelet analysis gives evidence of the same seasonal pattern reported in *Chapter 2* for diurnal wind over three different locations placed off the Iberian Peninsula coast. Thus, the variability for this frequency band exhibits, as expected, a stronger and more recurrent presence of sea-land breezes during the summer months.

These results, together with previous analysis, suggest that the Bay of Setúbal, which is framed within the critical latitudes for diurnal-inertial resonance, seems to be a suitable candidate area for the enhancement of diurnal-inertial motions when sea-land breezes are acting and, hence, to promote diapycnal vertical mixing with important consequences for the shelf dynamics in the interior of the bay.

3. BREEZE-FORCED OSC. AND DIAPYCNAL MIXING

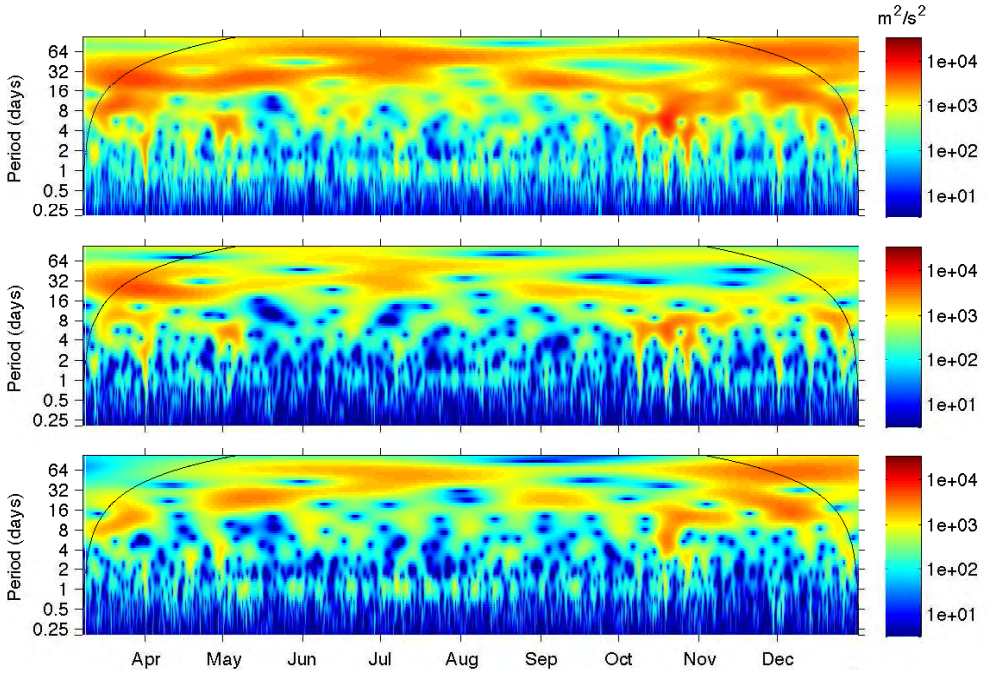


Figure 3.6: Rotary Wavelet Power Spectrum of Wind from a Meteorological Station at Sines - Rotary wavelet power spectrum of winds (at 10 m above the ground) measured at Sines from April 2004 to December 2004. (upper panel) Total rotary wavelet power spectrum. (intermediate panel) Rotary wavelet power spectrum of clockwise component. (lower panel) Rotary wavelet power spectrum of counterclockwise component. The two black lines on either end indicate the ‘cone of influence’ where edge effects become important.

3.4 Conclusions

The Bay of Setúbal is located within the critical latitudes ($30^\circ \pm 10^\circ$ N/S) where inertial period approaches diurnal period and a near-resonance response between free inertial oscillations and diurnal wind forcing may occur. Under these conditions, we show evidence of breeze-forced oscillations (BFOs) enhancing diurnal-inertial energy in the interior of the bay and promoting vertical diapycnal mixing.

The squared vertical shear (S^2), squared buoyancy frequency (N^2) and the gradient Richardson Number (Ri) were estimated to analyse the scenario in

which enhanced vertical shears developed during breeze-forced events led to stratified and vertically sheared flows with subcritical values of Ri . These zones were found to promote vertical mixing across the pycnocline due to strong squared vertical shears about 10^{-5} s^{-2} . In the end, these mixing processes drove the self-erosion of the pycnocline that partially supported the interface between the two-layers, thereby homogenising the water column in their wake. At the Barny South ADCP site, the vertical variation in the highest peaks of stratification was especially clear, shifting approximately 15 m in two and a half days and involving an efficient mechanism to transport properties vertically throughout the water column.

The above results point out that there may exist an internal control on the strength of the ocean response to breeze forcing that has not been described before to the best of our knowledge. This follows from the previously discussed role that the depth of the mixed layer plays on the vertical structure of BFOs supporting its baroclinic mode and determining the intensity of the forced currents above and below the pycnocline (Rippeth et al., 2002; Simpson et al., 2002). Starting from this basis, we observe that vertical diapycnal mixing promoted by breeze-forced oscillations led to the deepening and smoothing of the pycnocline which supported them and, hence, weakened the ocean response to breeze-forcing following a self-erosion mechanism. Hence, we suggest that the effect of the vertical mixing must be included in theoretical models to realistically predict the evolution of the vertical structure of breeze-forced oscillations; otherwise, initialising a model with a prescribed pycnocline which is fixed along the simulation will not allow the decay of breeze-forced oscillations due to the deepening of the mixed layer driven by the associated vertical mixing.

From this basis, we consider that further research of time series data (currents, temperature and salinity) covering the total water depth in combination with co-located simultaneous wind data would benefit greatly the understanding of how breeze-forced oscillations evolve in time and space, with special attention to the role that associated diapycnal mixing may be playing on the vertical structure of these forced-motions.

Remarks on this Chapter

The rotary wavelet spectrum of wind data shown in this chapter represents an extension to the publication of Aguiar-González et al. (2011).

3. BREEZE-FORCED OSC. AND DIAPYCNAL MIXING

The analysis of diapycnal mixing processes associated to breeze-forced oscillations and the discussion of the role that enhanced mixing might be playing on the vertical structure of these forced motions Aguiar-González et al. (2011) represents the main contribution of *Chapter 3* to this topic.

To this regard we find of interest to discuss a later paper of Hyder et al. (2011) in which the authors report observations and simulations of wind-forced oscillations on the Namibian shelf, i. e. equatorward the critical latitude for diurnal-inertial resonance. They found that the General Ocean Turbulence Model (GOTM) 1-D simulations of diurnal forcing, including the first order coast-normal surface slope response to diurnal forcing, represented the principal features of the observed diurnal anticyclonic current. However, they also found that the vertical structure of simulated diurnal anti-cyclonic amplitudes was significantly different to those observed. The problem was mainly based on the upper layer depth was too shallow and the upper layer amplitude was too strong. They suggest that differences could arise because the simulated downward transfer of wind forced momentum is too small or the relative magnitude of diurnal wind and slope forcing for the model is not correct, i. e. the Craig approximation is invalid. As the downward transfer of wind momentum is controlled by mixing, they point out that in their 1-D simulations unresolved 3-D processes such as internal waves may be missrepresenting an important source of mixing. Also, the sensitivity of the upper layer thickness and amplitude to latitude in their simulations was discussed and tested as possible explanation for the disagreement between observations and model results.

The most interesting aspect to our concern is the series of experiments that the authors undertook to elucidate the origin of this disagreement. With this aim they modified the standard configuration of their runs. Among those experiments, they included a simulation *employing an unrealistic minimum TKE of $1 \times 10^{-3} \text{ m}^2 \text{ s}^{-2}$ to represent a large unknown unresolved mixing source*¹. For standard model runs the authors had employed a minimum turbulence kinetic energy (TKE) k_{min} of $1 \times 10^{-6} \text{ m}^2 \text{ s}^{-2}$. With this modification, the simulations improved and provided a much better representation of vertical phase variation, deepening the upper layer depth and reducing the error in the lag between the wind and the upper layer current.

Broadly, we find those modeling results of great importance as they support our earlier suggestion, based on observational analysis, that there may exist an

¹Literally reproduced from Hyder et al. (2011).

internal control on the strength of the ocean response to breeze forcing owing to associated diapycnal mixing processes which erodes the baroclinic mode of the breeze-forced oscillations deepening the upper layer and modifying its vertical structure.

3. BREEZE-FORCED OSC. AND DIAPYCNAL MIXING

Chapter 4

Introduction to a Solitons Scenario

This chapter opens the second half of this PhD study and introduces observations and theoretical works on solitary waves in the ocean. The goal here is to provide to the non-expert reader with a brief background on this topic and focus the attention on those aspects surrounding the generation and evolution of topographic-caused large amplitude solitons. In Section 8.2 we describe the key features which characterize oceanic observations of solitons: its dynamics and kinematics, typical scales, and generation mechanisms. Once the observational picture of solitary waves in the ocean has been drawn, we discuss the theoretical approach to the phenomenon in Section 8.2.2. There, we review the mathematical physics behind solitary wave theory, highlighting those works which are of the main concern to our problem. Lastly, we discuss in Section 8.2.3 the scope of this PhD study within the described context.

4.1 Solitary Waves in the Ocean

Solitary waves, also known as solitons, are a widespread phenomenon in the ocean which are part of the higher frequency band of the internal waves. This term defines a type of waves which travel within the interior of a stratified fluid after a perturbation moves water particles away from their equilibrium position. In a rotating fluid at large scales, as it is the case of the ocean, these

4. INTRODUCTION TO A SOLITONS SCENARIO

internal waves propagate at a range between the buoyancy N and the inertial f frequencies, which set the maximum and minimum limits of the internal wave frequency-band¹. When the perturbation is caused by the barotropic tidal flow interaction with topography, the waves thus generated are known as ‘internal tides’ (baroclinic tides), and hence propagate at tidal frequencies.

Most frequently, the origin of internal solitary waves in the ocean appear to be related with the latter, the baroclinic tides. Thus, solitary waves appearance have been detected, using remote or *in situ* sensors, specially in the proximity of coastal regions.

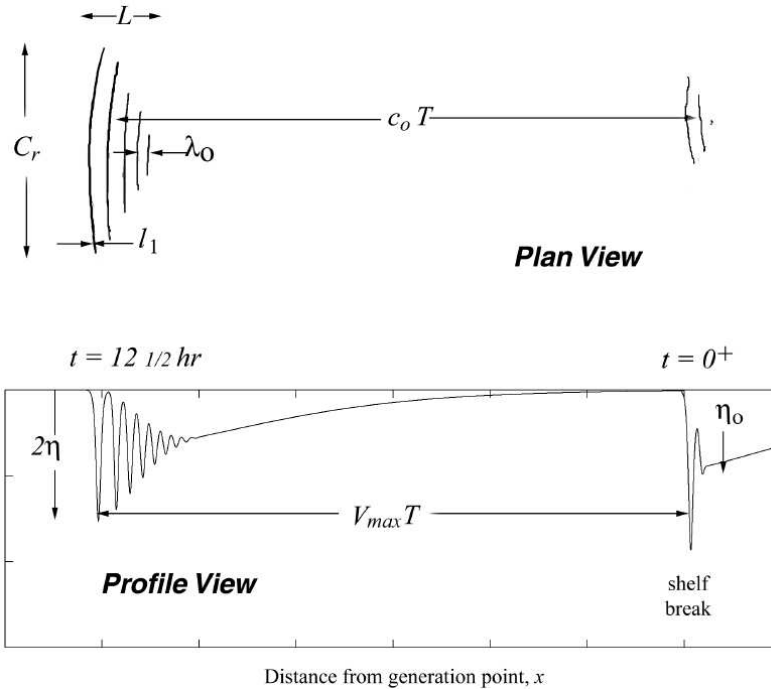


Figure 4.1: Schematic of Canonical Soliton Packets - Diagram of soliton packets showing notation for length scales (see Table 4.1 for typical values of continental shelf solitons). $V_{max}T$ is the internal wavelength; c_0T is distance between packet centroids. [From Apel (2002) - Fig. 2].

¹This frequency range may be different when ‘non-traditional effects’ come into play. However, this is not the framework of our research. For details on the ‘non-traditional approach’ see (Gerkema and Shrira, 2005; Gerkema et al., 2008). Also, nonlinear effects can enlarge this range slightly.

The ‘direct’ generation of internal solitary waves driven by a barotropic tidal flow over topography is associated to areas of shelf break and irregular topographies (sills, banks, seamounts, ...). The generation mechanism involves the lee-wave release from topography of a first-mode internal tide which steepens into shorter-like waves (Maxworthy, 1979; Gerkema, 1994; Helfrich and Grimshaw, 2008). The nonlinear effects in the internal tide are balanced by nonhydrostatic and, and to lesser extension, Coriolis dispersion giving rise to a rank-ordered packet of solitary waves of a few to a few dozen of pulses moving at their own individual speeds (Gerkema and Zimmerman, 1995; Gerkema, 1996; Apel, 2002). These nonsinusoidal, higher-frequency waves are form-preserving (nonlinearity and dispersion effects counteract) and travel with the largest, fastest and long-crested solitons at the front of the sequence. Thus, the leading waves present longer distances between successive solitons in comparison with adjacent pulses at the rear.

An idealization of a solitary wave packet generated over a shelf break (or a sill) is shown in Figure 4.1 of Apel (2002), detailing its main components. Top view in Figure 4.1 presents the evolution of two solitary wave packets formed during two successive tidal cycles (the leftmost packet being generated during the first tidal cycle). Each packet lengthens and increases its number of individual solitons in time. Complementary, the profile view in Figure 4.1 shows solitons as vertical displacements of the interface constituting two different packets which change their profile as they propagate away from the generation area.

The distance observed between the packets is termed in this context as the ‘wavelength’ of the internal tide. The theoretical nonlinear velocity of the leading soliton V_{max} (Profile View in Figure 4.1) is defined by that wavelength, the amplitude and the tidal period, T . Typical values for continental shelf solitons are given by Apel (2002) as a reference (see Table 4.1), assuming the shelf sea is stratified approximately in a two layer configuration with h_1 being the upper layer and h_2 the lower layer.

A well-known example of solitary waves in the ocean can be found in Stanton and Ostrovsky (1998) where solitons propagate in shallow waters off Northern Oregon (Figure 4.2). Observations show clearly how the internal tide steepens and develops a nonlinear leading edge. Resulting waves are considered to be highly nonlinear due to large downward displacements (by up to 25 m) in comparison with the undisturbed depth of the pycnocline (~ 7 m).

4. INTRODUCTION TO A SOLITONS SCENARIO

Characteristic	Symbol	Scale
Packet Length	L (km)	1 - 10
Amplitude Factor	$2\eta_0$ (m)	-15
Upper Layer Depth	h_1 (m)	20 - 35
Lower Layer Depth	h_2 (m)	30 - 200
Long Wave Speed	c_0 (m s ⁻¹)	0.5 - 1.0
Maximum Wavelength	λ_{max} (m)	100 - 1000
Crest Length	C_r (km)	0 - 30
Internal Tide Wavelength	$D = VT$ (km)	15 - 40
Characteristic Soliton Width	l_1 (m)	100

Table 4.1: Typical Scales for Shelf Solitons - Typical values for continental shelf solitons assuming the shelf sea is stratified approximately in a two layer configuration with h_1 being the upper layer and h_2 the lower layer. [From Apel (2002) - Table 1.1].

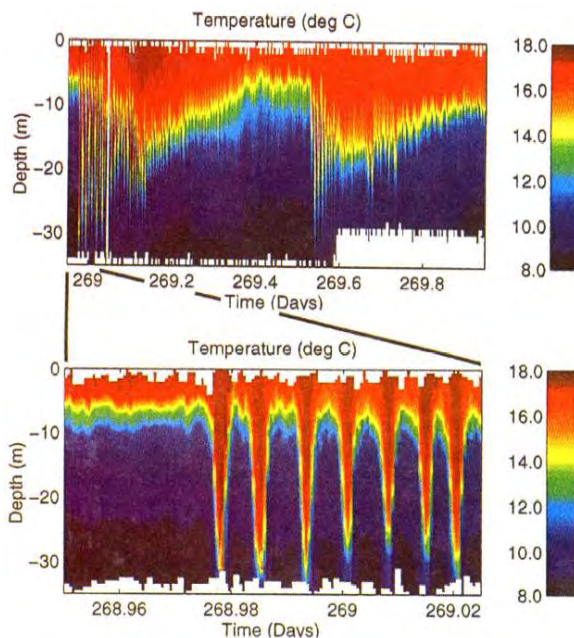


Figure 4.2: Solitary Waves over the Oregon shelf - (a) A color contour time series of temperature profiles from the surface to 35 m depth measured by the Loose-tethered Microstructure Profiler (LMP) over a one day period. The 10°C span color contour scale is shown on the right of the time series panel. The low frequency, semidiurnal internal tide displacement can clearly be seen along the yellow isotherm. (b) A profile time series of the first 1.7 hours of the time series shown in (a). White areas indicate times with no data. [From Stanton and Ostrovsky (1998) - Figure 1].

4.1 Solitary Waves in the Ocean

As long as soliton generation is linked to internal tide activity, solitary wave packets will exhibit the same variability as tides, and hence the properties of generated solitons will vary on semidiurnal, diurnal, fortnightly, seasonal and semiannual cycles. Therefore one can expect, for instance, more and larger solitons during spring tides than during neap tides (Pingree and Mardell, 1985). Depending on the site and time, solitary wave generation may be even possible only during spring tides, being absent at neap tides (Apel et al., 1985; Osborne and Burch, 1980).

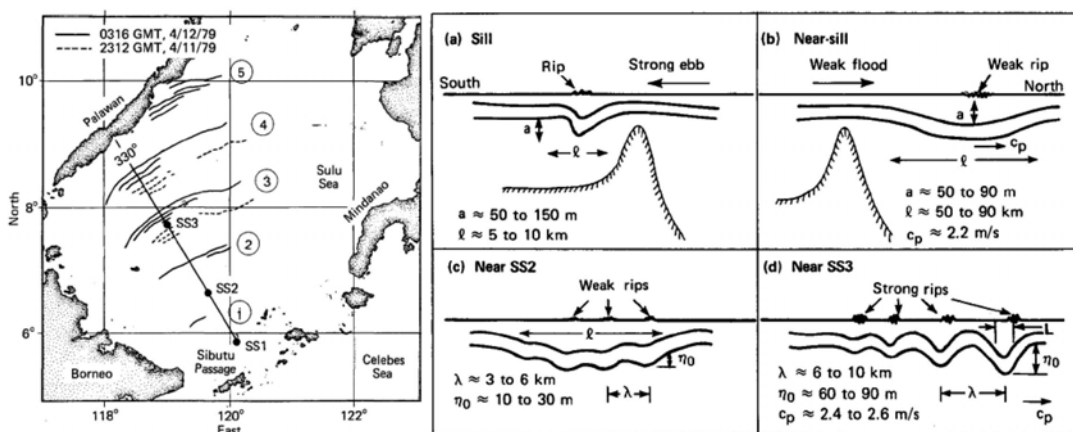


Figure 4.3: Evolution of a Solitons Packet in the Sulu Sea - Composite of two figures reported in Apel et al. (1985). Left-hand side: Line drawing renditions of DMSP (Defense Meteorological Satellite Program) images, interpreting striations as surface signatures of packets of internal solitary waves. Several solitons occur in each group, and up to five packets are visible in images. Interpacket distance range from 56 to 198 km, depending on azimuth and fortnightly tidal phase. Intersoliton distances, which defines wavelengths, range from 5 to 16 km. Two different DMSP images at times yield direct time-of-flight speeds of approximately 2.4 m s^{-1} . Right-hand side: Schematic diagram summarizing the evolution of a soliton packet in the Sulu Sea: (a) In the sill region an internal hydraulic jump is produced by strong ebb (southward) flow over the Pearl Bank sill. (b) As the tidal flow changes to a weak flow, a broad thermocline depression moves over the sill, propagating northward. (c) Eventually solitary waves begin to form on this depression as nonlinear and dispersive effects begin to balance. (d) After traveling a distance approximately 200 km the soliton packet is well-developed. Scales shown are typical. [From Apel et al. (1985): Right-hand side of Fig. 13; and Fig. 25].

4. INTRODUCTION TO A SOLITONS SCENARIO

An illustrative case of large-amplitude solitons generated from a sill occur in the Sulu Sea (Apel et al., 1985; Liu et al., 1985). The study area is shown in the left-hand side of Figure 4.3. The mechanism consists on the release of a low-mode internal tide from the Pearl Bank sill (Figure 4.3 - Right-hand side: a - b). Subsequently, as the internal tide propagates nonlinear steepening and dispersive effects come into play leading to the appearance of solitary waves distributed into packets separated by tidal cycles (Figure 4.3 - Right-hand side: c - d).

The generation mechanism over a shelf break and over a shallow promontory (sills, banks, seamounts, ...) is similar, however solitons propagating oceanward evolves differently than those traveling shoreward since the former are generally out of the area controlled by bathymetry. Hence, solitary waves propagating on the shelf, where the pycnocline depth shoals and the water depth diminishes, are conditioned by bottom friction effects. This leads to refraction of the waves, driving the packet crests along isobaths and decreasing their amplitudes, speeds and wavelengths, independently from wherever solitons were generated. A clear example of wave refraction of solitons when water depth shoals can be found in Zeng and Alpers (2004) for solitary waves traveling to shallow waters, afresh in the Sulu Sea (Figure 4.4).

Nevertheless, solitary wave packets have been also observed traveling oceanward far away from shelf breaks and promontory areas (e.g. solitons in the Bay of Biscay (Gerkema, 2001; New and da Silva, 2002)). These solitons respond to a different generation mechanism. Then, we need to consider that internal tidal energy may radiate away either horizontally as interfacial waves in the thermocline (mechanism explained above and termed ‘direct generation’) and/or vertically as ‘beams’ into the stratified continuum below (mechanism known as ‘local generation’) (New, 1988, 1990; New and Pingree, 1992; Gerkema, 2001; Akylas et al., 2007; da Silva et al., 2007; Da Silva and New, 2009). These beams emanate from critical topographies where bottom slope matches the slope of the beam paths and travel at an angle to the vertical into the deep ocean. After reflection from the seafloor, scattering of these beams at the base of the thermocline induces the generation of internal solitary waves propagating at long distances from the shelf break or promontory which caused the initial beam of internal tidal energy (New, 1990; Gerkema, 2001; Da Silva and New, 2009). Other possible mechanism of soliton generation include shear-flow instability just up-current of the break/sill (Farmer and Armi, 1999), upstream blocking (Lee and Beardsley, 1974), transcritical generation (Grimshaw, 1986;

Melville and Helfrich, 1987).

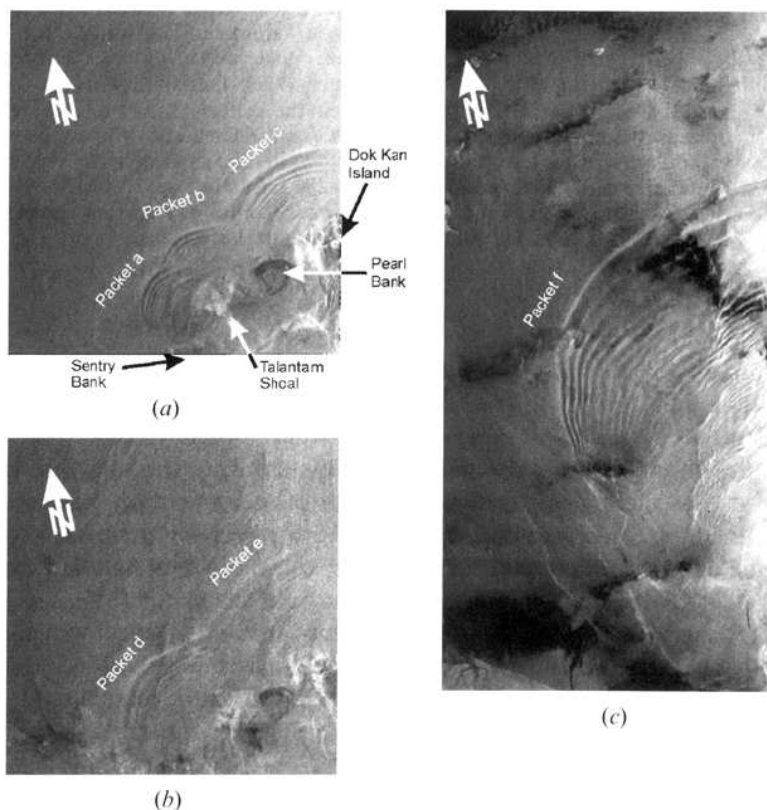


Figure 4.4: Remote Sensing SAR (Synthetic Aperture Radar) images of Solitons in the Sulu Sea - (a) ERS-2 SAR image acquired during orbit 14529 on 30 January, 1998, at 02:24 UTC showing sea surface manifestations of three internal wave packets generated at (three different locations; (b) ERS-2 SAR image of the same area, but aquired during orbit 09018 on 10 January, 1997, at 02:24 UTC which was at a slightly later phase of the tidal cycle; (c) ERS-2 SAR acquired during orbit 06284 on 3 July, 1996, at 02:27 UTC showing strong refraction of internal solitary waves by bottom topography. [From Zeng and Alpers (2004) - Figure 1].

As one can imagine, a better understanding of the dominating mechanisms by which solitons are generated will benefit from the assessment of the candidate areas for soliton activity. Additionally, the interest on oceanic solitons is supported by the impact these waves have on various aspects: ocean mixing

4. INTRODUCTION TO A SOLITONS SCENARIO

and biological productivity (Sandstrom and Elliott, 1984; Pinkel, 2000; Sangrà et al., 2001; Moum et al., 2003; Macias et al., 2006), water acoustics (Tiemann et al., 2001), sediment transport (Sandstrom and Elliott, 1984; Bogucki et al., 1997; Butman et al., 2006), oil platforms (Osborne and Burch, 1980), etc. The uncertainty about the relative importance of each generating mechanism worldwide leads to the topic of oceanic solitons still represents a challenging fieldwork. Fine reviews of the existing empirical and theoretical background on solitons can be found in Ostrovsky and Stepanyants (1989); Grimshaw et al. (1998); Apel (2002); Apel et al. (2006); Helfrich and Melville (2006).

The seed for next section is linked to the earliest scientific report describing the surface manifestation of a solitary wave, which was made by J. Scott Russell in 1838 on a propagating and unchanging single hump in a Scottish canal (Russell, 1838b,a). Half a century later, Korteweg and de Vries provided for the first time a theoretical explanation to this important phenomenon in the field of mathematical physics (Korteweg and de Vries, 1895). That work opened an entire research line on the study of soliton properties from a theoretical point of view whose interest persists in time. In the following we focus on introducing the solitary wave theory which is of main concern for the background of this PhD research.

4.2 A Mathematical Approach to Solitons

To set the scope of the present thesis, we first discuss soliton wave theory based on the applications of the quadratic Korteweg-de Vries equation (KdV) and its extended cubic version (eKdV), which describe the dominant wave characteristics and evolution of solitons under weakly (KdV) and more strongly nonlinear conditions (eKdV), respectively, given an initial profile. Theoretical models are traditionally built up starting from the most simplified situation possible, which gets more comprehensive by including new elements in modeling the process as long as a previous scenario is understood. On solitary wave theory, it is not surprising that KdV-type models have become the classical approach to describe nonlinear dispersive waves. They have been widely used in the literature and show good agreement with dominant relationships between phase speed, amplitude and wavelength scales in comparison with reported observations of oceanic solitons (Osborne and Burch, 1980; Pingree and Mardell, 1985; Ostrovsky and Stepanyants, 1989; Stanton and Ostrovsky, 1998; Xu and Yin, 2012). Additionally, they permit modeling the phenomenon of interest

with a reduced set of equations. However, not all quantitative features are fully well captured.

The Korteweg-de Vries (KdV) equation is a quadratic nonlinear model which admits form-preserving solitary wave solutions travelling in one dimension and based on a balance between nonlinearity and dispersive effects. For simplicity, here we discuss the KdV equation in terms of a two-layer fluid with a rigid lid at the surface, even bottom and no mean flow (Djordjevic and Redekopp, 1978; Kakutani and Yamasaki, 1978), following

$$\frac{\partial \eta}{\partial t} + c_0 \frac{\partial \eta}{\partial x} + \alpha \eta \frac{\partial \eta}{\partial x} + \beta \frac{\partial^3 \eta}{\partial x^3} = 0 \quad (4.1)$$

where t is time; x is the spatial variable in the direction of wave propagation; h_1 (h_2) is the thickness of the upper (lower) layer; g is the gravitational acceleration; $\eta(x, t)$ is the interfacial displacement from its rest level; and α , β and c_0 are the so-called environmental coefficients of the medium describing nonlinearity, dispersion and long-wavelength phase speed which read

$$c_0^2 = \Lambda \rho g \frac{h_1 h_2}{h_1 + h_2}, \quad \alpha = \frac{3}{2} \frac{h_1 - h_2}{h_1 h_2} c_0, \quad \beta = \frac{1}{6} h_1 h_2 c_0, \quad (4.2)$$

with $\Lambda \rho = (\rho_2 - \rho_1) / \rho_2$. Additionally, relative differences in density between the two layers ($\Lambda \rho$) are assumed to be small (Boussinesq approximation), what holds in the ocean with typical values of the order 10^{-3} .

This KdV equation is applicable in shallow waters to stratified fluids where two main assumptions are taken: 1) The interfacial displacement is much smaller (but of finite amplitude) than the depth of either layer (i. e., weak nonlinearity); and, 2) waves are long (but of finite length) in comparison with the fluid depth (i. e., weak nonhydrostatic dispersion). Thus, the KdV equation is scaled by the small parameters $\alpha = a/H$ and $\beta = (H/l)^2$ in such a form that both are small and of comparable order ($\beta = O(\alpha) \ll 1$); taking a as a measure of the wave amplitude, l as the length scale of the wave, and H as the intrinsic vertical scale. The limit in which waves are infinitesimal ($\alpha \rightarrow 0$ leads to linearity) and of infinite length ($\beta \rightarrow 0$ leads to hydrostacy) reduces 4.1 to $\frac{\partial \eta}{\partial t} + c_0 \frac{\partial \eta}{\partial x}$, which simply describes rightward travelling waves. Wherever waves are assumed to be small but of finite amplitude and long

4. INTRODUCTION TO A SOLITONS SCENARIO

but of finite wavelength, parameters α and β take values different from zero to include, respectively, nonlinear and nonhydrostatic dispersive effects in the KdV evolution equation.

The prototypical analytical solution to the KdV equation for a single soliton is the hyperbolic secant profile, which reads

$$\eta(x, t) = \eta_0 \operatorname{sech}^2\left(\frac{x - ct}{\lambda}\right) \quad (4.3)$$

where c is the nonlinear phase speed derived from KdV theory and related to the linear phase speed c_0 and amplitude; and λ is the characteristic width of the soliton, being related to the amplitude of the displacement η_0 and the environmental coefficients:

$$c = c_0 + \frac{\alpha\eta_0}{3}, \quad \lambda^2 = \frac{12\beta}{\alpha\eta_0} \quad (4.4)$$

As λ^2 must be positive, for a thin upper layer with $h_1 < h_2$ we have that $\alpha < 0$, what results in downgoing displacements of the interface between the layers ($\eta < 0$). On the other hand, if the lower layer shoals in such a manner that $h_2 < h_1$, then solitons reverse to upgoing displacements ($\alpha < 0$, $\eta < 0$). At the configuration in which $h_1 = h_2$, the quadratic nonlinear coefficient α vanishes and a higher-order (cubic) nonlinear coefficient must be included in the KdV equation (Djordjevic and Redekopp, 1978; Kakutani and Yamasaki, 1978), leading to its extended version (eKdV):

$$\frac{\partial\eta}{\partial t} + (c_0 + \alpha\eta + \alpha_1\eta^2)\frac{\partial\eta}{\partial x} + \beta\frac{\partial^3\eta}{\partial x^3} = 0 \quad (4.5)$$

where the coefficient α_1 , absent in the Kdv equation (4.1), is the above mentioned cubic nonlinear coefficient

$$\alpha_1 = \frac{3c_0}{(h_1 h_2)^2} \left[\frac{7}{8}(h_1 - h_2)^2 - \left(\frac{h_2^3 + h_1^3}{h_1 + h_2} \right) \right] \quad (4.6)$$

4.2 A Mathematical Approach to Solitons

It should be noticed that while the sign of α depends on the layer depths, it turns out that α_1 is always negative. As the cubic term α_1 is $O(\alpha^2)$, the eKdV should formally include also additional dispersive and nonlinear dispersive terms of order $O(\beta^2)$ and $O(\alpha\beta)$, respectively, to balance nonlinear and dispersive effects at a higher-order of the KdV equation (Koop and Butler, 1981; Lamb and Yan, 1996; Grimshaw et al., 2002). Nevertheless, if the quadratic nonlinear coefficient α is of order $O(\alpha)$ (i. e., nonlinear quadratic effects are small), as occurs when $|h_1 - h_2| / (h_1 h_2) \ll 1$, then the eKdV is asymptotically consistent, but requires the balance $\beta = O(\alpha^2)$ (Helfrich and Melville, 2006).

The modified KdV (mKdV) equation appears when the interface is located at the critical thickness ratio ($h_1 = h_2$) and the quadratic nonlinear coefficient α is zero. Then the equation (4.5) reduces to

$$\frac{\partial \eta}{\partial t} + (c_0 + \alpha_1 \eta^2) \frac{\partial \eta}{\partial x} + \beta \frac{\partial^3 \eta}{\partial x^3} = 0 \quad (4.7)$$

Kakutani and Yamasaki (1978) found that cubic nonlinearity of the mKdV equation governs nonlinear long gravity waves at the critical thickness ratio, whereas near this configuration nonlinearity is governed by an equation of a combined form of the KdV and modified KdV equation.

Solitary wave behaviour of eKdV equation (Kakutani and Yamasaki, 1978; Ostrovsky and Stepanyants, 1989; Gerkema and Zimmerman, 2008) can be described by

$$\eta(x, t) = \frac{\eta_0}{b + (1 - b) \cosh^2 \gamma(x - ct)}, \quad (4.8)$$

where

$$c = c_0 + \frac{\eta_0}{3} \left(\alpha + \frac{1}{2} \alpha_1 \eta_0 \right), \quad \gamma^2 = \frac{\eta_0 (\alpha + \frac{1}{2} \alpha_1 \eta_0)}{12\beta}, \quad (4.9)$$

$$b = \frac{-\eta_0 \alpha_1}{2\alpha + \alpha_1 \eta_0}, \quad Lw = \eta_0^{-1} \int_{-\infty}^{\infty} \eta dx \quad (4.10)$$

4. INTRODUCTION TO A SOLITONS SCENARIO

with η_0 being a measure of the maximum amplitude of the soliton; Lw the characteristic wave-width; c , the nonlinear phase speed derived from eKdV theory; and, b and γ parameters defining the system.

Figure 4.5 shows eKdV solitary waves approaching its maximum amplitude and becoming flat-topped, a radical departure from the classical KdV soliton which has no formal mathematical limit to its amplitude.

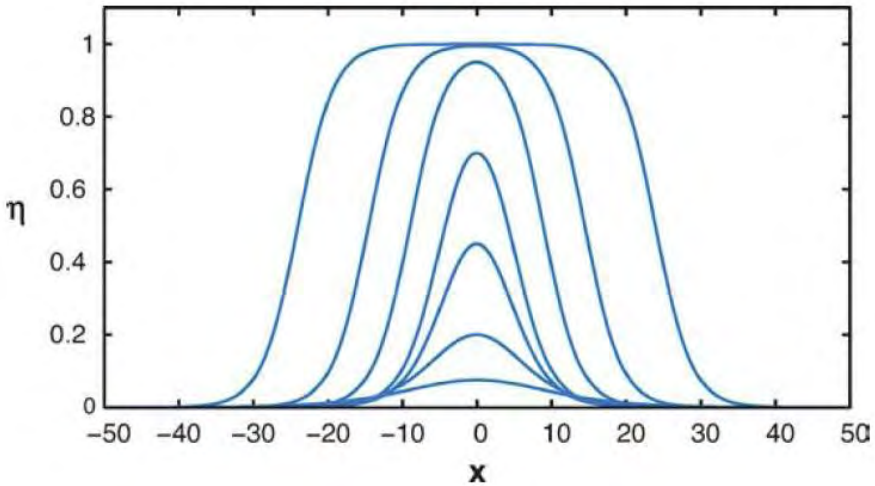


Figure 4.5: Solitary wave solutions of the eKdV equation - Examples of solitary wave solutions of the eKdV equation (Equation 6) for the arbitrary choice of the parameters $\beta = \alpha = \alpha_1$. As the maximum wave amplitude increases, the waves eventually broaden and develop a flat crest at the maximum amplitude $\eta_{0max} = 1$. [From Helfrich and Melville (2006) - Figure 4].

As previously pointed out, within the framework of the two-layer model, α_1 is always negative (4.6). However, for more general stratifications and background shear flows the cubic nonlinear coefficient may be either negative or positive. In the latter case, soliton solutions of both positive and negative polarities may exist regardless of the sign of α (Grimshaw et al., 1997, 2004).

Cubic KdV, though including higher nonlinearities, is still based on an expansion of a small parameter ($\alpha = a/H$) and so is still subject to the assumption of weak nonlinearity. A useful and well-known radical departure from the weakly nonlinear two-layer KdV model was derived by Miyata (1985, 1988) and Choi and Camassa (1999). The result of their work was an equiva-

lent set of bi-directional wave equations with *full* nonlinearity, $\alpha = O(1)$ and first-order weakly dispersive effects, $\beta \ll 1$.

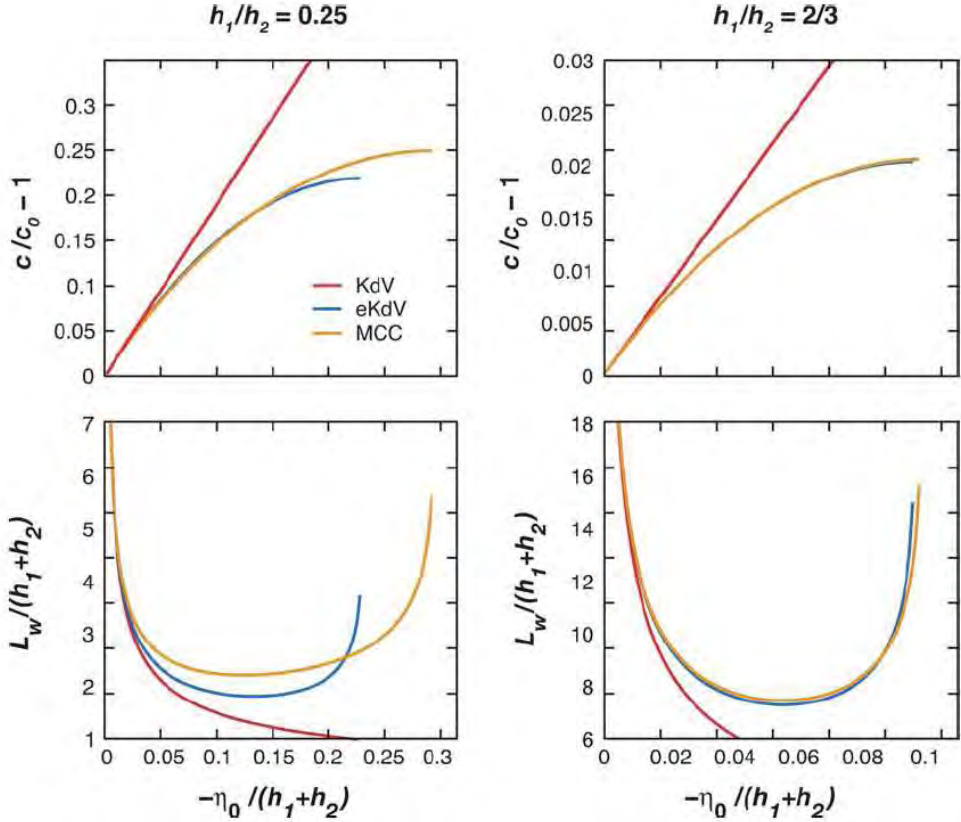


Figure 4.6: Comparison of KdV and MCC theories - Comparison of solitary wave properties from the two-layer KdV (red), eKdV (blue), and MCC (orange) theories. The top row shows the wave speed c vs. amplitude η_0 ; and the bottom row shows the wavelength (*here read characteristic wave-width of the soliton*) L_w vs. η_0 . The comparison is done for the two stratifications $h_1/h_2 = 1/4$ (left column) and $h_1/h_2 = 2/3$ (right column). For both the eKdV and MCC waves the maximum wave amplitude corresponds to the end of the speed curves. [From Helfrich and Melville (2006) - Figure 5].

Helfrich and Melville (2006) highlighted with Figure 4.6 the deviation among the weakly nonlinear KdV, the more strongly nonlinear eKdV and the *fully* nonlinear Miyata-Choi-Camassa (MCC) models. The amplitude depen-

4. INTRODUCTION TO A SOLITONS SCENARIO

dence of the wave speed c and characteristic wave-width Lw ¹ from the three models is shown for two different layer-thickness ($h_1/h_2 = 1/4$ and $h_1/h_2 = 2/3$) in a two-fluid layer system.

Remarkable differences arise when comparing results from the weakly nonlinear KdV and the strongly nonlinear eKdV and MCC models, for both c and Lw , even for relatively small amplitudes. The solitary wave solutions of the eKdV and MCC equations increase its phase speed c with growing amplitude until they start to slow as they approach its maximum η_{0max} (Figure 4.6 - top row). On the contrary, KdV solutions show the phase speed increasing linearly with amplitude. Additionally, it also worth noting that the maximum wave amplitude for both the eKdV and MCC waves corresponds to the end of the speed curves (what it does not occur with KdV solitons).

As previously shown in Figure 4.5 for eKdV solitary waves, its characteristic wave-width becomes narrower as they grow (increasing η_0) to lately broaden when the upper limit is approached (η_{0max}). This behaviour is also exhibited by the MCC theory (Figure 4.6 - bottom row); and, unlike classical KdV solitary waves whose wave-width gets narrower as they become larger until its maximum amplitude.

On a whole, comparison of the wave shapes and properties between the eKdV and MCC theories agree quite well for $0.4 < h_1/(h_1 + h_2) < 0.6$, where the scaling requirements of eKdV are reasonably met (Helfrich and Melville, 2006). Outside this range, differences among the two theories start to grow (see Figure 4.6 - left column, bottom row).

As we have described, the Korteweg-de Vries (KdV) equation and its extended version (eKdV) with no forcing terms included, provide an appropriate mathematical tool for studying the evolution of a given initial profile under weakly nonlinear (KdV and eKdV) conditions. To go to strongly nonlinear settings, MCC-type of equations need to be used. But for these, no model exists that includes a forcing mechanism. It is the principal goal of the following chapters to extend MCC to include the mechanism of forcing by barotropic tides over topography.

Throughout the next section, the basis and scope of the present thesis are discussed.

¹For KdV solitary waves $Lw = 2\gamma^{-1}$.

4.3 Scope of the Study

It is now our interest to include a forcing element in the system to reproduce the generation and evolution of fully nonlinear weakly nonhydrostatic solitons in a rotating ocean through the disintegration of a low-mode internal tide released from topography interaction. However, tide-topography interaction gives rises to waves propagating in two directions (left- and rightward of the topographic obstacle) and the KdV theory describes waves travelling in one unique direction. Additionally, Coriolis dispersion needs to be included, which is not accounted for in (e)KdV. Hence, the KdV-type models are not suitable to be generalized for including this forcing mechanism. We shall use a different starting point from that of the Korteweg-de Vries equation. The framework of our generation model will be the Euler and continuity equations, which are not unidirectionally restricted. In the following we discuss the main assumptions and approximations taken in our study, its validity and, therefore, the scope of the resulting generation model. However, for clarity, we will recall the assumptions and approximations again in *Chapter 5*.

We choose the simplest possible configuration, widely used in the literature for analogous models: a two-fluid layer system in which each layer consists of an incompressible, homogeneous and inviscid fluid. This configuration supports our study as it can describe the first mode of a generated internal tide (Gerkema, 1994); and we are concerned with the generation of internal solitary waves by disintegration of a low-mode internal tide (the generation of solitons by internal tide beams is here discarded).

The waves will be taken to propagate in the x direction. With rotation, motion in the transverse y direction will occur; however, a further simplification will consist in omitting transverse dependences (hence we consider plane waves). Otherwise, derivation of the model would have to face with more complicated equations that may not outweigh the improvement in the results.

Relative differences in density within the ocean are extremely small (typical values are of order 10^{-3}), and so in terms of a two-layer system we can apply the Boussinesq approximation ($\Delta\rho = (\rho_2 - \rho_1)/\rho_2 \ll 1$). Additionally, we exclude any motion at the upper surface with a rigid lid what enable us to reduce the set of evolution equations.

The forcing for internal tide generation consists of an oscillating non-flat bottom mimicking a barotropic tidal flow over topography. Subsequently,

4. INTRODUCTION TO A SOLITONS SCENARIO

solitons are generated by strongly nonlinear disintegration of the first-mode of the internal tide, with waves taken to be long in comparison with the total fluid depth (weakly nonhydrostatic dispersive waves).

Dispersion due to the Earth's rotation cannot be neglected, as the wavelength of the internal tides are of the order of the 'internal Rossby radius of deformation' (c_0/f). We therefore include these effects by using the so-called f -plane approximation. Hence, on a whole, our system includes dispersive effects due to weakly nonhydrostatic and Coriolis dispersion.

Therefore, our theoretical approach allows us to study the generation and evolution of nonlinear interfacial waves in the limit of fully nonlinear weakly nonhydrostatic long waves. The strongly nonlinearities arise via disintegration of a low-mode internal tide released from topography interaction in rotating ocean. Dispersive effects include weakly nonhydrostatic and Coriolis dispersion (due to the Earth's rotation). In the absence of a mechanism for the generation of the internal tide and neglecting Earth's rotation effects, our set of equations reduces to equivalent Choi & Camassa equations.

The interpretation of a mathematical model like the one we are dealing here is always made easier if analytical solutions are feasible; however, even when analytical solving is doable, sometimes it is cumbersome because equations become extremely complicated and puzzle the physics behind the phenomenon. In our case, numerical solving represents a more suitable treatment to explore the theoretical model and its behaviour.

Chapter 5

A Model for the Generation of Strongly Nonlinear, Weakly Nonhydrostatic Interfacial Waves¹

5.1 Outline

In this chapter we derive a new two-fluid layer model consisting of a set of forced rotation-modified Boussinesq equations for studying the generation and evolution of strongly nonlinear weakly nonhydrostatic dispersive interfacial waves. The forcing for internal tide generation is due to tide-topography interaction (an oscillating non-flat bottom mimicking a barotropic tidal flow over topography). Solitons are generated by disintegration of the first-mode of the internal tide. Dispersive effects include weakly nonhydrostatic and Coriolis dispersion (due to the Earth's rotation). The model equations are derived in *Sections 5.2 to 5.5*. The basic equations of *Section 5.2* are scaled in *Sections 5.3* and vertically integrated over the layers in *Section 5.4*. Up to this point, the resulting equations are exact but do not form a closed set. The set is closed in *Section 5.5* by making an expansion in the small parameter δ (measuring the

¹Aguiar -González B., Gerkema T. A Model for the Generation of Strongly Nonlinear, Weakly Nonhydrostatic Interfacial Waves. *In Preparation to be Submitted to an International refereed Journal*

5. A GENERATION MODEL OF SOLITONS

strength of non-hydrostaticity). The forcing is introduced in *Section 5.6* and the set of equations is rearranged to put it in a form convenient for numerical solving. (Readers who are primarily interested in the results may want to skip *Sections 5.3-5.5*). Application of the numerical scheme requires further rearranging, presented in *Section 5.7*, the end-result of which is presented in *Section 5.7.3*. The model turns out equivalent to Choi & Camassa (CC) equations plus additional terms which provide the forcing and rotation effects to the system. A numerical algorithm for solving the fully nonlinear model is developed and described in *Section 5.7*. Numerical experiments for various regimes are discussed in *Chapter 6*.

5.2 Preliminaries

We start from the continuity and Euler equations and consider a two-fluid layer configuration in which each layer is composed of a homogeneous, inviscid, incompressible fluid, applying the Boussinesq approximation. We also assume uniformity in one of the horizontal directions, taking $\partial/\partial y = 0$. Hence, the continuity and momentum equations read

$$\frac{\partial u_i}{\partial x} + \frac{\partial w_i}{\partial z} = 0 \quad (5.1)$$

$$\bar{\rho} \left(\frac{\partial u_i}{\partial t} + u_i \frac{\partial u_i}{\partial x} + w_i \frac{\partial u_i}{\partial z} - f v_i \right) = - \frac{\partial p_i}{\partial x} \quad (5.2)$$

$$\frac{\partial v_i}{\partial t} + u_i \frac{\partial v_i}{\partial x} + w_i \frac{\partial v_i}{\partial z} + f u_i = 0 \quad (5.3)$$

$$\bar{\rho} \left(\frac{\partial w_i}{\partial t} + u_i \frac{\partial w_i}{\partial x} + w_i \frac{\partial w_i}{\partial z} \right) = - \frac{\partial p_i}{\partial z} - \rho_i g \quad (5.4)$$

where ρ_i is density, (u_i, v_i, w_i) are the velocity components in Cartesian coordinates, p_i is pressure, g the gravitational acceleration, f the Coriolis parameter ($f = 2\Omega \sin\phi$, at latitude ϕ) and $\bar{\rho}$ the mean density. The subscript $i = 1$ ($i = 2$) refers to the upper (lower) layer and a stable stratification, $\rho_1 < \rho_2$, is assumed.

Boundaries are defined at the surface, taken to be a rigid lid, which is located at $z = H_1$, and at the bottom, located at $z = -H_2 + H(x, t)$. The time-dependence of the bottom will later be specified as a horizontal oscillation, mimicking a barotropic tidal flow over topography, the forcing mechanism for internal tides. However, the two are not exactly equivalent, since the

transformation from one frame of reference to the other involves acceleration and is therefore not Galilean.

The kinematic boundary conditions at the surface and bottom read

$$w_1 = 0 \quad \text{at } z = H_1 \quad (5.5)$$

$$w_2 = \frac{\partial H}{\partial t} + \frac{\partial H}{\partial x} u_2 \quad \text{at } z = -H_2 + H(x, t). \quad (5.6)$$

At the interface ($z = Z(x, t)$), which if at rest is located at $z = 0$, the boundary conditions are given by the continuity of normal velocity and pressure:

$$w_i = \frac{\partial Z}{\partial t} + u_i \frac{\partial Z}{\partial x} \quad \text{and} \quad p_1 = p_2 \quad \text{at } z = Z. \quad (5.7)$$

For later convenience, we write pressure as the sum of hydrostatic and dynamic parts, the latter being denoted by primes:

$$p_i = \rho_i g H_1 - \rho_i g z + p'_i(t, x, z).$$

In the horizontal momentum equation, this amounts to replacing $\partial p_i / \partial x$ by $\partial p'_i / \partial x$, whereas the vertical momentum equation (5.4) gives

$$\bar{\rho} \left(\frac{\partial w_i}{\partial t} + u_i \frac{\partial w_i}{\partial x} + w_i \frac{\partial w_i}{\partial z} \right) = - \frac{\partial p'_i}{\partial z}.$$

Continuity of pressure at the interface, the second equation in (5.7), now becomes

$$(p'_1 - p'_2)|_{z=Z} = (\rho_1 - \rho_2) g Z.$$

5.3 Scaling

In order to bring the equations into a dimensionless form, we introduce scales. The scale for the undisturbed water depth is taken to be D , and the typical wavelength L . Crucially, we will assume waves to be long, i.e. nonhydrostatic effects to be weak. This will be expressed by the small parameter δ :

$$\delta = \left(\frac{D}{L} \right)^2 \ll 1.$$

(NB: in Choi and Camassa (1999) a small parameter ϵ was used instead, which relates to ours as $\delta = \epsilon^2$).

5. A GENERATION MODEL OF SOLITONS

Since we allow waves to have large amplitudes (i.e. being strongly nonlinear), we may take horizontal velocities to scale with $c = (g'D)^{1/2}$, where g' is reduced gravity,

$$g' = g \frac{\rho_2 - \rho_1}{\bar{\rho}}.$$

c , roughly, is a measure of the linear long-wave phase speed for interfacial waves. Thus, u and v will be scaled with c . For the interfacial displacement being allowed to be large, an appropriate scale of Z is D .

The typical scale of w now follows from the continuity equation as Dc/L . Finally, the scale of pressure follows from assuming a primary balance between the acceleration term $\bar{\rho}\partial u/\partial t$ and $\partial p/\partial x$ in the horizontal momentum equation.

In summary, then, we can introduce the following dimensionless variables, indicated by asterisks,

$$\begin{aligned} x &= L x^*, & z &= D z^*, & t &= (L/c) t^*, \\ p'_i &= (\bar{\rho} c^2) p'^*_i, & u_i &= c u^*_i, & v_i &= c v^*_i, & w_i &= (D/L) c w^*_i. \end{aligned} \quad (5.8)$$

With these scales, the dimensionless continuity and Euler equations yield (for convenience, we drop the asterisks right away):

$$\frac{\partial u_i}{\partial x} + \frac{\partial w_i}{\partial z} = 0 \quad (5.9)$$

$$\frac{\partial u_i}{\partial t} + u_i \frac{\partial u_i}{\partial x} + w_1 \frac{\partial u_i}{\partial z} - \mu v_i = -\frac{\partial p'_i}{\partial x} \quad (5.10)$$

$$\frac{\partial v_i}{\partial t} + u_i \frac{\partial v_i}{\partial x} + w_1 \frac{\partial v_i}{\partial z} + \mu u_i = 0 \quad (5.11)$$

$$\delta \left(\frac{\partial w_i}{\partial t} + u_i \frac{\partial w_i}{\partial x} + w_i \frac{\partial w_i}{\partial z} \right) = -\frac{\partial p'_i}{\partial z}. \quad (5.12)$$

Here μ is the scaled Coriolis parameter, $\mu = fL/c$. Furthermore we introduce the dimensionless quantities ζ , h_i , and h via $(Z, H_1, H_2, D) = (\zeta, h_1, h_2, h)$, so that the scaled form of the boundary conditions is

$$w_1 = 0 \quad \text{at } z = h_1 \quad (5.13)$$

$$w_2 = \frac{\partial h}{\partial t} + u_2 \frac{\partial h}{\partial x} \quad \text{at } z = -h_2 + h(x, t) \quad (5.14)$$

$$w_i = \frac{\partial \zeta}{\partial t} + u_i \frac{\partial \zeta}{\partial x} \quad \text{at } z = \zeta(x, t) \quad (5.15)$$

$$p'_2 - p'_1 = \zeta \quad \text{at } z = \zeta(x, t). \quad (5.16)$$

5.4 Vertically Integrated Equations

From here on we follow a procedure analagous to that of Choi & Camassa (1999), i.e. we vertically integrate the equations over their layers, and then consider subsequently the orders δ^0 and δ^1 in order to obtain a closed set for the weakly nonhydrostatic equations.

The layer-mean \bar{f}_1 of a function $f_1(x, z, t)$ for the upper layer is defined as

$$\bar{f}_1(x, t) = \frac{1}{\eta_1} \int_{\zeta}^{h_1} dz f_1(x, z, t), \quad \eta_1 = h_1 - \zeta \quad (5.17)$$

and for the lower layer as

$$\bar{f}_2(x, t) = \frac{1}{\eta_2} \int_{-h_2+h}^{\zeta} dz f_2(x, z, t), \quad \eta_2 = h_2 - h + \zeta. \quad (5.18)$$

Here, η_i represents the thickness of the layer (depending on the interfacial displacement ζ). Notice that the boundaries contain a dependence on t and x via $\zeta(t, x)$ and $h(t, x)$.

5.4.1 Upper Fluid-Layer

Vertical integration of the continuity equation (5.9), from the interface (ζ) to the surface (h_1) yields

$$\frac{\partial \eta_1}{\partial t} + \frac{\partial(\eta_1 \bar{u}_1)}{\partial x} = 0. \quad (5.19)$$

Here we used the theorem for derivatives of integrals with variable boundaries (see Appendix B):

$$\frac{\partial}{\partial x} \int_{A(x)}^{B(x)} f(x, z) dz = \int_{A(x)}^{B(x)} \frac{\partial f(x, z)}{\partial x} dz + f(x, B(x)) \frac{dB(x)}{dx} - f(x, A(x)) \frac{dA(x)}{dx}.$$

The vertical integration of the Euler equation (5.10) involves the following steps. For the acceleration term we get

$$\int_{\zeta}^{h_1} dz \frac{\partial u_1}{\partial t} = \frac{\partial}{\partial t} \int_{\zeta}^{h_1} dz u_1 + u_1|_{z=\zeta} \frac{\partial \zeta}{\partial t} = \frac{\partial(\eta_1 \bar{u}_1)}{\partial t} + u_1|_{z=\zeta} \frac{\partial \zeta}{\partial t}.$$

5. A GENERATION MODEL OF SOLITONS

The vertical integration of the nonlinear terms, which can be rewritten $(u_1^2)_x + (w_1 u_1)_z$, yields

$$\begin{aligned} \int_{\zeta}^{h_1} dz [(u_1^2)_x + (w_1 u_1)_z] &= \frac{\partial}{\partial x} \int_{\zeta}^{h_1} dz u_1^2 + u_1^2 \Big|_{z=\zeta} \frac{\partial \zeta}{\partial x} + (w_1 u_1) \Big|_{\zeta}^{h_1} \\ &= \frac{\partial \overline{\eta_1 u_1^2}}{\partial x} - \frac{\partial \zeta}{\partial t} u_1 \Big|_{z=\zeta} \end{aligned}$$

The vertically integrated first horizontal momentum equation becomes

$$\frac{\partial(\eta_1 \bar{u}_1)}{\partial t} + \frac{\partial(\eta_1 \overline{u_1 u_1})}{\partial x} - \mu \eta_1 \bar{v}_1 = -\eta_1 \overline{\left(\frac{\partial p_1'}{\partial x}\right)}. \quad (5.20)$$

The other horizontal momentum equation is treated similarly. The nonlinear terms can be rewritten as $(uv)_x + (wv)_z$, and become after vertical integration

$$\begin{aligned} \int_{\zeta}^{h_1} dz (u_1 v_1)_x + (w_1 v_1)_z &= \frac{\partial}{\partial x} \int_{\zeta}^{h_1} dz u_1 v_1 + (u_1 v_1) \Big|_{z=\zeta} \frac{\partial \zeta}{\partial x} - (w_1 v_1) \Big|_{z=\zeta} \\ &= \frac{\partial}{\partial x} (\eta_1 \overline{u_1 v_1}) - \frac{\partial \zeta}{\partial t} v_1 \Big|_{z=\zeta} \end{aligned}$$

Then, the vertically integrated second horizontal momentum equation gives

$$\frac{\partial(\eta_1 \bar{v}_1)}{\partial t} + \frac{\partial(\eta_1 \overline{u_1 v_1})}{\partial x} + \mu \eta_1 \bar{u}_1 = 0. \quad (5.21)$$

5.4.2 Lower Fluid-Layer

For the lower layer one proceeds similarly, except that now *both* boundaries are variable when one integrates vertically from the interface (ζ) to the bottom ($-h_2 + h$).

First, the vertical integration of the continuity equation yields

$$\int_{-h_2+h}^{\zeta} dz \frac{\partial u_2}{\partial x} = \frac{\partial}{\partial x} \int_{-h_2+h}^{\zeta} dz u_2 - u_2 \Big|_{z=\zeta} \frac{\partial \zeta}{\partial x} + u_2 \Big|_{z=-h_2+h} \frac{\partial h}{\partial x}$$

5.4 Vertically Integrated Equations

and

$$w_2|_{-h_2+h}^{\zeta} = \frac{\partial \zeta}{\partial t} + u_2|_{z=\zeta} \frac{\partial \zeta}{\partial x} - \frac{\partial h}{\partial t} - u_2|_{z=-h_2+h} \frac{\partial h}{\partial x}$$

Combined, this yields

$$\frac{\partial \eta_2}{\partial t} + \frac{\partial(\eta_2 \bar{u}_2)}{\partial x} = 0. \quad (5.22)$$

The vertical integration of the Euler equation (5.10) involves the following steps. For the acceleration term we get

$$\begin{aligned} \int_{-h_2+h}^{\zeta} dz \frac{\partial u_2}{\partial t} &= \frac{\partial}{\partial t} \int_{-h_2+h}^{\zeta} dz u_2 - u_2|_{z=\zeta} \frac{\partial \zeta}{\partial t} + u_2|_{z=-h_2+h} \frac{\partial h}{\partial t} \\ &= \frac{\partial(\eta_2 \bar{u}_2)}{\partial t} - u_2|_{z=\zeta} \frac{\partial \zeta}{\partial t} + u_2|_{z=-h_2+h} \frac{\partial h}{\partial t}. \end{aligned}$$

The vertical integration of the nonlinear terms, which can be rewritten $(u_2^2)_x + (w_2 u_2)_z$, yields

$$\begin{aligned} &\int_{-h_2+h}^{\zeta} dz [(u_2^2)_x + (w_2 u_2)_z] \\ &= \frac{\partial}{\partial x} \int_{-h_2+h}^{\zeta} dz u_2^2 - u_2^2|_{z=\zeta} \frac{\partial \zeta}{\partial x} + u_2^2|_{z=-h_2+h} \frac{\partial h}{\partial x} + (w_2 u_2)|_{-h_2+h}^{\zeta} \\ &= \frac{\partial \eta_2 \bar{u}_2^2}{\partial x} - u_2^2|_{z=\zeta} \frac{\partial \zeta}{\partial x} + u_2^2|_{z=-h_2+h} \frac{\partial h}{\partial x} + \left(\frac{\partial \zeta}{\partial t} + u_2 \frac{\partial \zeta}{\partial x} \right) u_2|_{z=\zeta} \\ &\quad - \left(\frac{\partial h}{\partial t} + u_2 \frac{\partial h}{\partial x} \right) u_2|_{z=-h_2+h} \\ &= \frac{\partial \eta_2 \bar{u}_2^2}{\partial x} + \frac{\partial \zeta}{\partial t} u_2|_{z=\zeta} - \frac{\partial h}{\partial t} u_2|_{z=-h_2+h} \end{aligned}$$

The vertically integrated first horizontal momentum equation becomes

$$\frac{\partial(\eta_2 \bar{u}_2)}{\partial t} + \frac{\partial(\eta_2 \bar{u}_2 \bar{u}_2)}{\partial x} - \mu \eta_2 \bar{v}_2 = -\eta_2 \left(\frac{\partial p'_2}{\partial x} \right). \quad (5.23)$$

5. A GENERATION MODEL OF SOLITONS

The other horizontal momentum equation is treated similarly. The acceleration term gives

$$\int_{-h_2+h}^{\zeta} dz \frac{\partial v_2}{\partial t} = \frac{\partial(\eta_2 \bar{v}_2)}{\partial t} - v_2|_{z=\zeta} \frac{\partial \zeta}{\partial t} + v_2|_{z=-h_2+h} \frac{\partial h}{\partial t}.$$

The nonlinear terms can be rewritten as $(uv)_x + (wv)_z$, and yield after vertical integration

$$\begin{aligned} & \int_{-h_2+h}^{\zeta} dz (u_2 v_2)_x + (w_2 v_2)_z \\ &= \frac{\partial}{\partial x} \int_{\zeta}^{h_1} dz u_2 v_2 - (u_2 v_2)|_{z=\zeta} \frac{\partial \zeta}{\partial x} + (u_2 v_2)|_{z=-h_2+h} \frac{\partial h}{\partial x} \\ & \quad + \left(\frac{\partial \zeta}{\partial t} + u_2 \frac{\partial \zeta}{\partial x} \right) v_2|_{z=\zeta} - \left(\frac{\partial h}{\partial t} + u_2 \frac{\partial h}{\partial x} \right) v_2|_{z=-h_2+h} \\ &= \frac{\partial}{\partial x} (\eta_2 \overline{u_2 v_2}) + \frac{\partial \zeta}{\partial t} v_2|_{z=\zeta} - \frac{\partial h}{\partial t} v_2|_{z=-h_2+h} \end{aligned}$$

Thus, the vertically integrated second horizontal momentum equation gives

$$\frac{\partial(\eta_2 \bar{v}_2)}{\partial t} + \frac{\partial(\eta_2 \overline{u_2 v_2})}{\partial x} + \mu \eta_2 \bar{u}_2 = 0. \quad (5.24)$$

5.5 Expansion in δ

The six integrated equations (5.19 - 5.24) derived so far, are exact but do not form a closed set. The variables η_1 , η_2 and ζ count as one unknown, but we have also \bar{u}_i , \bar{v}_i , $\overline{p'_{i,x}}$, $\overline{u_i u_i}$ and $\overline{u_i v_i}$. The last two expressions will be cast in terms of \bar{u}_i and \bar{v}_i by using the vertical momentum equation, expanded in terms of the small parameter δ . Moreover, continuity of pressure at the interface is used to connect the pressure in the lower and upper layer. All in all, the six equations are thus modified to contain only six unknowns.

We make a formal expansion of the unknowns as, for example,

$$\bar{u}_i = \bar{u}_i^{(0)} + \delta \bar{u}_i^{(1)} + \dots$$

5.5.1 Lowest Order

The vertical momentum equation reduces to $\partial p_i^{(0)}/\partial z = 0$ neglecting terms of order δ . At lowest order, (perturbation) pressure is vertically constant in each layer. For convenience, we introduce $P = p_2^{(0)}$, being a function of t and x . It then follows from continuity of pressure at the interface, that $p_1^{(0)} = P - \zeta$. Thus,

$$\overline{\left(\frac{\partial p_1'}{\partial x}\right)} = \frac{\partial P}{\partial x} - \frac{\partial \zeta}{\partial x} + O(\delta), \quad \overline{\left(\frac{\partial p_2'}{\partial x}\right)} = \frac{\partial P}{\partial x} + O(\delta).$$

Returning to the original horizontal momentum equations, it is now natural to assume that the horizontal velocities, too, are independent of z within each layer, given the z -independence of pressure. Thus,

$$\overline{u_i u_i} = \bar{u}_i^2 + O(\delta), \quad \overline{u_i v_i} = \bar{u}_i \bar{v}_i + O(\delta).$$

At lowest order, then, the set of integrated equations is closed, in terms of the six variables \bar{u}_i , \bar{v}_i , ζ and P :

$$\frac{\partial(\eta_1 \bar{u}_1)}{\partial t} + \frac{\partial(\eta_1 \bar{u}_1^2)}{\partial x} - \mu \eta_1 \bar{v}_1 = -\eta_1 \left(\frac{\partial P}{\partial x} - \frac{\partial \zeta}{\partial x} \right) + O(\delta) \quad (5.25)$$

$$\frac{\partial(\eta_2 \bar{u}_2)}{\partial t} + \frac{\partial(\eta_2 \bar{u}_2^2)}{\partial x} - \mu \eta_2 \bar{v}_2 = -\eta_2 \frac{\partial P}{\partial x} + O(\delta) \quad (5.26)$$

$$\frac{\partial(\eta_i \bar{v}_i)}{\partial t} + \frac{\partial(\eta_i \bar{u}_i \bar{v}_i)}{\partial x} + \mu \eta_i \bar{u}_i = O(\delta) \quad (5.27)$$

$$\frac{\partial \eta_i}{\partial t} + \frac{\partial(\eta_i \bar{u}_i)}{\partial x} = 0. \quad (5.28)$$

(Notice that the last equation, representing the vertically integrated continuity equations, is exact and involves no approximation in terms of δ .)

We can obtain the lowest-order expressions $w_i^{(0)}$ from the continuity equation

$$w_i^{(0)} = -z \frac{\partial \bar{u}_i^{(0)}}{\partial x} + c_i(t, x)$$

where c_i are constants of integration, which are determined by using the boundary conditions at the surface (5.13) and bottom (5.14). For these we get:

$$w_1^{(0)} = (h_1 - z) \frac{\partial \bar{u}_1^{(0)}}{\partial x} \quad (5.29)$$

$$w_2^{(0)} = (h - h_2 - z) \frac{\partial \bar{u}_2^{(0)}}{\partial x} + D_2 h \quad (5.30)$$

5. A GENERATION MODEL OF SOLITONS

where the operator D_i is defined as $\partial/\partial t + \bar{u}_i^{(0)}\partial/\partial x$

5.5.2 Next Order

At this order, we include terms of order δ . The key problem is, again, to close the set of six vertically integrated equations by deriving closed expressions for the horizontal pressure gradients $\overline{p'_{i,x}}$ as well as for the contributions of $\overline{u_i u_i}$ and $\overline{u_i v_i}$ in the nonlinear terms.

The latter problem is particularly simple. At order δ , the products contain one lowest-order field, which is independent of z , hence

$$\begin{aligned}
 \overline{u_i u_i} &= \frac{1}{\eta_i} \int dz u_i^2 = \frac{1}{\eta_i} \int dz (u_i^{(0)} + \delta u_i^{(1)} + \dots)^2 \\
 &= \frac{1}{\eta_i} \int dz (u_i^{(0)2} + 2\delta u_i^{(0)} u_i^{(1)} + \dots) \\
 &= u_i^{(0)2} + 2\delta u_i^{(0)} \frac{1}{\eta_i} \int dz u_i^{(1)} + \dots \\
 &= \bar{u}_i^{(0)2} + 2\delta \bar{u}_i^{(0)} \bar{u}_i^{(1)} + \dots \\
 &= (\bar{u}_i^{(0)} + \delta \bar{u}_i^{(1)} + \dots)^2 \\
 &= \bar{u}_i^2 + O(\delta^2)
 \end{aligned}$$

what leads to

$$\overline{u_i u_i} = \bar{u}_i^2 + O(\delta^2), \quad \overline{u_i v_i} = \bar{u}_i \bar{v}_i + O(\delta^2).$$

This means that we can write the horizontal momentum equations as

$$\frac{\partial(\eta_i \bar{u}_i)}{\partial t} + \frac{\partial(\eta_i \bar{u}_i^2)}{\partial x} - \mu \eta_i \bar{v}_i = -\eta_i \left(\overline{\frac{\partial p'_i{}^{(0)} + \delta \partial p'_i{}^{(1)}}{\partial x}} \right) + O(\delta^2) \quad (5.31)$$

$$\frac{\partial(\eta_i \bar{v}_i)}{\partial t} + \frac{\partial(\eta_i \bar{u}_i \bar{v}_i)}{\partial x} + \mu \eta_i \bar{u}_i = O(\delta^2) \quad (5.32)$$

$$\frac{\partial \eta_i}{\partial t} + \frac{\partial(\eta_i \bar{u}_i)}{\partial x} = 0. \quad (5.33)$$

The remaining problem is to find an expression for $p_i^{\prime(1)}$. Before we enter that problem, we first simplify the above equations by combining them, using

$$\begin{aligned} \frac{\partial(\eta_i \bar{u}_i)}{\partial t} + \frac{\partial(\eta_i \bar{u}_i^2)}{\partial x} &= \eta_i \frac{\partial \bar{u}_i}{\partial t} + \bar{u}_i \frac{\partial \eta_i}{\partial t} + \eta_i \bar{u}_i \frac{\partial \bar{u}_i}{\partial x} + \bar{u}_i \frac{\partial(\eta_i \bar{u}_i)}{\partial x} \\ &= \eta_i \frac{\partial \bar{u}_i}{\partial t} + \eta_i \bar{u}_i \frac{\partial \bar{u}_i}{\partial x} \end{aligned} \quad (5.34)$$

and

$$\begin{aligned} \frac{\partial(\eta_i \bar{v}_i)}{\partial t} + \frac{\partial(\eta_i \bar{u}_i \bar{v}_i)}{\partial x} &= \eta_i \frac{\partial \bar{v}_i}{\partial t} + \bar{v}_i \frac{\partial \eta_i}{\partial t} + \eta_i \bar{u}_i \frac{\partial \bar{v}_i}{\partial x} + \bar{v}_i \frac{\partial(\eta_i \bar{u}_i)}{\partial x} \\ &= \eta_i \frac{\partial \bar{v}_i}{\partial t} + \eta_i \bar{u}_i \frac{\partial \bar{v}_i}{\partial x}. \end{aligned} \quad (5.35)$$

Hence,

$$\frac{\partial \bar{u}_i}{\partial t} + \bar{u}_i \frac{\partial \bar{u}_i}{\partial x} - \mu \bar{v}_i = - \overline{\left(\frac{\partial p_i^{\prime(0)} + \delta \partial p_i^{\prime(1)}}{\partial x} \right)} + O(\delta^2) \quad (5.36)$$

$$\frac{\partial \bar{v}_i}{\partial t} + \bar{u}_i \frac{\partial \bar{v}_i}{\partial x} + \mu \bar{u}_i = O(\delta^2) \quad (5.37)$$

$$\frac{\partial \eta_i}{\partial t} + \frac{\partial(\eta_i \bar{u}_i)}{\partial x} = 0. \quad (5.38)$$

At order δ , the vertical momentum equations reads

$$\frac{\partial w_i^{(0)}}{\partial t} + u_i^{(0)} \frac{\partial w_i^{(0)}}{\partial x} + w_i^{(0)} \frac{\partial w_i^{(0)}}{\partial z} = - \frac{\partial p_i^{\prime(1)}}{\partial z}. \quad (5.39)$$

We now use the lowest order expressions for the velocity components to find an expression for $p_i^{\prime(1)}$.

5.5.2.1 Pressure in Upper Layer

With the lowest-order expression for the vertical velocity,

$$w_1^{(0)} = (h_1 - z) \frac{\partial \bar{u}_1^{(0)}}{\partial x},$$

5. A GENERATION MODEL OF SOLITONS

the left-hand side of (5.39) becomes

$$\begin{aligned}
 & (h_1 - z) \frac{\partial^2 \bar{u}_1^{(0)}}{\partial x \partial t} + \bar{u}_1^{(0)} (h_1 - z) \frac{\partial^2 \bar{u}_1^{(0)}}{\partial x^2} - (h_1 - z) \left(\frac{\partial \bar{u}_1^{(0)}}{\partial x} \right)^2 \\
 = & (h_1 - z) \left[\frac{\partial^2 \bar{u}_1^{(0)}}{\partial x \partial t} + \bar{u}_1^{(0)} \frac{\partial^2 \bar{u}_1^{(0)}}{\partial x^2} - \left(\frac{\partial \bar{u}_1^{(0)}}{\partial x} \right)^2 \right] \\
 \equiv & (h_1 - z) G_1, \tag{5.40}
 \end{aligned}$$

where we introduced

$$G_i = \frac{\partial^2 \bar{u}_i^{(0)}}{\partial x \partial t} + \bar{u}_i^{(0)} \frac{\partial^2 \bar{u}_i^{(0)}}{\partial x^2} - \left(\frac{\partial \bar{u}_i^{(0)}}{\partial x} \right)^2 \tag{5.41}$$

Hence,

$$\frac{\partial p_1^{\prime(1)}}{\partial z} = (z - h_1) G_1. \tag{5.42}$$

Integration now gives

$$\begin{aligned}
 p_1^{\prime(1)} &= (z^2/2 - h_1 z) G_1 - (\zeta^2/2 - h_1 \zeta) G_1 \\
 &= \frac{1}{2} \left[z(z - 2h_1) - \zeta(\zeta - 2h_1) \right] G_1 \tag{5.43}
 \end{aligned}$$

In the first equality, we used the freedom to add a constant of integration (in fact, a function of x and t), to add terms such that pressure is zero at the interface¹. Taking the derivative to x ,

$$\frac{\partial p_1^{\prime(1)}}{\partial x} = (h_1 - \zeta) \frac{\partial \zeta}{\partial x} G_1 + \frac{1}{2} \left[z(z - 2h_1) - \zeta(\zeta - 2h_1) \right] \frac{\partial G_1}{\partial x}, \tag{5.44}$$

and then the mean over the upper layer,

$$\begin{aligned}
 \overline{\left(\frac{\partial p_1^{\prime(1)}}{\partial x} \right)} &= (h_1 - \zeta) \frac{\partial \zeta}{\partial x} G_1 - \frac{1}{2} \zeta(\zeta - 2h_1) \frac{\partial G_1}{\partial x} + \frac{1}{2} \frac{\partial G_1}{\partial x} \frac{1}{\eta_1} \int_{\zeta}^{h_1} dz z(z - 2h_1) \\
 &= \eta_1 \frac{\partial \zeta}{\partial x} G_1 - \frac{1}{2} \zeta(\zeta - 2h_1) \frac{\partial G_1}{\partial x} + \frac{1}{2} \frac{\partial G_1}{\partial x} \frac{1}{\eta_1} \left(z^3/3 - h_1 z^2 \right) \Big|_{\zeta}^{h_1} \\
 &= \eta_1 \frac{\partial \zeta}{\partial x} G_1 - \frac{1}{2} \zeta(\zeta - 2h_1) \frac{\partial G_1}{\partial x} - \frac{1}{2} \frac{\partial G_1}{\partial x} \frac{1}{\eta_1} \left[2h_1^3/3 + \zeta^2(\zeta/3 - h_1) \right] \\
 &= \eta_1 \frac{\partial \zeta}{\partial x} G_1 - \frac{\eta_1^2}{3} \frac{\partial G_1}{\partial x} \\
 &= -\eta_1 \frac{\partial \eta_1}{\partial x} G_1 - \frac{\eta_1^2}{3} \frac{\partial G_1}{\partial x} \\
 &= -\frac{1}{3\eta_1} \frac{\partial}{\partial x} (\eta_1^3 G_1). \tag{5.45}
 \end{aligned}$$

¹The same condition must later be imposed on $p_2^{\prime(1)}$, since at first order the requirement of continuity of pressure becomes $p_1^{\prime(1)} = p_2^{\prime(1)}$ at $z = \zeta$.

The last equality allow us to write

$$\overline{\left(\frac{\partial p'_1}{\partial x}\right)} = \overline{\left(\frac{\partial p'_1{}^{(0)}}{\partial x}\right)} + \delta \overline{\left(\frac{\partial p'_1{}^{(1)}}{\partial x}\right)} + O(\delta^2)$$

as

$$\overline{\left(\frac{\partial p'_1}{\partial x}\right)} = \frac{\partial P}{\partial x} - \frac{\partial \zeta}{\partial x} - \delta \left[\frac{1}{3\eta_1} \frac{\partial(\eta_1^3 G_1)}{\partial x} \right] + O(\delta^2). \quad (5.46)$$

5.5.2.2 Pressure in Lower Layer

With the lowest-order expression for the vertical velocity,

$$w_2^{(0)} = (h - h_2 - z) \frac{\partial \bar{u}_2^{(0)}}{\partial x} + D_2 h$$

the left-hand side of (5.39) becomes

$$\begin{aligned} & \frac{\partial h}{\partial t} \frac{\partial \bar{u}_2^{(0)}}{\partial x} + (h - h_2 - z) \frac{\partial^2 \bar{u}_2^{(0)}}{\partial x \partial t} + \frac{\partial^2 h}{\partial t^2} + \frac{\partial \bar{u}_2^{(0)}}{\partial t} \frac{\partial h}{\partial x} + \bar{u}_2^{(0)} \frac{\partial^2 h}{\partial x \partial t} \\ & + \bar{u}_2^{(0)} \left[\frac{\partial h}{\partial x} \frac{\partial \bar{u}_2^{(0)}}{\partial x} + (h - h_2 - z) \frac{\partial^2 \bar{u}_2^{(0)}}{\partial x^2} + \frac{\partial^2 h}{\partial x \partial t} + \frac{\partial \bar{u}_2^{(0)}}{\partial x} \frac{\partial h}{\partial x} + \bar{u}_2^{(0)} \frac{\partial^2 h}{\partial x^2} \right] \\ & - \left[(h - h_2 - z) \frac{\partial \bar{u}_2^{(0)}}{\partial x} + \frac{\partial h}{\partial t} + \bar{u}_2^{(0)} \frac{\partial h}{\partial x} \right] \frac{\partial \bar{u}_2^{(0)}}{\partial x} \\ & = (h - h_2 - z) G_2 + \frac{\partial^2 h}{\partial t^2} + \frac{\partial \bar{u}_2^{(0)}}{\partial t} \frac{\partial h}{\partial x} + 2\bar{u}_2^{(0)} \frac{\partial^2 h}{\partial x \partial t} + \bar{u}_2^{(0)} \frac{\partial \bar{u}_2^{(0)}}{\partial x} \frac{\partial h}{\partial x} \\ & + \bar{u}_2^{(0)2} \frac{\partial^2 h}{\partial x^2} \\ & = (h - h_2 - z) G_2 + D_2^2 h, \end{aligned} \quad (5.47)$$

Hence

$$\frac{\partial p'_2{}^{(1)}}{\partial z} = (h_2 - h + z) G_2 - D_2^2 h. \quad (5.48)$$

5. A GENERATION MODEL OF SOLITONS

Integration now gives

$$p_2'^{(1)} = ([h_2 - h]z + z^2/2)G_2 - zD_2^2h - ([h_2 - h]\zeta + \zeta^2/2)G_2 + \zeta D_2^2h$$

where the constant' of integration has been chosen such that $p_2'^{(1)}$ vanishes at the interface (in accordance with the requirement stated above).

Next we take the derivative to x :

$$\begin{aligned} \frac{\partial p_2'^{(1)}}{\partial x} &= -z \frac{\partial h}{\partial x} G_2 + ([h_2 - h]z + z^2/2) \frac{\partial G_2}{\partial x} - z \frac{\partial}{\partial x} (D_2^2h) \\ &\quad + \frac{\partial h}{\partial x} \zeta G_2 - (h_2 - h) \frac{\partial \zeta}{\partial x} G_2 - \zeta \frac{\partial \zeta}{\partial x} G_2 - ([h_2 - h]\zeta + \zeta^2/2) \frac{\partial G_2}{\partial x} \\ &\quad + \frac{\partial \zeta}{\partial x} D_2^2h + \zeta \frac{\partial}{\partial x} (D_2^2h) \\ &= z \left[(h_2 - h) \frac{\partial G_2}{\partial x} - \frac{\partial h}{\partial x} G_2 - \frac{\partial}{\partial x} (D_2^2h) \right] + \frac{z^2}{2} \frac{\partial G_2}{\partial x} \\ &\quad + \frac{\partial h}{\partial x} \zeta G_2 - \eta_2 \frac{\partial \zeta}{\partial x} G_2 - ([h_2 - h]\zeta + \zeta^2/2) \frac{\partial G_2}{\partial x} \\ &\quad + \frac{\partial \zeta}{\partial x} D_2^2h + \zeta \frac{\partial}{\partial x} (D_2^2h). \end{aligned}$$

Finally, taking the depth-average we have

$$\begin{aligned} \overline{\left(\frac{\partial p_2'^{(1)}}{\partial x} \right)} &= \left[(h_2 - h) \frac{\partial G_2}{\partial x} - \frac{\partial h}{\partial x} G_2 - \frac{\partial}{\partial x} (D_2^2h) \right] \frac{1}{\eta_2} \int_{-h_2+h}^{\zeta} dz z \\ &\quad + \frac{1}{2} \frac{\partial G_2}{\partial x} \frac{1}{\eta_2} \int_{-h_2+h}^{\zeta} dz z^2 + \frac{\partial h}{\partial x} \zeta G_2 - \eta_2 \frac{\partial \zeta}{\partial x} G_2 \\ &\quad - ([h_2 - h]\zeta + \zeta^2/2) \frac{\partial G_2}{\partial x} + \frac{\partial \zeta}{\partial x} D_2^2h + \zeta \frac{\partial}{\partial x} (D_2^2h) \end{aligned} \quad (5.49)$$

This expression, following the derivation in *Appendix D*, evolves to

$$\overline{\left(\frac{\partial p_2'^{(1)}}{\partial x} \right)} = -\frac{1}{3\eta_2} \frac{\partial}{\partial x} (\eta_2^3 G_2) - \frac{1}{2} \eta_2 G_2 \frac{\partial h}{\partial x} + \frac{\eta_2}{2} \frac{\partial}{\partial x} (D_2^2h) + \frac{\partial \zeta}{\partial x} D_2^2h \quad (5.50)$$

The last equality allow us to write

$$\overline{\left(\frac{\partial p'_2}{\partial x}\right)} = \overline{\left(\frac{\partial p'_2{}^{(0)}}{\partial x}\right)} + \delta \overline{\left(\frac{\partial p'_2{}^{(1)}}{\partial x}\right)} + O(\delta^2),$$

as

$$\overline{\left(\frac{\partial p'_2}{\partial x}\right)} = \frac{\partial P}{\partial x} - \delta \left[\frac{1}{3\eta_2} \frac{\partial}{\partial x} (\eta_2^3 G_2) + \frac{1}{2} \eta_2 G_2 \frac{\partial \bar{h}}{\partial x} - \frac{\eta_2}{2} \frac{\partial}{\partial x} (D_2^2 h) - \frac{\partial \zeta}{\partial x} D_2^2 h \right] + O(\delta^2). \quad (5.51)$$

5.6 The Generation Model

For the two fluid-layer rotating system we have thus obtained a closed set of six dimensionless equations for six unknowns (\bar{u}_1 , \bar{u}_2 , \bar{v}_1 , \bar{v}_2 , P , ζ)

$$\frac{\partial \eta_1}{\partial t} + \frac{\partial(\eta_1 \bar{u}_1)}{\partial x} = 0, \quad \eta_1 = h_1 - \zeta \quad (5.19)$$

$$\frac{\partial \eta_2}{\partial t} + \frac{\partial(\eta_2 \bar{u}_2)}{\partial x} = 0, \quad \eta_2 = h_2 - h(x, t) + \zeta \quad (5.22)$$

$$\frac{\partial(\eta_1 \bar{u}_1)}{\partial t} + \frac{\partial(\eta_1 \bar{u}_1^2)}{\partial x} - \mu \eta_1 \bar{v}_1 = -\eta_1 \left(\frac{\partial P}{\partial x} - \frac{\partial \zeta}{\partial x} - \delta \left[\frac{1}{3\eta_1} \frac{\partial(\eta_1^3 G_1)}{\partial x} \right] \right), \quad (5.52)$$

$$\begin{aligned} \frac{\partial(\eta_2 \bar{u}_2)}{\partial t} + \frac{\partial(\eta_2 \bar{u}_2^2)}{\partial x} - \mu \eta_2 \bar{v}_2 = & -\eta_2 \left(\frac{\partial P}{\partial x} - \delta \left[\frac{1}{3\eta_2} \frac{\partial(\eta_2^3 G_2)}{\partial x} \right. \right. \\ & \left. \left. + \frac{1}{2} \eta_2 G_2 \frac{\partial \bar{h}}{\partial x} - \frac{\eta_2}{2} \frac{\partial(D_2^2 h)}{\partial x} - \frac{\partial \zeta}{\partial x} D_2^2 h \right] \right), \end{aligned} \quad (5.53)$$

$$\frac{\partial(\eta_1 \bar{v}_1)}{\partial t} + \frac{\partial(\eta_1 \bar{u}_1 \bar{v}_1)}{\partial x} + \mu \eta_1 \bar{u}_1 = 0, \quad (5.21)$$

$$\frac{\partial(\eta_2 \bar{v}_2)}{\partial t} + \frac{\partial(\eta_2 \bar{u}_2 \bar{v}_2)}{\partial x} + \mu \eta_2 \bar{u}_2 = 0. \quad (5.24)$$

5. A GENERATION MODEL OF SOLITONS

This set of equations can be further simplified if we add up equations (5.52) and (5.53) and work off $\frac{\partial P}{\partial x}$, what leads to

$$\begin{aligned} \frac{\partial P}{\partial x} = & \frac{1}{(1-h)} \left(-\frac{\partial}{\partial t}(\eta_1 \bar{u}_1 + \eta_2 \bar{u}_2) - \frac{\partial}{\partial x}(\eta_1 \bar{u}_1^2 + \eta_2 \bar{u}_2^2) + \mu(\eta_1 \bar{v}_1 + \eta_2 \bar{v}_2) \right. \\ & + \eta_1 \frac{\partial \zeta}{\partial x} + \delta \eta_1 \left[\frac{1}{3\eta_1} \frac{\partial(\eta_1^3 G_1)}{\partial x} \right] + \delta \eta_2 \left[\frac{1}{3\eta_2} \frac{\partial(\eta_2^3 G_2)}{\partial x} + \frac{1}{2} \eta_2 G_2 \frac{\partial h}{\partial x} \right. \\ & \left. \left. - \frac{1}{2} \eta_2 \frac{\partial}{\partial x}(D_2^2 h) - \frac{\partial \zeta}{\partial x} D_2^2 h \right] \right). \end{aligned} \quad (5.54)$$

For further simplification in (5.54) we deal with the term $\frac{\partial}{\partial t}(\eta_1 \bar{u}_1 + \eta_2 \bar{u}_2)$, which brings along a combination of time derivatives of unknown quantities, by adding up the continuity equations (5.19) and (5.22)

$$\frac{\partial}{\partial t}(\eta_1 + \eta_2) + \frac{\partial}{\partial x}(\eta_1 \bar{u}_1 + \eta_2 \bar{u}_2) = 0, \quad (5.55)$$

where recalling that $\eta_1 + \eta_2 = h_1 + h_2 - h$ with the two-fluid system depth $h_1 + h_2 = 1$, this leads to

$$-\frac{\partial h}{\partial t} + \frac{\partial}{\partial x}(\eta_1 \bar{u}_1 + \eta_2 \bar{u}_2) = 0. \quad (5.56)$$

At this point we need an expression for the oscillating topography, which we define here as $h = h(X)$ with $X(x, t) = x - a \cos t$ with a being an arbitrary constant. Taking its derivative to time we get

$$\frac{\partial h}{\partial t} = \frac{\partial h}{\partial x} a \sin t, \quad U = a \sin t, \quad (5.57)$$

and replacing this into (5.56), it yields

$$\frac{\partial}{\partial x}(\eta_1 \bar{u}_1 + \eta_2 \bar{u}_2) = U \frac{\partial h}{\partial x}, \quad (5.58)$$

The latter expression can be now integrated in x following

$$\eta_1 \bar{u}_1 + \eta_2 \bar{u}_2 = Uh + A(t), \quad (5.59)$$

where we assume that initially $\bar{u}_1 = \bar{u}_2 = U = 0$ so that $A(t) = 0$

$$\eta_1 \bar{u}_1 + \eta_2 \bar{u}_2 = Uh, \quad (5.60)$$

and, consequently,

$$\frac{\partial}{\partial t}(\eta_1 \bar{u}_1 + \eta_2 \bar{u}_2) = \frac{\partial}{\partial t}(Uh), \quad (5.61)$$

which, finally, allow us to replace the term $\frac{\partial}{\partial t}(\eta_1 \bar{u}_1 + \eta_2 \bar{u}_2)$ (unknown quantity) by $\frac{\partial}{\partial t}(Uh)$ (known quantity) into (5.54) for simplification of $\frac{\partial P}{\partial x}$

$$\begin{aligned} \frac{\partial P}{\partial x} &= \frac{1}{(1-h)} \left(-\frac{\partial}{\partial t}(Uh) - \frac{\partial}{\partial x}(\eta_1 \bar{u}_1^2 + \eta_2 \bar{u}_2^2) + \mu(\eta_1 \bar{v}_1 + \eta_2 \bar{v}_2) + \eta_1 \frac{\partial \zeta}{\partial x} \right. \\ &\quad + \delta \eta_1 \left[\frac{1}{3\eta_1} \frac{\partial(\eta_1^3 G_1)}{\partial x} \right] + \delta \eta_2 \left[\frac{1}{3\eta_2} \frac{\partial(\eta_2^3 G_2)}{\partial x} + \frac{\eta_2 G_2}{2} \frac{\partial h}{\partial x} - \frac{\eta_2}{2} \frac{\partial(D_2^2 h)}{\partial x} \right. \\ &\quad \left. \left. - \frac{\partial \zeta}{\partial x} D_2^2 h \right] \right). \end{aligned} \quad (5.62)$$

For further reduction of the horizontal momentum equation for \bar{u}_1 (5.52), we introduce here simplifications made in (5.34), what results in

$$\frac{\partial \bar{u}_1}{\partial t} + \bar{u}_1 \frac{\partial \bar{u}_1}{\partial x} - \mu \bar{v}_1 = -\frac{\partial P}{\partial x} + \frac{\partial \zeta}{\partial x} + \delta \left[\eta_1 \frac{\partial \eta_1}{\partial x} G_1 + \frac{\eta_1^2}{3} \frac{\partial G_1}{\partial x} \right] + O(\delta^2) \quad (5.63)$$

5. A GENERATION MODEL OF SOLITONS

where we replace $\frac{\partial P}{\partial x}$ by its equivalent expression above, what yields

$$\begin{aligned} \frac{\partial \bar{u}_1}{\partial t} + \bar{u}_1 \frac{\partial \bar{u}_1}{\partial x} + \mu \bar{v}_1 &= \frac{\partial \zeta}{\partial x} + \frac{1}{(1-h)} \left(\frac{\partial(Uh)}{\partial t} + \frac{\partial}{\partial x} (\eta_1 \bar{u}_1^2 + \eta_2 \bar{u}_2^2) \right. \\ &\quad \left. - \mu (\eta_1 \bar{v}_1 + \eta_2 \bar{v}_2) - \eta_1 \frac{\partial \zeta}{\partial x} \right) + \delta \left(1 - \frac{\eta_1}{(1-h)} \right) \left[\eta_1 G_1 \frac{\partial \eta_1}{\partial x} + \frac{\eta_1^2}{3} \frac{\partial G_1}{\partial x} \right] \\ + \frac{\delta \eta_2}{(1-h)} &\left[-\eta_2 G_2 \frac{\partial \zeta}{\partial x} - \frac{\eta_2^2}{3} \frac{\partial G_2}{\partial x} + \frac{\eta_2 G_2}{2} \frac{\partial h}{\partial x} + \frac{\eta_2}{2} \frac{\partial(D_2^2 h)}{\partial x} + \frac{\partial \zeta}{\partial x} D_2^2 h \right] + O(\delta^2). \end{aligned} \quad (5.64)$$

Finally, our two fluid-layer rotating system has been simplified throughout this section from a set of six dimensionless equations for six unknowns (\bar{u}_1 , \bar{u}_2 , \bar{v}_1 , \bar{v}_2 , P , ζ) to a set of five dimensionless equations for five unknowns (\bar{u}_1 , \bar{u}_2 , \bar{v}_1 , \bar{v}_2 , ζ). It is important to recall that, on the way of working off $\frac{\partial P}{\partial x}$, we obtained the expression (5.60), which is a much simpler equation for \bar{u}_2 than (5.53). To conclude with the work of simplifying our set of equations, below we introduce simplifications made in (5.35) for the horizontal momentum equations of \bar{v}_i (5.37) and present our generation model of solitons as

$$\begin{aligned} \frac{\partial \bar{u}_1}{\partial t} + \bar{u}_1 \frac{\partial \bar{u}_1}{\partial x} + \mu \bar{v}_1 &= \frac{\partial \zeta}{\partial x} + \frac{1}{(1-h)} \left(\frac{\partial(Uh)}{\partial t} + \frac{\partial}{\partial x} (\eta_1 \bar{u}_1^2 + \eta_2 \bar{u}_2^2) \right. \\ &\quad \left. - \mu (\eta_1 \bar{v}_1 + \eta_2 \bar{v}_2) - \eta_1 \frac{\partial \zeta}{\partial x} \right) + \delta \left(1 - \frac{\eta_1}{(1-h)} \right) \left[\eta_1 G_1 \frac{\partial \eta_1}{\partial x} + \frac{\eta_1^2}{3} \frac{\partial G_1}{\partial x} \right] \\ + \frac{\delta \eta_2}{(1-h)} &\left[-\eta_2 G_2 \frac{\partial \zeta}{\partial x} - \frac{\eta_2^2}{3} \frac{\partial G_2}{\partial x} + \frac{\eta_2 G_2}{2} \frac{\partial h}{\partial x} + \frac{\eta_2}{2} \frac{\partial(D_2^2 h)}{\partial x} + \frac{\partial \zeta}{\partial x} D_2^2 h \right] + O(\delta^2) \end{aligned} \quad (5.64)$$

$$\bar{u}_2 = \frac{Uh - \eta_1 \bar{u}_1}{\eta_2}, \quad (5.60)$$

$$\frac{\partial \bar{v}_1}{\partial t} + \bar{u}_1 \frac{\partial \bar{v}_1}{\partial x} + \mu \bar{u}_1 = 0 + O(\delta^2), \quad (5.65)$$

$$\frac{\partial \bar{v}_2}{\partial t} + \mu \bar{u}_2 + \bar{u}_2 \frac{\partial \bar{v}_2}{\partial x} = 0 + O(\delta^2), \quad (5.66)$$

$$\frac{\partial \zeta}{\partial t} - (h_1 - \zeta) \frac{\partial \bar{u}_1}{\partial x} + \bar{u}_1 \frac{\partial \zeta}{\partial x} = 0. \quad (5.38)$$

5.7 Numerical Modeling

We solve the fully nonlinear generation model using numerical techniques, i.e. equations will be discretized and solved following a time stepping algorithm for a certain space-time grid. Throughout this section we detail how the set of equations which composes the model (5.64, 5.60, 5.37, 5.38) is solved numerically.

5.7.1 Numerical Strategy

Firstly we define a grid in time and space for discretization of the various derivatives of the system. Then,

$$t_n = n\Delta t \quad \text{and} \quad x_j = j\Delta x$$

are introduced for integer values of n (time-step) and j (spatial-step), where Δt and Δx are the magnitude of the steps. Hence, we can easily describe time and spatial dependent variables, e.g. $y(t_n, x_j)$, at any time and position. Thus, y_j^n means the value of the variable y at the current time and spatial-step, n and j , respectively. And, consequently, $n + 1$ would represent the ‘*next time-step*’, and so $n - 1$ the ‘*previous time-step*’, what applies analogously for j in the space grid. This notation help us to determine grid points and distinguish between known and unknown values at every time step, what is important to design an efficient numerical strategy to solve our equations.

We discretize the various derivatives in the model with *centered difference approximations* (Durrant, 1999) as follows

$$\frac{\partial y}{\partial t}(t_n, x_j) \hat{=} \frac{y_j^{n+1} - y_j^n}{\Delta t}, \quad (5.67)$$

5. A GENERATION MODEL OF SOLITONS

$$\frac{\partial y}{\partial x}(t_n, x_j) \hat{=} \frac{y_{j+1}^n - y_j^n}{\Delta t}, \quad (5.68)$$

$$\frac{\partial^2 y}{\partial x^2}(t_n, x_j) \hat{=} \frac{y_{j+1}^n - 2y_j^n + y_{j-1}^n}{(\Delta x)^2}, \quad (5.69)$$

$$\frac{\partial^2 y}{\partial x \partial t}(t_n, x_j) \hat{=} \frac{y_{j+1}^{n+1} - y_{j+1}^n - (y_{j-1}^{n+1} - y_{j-1}^n)}{2\Delta x \Delta t}, \quad (5.70)$$

$$\frac{\partial^3 y}{\partial x^2 \partial t}(t_n, x_j) \hat{=} s \frac{y_{j+1}^{n+1} - y_{j+1}^n - 2(y_j^{n+1} - y_j^n) + (y_{j-1}^{n+1} - y_{j-1}^n)}{(\Delta x)^2 \Delta t}. \quad (5.71)$$

Initiailly the system is at rest with mean horizontal velocities, \bar{u}_i and \bar{v}_i , and displacement of the interface, ζ , being all zero at the first two time levels ($n-1, n$), what represent the initialization fields. The thickness of the upper, h_1 , and lower layer, h_2 , together with the topography, $h(X)$, draw the scenario where the two-layer system runs.

At the next time-step ($n+1$), we start to move the topography to the right creating the effect of a tidal motion flowing to the left. For given U (velocity of moving topography, (5.57)) and time-step, the excursion of the topography is a known quantity which is used to shift (first, second and third) spatial derivatives of $h(X)$ at every new time-step. The momentum (5.37) and continuity (5.38) equations can now be solved for \bar{v}_1^{n+1} , \bar{v}_2^{n+1} and ζ_j^{n+1} at all j positions in terms of the known quantities at the previous two time levels ($n-1, n$).

The goal consists on getting all terms with time-derivatives in the left-hand side of every equation which composes our model, leaving remaining terms in the right-hand side. At the last stage, we look for an expression in the form

$$\frac{\partial y}{\partial t} = Y(t_n, x_j) \quad (5.72)$$

where $Y(t_n, x_j)$ represents a collection of known variables whose values may be dependent on time and/or space. If we now discretize the derivative in the expression above, we get

$$\frac{y_j^{n+1} - y_j^n}{\Delta t} = Y(t_n, x_j) \quad (5.73)$$

where y_j^{n+1} is an unknown quantity which can be expressed for all j positions in terms of the known quantities of the previous time-levels of $y(t_n, x_j)$ and $Y(t_n, x_j)$. This operation is solved numerically using third-order Adams-Bashforth approximation (Durrant, 1999) as

$$y_j^{n+1} = y_j^n + \frac{\Delta t}{12} \left(23Y_j^n - 16Y_j^{n-1} + 5Y_j^{n-2} \right) \quad (5.74)$$

This is the idea we keep in mind, we calculate values at the new time-steps by using known values at the previous time-steps for all spatial positions. Hence, we need an scheme which coherently solve our equations in a way that we always count with the required known values to move our system to the new time-step over the space domain.

To this end, equations for v_1 (5.65), v_2 (5.66) and ζ (5.38) are easily reorganized to be solved numerically with the time derivative in the left hand-side following

$$\frac{\partial \bar{v}_1}{\partial t} = -\bar{u}_1 \frac{\partial \bar{v}_1}{\partial x} - \mu \bar{u}_1 + O(\delta^2) \quad (5.65)$$

$$\frac{\partial \bar{v}_2}{\partial t} = -\mu \bar{u}_2 - \bar{u}_2 \frac{\partial \bar{v}_2}{\partial x} + O(\delta^2) \quad (5.66)$$

$$\frac{\partial \zeta}{\partial t} = (h_1 - \zeta) \frac{\partial \bar{u}_1}{\partial x} - \bar{u}_1 \frac{\partial \zeta}{\partial x} \quad (5.38)$$

as required for applying Adams-Bashforth approximation.

5. A GENERATION MODEL OF SOLITONS

However, solving \bar{u}_1 numerically is not straightforward. After collecting time derivatives in the left hand-side and remaining terms in the right hand-side, the horizontal momentum equation of \bar{u}_1 (5.64) evolves to an expression ¹ in the form of

$$a \frac{\partial \bar{u}_1}{\partial t} + b \frac{\partial^2 \bar{u}_1}{\partial x \partial t} + c \frac{\partial^3 \bar{u}_1}{\partial x^2 \partial t} = Y(t_n, x_j) \quad (5.75)$$

where a , b and c collect spatial derivatives of $\zeta(x, t)$ and $h(x, t)$ (space-time dependent variables); and $Y(t_n, x_j)$ represents remaining terms, as previously. If now we operate the time derivative as a common factor in the left-hand side, the result leads to

$$\frac{\partial}{\partial t} \left(a \bar{u}_1 + b \frac{\partial \bar{u}_1}{\partial x} + c \frac{\partial^2 \bar{u}_1}{\partial x^2} \right) = Y(t_n, x_j) + \left(\frac{\partial a}{\partial t} \bar{u}_1 + \frac{\partial b}{\partial t} \frac{\partial \bar{u}_1}{\partial x} + \frac{\partial c}{\partial t} \frac{\partial^2 \bar{u}_1}{\partial x^2} \right) \quad (5.76)$$

what helps us to introduce a new variable, \bar{U}_1 , to turn our problem into a numerically solvable expression following

$$\frac{\partial \bar{U}_1}{\partial t} = Y(t_n, x_j) + \left(\frac{\partial a}{\partial t} \bar{u}_1 + \frac{\partial b}{\partial t} \frac{\partial \bar{u}_1}{\partial x} + \frac{\partial c}{\partial t} \frac{\partial^2 \bar{u}_1}{\partial x^2} \right) \quad (5.77)$$

In the following, for clarity purposes, we refer to the right-hand side above as $R(t_n, x_j)$

$$\frac{\partial \bar{U}_1}{\partial t} = R(t_n, x_j) \quad (5.78)$$

It is important to recall here that $R(t_n, x_j)$ is a known quantity since both $Y(t_n, x_j)$ and the spatial derivatives of \bar{u}_1 are both evaluated at the current time-step (n); and, the time derivatives of a , b and c , which involve values of ζ at the current (n) and new time-step ($n + 1$), have been previously achieved with (5.38) via Adams-Bashforth approximation (5.74).

¹For simplicity, we deal at this point with the generic expression (5.75) which represents the the horizontal momentum equation of \bar{u}_1 (5.64) to be solved numerically. The procedure to that end is the matter of *Section 5.7.2*. Here we leave that work aside, as now we focused on explaining the numerical strategy we applied to solve \bar{u}_1 once we get an expression as (5.75).

Next, we proceed to discretize the spatial derivatives in \bar{U}_1 using (5.68 and 5.69), what results in

$$\bar{U}_1 = a_j \bar{u}_{1j} + b_j \frac{\bar{u}_{1j+1}}{2\Delta x} - b_j \frac{\bar{u}_{1j-1}}{2\Delta x} - c_j \frac{\bar{u}_{1j+1}}{(\Delta x)^2} - 2 c_j \frac{\bar{u}_{1j}}{(\Delta x)^2} + c_j \frac{\bar{u}_{1j-1}}{(\Delta x)^2} \quad (5.79)$$

and grouping terms, it yields

$$\bar{U}_1 = \left(a_j - \frac{2 c_j}{2\Delta x} \right) \bar{u}_{1j} + \left(\frac{-b_j}{2\Delta x} + \frac{c_j}{(\Delta x)^2} \right) \bar{u}_{1j-1} + \left(\frac{b_j}{2\Delta x} - \frac{c_j}{(\Delta x)^2} \right) \bar{u}_{1j+1} \quad (5.80)$$

which we rewrite by introducing factors d , e and f as follows

$$U_{1j} = d_j \bar{u}_{1j} + e_j \bar{u}_{1j-1} + f_j \bar{u}_{1j+1} \quad (5.81)$$

Subsequently, when we discretize the time derivative of \bar{U}_1

$$\frac{\partial U_1}{\partial t} = \frac{U_{1j}^{n+1} - U_{1j}^n}{\Delta t}$$

and apply Adams-Bashforth (5.74), we obtain

$$\bar{U}_{1j}^{n+1} = \bar{U}_{1j}^n + \frac{\Delta t}{12} \left(23R_j^n - 16R_j^{n-1} + 5R_j^{n-2} \right) \quad (5.82)$$

where \bar{U}_{1j}^{n+1} actually includes

$$\bar{U}_{1j}^{n+1} = d_j^{n+1} \bar{u}_{1j}^{n+1} + e_j^{n+1} \bar{u}_{1j-1}^{n+1} + f_j^{n+1} \bar{u}_{1j+1}^{n+1} \quad (5.83)$$

To close our system we still need to obtain \bar{u}_{1j}^{n+1} for all j terms. To that end, the equation above is more complicated to solve and gives rise to

$$\bar{d}_j = d_j - e_j f_{j-1} \quad (5.88)$$

$$\bar{f}_j = f_j / \bar{d}_j \quad (5.89)$$

$$\bar{g}_j = (\bar{U}_{1j} - e_j g_{j-1}) / \bar{d}_j \quad (5.90)$$

for $j = 2 \dots J - 1$ (notice that $f_{J-1} = 0$), and subsequently

$$\bar{u}_{1J-j}^{n+1} = g_{J-j} - \bar{f}_{J-j} \bar{u}_{1J-j+1}^{n+1} \quad (5.91)$$

for $j = 1 \dots J - 2$. Following this, we accomplish \bar{u}_1^{n+1} for all j terms and, hence, \bar{u}_2^{n+1} in a straightforward manner using the expression (5.60), what closes the model resolution for every new time level $n + 1$.

With this we have drawn a numerical strategy which can be used to solve successfully the model object of this thesis with numerical techniques.

5.7.2 Preliminaries to Solve \bar{u}_1

The mathematical work presented throughout this subsection is optional under the reader's convenience and may be skipped without loss of continuity for the understanding of the numerical strategy we use to solve the model.

The main goal here is to detail the procedure we follow to obtain a numerically solvable expression for \bar{u}_1 in the form of (5.75) taking its horizontal momentum equation (5.64) as starting point. For simplicity in future manipulations we work by collecting terms with analogous physical effects: linear, non-linear and non-hydrostatic dispersive effects:

$$\begin{aligned} \frac{\partial \bar{u}_1}{\partial t} = & \mu \bar{v}_1 - \bar{u}_1 \frac{\partial \bar{u}_1}{\partial x} + \frac{\partial \zeta}{\partial x} + \frac{1}{(1-h)} \left(\frac{\partial(Uh)}{\partial t} + \frac{\partial}{\partial x} (\eta_1 \bar{u}_1^2 + \eta_2 \bar{u}_2^2) \right. \\ & \left. - \mu (\eta_1 \bar{v}_1 + \eta_2 \bar{v}_2) - \eta_1 \frac{\partial \zeta}{\partial x} \right) + \delta \left(1 - \frac{\eta_1}{(1-h)} \right) \left[\eta_1 G_1 \frac{\partial \eta_1}{\partial x} + \frac{\eta_1^2}{3} \frac{\partial G_1}{\partial x} \right] \\ & + \frac{\delta \eta_2}{(1-h)} \left[-\eta_2 G_2 \frac{\partial \zeta}{\partial x} - \frac{\eta_2^2}{3} \frac{\partial G_2}{\partial x} + \frac{\eta_2 G_2}{2} \frac{\partial h}{\partial x} + \frac{\eta_2}{2} \frac{\partial(D_2^2 h)}{\partial x} + \frac{\partial \zeta}{\partial x} D_2^2 h \right] \quad (5.92) \end{aligned}$$

5. A GENERATION MODEL OF SOLITONS

where we introduce for convenience the factors δ_1 and δ_2 in front of dispersive terms from the upper layer, and dispersive terms from the lower layer and the topography, respectively,

$$\delta_1 = \delta \left(1 - \frac{\eta_1}{(1-h)} \right); \quad \delta_2 = \frac{\delta \eta_2}{(1-h)} \quad (5.93)$$

leading to

$$\begin{aligned} \frac{\partial \bar{u}_1}{\partial t} = & \mu \bar{v}_1 - \bar{u}_1 \frac{\partial \bar{u}_1}{\partial x} + \frac{\partial \zeta}{\partial x} + \frac{1}{(1-h)} \left(\frac{\partial(Uh)}{\partial t} + \frac{\partial}{\partial x} (\eta_1 \bar{u}_1^2 + \eta_2 \bar{u}_2^2) \right. \\ & \left. - \mu (\eta_1 \bar{v}_1 + \eta_2 \bar{v}_2) - \eta_1 \frac{\partial \zeta}{\partial x} \right) + \delta_1 \left[\eta_1 G_1 \frac{\partial \eta_1}{\partial x} + \frac{\eta_1^2}{3} \frac{\partial G_1}{\partial x} \right] \\ & + \delta_2 \left[-\eta_2 G_2 \frac{\partial \zeta}{\partial x} - \frac{\eta_2^2}{3} \frac{\partial G_2}{\partial x} + \frac{\eta_2 G_2}{2} \frac{\partial h}{\partial x} + \frac{\eta_2}{2} \frac{\partial(D_2^2 h)}{\partial x} + \frac{\partial \zeta}{\partial x} D_2^2 h \right] \end{aligned} \quad (5.94)$$

We proceed working out linear and non-linear terms of equation above, what leads to deal with the following

$$\mu \bar{v}_1 - \bar{u}_1 \frac{\partial \bar{u}_1}{\partial x} + \frac{\partial \zeta}{\partial x} + \frac{1}{(1-h)} \left(\frac{\partial(Uh)}{\partial t} + \frac{\partial}{\partial x} (\eta_1 \bar{u}_1^2 + \eta_2 \bar{u}_2^2) \right) - \mu (\eta_1 \bar{v}_1 + \eta_2 \bar{v}_2) - \eta_1 \frac{\partial \zeta}{\partial x}$$

where we introduce equation (5.57) to substitute the time-derivative of the oscillating topography, h , by its space-derivative

$$\begin{aligned} \mu \bar{v}_1 - \bar{u}_1 \frac{\partial \bar{u}_1}{\partial x} + \frac{\partial \zeta}{\partial x} + \frac{1}{(1-h)} \left(h \frac{\partial U}{\partial t} + U^2 \frac{\partial h}{\partial x} + \bar{u}_1 \frac{\partial \eta_1 \bar{u}_1}{\partial x} + \bar{u}_1 \eta_1 \frac{\partial \bar{u}_1}{\partial x} \right. \\ \left. + \bar{u}_2 \frac{\partial \eta_2 \bar{u}_2}{\partial x} + \bar{u}_2 \eta_2 \frac{\partial \bar{u}_2}{\partial x} - \mu (\eta_1 \bar{v}_1 + \eta_2 \bar{v}_2) - \eta_1 \frac{\partial \zeta}{\partial x} \right) \end{aligned}$$

Next, we introduce the continuity equation (5.38)

$$\begin{aligned} \mu \bar{v}_1 - \bar{u}_1 \frac{\partial \bar{u}_1}{\partial x} + \frac{\partial \zeta}{\partial x} + \frac{1}{(1-h)} \left(h \frac{\partial U}{\partial t} + U^2 \frac{\partial h}{\partial x} - \bar{u}_1 \frac{\partial \eta_1}{\partial t} + \bar{u}_1 \eta_1 \frac{\partial \bar{u}_1}{\partial x} \right. \\ \left. - \bar{u}_2 \frac{\partial \eta_2}{\partial t} + \bar{u}_2 \eta_2 \frac{\partial \bar{u}_2}{\partial x} - \mu \left(\eta_1 \bar{v}_1 + \eta_2 \bar{v}_2 \right) - \eta_1 \frac{\partial \zeta}{\partial x} \right) \end{aligned}$$

as well as the definition of η_1 and η_2 for involved derivatives

$$\begin{aligned} \mu \bar{v}_1 - \bar{u}_1 \frac{\partial \bar{u}_1}{\partial x} + \frac{\partial \zeta}{\partial x} + \frac{1}{(1-h)} \left(h \frac{\partial U}{\partial t} + U^2 \frac{\partial h}{\partial x} + (\bar{u}_1 - \bar{u}_2) \frac{\partial \zeta}{\partial t} + \bar{u}_1 \eta_1 \frac{\partial \bar{u}_1}{\partial x} \right. \\ \left. + \bar{u}_2 \frac{\partial h}{\partial t} + \bar{u}_2 \eta_2 \frac{\partial \bar{u}_2}{\partial x} - \mu \left(\eta_1 \bar{v}_1 + \eta_2 \bar{v}_2 \right) - \eta_1 \frac{\partial \zeta}{\partial x} \right) \end{aligned}$$

At this point, we can clearly separate *linear* and *non-linear* terms grouped as

$$\boxed{\text{linear} = \mu \bar{v}_1 + \frac{\partial \zeta}{\partial x} + \frac{1}{(1-h)} \left(h \frac{\partial U}{\partial t} + U^2 \frac{\partial h}{\partial x} + \bar{u}_2 \frac{\partial h}{\partial t} - \mu \left(\eta_1 \bar{v}_1 + \eta_2 \bar{v}_2 \right) - \eta_1 \frac{\partial \zeta}{\partial x} \right)}$$

(5.95)

and

$$\boxed{\text{nonlinear} = -\bar{u}_1 \frac{\partial \bar{u}_1}{\partial x} + \frac{1}{(1-h)} \left((\bar{u}_1 - \bar{u}_2) \frac{\partial \zeta}{\partial t} + \bar{u}_1 \eta_1 \frac{\partial \bar{u}_1}{\partial x} + \bar{u}_2 \eta_2 \frac{\partial \bar{u}_2}{\partial x} \right)}$$

(5.96)

Accordingly, equation (5.94) can be rewritten as

$$\begin{aligned} \frac{\partial \bar{u}_1}{\partial t} = \text{linear} + \text{nonlinear} + \delta_1 \left[\eta_1 G_1 \frac{\partial \eta_1}{\partial x} + \frac{\eta_1^2}{3} \frac{\partial G_1}{\partial x} \right] \\ + \delta_2 \left[-\eta_2 G_2 \frac{\partial \zeta}{\partial x} - \frac{\eta_2^2}{3} \frac{\partial G_2}{\partial x} + \frac{\eta_2 G_2}{2} \frac{\partial h}{\partial x} + \frac{\eta_2}{2} \frac{\partial (D_2^2 h)}{\partial x} + \frac{\partial \zeta}{\partial x} D_2^2 h \right] \end{aligned} \quad (5.97)$$

5. A GENERATION MODEL OF SOLITONS

We continue working out dispersive terms from the upper layer in equation (5.97), what leads to deal with

$$\delta_1 \left[\eta_1 G_1 \frac{\partial \eta_1}{\partial x} + \frac{\eta_1^2}{3} \frac{\partial G_1}{\partial x} \right] \quad (5.98)$$

taking special care of terms with $\frac{\partial \bar{u}_1}{\partial t}$ involved in G_1 (5.41). Therefore, it yields

$$\delta_1 \left[-\eta_1 \frac{\partial \zeta}{\partial x} \left[\frac{\partial^2 \bar{u}_1}{\partial x \partial t} + \bar{u}_1 \frac{\partial^2 \bar{u}_1}{\partial x^2} - \left(\frac{\partial \bar{u}_1}{\partial x} \right)^2 \right] + \frac{\eta_1^2}{3} \frac{\partial}{\partial x} \left(\frac{\partial^2 \bar{u}_1}{\partial x \partial t} + \bar{u}_1 \frac{\partial^2 \bar{u}_1}{\partial x^2} - \left(\frac{\partial \bar{u}_1}{\partial x} \right)^2 \right) \right]$$

$$\delta_1 \left[-\eta_1 \frac{\partial \zeta}{\partial x} \left[\frac{\partial^2 \bar{u}_1}{\partial x \partial t} + \bar{u}_1 \frac{\partial^2 \bar{u}_1}{\partial x^2} - \left(\frac{\partial \bar{u}_1}{\partial x} \right)^2 \right] + \frac{\eta_1^2}{3} \frac{\partial^3 \bar{u}_1}{\partial x^2 \partial t} + \frac{\eta_1^2}{3} \left[\bar{u}_1 \frac{\partial^3 \bar{u}_1}{\partial x^3} - \frac{\partial \bar{u}_1}{\partial x} \frac{\partial^2 \bar{u}_1}{\partial x^2} \right] \right]$$

Leaving on the left-hand side terms with time-derivatives for u-velocity components, equation (5.97) develops as

$$\begin{aligned} & \frac{\partial \bar{u}_1}{\partial t} + \delta_1 \left[\eta_1 \frac{\partial \zeta}{\partial x} \frac{\partial^2 \bar{u}_1}{\partial x \partial t} - \frac{\eta_1^2}{3} \frac{\partial^3 \bar{u}_1}{\partial x^2 \partial t} \right] = \text{linear} + \text{nonlinear} \\ & + \delta_1 \left[-\eta_1 \frac{\partial \zeta}{\partial x} \left[\bar{u}_1 \frac{\partial^2 \bar{u}_1}{\partial x^2} - \left(\frac{\partial \bar{u}_1}{\partial x} \right)^2 \right] + \frac{\eta_1^2}{3} \left[\bar{u}_1 \frac{\partial^3 \bar{u}_1}{\partial x^3} - \frac{\partial \bar{u}_1}{\partial x} \frac{\partial^2 \bar{u}_1}{\partial x^2} \right] \right] \\ & + \delta_2 \left[-\eta_2 G_2 \frac{\partial \zeta}{\partial x} - \frac{\eta_2^2}{3} \frac{\partial G_2}{\partial x} + \frac{\eta_2 G_2}{2} \frac{\partial h}{\partial x} + \frac{\eta_2}{2} \frac{\partial (D_2^2 h)}{\partial x} + \frac{\partial \zeta}{\partial x} D_2^2 h \right] \end{aligned} \quad (5.99)$$

where we can group the non-hydrostatic dispersive terms related to upper layer on the right-hand side under the variable $dispersive_1$, following

$$\boxed{dispersive_1 = \delta_1 \left[-\eta_1 \frac{\partial \zeta}{\partial x} \left[\bar{u}_1 \frac{\partial^2 \bar{u}_1}{\partial x^2} - \left(\frac{\partial \bar{u}_1}{\partial x} \right)^2 \right] + \frac{\eta_1^2}{3} \left[\bar{u}_1 \frac{\partial^3 \bar{u}_1}{\partial x^3} - \frac{\partial \bar{u}_1}{\partial x} \frac{\partial^2 \bar{u}_1}{\partial x^2} \right] \right]} \quad (5.100)$$

and the equation (5.99) can be rewritten as

$$\begin{aligned} \frac{\partial \bar{u}_1}{\partial t} + \delta_1 \left[\eta_1 \frac{\partial \zeta}{\partial x} \frac{\partial^2 \bar{u}_1}{\partial x \partial t} - \frac{\eta_1^2}{3} \frac{\partial^3 \bar{u}_1}{\partial x^2 \partial t} \right] &= \text{linear} + \text{nonlinear} + \text{dispersive}_1 \\ + \delta_2 \left[-\eta_2 G_2 \frac{\partial \zeta}{\partial x} - \frac{\eta_2^2}{3} \frac{\partial G_2}{\partial x} + \frac{\eta_2 G_2}{2} \frac{\partial h}{\partial x} + \frac{\eta_2}{2} \frac{\partial (D_2^2 h)}{\partial x} + \frac{\partial \zeta}{\partial x} D_2^2 h \right] & \end{aligned} \quad (5.101)$$

Next, we continue working out dispersive terms from the lower layer in equation (5.101), what leads to deal with

$$\delta_2 \left[-\eta_2 G_2 \frac{\partial \zeta}{\partial x} - \frac{\eta_2^2}{3} \frac{\partial G_2}{\partial x} \right]$$

taking special care of terms with $\frac{\partial \bar{u}_2}{\partial t}$ involved in G_2 (5.41). Then, we obtain

$$\delta_2 \left[-\eta_2 \frac{\partial \zeta}{\partial x} \left[\frac{\partial^2 \bar{u}_2}{\partial x \partial t} + \bar{u}_2 \frac{\partial^2 \bar{u}_2}{\partial x^2} - \left(\frac{\partial \bar{u}_2}{\partial x} \right)^2 \right] - \frac{\eta_2^2}{3} \left[\frac{\partial^3 \bar{u}_2}{\partial x^2 \partial t} + \bar{u}_2 \frac{\partial^3 \bar{u}_2}{\partial x^3} - \frac{\partial \bar{u}_2}{\partial x} \frac{\partial^2 \bar{u}_2}{\partial x^2} \right] \right]$$

Leaving on the left-hand side terms with time-derivatives for u-velocity components, equation (5.101) develops as

$$\begin{aligned} \frac{\partial \bar{u}_1}{\partial t} + \delta_1 \left[\eta_1 \frac{\partial \zeta}{\partial x} \frac{\partial^2 \bar{u}_1}{\partial x \partial t} - \frac{\eta_1^2}{3} \frac{\partial^3 \bar{u}_1}{\partial x^2 \partial t} \right] + \delta_2 \left[\eta_2 \frac{\partial \zeta}{\partial x} \frac{\partial^2 \bar{u}_2}{\partial x \partial t} + \frac{\eta_2^2}{3} \frac{\partial^3 \bar{u}_2}{\partial x^2 \partial t} \right] &= \\ \text{linear} + \text{nonlinear} + \text{dispersive}_1 + \delta_2 \left[-\eta_2 \frac{\partial \zeta}{\partial x} \left[\bar{u}_2 \frac{\partial^2 \bar{u}_2}{\partial x^2} - \left(\frac{\partial \bar{u}_2}{\partial x} \right)^2 \right] \right. & \\ \left. - \frac{\eta_2^2}{3} \left[\bar{u}_2 \frac{\partial^3 \bar{u}_2}{\partial x^3} - \frac{\partial \bar{u}_2}{\partial x} \frac{\partial^2 \bar{u}_2}{\partial x^2} \right] + \frac{\eta_2 G_2}{2} \frac{\partial h}{\partial x} + \frac{\eta_2}{2} \frac{\partial (D_2^2 h)}{\partial x} + \frac{\partial \zeta}{\partial x} D_2^2 h \right] & \end{aligned} \quad (5.102)$$

where we can group the non-hydrostatic dispersive terms related to upper layer on the right-hand side under the variable dispersive_2 , following

$$\boxed{\text{dispersive}_2 = \delta_2 \left[-\eta_2 \frac{\partial \zeta}{\partial x} \left[\bar{u}_2 \frac{\partial^2 \bar{u}_2}{\partial x^2} - \left(\frac{\partial \bar{u}_2}{\partial x} \right)^2 \right] - \frac{\eta_2^2}{3} \left[\bar{u}_2 \frac{\partial^3 \bar{u}_2}{\partial x^3} - \frac{\partial \bar{u}_2}{\partial x} \frac{\partial^2 \bar{u}_2}{\partial x^2} \right] \right]} \quad (5.103)$$

5. A GENERATION MODEL OF SOLITONS

and the equation (5.102) can be rewritten as

$$\begin{aligned} \frac{\partial \bar{u}_1}{\partial t} + \delta_1 \left[\eta_1 \frac{\partial \zeta}{\partial x} \frac{\partial^2 \bar{u}_1}{\partial x \partial t} - \frac{\eta_1^2}{3} \frac{\partial^3 \bar{u}_1}{\partial x^2 \partial t} \right] + \delta_2 \left[\eta_2 \frac{\partial \zeta}{\partial x} \frac{\partial^2 \bar{u}_2}{\partial x \partial t} + \frac{\eta_2^2}{3} \frac{\partial^3 \bar{u}_2}{\partial x^2 \partial t} \right] = \\ \text{linear} + \text{nonlinear} + \text{dispersive}_1 + \text{dispersive}_2 \\ + \delta_2 \left[\frac{\eta_2 G_2}{2} \frac{\partial h}{\partial x} + \frac{\eta_2}{2} \frac{\partial (D_2^2 h)}{\partial x} + \frac{\partial \zeta}{\partial x} D_2^2 h \right] \quad (5.104) \end{aligned}$$

At this stage it is important to notice that we have obtained in equation (5.104) terms with time derivatives of \bar{u}_2 on the left-hand side. Once we finish to turn out all dispersive terms from topography, we will deal with the complete left-hand side, grouping terms and substituting \bar{u}_2 in terms of \bar{u}_1 following *Appendix E*.

Now we continue working out dispersive terms from the topography in equation (5.104), what leads to deal with

$$\delta_2 \left[\frac{\eta_2 G_2}{2} \frac{\partial h}{\partial x} + \frac{\eta_2}{2} \frac{\partial (D_2^2 h)}{\partial x} + \frac{\partial \zeta}{\partial x} D_2^2 h \right]$$

taking special care of terms with $\frac{\partial \bar{u}_2}{\partial t}$ involved in G_2 (5.41). Then we get

$$\begin{aligned} \delta_2 \left[\frac{\eta_2}{2} \frac{\partial h}{\partial x} \left[\frac{\partial^2 \bar{u}_2}{\partial x \partial t} + \bar{u}_2 \frac{\partial^2 \bar{u}_2}{\partial x^2} - \left(\frac{\partial \bar{u}_2}{\partial x} \right)^2 \right] \right. \\ \left. + \frac{\eta_2}{2} \frac{\partial}{\partial x} \left(\frac{\partial^2 h}{\partial t^2} + \frac{\partial \bar{u}_2}{\partial t} \frac{\partial h}{\partial x} + 2\bar{u}_2 \frac{\partial^2 h}{\partial x \partial t} + \bar{u}_2 \frac{\partial \bar{u}_2}{\partial x} \frac{\partial h}{\partial x} + \bar{u}_2^2 \frac{\partial^2 h}{\partial x^2} \right) \right. \\ \left. + \frac{\partial \zeta}{\partial x} \left[\frac{\partial^2 h}{\partial t^2} + \frac{\partial \bar{u}_2}{\partial t} \frac{\partial h}{\partial x} + 2\bar{u}_2 \frac{\partial^2 h}{\partial x \partial t} + \bar{u}_2 \frac{\partial \bar{u}_2}{\partial x} \frac{\partial h}{\partial x} + \bar{u}_2^2 \frac{\partial^2 h}{\partial x^2} \right] \right] \quad (5.105) \end{aligned}$$

where making some simplifications we obtain

$$\begin{aligned} \delta_2 \left[\eta_2 \frac{\partial^2 \bar{u}_2}{\partial x \partial t} \frac{\partial h}{\partial x} + \eta_2 \bar{u}_2 \frac{\partial^2 \bar{u}_2}{\partial x^2} \frac{\partial h}{\partial x} + \frac{\eta_2}{2} \left[\frac{\partial^3 h}{\partial x \partial t^2} + \frac{\partial \bar{u}_2}{\partial t} \frac{\partial^2 h}{\partial x^2} + 2 \frac{\partial \bar{u}_2}{\partial x} \frac{\partial^2 h}{\partial x \partial t} \right. \right. \\ \left. \left. + 2\bar{u}_2 \frac{\partial^3 h}{\partial x^2 \partial t} + 3\bar{u}_2 \frac{\partial \bar{u}_2}{\partial x} \frac{\partial^2 h}{\partial x^2} + \bar{u}_2^2 \frac{\partial^3 h}{\partial x^3} \right] + \frac{\partial \zeta}{\partial x} \left[\frac{\partial^2 h}{\partial t^2} + \frac{\partial \bar{u}_2}{\partial t} \frac{\partial h}{\partial x} + 2\bar{u}_2 \frac{\partial^2 h}{\partial x \partial t} \right. \right. \\ \left. \left. + \bar{u}_2 \frac{\partial \bar{u}_2}{\partial x} \frac{\partial h}{\partial x} + \bar{u}_2^2 \frac{\partial^2 h}{\partial x^2} \right] \right] \quad (5.106) \end{aligned}$$

Leaving on the left-hand side terms with time-derivatives for u-velocity components, equation (5.104) now develops as

$$\begin{aligned}
 \frac{\partial \bar{u}_1}{\partial t} + \delta_1 \left[\eta_1 \frac{\partial \zeta}{\partial x} \frac{\partial^2 \bar{u}_1}{\partial x \partial t} - \frac{\eta_1^2}{3} \frac{\partial^3 \bar{u}_1}{\partial x^2 \partial t} \right] + \delta_2 \left[\eta_2 \frac{\partial \zeta}{\partial x} \frac{\partial^2 \bar{u}_2}{\partial x \partial t} + \frac{\eta_2^2}{3} \frac{\partial^3 \bar{u}_2}{\partial x^2 \partial t} \right] \\
 + \delta_2 \left[-\eta_2 \frac{\partial h}{\partial x} \frac{\partial^2 \bar{u}_2}{\partial x \partial t} - \left(\frac{\eta_2}{2} \frac{\partial^2 h}{\partial x^2} + \frac{\partial \zeta}{\partial x} \frac{\partial h}{\partial x} \right) \frac{\partial \bar{u}_2}{\partial t} \right] = \\
 \text{linear} + \text{nonlinear} + \text{dispersive}_1 + \text{dispersive}_2 \\
 + \delta_2 \left[\eta_2 \bar{u}_2 \frac{\partial^2 \bar{u}_2}{\partial x^2} \frac{\partial h}{\partial x} + \frac{\eta_2}{2} \left[\frac{\partial^3 h}{\partial x \partial t^2} + 2 \frac{\partial \bar{u}_2}{\partial x} \frac{\partial^2 h}{\partial x \partial t} + 2 \bar{u}_2 \frac{\partial^3 h}{\partial x^2 \partial t} \right. \right. \\
 \left. \left. + 3 \bar{u}_2 \frac{\partial \bar{u}_2}{\partial x} \frac{\partial^2 h}{\partial x^2} + \bar{u}_2^2 \frac{\partial^3 h}{\partial x^3} \right] + \frac{\partial \zeta}{\partial x} \left[\frac{\partial^2 h}{\partial t^2} + 2 \bar{u}_2 \frac{\partial^2 h}{\partial x \partial t} + \bar{u}_2 \frac{\partial \bar{u}_2}{\partial x} \frac{\partial h}{\partial x} + \bar{u}_2^2 \frac{\partial^2 h}{\partial x^2} \right] \right]
 \end{aligned} \tag{5.107}$$

where we can group the non-hydrostatic dispersive terms related to upper layer on the right-hand side under the variable dispersive_{topo} following

$$\begin{aligned}
 \text{dispersive}_{topo} = \delta_2 \left[\eta_2 \bar{u}_2 \frac{\partial^2 \bar{u}_2}{\partial x^2} \frac{\partial h}{\partial x} + \frac{\eta_2}{2} \left[\frac{\partial^3 h}{\partial x \partial t^2} + 2 \frac{\partial \bar{u}_2}{\partial x} \frac{\partial^2 h}{\partial x \partial t} + 2 \bar{u}_2 \frac{\partial^3 h}{\partial x^2 \partial t} \right. \right. \\
 \left. \left. + 3 \bar{u}_2 \frac{\partial \bar{u}_2}{\partial x} \frac{\partial^2 h}{\partial x^2} + \bar{u}_2^2 \frac{\partial^3 h}{\partial x^3} \right] + \frac{\partial \zeta}{\partial x} \left[\frac{\partial^2 h}{\partial t^2} + 2 \bar{u}_2 \frac{\partial^2 h}{\partial x \partial t} + \bar{u}_2 \frac{\partial \bar{u}_2}{\partial x} \frac{\partial h}{\partial x} + \bar{u}_2^2 \frac{\partial^2 h}{\partial x^2} \right] \right]
 \end{aligned} \tag{5.108}$$

and introducing the equivalence for $\frac{\partial h}{\partial t}$, equation (5.57), we get

$$\begin{aligned}
 \text{dispersive}_{topo} = \delta_2 \left[\bar{u}_2 \frac{\partial h}{\partial x} \left[\eta_2 \frac{\partial^2 \bar{u}_2}{\partial x^2} + \frac{\partial \zeta}{\partial x} \frac{\partial \bar{u}_2}{\partial x} \right] + \frac{\eta_2}{2} \left[\frac{\partial U}{\partial t} \frac{\partial^2 h}{\partial x^2} + U^2 \frac{\partial^3 h}{\partial x^3} \right. \right. \\
 \left. \left. + 2U \frac{\partial \bar{u}_2}{\partial x} \frac{\partial^2 h}{\partial x^2} + 2 \bar{u}_2 U \frac{\partial^3 h}{\partial x^3} + 3 \bar{u}_2 \frac{\partial \bar{u}_2}{\partial x} \frac{\partial^2 h}{\partial x^2} + \bar{u}_2^2 \frac{\partial^3 h}{\partial x^3} \right] + \frac{\partial \zeta}{\partial x} \left[\frac{\partial U}{\partial t} \frac{\partial h}{\partial x} + U^2 \frac{\partial^2 h}{\partial x^2} \right. \right. \\
 \left. \left. + 2 \bar{u}_2 U \frac{\partial^2 h}{\partial x^2} + \bar{u}_2^2 \frac{\partial^2 h}{\partial x^2} \right] \right]
 \end{aligned} \tag{5.109}$$

Now, equation (5.104) can be rewritten as

5. A GENERATION MODEL OF SOLITONS

$$\begin{aligned} \frac{\partial \bar{u}_1}{\partial t} + \delta_1 \left[\eta_1 \frac{\partial \zeta}{\partial x} \frac{\partial^2 \bar{u}_1}{\partial x \partial t} - \frac{\eta_1^2}{3} \frac{\partial^3 \bar{u}_1}{\partial x^2 \partial t} \right] + \delta_2 \left[\eta_2 \frac{\partial \zeta}{\partial x} \frac{\partial^2 \bar{u}_2}{\partial x \partial t} + \frac{\eta_2^2}{3} \frac{\partial^3 \bar{u}_2}{\partial x^2 \partial t} \right] \\ + \delta_2 \left[-\eta_2 \frac{\partial h}{\partial x} \frac{\partial^2 \bar{u}_2}{\partial x \partial t} - \left(\frac{\eta_2}{2} \frac{\partial^2 h}{\partial x^2} + \frac{\partial \zeta}{\partial x} \frac{\partial h}{\partial x} \right) \frac{\partial \bar{u}_2}{\partial t} \right] = \\ \text{linear} + \text{nonlinear} + \text{dispersive}_1 + \text{dispersive}_2 + \text{dispersive}_{\text{topo}} \end{aligned} \quad (5.110)$$

Finally, we are interested in substituting \bar{u}_2 in terms of \bar{u}_1 for time-derivatives on the left-hand side of equation (5.110) with the equivalences described in *Appendix E*. With this aim, we first proceed to group common terms on the left-hand side

$$\begin{aligned} \frac{\partial \bar{u}_1}{\partial t} + \delta_1 \left[\eta_1 \frac{\partial \zeta}{\partial x} \frac{\partial^2 \bar{u}_1}{\partial x \partial t} - \frac{\eta_1^2}{3} \frac{\partial^3 \bar{u}_1}{\partial x^2 \partial t} \right] + \delta_2 \left[\left(\eta_2 \frac{\partial \zeta}{\partial x} - \eta_2 \frac{\partial h}{\partial x} \right) \frac{\partial^2 \bar{u}_2}{\partial x \partial t} + \frac{\eta_2^2}{3} \frac{\partial^3 \bar{u}_2}{\partial x^2 \partial t} \right. \\ \left. - \left(\frac{\eta_2}{2} \frac{\partial^2 h}{\partial x^2} + \frac{\partial \zeta}{\partial x} \frac{\partial h}{\partial x} \right) \frac{\partial \bar{u}_2}{\partial t} \right] \\ = \text{linear} + \text{nonlinear} + \text{dispersive}_1 + \text{dispersive}_2 + \text{dispersive}_{\text{topo}} \end{aligned} \quad (5.111)$$

and then substitute \bar{u}_2 in terms of \bar{u}_1 on the basis of *Appendix E* (where we introduce ϕ)

$$\begin{aligned} \frac{\partial \bar{u}_1}{\partial t} + \delta_1 \left[\eta_1 \frac{\partial \zeta}{\partial x} \frac{\partial^2 \bar{u}_1}{\partial x \partial t} - \frac{\eta_1^2}{3} \frac{\partial^3 \bar{u}_1}{\partial x^2 \partial t} \right] + \delta_2 \left[\left(\eta_2 \frac{\partial \zeta}{\partial x} - \eta_2 \frac{\partial h}{\partial x} \right) \left[-\frac{\eta_1}{\eta_2} \frac{\partial^2 \bar{u}_1}{\partial x \partial t} \right. \right. \\ \left. \left. - \frac{\partial(\eta_1/\eta_2)}{\partial x} \frac{\partial \bar{u}_1}{\partial t} + \frac{\partial \phi}{\partial x} \right] + \frac{\eta_2^2}{3} \left[-2 \frac{\partial(\eta_1/\eta_2)}{\partial x} \frac{\partial^2 \bar{u}_1}{\partial x \partial t} - \frac{\eta_1}{\eta_2} \frac{\partial^3 \bar{u}_1}{\partial x^2 \partial t} \right. \right. \\ \left. \left. - \frac{\partial^2(\eta_1/\eta_2)}{\partial x^2} \frac{\partial \bar{u}_1}{\partial t} + \frac{\partial^2 \phi}{\partial x^2} \right] - \left(\frac{\eta_2}{2} \frac{\partial^2 h}{\partial x^2} + \frac{\partial \zeta}{\partial x} \frac{\partial h}{\partial x} \right) \left[-\frac{\eta_1}{\eta_2} \frac{\partial \bar{u}_1}{\partial t} + \phi \right] \right] = \\ \text{linear} + \text{nonlinear} + \text{dispersive}_1 + \text{dispersive}_2 + \text{dispersive}_{\text{topo}} \end{aligned} \quad (5.112)$$

To finish with this procedure we take terms involving ϕ to the right-hand side and collect terms with same time-derivative of \bar{u}_1 on the left-hand side

$$\begin{aligned}
 \frac{\partial \bar{u}_1}{\partial t} & \left[1 + \delta_2 \left[\left(\eta_2 \frac{\partial h}{\partial x} - \eta_2 \frac{\partial \zeta}{\partial x} \right) \frac{\partial(\eta_1/\eta_2)}{\partial x} - \frac{\eta_2^2}{3} \frac{\partial^2(\eta_1/\eta_2)}{\partial x^2} + \frac{\eta_1}{\eta_2} \left(\frac{\eta_2}{2} \frac{\partial^2 h}{\partial x^2} + \frac{\partial \zeta}{\partial x} \frac{\partial h}{\partial x} \right) \right] \right] \\
 & + \frac{\partial^2 \bar{u}_1}{\partial x \partial t} \left[\delta_1 \eta_1 \frac{\partial \zeta}{\partial x} + \delta_2 \left[\frac{\eta_1}{\eta_2} \left(\eta_2 \frac{\partial h}{\partial x} - \eta_2 \frac{\partial \zeta}{\partial x} \right) - \frac{2\eta_2^2}{3} \frac{\partial(\eta_1/\eta_2)}{\partial x} \right] \right] \\
 & + \frac{\partial^3 \bar{u}_1}{\partial x^2 \partial t} \left[-\delta_1 \frac{\eta_1^2}{3} - \delta_2 \frac{\eta_1 \eta_2}{3} \right] = \\
 & \text{linear} + \text{nonlinear} + \text{dispersive}_1 + \text{dispersive}_2 + \text{dispersive}_{topo} \\
 & + \delta_2 \left[\left(\eta_2 \frac{\partial h}{\partial x} - \eta_2 \frac{\partial \zeta}{\partial x} \right) \frac{\partial \phi}{\partial x} - \frac{\eta_2^2}{3} \frac{\partial^2 \phi}{\partial x^2} + \phi \left(\frac{\eta_2}{2} \frac{\partial^2 h}{\partial x^2} + \frac{\partial \zeta}{\partial x} \frac{\partial h}{\partial x} \right) \right]
 \end{aligned} \tag{5.113}$$

Terms accompanying the first, second, and third time-derivatives of \bar{u}_1 are grouped¹ as a , b and c , respectively; and dispersive effects on the right-hand side of the equation are grouped under the variable $dispersive_{1,2,topo}$ leading to

$$a \frac{\partial \bar{u}_1}{\partial t} + b \frac{\partial^2 \bar{u}_1}{\partial x \partial t} + c \frac{\partial^3 \bar{u}_1}{\partial x^2 \partial t} = \text{linear} + \text{nonlinear} + \text{dispersive}_{1,2,topo} \tag{5.114}$$

with

$$a(x, t) = \left[1 + \delta_2 \left[\left(\eta_2 \frac{\partial h}{\partial x} - \eta_2 \frac{\partial \zeta}{\partial x} \right) \frac{\partial(\eta_1/\eta_2)}{\partial x} - \frac{\eta_2^2}{3} \frac{\partial^2(\eta_1/\eta_2)}{\partial x^2} + \frac{\eta_1}{\eta_2} \left(\frac{\eta_2}{2} \frac{\partial^2 h}{\partial x^2} + \frac{\partial \zeta}{\partial x} \frac{\partial h}{\partial x} \right) \right] \right] \tag{5.115}$$

$$b(x, t) = \left[\delta_1 \eta_1 \frac{\partial \zeta}{\partial x} + \delta_2 \left[\frac{\eta_1}{\eta_2} \left(\eta_2 \frac{\partial h}{\partial x} - \eta_2 \frac{\partial \zeta}{\partial x} \right) - \frac{2\eta_2^2}{3} \frac{\partial(\eta_1/\eta_2)}{\partial x} \right] \right] \tag{5.116}$$

¹It is important to notice that coefficients a , b and c involve derivatives of space-time dependent variables. This circumstance requires special attention in the numerical solving as it was already explained on page 108

5. A GENERATION MODEL OF SOLITONS

$$c(x, t) = \left[-\delta_1 \frac{\eta_1^2}{3} - \delta_2 \frac{\eta_1 \eta_2}{3} \right] \quad (5.117)$$

Finally we take out the time derivative from (5.118) and obtain

$$\begin{aligned} \frac{\partial}{\partial t} \left(a \bar{u}_1 + b \frac{\partial \bar{u}_1}{\partial x} + c \frac{\partial^2 \bar{u}_1}{\partial x^2} \right) = & \text{linear} + \text{nonlinear} + \text{dispersive}_{1,2,\text{topo}} \\ & + \left(\frac{\partial a}{\partial t} \bar{u}_1 + \frac{\partial b}{\partial t} \frac{\partial \bar{u}_1}{\partial x} + \frac{\partial c}{\partial t} \frac{\partial^2 \bar{u}_1}{\partial x^2} \right) \end{aligned} \quad (5.118)$$

At this point the horizontal momentum equation of \bar{u}_1 (5.64) turns into a form which is suitable to be solve with numerical techniques

$$a \frac{\partial \bar{u}_1}{\partial t} + b \frac{\partial^2 \bar{u}_1}{\partial x \partial t} + c \frac{\partial^3 \bar{u}_1}{\partial x^2 \partial t} = \text{linear} + \text{nonlinear} + \text{dispersive}_{1,2,\text{topo}} \quad (5.119)$$

5.7.3 Summary of Equations

The final set of nondimensional equations we actually solve numerically in *Chapter 6* can be summarized as follows:

$$a \frac{\partial \bar{u}_1}{\partial t} + b \frac{\partial^2 \bar{u}_1}{\partial x \partial t} + c \frac{\partial^3 \bar{u}_1}{\partial x^2 \partial t} = \text{linear} + \text{nonlinear} + \text{dispersive}_{1,2,\text{topo}}, \quad (5.119)$$

$$\bar{u}_2 = \frac{Uh - \eta_1 \bar{u}_1}{\eta_2}, \quad (5.60)$$

$$\frac{\partial \bar{v}_1}{\partial t} = -\mu \bar{u}_1 - \bar{u}_1 \frac{\partial \bar{v}_1}{\partial x} + O(\delta^2), \quad (5.65)$$

$$\frac{\partial \bar{v}_2}{\partial t} = -\mu \bar{u}_2 - \bar{u}_2 \frac{\partial \bar{v}_2}{\partial x} + O(\delta^2), \quad (5.66)$$

$$\frac{\partial \zeta}{\partial t} = (h_1 - \zeta) \frac{\partial \bar{u}_1}{\partial x} - \bar{u}_1 \frac{\partial \zeta}{\partial x}. \quad (5.38)$$

with

$$a(\zeta, h) = \left[1 + \delta_2 \left[\left(\eta_2 \frac{\partial h}{\partial x} - \eta_2 \frac{\partial \zeta}{\partial x} \right) \frac{\partial(\eta_1/\eta_2)}{\partial x} - \frac{\eta_2^2}{3} \frac{\partial^2(\eta_1/\eta_2)}{\partial x^2} + \frac{\eta_1}{\eta_2} \left(\frac{\eta_2}{2} \frac{\partial^2 h}{\partial x^2} + \frac{\partial \zeta}{\partial x} \frac{\partial h}{\partial x} \right) \right] \right], \quad (5.115)$$

$$b(\zeta, h) = \left[\delta_1 \eta_1 \frac{\partial \zeta}{\partial x} + \delta_2 \left[\frac{\eta_1}{\eta_2} \left(\eta_2 \frac{\partial h}{\partial x} - \eta_2 \frac{\partial \zeta}{\partial x} \right) - \frac{2\eta_2^2}{3} \frac{\partial(\eta_1/\eta_2)}{\partial x} \right] \right], \quad (5.116)$$

$$c(\zeta, h) = \left[-\delta_1 \frac{\eta_1^2}{3} - \delta_2 \frac{\eta_1 \eta_2}{3} \right], \quad (5.117)$$

$$\begin{aligned} linear = \mu \bar{v}_1 + \frac{\partial \zeta}{\partial x} + \frac{1}{(1-h)} \left(h \frac{\partial U}{\partial t} + U^2 \frac{\partial h}{\partial x} + \bar{u}_2 \frac{\partial h}{\partial t} - \mu \left(\eta_1 \bar{v}_1 + \eta_2 \bar{v}_2 \right) \right. \\ \left. - \eta_1 \frac{\partial \zeta}{\partial x} \right), \end{aligned} \quad (5.95)$$

5. A GENERATION MODEL OF SOLITONS

$$nonlinear = -\bar{u}_1 \frac{\partial \bar{u}_1}{\partial x} + \frac{1}{(1-h)} \left((\bar{u}_1 - \bar{u}_2) \frac{\partial \zeta}{\partial t} + \bar{u}_1 \eta_1 \frac{\partial \bar{u}_1}{\partial x} + \bar{u}_2 \eta_2 \frac{\partial \bar{u}_2}{\partial x} \right), \quad (5.96)$$

$$dispersive_1 = \delta_1 \left[-\eta_1 \frac{\partial \zeta}{\partial x} \left[\bar{u}_1 \frac{\partial^2 \bar{u}_1}{\partial x^2} - \left(\frac{\partial \bar{u}_1}{\partial x} \right)^2 \right] + \frac{\eta_1^2}{3} \left[\bar{u}_1 \frac{\partial^3 \bar{u}_1}{\partial x^3} - \frac{\partial \bar{u}_1}{\partial x} \frac{\partial^2 \bar{u}_1}{\partial x^2} \right] \right], \quad (5.100)$$

$$dispersive_2 = \delta_2 \left[-\eta_2 \frac{\partial \zeta}{\partial x} \left[\bar{u}_2 \frac{\partial^2 \bar{u}_2}{\partial x^2} - \left(\frac{\partial \bar{u}_2}{\partial x} \right)^2 \right] - \frac{\eta_2^2}{3} \left[\bar{u}_2 \frac{\partial^3 \bar{u}_2}{\partial x^3} - \frac{\partial \bar{u}_2}{\partial x} \frac{\partial^2 \bar{u}_2}{\partial x^2} \right] \right], \quad (5.103)$$

$$dispersive_{topo} = \delta_2 \left[\bar{u}_2 \frac{\partial h}{\partial x} \left[\eta_2 \frac{\partial^2 \bar{u}_2}{\partial x^2} + \frac{\partial \zeta}{\partial x} \frac{\partial \bar{u}_2}{\partial x} \right] + \frac{\eta_2}{2} \left[\frac{\partial U}{\partial t} \frac{\partial^2 h}{\partial x^2} + U^2 \frac{\partial^3 h}{\partial x^3} \right] \right. \\ \left. + 2U \frac{\partial \bar{u}_2}{\partial x} \frac{\partial^2 h}{\partial x^2} + 2\bar{u}_2 U \frac{\partial^3 h}{\partial x^3} + 3\bar{u}_2 \frac{\partial \bar{u}_2}{\partial x} \frac{\partial^2 h}{\partial x^2} + \bar{u}_2^2 \frac{\partial^3 h}{\partial x^3} \right] + \frac{\partial \zeta}{\partial x} \left[\frac{\partial U}{\partial t} \frac{\partial h}{\partial x} + U^2 \frac{\partial^2 h}{\partial x^2} \right. \\ \left. + 2\bar{u}_2 U \frac{\partial^2 h}{\partial x^2} + \bar{u}_2^2 \frac{\partial^2 h}{\partial x^2} \right], \quad (5.109)$$

Chapter 6

Numerical Experiments on Solitons¹

6.1 Outline

The main goal of this chapter is to present various numerical experiments which demonstrate the capability of the model we have derived on reproducing two of the more distinguishable properties attributed to a fully nonlinear set of equations: the generation of ‘table-top’ solitons when approaching the theoretical maximum amplitude given appropriate initial conditions; and, 2) the appearance of nonlinearities under a configuration in which the two-fluid system consists of two layers of equal thickness.

In *Section 6.2* we deal with key aspects about the configuration of the numerical experiments before starting the presentation of the main results. In *Subsection 6.2.1* we recall to the reader the main components of the two-fluid layer system which configure the model. Discussion on the criteria to choose the resolution of the space-time grid needed for solving numerically the model is addressed in *Subsection 6.2.2*. As we have already described, the ‘tide-topography’ interaction is introduced in the model through a moving topography and a fluid initially at rest; unlike the original problem in which

¹Aguiar-González B., Gerkema T. A Model for the Generation of Strongly Nonlinear, Weakly Nonhydrostatic Interfacial Waves. *In Preparation to be Submitted to an International refereed Journal*

6. NUMERICAL EXPERIMENTS ON SOLITONS

a barotropic tidal flow over topography generates internal tides. This situation leads to the question of whether the model can be realistically considered equivalent to oceanic conditions. Consequently, we use in *Subsection 6.2.3* the generation model of weakly nonlinear weakly nonhydrostatic solitons derived in Gerkema (1996), which works with tidal motion, as a benchmark for testing our fully nonlinear weakly nonhydrostatic generation model of solitons, which works with moving topography. Next, we summarize in *Subsection 6.2.4* the main parameters we set for the numerical experiments shown throughout the chapter.

Firstly we present some simulations on the generation of the linear hydrostatic internal tides to test the model in absence of nonlinearities and nonhydrostatic effects (*Section 6.3*). Subsequently, we move forward and include the latter effects in the simulations focusing on two special cases. On one hand, we show in *Section 6.4.1* the generation of strongly nonlinear solitons approaching its theoretical limiting amplitude and hence evolving to large-amplitude flat ‘table-top’ solitons. On the other hand, we deal with two layers of equal thickness and nonlinearities in *Section 6.4.2*. Conclusions are addressed in *Section 6.5*.

6.2 Configuration of the Numerical Experiments

6.2.1 The Two-Fluid Layer System

A general diagram of the two-fluid layer system is shown in Figure 6.1. We assume that the upper and lower layer consists of incompressible, inviscid, homogeneous fluids of density ρ_1 and ρ_2 , and have a thickness of h_1 and h_2 , respectively. The rest level of the interface is located at $z = 0$, the upward direction of the z -axis is positive. Here, η_i represents the thickness of the layer (depending on the interfacial displacement ζ). Furthermore, the upper surface is covered by a rigid lid.

The system is supposed to be uniform in the y (i. e. *transverse*) direction; the topography is consequently assumed to be infinite in that direction. We mimick the ‘tide-topography’interaction which generates the internal tide in the system with a moving bottom which oscillates horizontally. However, in order to facilitate the interpretation of the simulations, we transformed the

6.2 Configuration of the Numerical Experiments

results with moving topography to the frame in which the topography is at rest and located symmetrically with respect to the center of the x -axis.

In all experiments fluid starts moving to the right at $t = 0$ (i. e. topography moving to the left). The waves are generated near the origin in x -axis due to the ‘tide-topography’ interaction; on the negative (positive) x -axis, waves travel to the left (right). As the forcing enters in the simulation asymmetrically with fluid at rest moving to the right, it is expected that wave packets in the front appear rather different when comparing both sides (negative vs. positive x -domain). These fronts are the transients, which are influenced by the way the experiment is started. Consequently, the steady solution at both sides of the x -axis is reached after several tidal periods have passed away. For this reason, we start the observation of all our results when the signal has become periodic (at least after 6 tidal periods) to avoid transient effects.

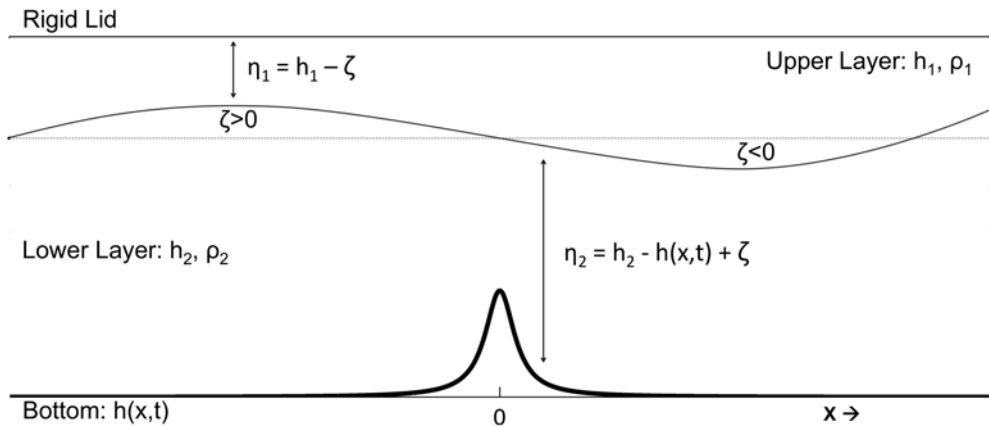


Figure 6.1: Configuration of the Numerical Experiments - A general diagram of the two-fluid layer system.

For the numerical experiments we present throughout this chapter we have defined the topography¹ as

$$h(x, t) = \frac{b_1}{1 + (x/b_2)^2} \quad (6.1)$$

¹The topography is set analytically to ensure an unstaggered domain for second and third derivatives of $h(x, t)$. Nevertheless, other analytical functions may be also used depending on the desired topography.

6. NUMERICAL EXPERIMENTS ON SOLITONS

with x being the grid positions in space; and, b_1 and b_2 being the parameters which set the height and width of a symmetric sill, respectively. Also, the topographic obstacle (ridge, sill, ...) is always centred in the x -axis and the length of the x -domain is chosen to be large enough to prevent that generated waves reach the boundaries.

It is worth while to recall that the oscillation of the topography is included within the model (on page 102) as $h = h(X)$ with $X(x, t) = x - a \cos t$ with a being an arbitrary constant.

6.2.2 Setting the Space-Time Grid

The choice of the steps Δt , Δx introduced in *Chapter 5 (Section 5.7)* was based on two main requirements. Firstly, the resolution in x (Δx) must be sufficiently fine to resolve third-derivative terms and ensure that any short, solitary-like waves are properly resolved. Nevertheless, dealing with equivalent equations to Miyata (1988) and Choi and Camassa (1999), as we do in our model, Kelvin-Helmholtz instabilities are not filtered out. In this regard, Jo and Choi (2002) found that solitary waves of sufficient amplitude could be unstable at high wave numbers to Kelvin-Helmholtz instability. Thus, if the grid resolution is too fine, unstable short waves will emerge near the wave crest and ultimately overwhelm the calculations and explode numerically (Jo and Choi, 2002; Helfrich and Melville, 2006; Helfrich and Grimshaw, 2008). In some cases, the instability can be controlled by filtering out wavenumbers above a threshold (W. Choi 2007, personal communication cited in Helfrich and Grimshaw (2008)). For our numerical experiments we consider a Δx course enough to prevent the problem. A second condition follows from the requirement of stability. Then, for a given spatial step one may take the Courant-Friedrichs-Lewy condition for the linearized equations as an indication of the required time step. The criterion implies that $\Delta x/\Delta t$ should be larger than the phase speed of the wave; taking special care where the advection by the barotropic tidal flow (here mimicked with the moving topography) should be added to the phase speed to apply the criterion properly (Gerkema, 1994).

For the simulations we present, it was not needed to filter out wavenumbers above a threshold to control Kelvin-Helmholtz instabilities as we designed the space-time grid to avoid this problem following previous conditions. However, in some cases, specially in the simulations where the forcing was fairly strong,

6.2 Configuration of the Numerical Experiments

an additional trick was needed to retain stability around the generation area¹ (Gerkema, 1994). In those cases averages were taken in the vicinity of the top of the ridge (around the steepest part of the topography), where the instabilities arised. At one particular point (x_j, t_n) in space-time, new values of \bar{u}_i , \bar{v}_i and ζ were calculated by taking the average of the old values at x_{j-1} , x_j and x_{j+1} , and subsequently in time between t_n and t_{n-1} . The disturbance provoked by this procedure was tested and found to be a minor effect only, as it was only applied over the closest region to the top of the topography.

6.2.3 Basic Tests

A Galilean (or inertial) reference frame is a frame with constant and rectilinear motion with respect to one another. Consequently, an inertial frame of reference describes time and space homogenously and isotropically with no time dependance. Hence, observations made in one inertial frame can be converted to observations in another inertial frame by a simple transformation (the so-called Galilean transformation), as physical laws follows the same behaviour in all inertial frames.

Our moving topography is not an inertial frame as it does not move with constant motion but accelerated. In theses cases, observations made in a non-inertial frame cannot be transformed directly to observations made in an inertial frame. Physics will vary depending on the acceleration of the non-inertial frame with respect to the inertial frame and, consequently, regular physics forces will need to be supplemented by ficticious forces.

In our case, this situation leads to the question of whether a moving topography can be realistically considered equivalent to a barotropic tidal flow over topography. This comparison is not straightforward and requires further research before the model can be applied to the simulation of oceanic observations. The main area of attention is the top of the topography from where the waves emerge and where our non-inertial frame (the moving topography) is accelerated. Far away from this point, nonlinear and nonhydrostatic effects acting over the internal tide are presumably equivalent as the bottom there does not move and is flat.

¹This was needed to be applied only in the case for the generation of ‘table-top’ solitons in *Section 6.4.1*.

6. NUMERICAL EXPERIMENTS ON SOLITONS

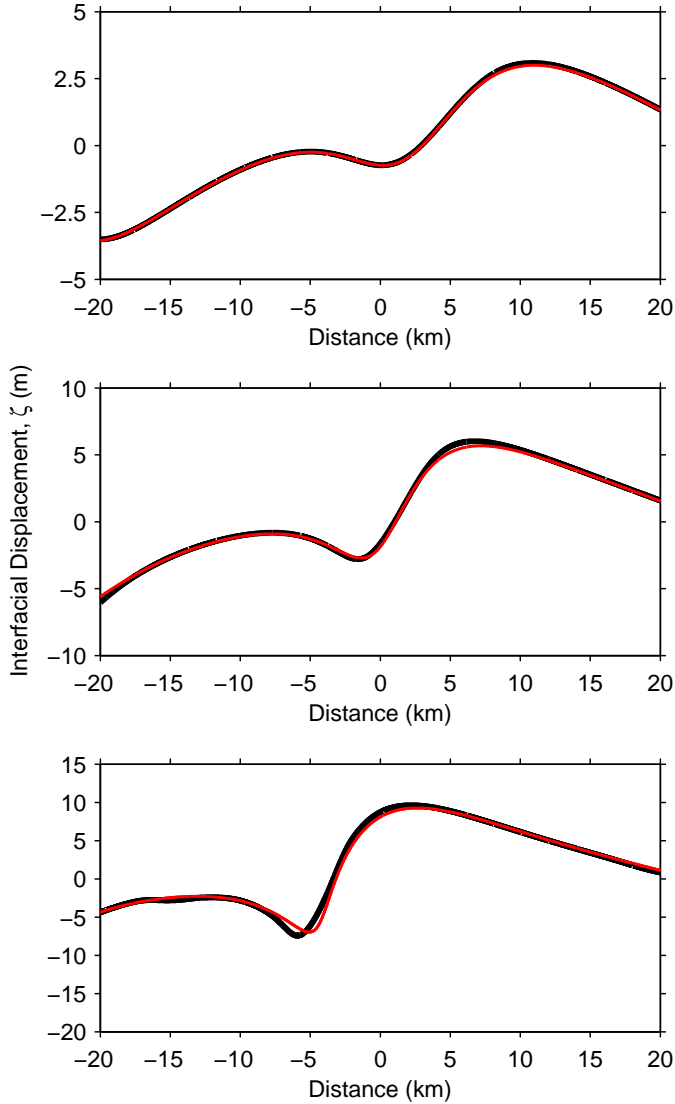


Figure 6.2: Moving Topography vs. Tidal Motion - Black lines is the model derived in this thesis and grey line is the model derived in Gerkema (1996). The upper and lower layer thickness are $h_1 = 30$ m and $h_2 = 70$ m, respectively. The tidal flow is 20 cm s^{-1} in (a); 40 cm s^{-1} in (b); and, 80 cm s^{-1} in (c).

Here we use the generation model of weakly nonlinear weakly nonhydrostatic solitons derived in Gerkema (1996), which works with tidal motion, as

6.2 Configuration of the Numerical Experiments

a benchmark for testing our fully nonlinear weakly nonhydrostatic generation model of solitons, which works with moving topography. The comparison is obviously not straightforward as both models are of different nature, weakly and strongly nonlinear effects already make them different. For this reason we focus only on comparing the response of the model over the top of the topography, where the fictitious forces may become important and the internal tide is generated. Any differences which may appear far away from the generation area are indeed expected due to different nonlinear effects acting in every model. Also for this reason we present the results centred only over this area and under weakly nonlinear settings in order to make them more comparable (the matter here is to test that the height of the topography is not a problem).

For clarity on the results we use for this comparison the same configuration¹ we use for the numerical experiments that we will present throughout the chapter. Thus, Figure 6.2 suggests that an internal tide generated with a relatively small moving topography is equivalent to that generated via a tidal flow over topography.

6.2.4 Set of Experiments

The model operates with equations in nondimensional form; however, we present results from the numerical experiments after dimensionalisation.

To organize the presentation of the numerical experiments, we chose a configuration which we keep fixed for most of the simulations. For simplicity on the magnitudes, we set a total water depth of 100 m ($h = 100$) with the parameters for the thickness of the upper and lower layers being $h_1 = 30$ and $h_2 = 70$ (the upper layer being thinner than the lower layer).

Regarding the topography, the height of the sill was set at 40 m with decreasing amplitude covering mainly the interval from -10 km to 10 km over the x-axis, thus $b_1 = 40$ and $b_2 = 10000$. Furthermore, the horizontal oscillation of the moving topography (forcing) is always of semidiurnal frequency. The strength of the stratification at the interface was set by a value of $g' = 0.01 \text{ m s}^{-2}$. For this configuration, the small parameter δ retaining weak nonhydrostatic effects keeps the same value of $\delta = 1.67\text{e-}06$.

¹See following subsection for details.

6. NUMERICAL EXPERIMENTS ON SOLITONS

The space-time grid is solved in all cases with $\Lambda x = 20$ m and $\Lambda t = \sim 4.5$ s. Nevertheless, for numerical experiments in *Section 6.3* (linear hydrostatic simulations) and *Section 6.4.2* (simulation with two layers of equal thickness), we use the same Λx , but a longer time step, $\Lambda t = \sim 10$ s.

In case any of the above mentioned values change in a simulation for a specific purpose, it will be mentioned in the text.

6.3 Generation of the Linear Hydrostatic Internal Tide

We start with the generation of the linear hydrostatic internal tide. With this aim, we linearize model equations derived throughout *Chapter 5* (and summarized in *Section 5.7.3*), which then read

$$\frac{\partial \bar{u}_1}{\partial t} = \mu \bar{v}_1 + \frac{\partial \zeta}{\partial x} + \frac{1}{(1-h)} \left(h \frac{\partial U}{\partial t} + U^2 \frac{\partial h}{\partial x} + \bar{u}_2 \frac{\partial h}{\partial t} - \mu \left(\eta_1 \bar{v}_1 + \eta_2 \bar{v}_2 \right) - h_1 \frac{\partial \zeta}{\partial x} \right), \quad (6.2)$$

$$\bar{u}_2 = \frac{Uh - \eta_1 \bar{u}_1}{\eta_2}, \quad (5.60)$$

$$\frac{\partial \bar{v}_1}{\partial t} = -\mu \bar{u}_1, \quad (6.3)$$

$$\frac{\partial \bar{v}_2}{\partial t} = -\mu \bar{u}_2, \quad (6.4)$$

$$\frac{\partial \zeta}{\partial t} = h_1 \frac{\partial \bar{u}_1}{\partial x}. \quad (6.5)$$

6.3 Generation of the Linear Hydrostatic Internal Tide

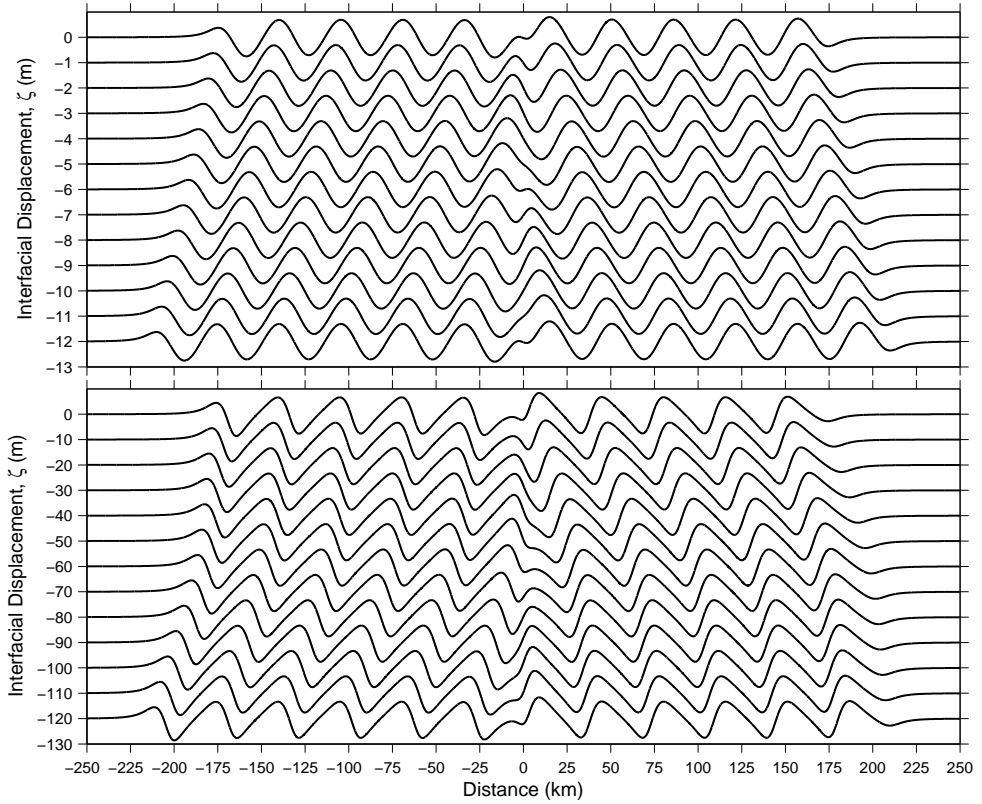


Figure 6.3: Generation of the Linear Hydrostatic Internal Tide (Rotationless case, $\mu = 0$) - Time evolution of the linear, hydrostatic internal tide during the sixth tidal period. Influence of the tidal advection is shown in (top) with weak ‘tidal flow’ (5 cm s^{-1}); and (bottom) with fairly strong ‘tidal flow’ (50 cm s^{-1}), where the wave is no longer sinusoidal (‘quasi-nonlinear’ case) because of the higher harmonics. Time evolves from the highest profiles downward.

First we consider the rotationless case ($\mu = 0$), so that there is no transverse velocity component either. Consequently, Eq. (6.3) and (6.4) drop as well as terms which involve Coriolis effects. Figure 6.3 presents two cases of a linear, hydrostatic internal tide after 6 tidal periods have passed away. The waves are generated over the topography, centred in the origin of the x -axis, and subsequently travel away to the left (negative x -axis) and to the right (x -axis) from the topography. The upper part of the figure shows ‘tidal flow’ moving to the left (topography moving to the right); the lower half shows ‘tidal flow’ moving to the right (topography moving to the left). The lapse of time between

6. NUMERICAL EXPERIMENTS ON SOLITONS

successive representations is $\frac{1}{12}$ of tidal period.

The ‘tidal flow’ in Figure 6.3 (top) is weak, 5 cm s^{-1} , and consequently internal tides arise as sinusoidal waves. On the contrary, in Figure 6.3 (bottom) the ‘tidal flow’ is strong, 50 cm s^{-1} ; hence, the barotropic tidal advection becomes significant as observed and higher harmonics give rise to ‘quasi-nonlinear’ waves (Maas and Zimmerman, 1989).

If we now include the effects of the Earth’s rotation on the generation of the linear hydrostatic internal tide, we need to solve the complete set of equations above. We present two cases: at mid ($\phi = 45^\circ$, $\mu = 4.61$) and high latitudes ($\phi = 90^\circ$, $\mu = 6.52$) for testing weak and strong Earth’s rotation effects, respectively.

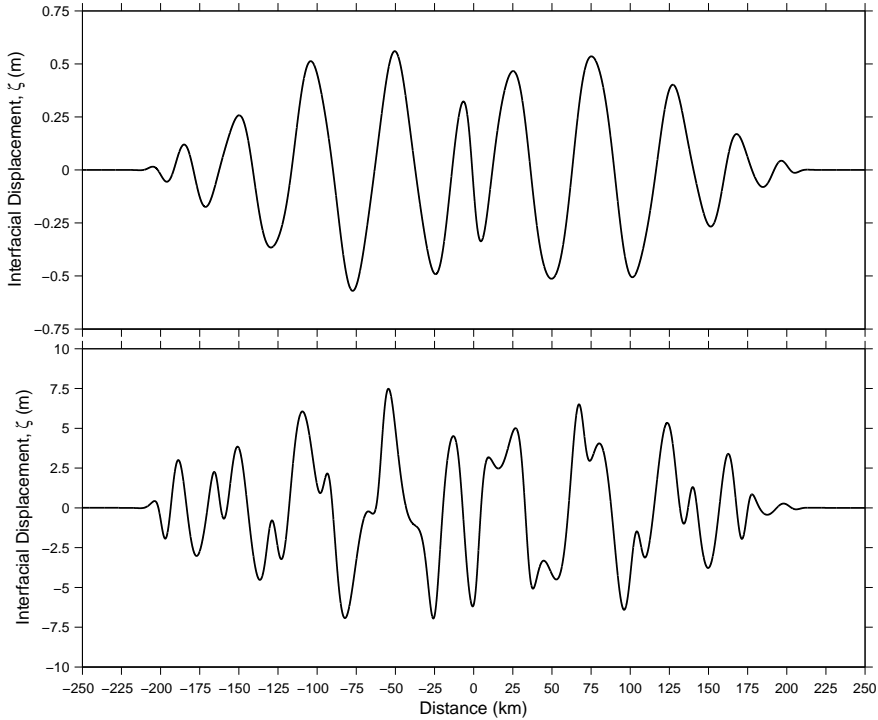


Figure 6.4: Generation of the Linear Hydrostatic Internal Tide (at Mid Latitudes: $\phi = 45^\circ$, $\mu = 4.61$) - The linear, hydrostatic internal tide during the sixth tidal period. Influence of the Earth’s rotation is shown in (top) over a weak ‘tidal flow’ (5 cm s^{-1}); and (bottom) over a strong ‘tidal flow’ (50 cm s^{-1}).

6.3 Generation of the Linear Hydrostatic Internal Tide

In Figure 6.4 (top) we present a simulation at mid-latitudes. There we observe that at the front of the wave train, the amplitude of the wave is much smaller than the others. This is because rotation decreases the group velocity, and hence the velocity at which energy is transported (Gerkema, 1994). However, as the presence of higher harmonics is negligible when ‘tidal flow’ is weak, the wave pattern of the internal tides is almost periodic and dispersive effects due to rotation do not manifest themselves since only one frequency is involved. On the other hand, in Figure 6.4 (bottom) the ‘tidal flow’ is strong and gives rise to higher harmonics. For this reason, waves in this case appear very irregular since due to Coriolis they all disperse and travel at different phase speeds.

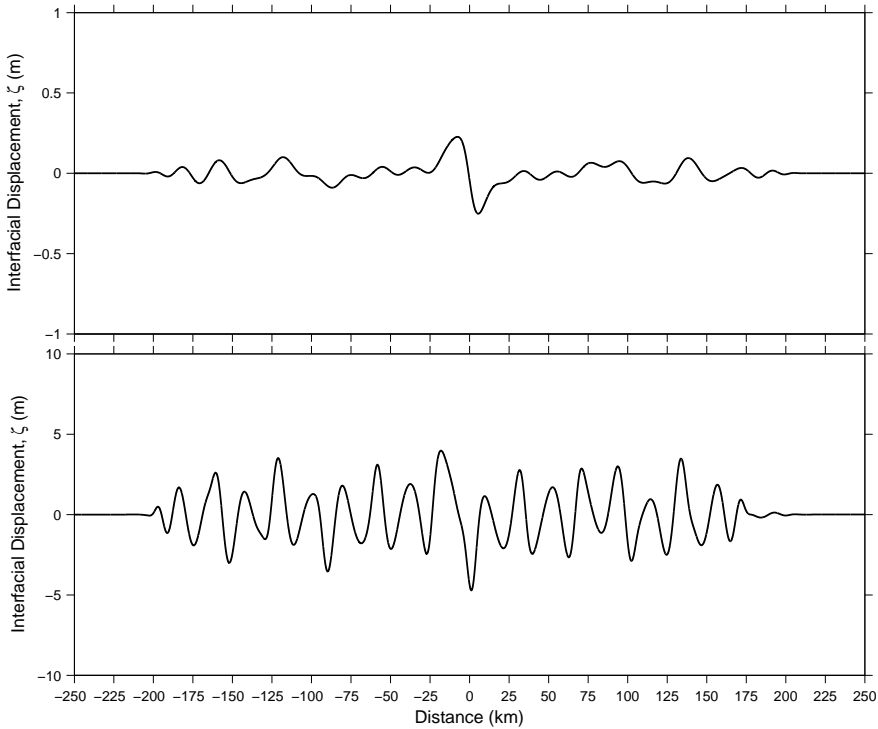


Figure 6.5: Generation of the Linear Hydrostatic Internal Tide (at High Latitudes: $\phi = 90^\circ$, $\mu = 6.52$) - The linear, hydrostatic internal tide during the sixth tidal period. Influence of the Earth’s rotation is shown in (top) over a weak ‘tidal flow’ (5 cm s^{-1}); and (bottom) over a strong ‘tidal flow’ (50 cm s^{-1}).

6. NUMERICAL EXPERIMENTS ON SOLITONS

In Figure 6.5 we increase the effects of Coriolis dispersion moving our two-fluid system to high latitudes. In the (top) simulation, the linear hydrostatic internal tide cannot propagate away from the generation point (Gerkema, 1994) and we can only appreciate tiny irregular waves doing so (note the change in vertical scale). They are due to the presence of small higher harmonics together with the basic linear hydrostatic internal tide. In the limit case of an infinitesimal ‘tidal flow’, higher harmonics are completely absent and no wave signal can propagate. In Figure 6.5 (bottom) the ‘tidal flow’ is again strong but Coriolis dispersion too; furthermore, the induced semidiurnal barotropic flow is subinertial at high latitudes (90°) so that only higher harmonics can propagate.

6.4 Generation of Strongly Nonlinear Solitons

In this section we solve numerically the full set of equations derived in previous chapter and summarized in *Section 5.7.3*. The main target is now to show the generation and evolution of strongly nonlinear solitons under critical conditions of strongly nonlinearity [as has been observed in the ocean, e. g. Stanton and Ostrovsky (1998)] in which classical KdV-type theories are not longer applicable due to quadratic nonlinearity effects vanishes.

Firstly we focus on the generation of ‘table-top’ solitons using exactly the same configuration as in previous simulations but now increasing the forcing to a ‘tidal flow’ of 80 cm s^{-1} . Secondly we explore the generation of solitons at the critical configuration of a two-fluid system in which both layers are of equal thickness. Again we force the internal tides with a ‘tidal flow’ of 80 cm s^{-1} .

6.4.1 ‘Table-Top’ Solitons (Rotationless Test, $\mu = 0$)

Figures 6.6 and 6.7 present the strongly nonlinear disintegration of an internal tide into ‘table-top’ solitons. On one hand, Figure 6.6 shows the generation of a long internal tide of about 30 km wavelength which, at a first stage, splits up into two different groups of rank-ordered solitons: a train of depressions on the leading edge; and a train of elevations, after the former packet, with initially smaller amplitudes (Figure 6.6a). As the tidal period passes, we observe that in the same internal tide as previous the largest elevations have now reached the smaller depressions in the train and three leading solitons at

6.4 Generation of Strongly Nonlinear Solitons

the front present almost equal amplitudes around 20 m at the end of the 8th tidal period (Figure 6.6b).

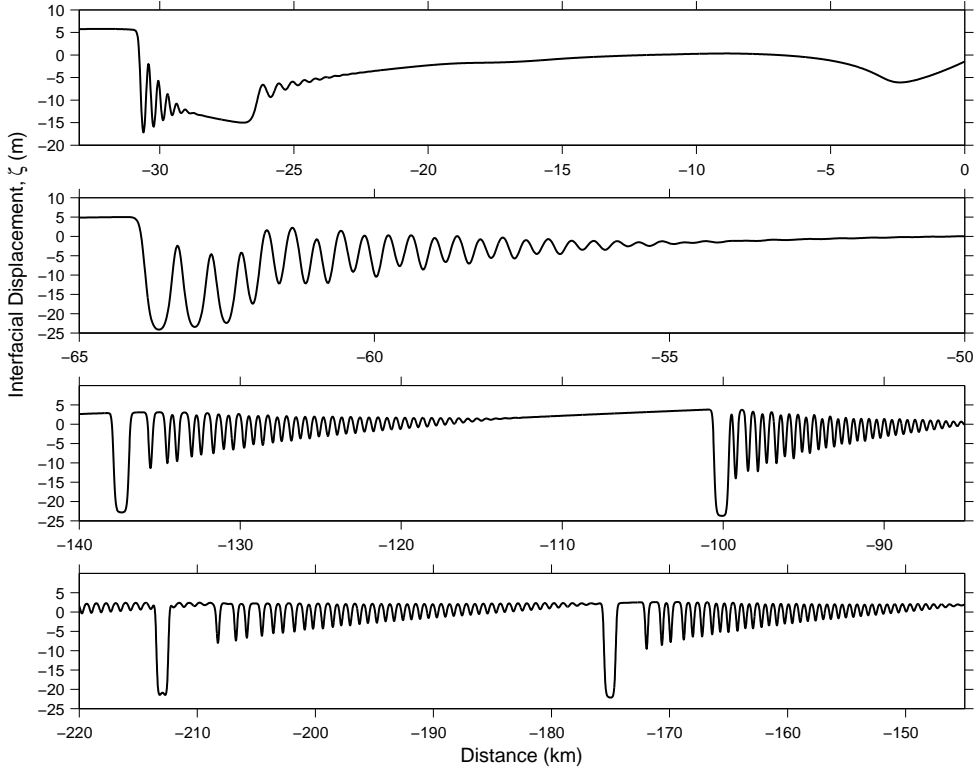


Figure 6.6: Generation of ‘Table-Top’ Solitons - Strongly nonlinear disintegration of the internal tide. (a) Generation of an internal tide at the beginning of the 8th tidal period. (b) Same disintegrated internal tide as in (a) but at the end of the 8th tidal period. (c) and (d) Disintegrated internal tides propagating away from the generation area. The results correspond to a simulation of 8 tidal periods forced with a ‘tidal flow’ of 80 cm s^{-1} .

Previous wave packets of solitons propagating away the generation area are shown in Figures 6.6c, d corresponding to preceding disintegrated internal tides also at the end of the 8th tidal period. The ‘table-top’ soliton observed at the leading edge of every preceding internal tide emerged in all cases from the first of the three solitons described previously for the front of an earlier stage of disintegration of the internal tide (Figure 6.6b). Once that soliton at the front starts to grow up and reach its maximum amplitude, it also starts to broaden

6. NUMERICAL EXPERIMENTS ON SOLITONS

in comparison with subsequent solitons of smaller amplitude. The ‘table-top’ shape finally arises when the soliton has reached its maximum amplitude, as predicted by soliton wave theory.

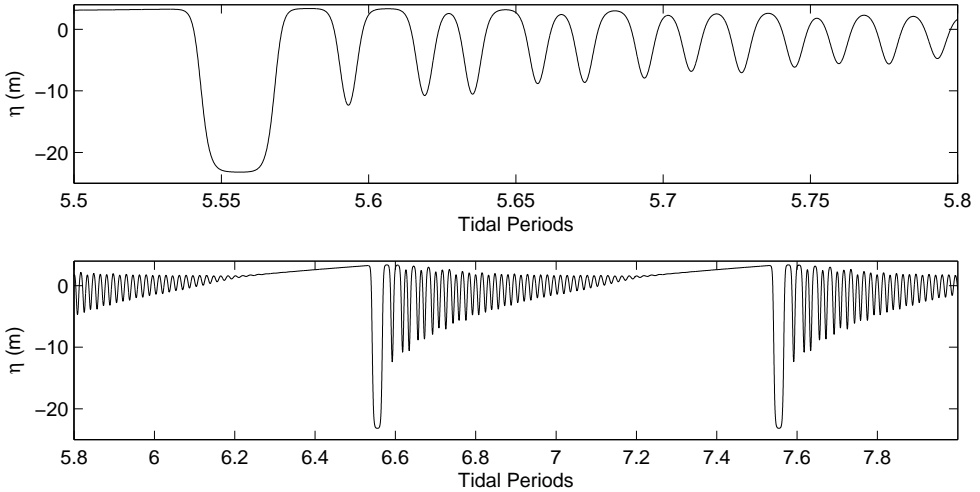


Figure 6.7: Time evolution of ‘Table-Top’ Solitons - (top) Time evolution of strongly nonlinear solitons. (bottom) Continuation of the time evolution in (top). The results correspond to a simulation of 8 tidal periods forced with a ‘tidal flow’ of 80 cm s^{-1} . Waves are recorded at -115 km from the generation point (top of the sill). The x -axis is here tidal periods.

6.4.2 Solitons with Two Layers of Equal Thickness (Rotationless Test, $\mu = 0$)

We change the common configuration of previous numerical experiments to a set up in which the two layers are of equal thickness ($h_1 = h_2 = 50 \text{ m}$) and hence quadratic nonlinearities from classical KdV approach vanishes. Under this situation, cubic nonlinearities held in fully nonlinear models becomes critical on producing internal solitons. In this regard, Figures 6.8 and 6.9 show that the model is capable of reproducing the disintegration of the internal tide into short-like solitary waves in a configuration of two layers of equal thickness.

The result is a sequence of disintegrated internal tides, of about 15 m amplitude and $\sim 40 \text{ km}$ wavelength, which every one splits up into two different packets of rank-ordered solitons: elevations of up to 5 m amplitude all along

the crest of the main body of the internal tide; and depressions along its sine (at this stage the largest one is observed to be overpassing the small elevations of the train of waves in the crest).

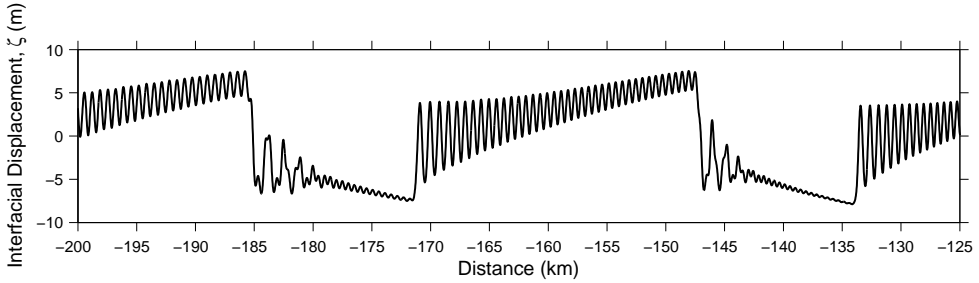


Figure 6.8: Generation of Solitons between Two Layers of Equal Thickness - Nonlinear disintegration of the internal tides propagating along the interface of two layers of equal thickness ($h_1 = h_2 = 50$). The waves respond to a simulation of 10 tidal periods forced with a fairly strong ‘tidal flow’ (80 cm s^{-1}).

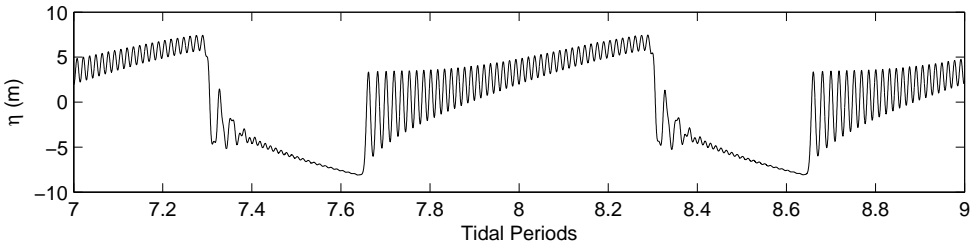


Figure 6.9: Time evolution of Solitons between Two Layers of Equal Thickness - Time evolution of solitons propagating along the interface of two layers of equal thickness ($h_1 = h_2 = 50$). The waves respond to a simulation of 10 tidal periods forced with a fairly strong ‘tidal flow’ (80 cm s^{-1}). Waves are recorded at -115 km from the generation point (top of the sill). The x -axis is here tidal periods.

6.4.3 Strongly Nonlinear Solitons dispersed by the Effects of the Earth’s Rotation

Figure 6.10 presents a simulation of strongly nonlinear disintegration of an internal tide at mid-latitudes ($\phi = 45^\circ$, $\mu = 4.61$) recorded at -50 km (top) and 50 km (bottom) from the generation point (top of the sill). After 10

6. NUMERICAL EXPERIMENTS ON SOLITONS

tidal periods have passed away, waves at a fixed position become periodic in time and is expected to find a symmetric nonlinear internal tide dispersed by the effects of the Earth's rotation at both sides of the generation area. However, though the influence of rotation (Coriolis dispersion) is noticeable as we observe solitary waves disperse, the result is asymmetric.

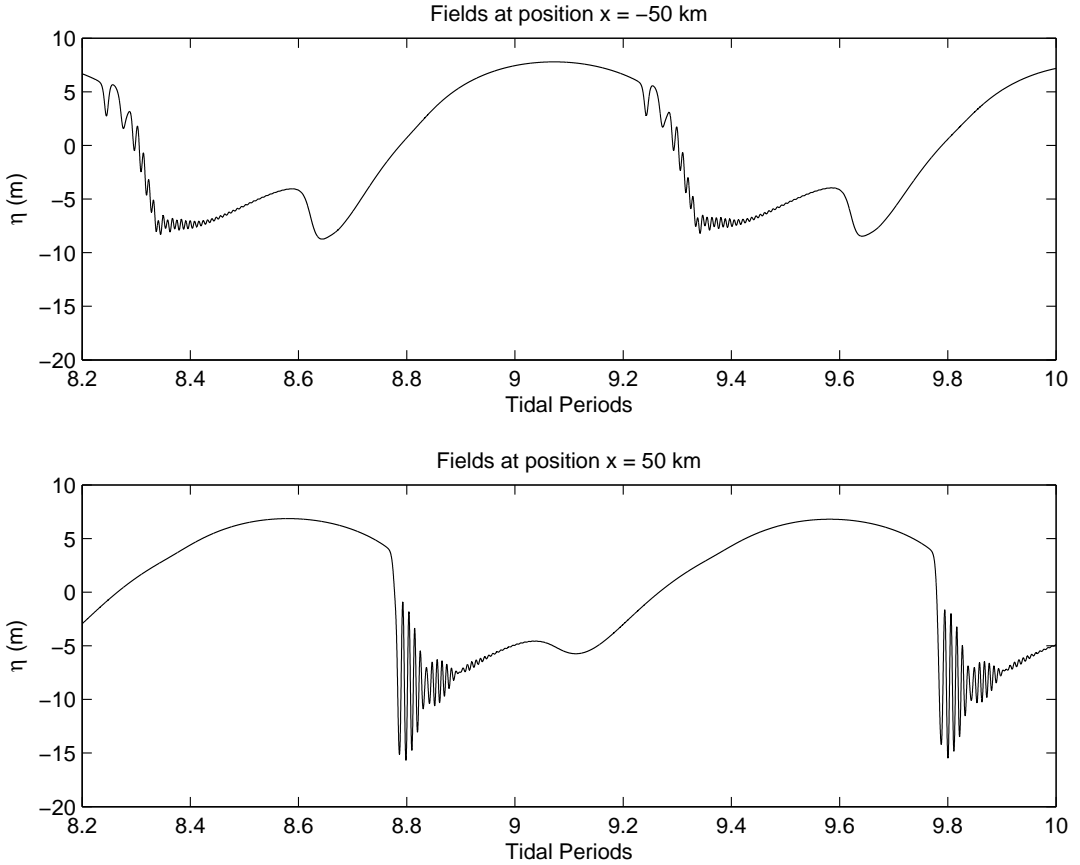


Figure 6.10: Time evolution of Strongly Nonlinear Solitons dispersed by the Effects of the Earth's Rotation (at Mid Latitudes: $\phi = 45^\circ$, $\mu = 4.61$) - (top) Time evolution of strongly nonlinear solitons recorded at -115 km from the generation point (top of the sill). (bottom) Time evolution of strongly nonlinear solitons recorded at -115 km from the generation point (top of the sill). The results correspond to a simulation of 10 tidal periods forced with a 'tidal flow' of 80 cm s^{-1} . The x -axis is here tidal periods.

This situation responds to the fact that the model is initialised with an asymmetric forcing, i. e. fluid at rest and topography moving to the right. This generates an asymmetry in the response of the model which in a rotating simulation is conserved in time over the top of the topography (conservation of potential vorticity) and is advected to leftward/rightward propagating waves; hence, the appearance in the results of asymmetric strongly nonlinear internal tides dispersed by Coriolis. This is supported when initialising the model with the fluid at rest and the topography moving to the left, the result we have obtained is equally asymmetric producing a mirrored image to Figure 6.10 (the mirrored image is not shown here). This demonstrates that the asymmetry really stems from the initial conditions and does not lie in our model equations as such, which are symmetric with respect to left and right.

Obviously, this asymmetry becomes smaller when the initial ‘tidal flow’ is weak and therefore the generated asymmetry is small as well.

6.5 Conclusions

In the previous chapter we derived a new model including full nonlinearity, as in Choi & Canmassa (1999), but with the added features of Coriolis dispersion, topography, and a forcing mechanism of internal tides.

The results of this chapter validate the model as a useful tool for exploring and interpreting the conditions under which full nonlinearity effects become important for soliton generation and a fully nonlinear set of equations need to be considered to study the phenomenon. In particular, this is the case for table-top solitons and appearance of nonlinearity in a two-layer system with equal layer thickness.

Future work should extend these calculations to make a comparison with field observations.

6. NUMERICAL EXPERIMENTS ON SOLITONS

Chapter 7

Conclusions and Future Research

In this chapter the main conclusions and scientific contributions of the thesis are summarized. Additionally, we also suggest where further research in the future may benefit the understanding of the phenomena we are dealing here.

I Breeze-forced oscillations

- 1 Results from a rotary wavelet analysis indicate that diurnal wind forcing (sea-land breezes) in the Gulf of Cádiz and the Gulf of Valencia enhances clockwise current oscillations (breeze-forced motions) during spring-summer months, contributing greatly to the near-inertial energy budget and its seasonal variability. The diurnal-inertial current variance has been estimated to be an order of magnitude higher than estimated variance during winter months. These results support the role of breeze-forced oscillations on the generation and accumulation of near-inertial energy within the critical latitudes for diurnal-inertial resonance.
- 2 Results from a rotary wavelet analysis indicate that clockwise current oscillations in the Cape Peñas area are enhanced during summer months; however, the increase of inertial current variance is not as large as has been estimated for the Gulf of Cádiz and the Gulf of Valencia.

7. CONCLUSIONS AND FUTURE RESEARCH

This mainly responds to the Cape Peñas area is out of the critical latitudes for diurnal-inertial resonance.

- 3 An analysis on diapycnal mixing processes associated to breeze-forced oscillations, within the critical latitudes for resonance (Bay of Setúbal), shows evidence of an enhancement of diurnal-inertial energy available to promote vertical mixing in stratified and vertically sheared flows with subcritical values of Ri . This research also suggests that there may exist an internal control on the strength of the ocean response to breeze forcing due to the deepening and smoothing of the pycnocline driven by diapycnal mixing processes.
- 4 Future Research: Further analysis of time series data (currents, temperature and salinity) covering the total water depth in combination with co-located and simultaneous wind data would greatly benefit the understanding of how breeze-forced oscillations evolve in time and space, with special attention to the role that associated diapycnal mixing may be playing on the vertical structure of these forced-motions. In this regard, we also find that measurements of the turbulent kinetic energy dissipation rate with a coastal turbulence microprofiler would help on the assessment of the diapycnal mixing processes promoted by breeze-forced oscillations.

II Strongly nonlinear tide-generated internal solitons

- 1 A new model for the study of strongly nonlinear tide-generated internal solitons has been derived including full nonlinearity, Coriolis dispersion, topography, and a forcing mechanism of internal tides.
- 2 Numerical experiments validate the model as a useful tool for exploring and interpreting the conditions under which full nonlinearity effects become important for soliton generation and a fully nonlinear set of equations need to be considered to study the phenomenon. In particular, this is the case for table-top solitons and appearance of nonlinearity in a two-layer system with equal layer thickness.
- 3 Future Research: Further analysis should extend these calculations to make a comparison with field observations.

Chapter 8

Summary of the Thesis in Spanish

La presente Tesis Doctoral se centra en el estudio de dos fenómenos oceanográficos diferenciados. Por un lado se presenta un estudio observacional sobre oscilaciones forzadas por las brisas en el marco de las latitudes críticas para la resonancia diurno-inercial; y, por otro, se desarrolla un modelo teórico para la simulación de ondas internas solitarias de origen mareal fuertemente no lineales.

En la *Sección 8.1* presentamos el ‘estado del arte’ en el estudio de las oscilaciones forzadas por las brisas abarcando los aspectos fundamentales que caracterizan el fenómeno desde un punto de vista teórico y observacional. Así mismo se detalla al final de esta sección el planteamiento de objetivos y metodología aplicada.

Posteriormente, en la *Sección 8.2* presentamos el ‘estado del arte’ en el estudio de las ondas internas solitarias de origen mareal fuertemente no lineales. Anlogo al tratamiento anterior, nos ocupamos aquí de aquellos aspectos fundamentales que caracterizan el fenómeno desde un punto de vista teórico y observacional. Del mismo modo, al final de esta sección se detalla el planteamiento de objetivos y metodología aplicada.

8. SUMMARY OF THE THESIS IN SPANISH

Dentro del contexto descrito sobre el estudio de ambos fenómenos, las principales conclusiones y contribuciones que nacen del trabajo de investigación de esta Tesis Doctoral se resumen en la *Sección 8.3*. Conjuntamente se detallan aquellos aspectos que en trabajos futuros pueden beneficiar nuestro conocimiento sobre las oscilaciones forzadas por las brisas en las latitudes críticas para la resonancia diurno-inercial y sobre las ondas internas solitarias de origen mareal fuertemente no lineales.

8.1 Un Escenario Forzado por las Brisas

8.1.1 Brisas Tierra-Mar

Las brisas mar-tierra son vientos térmicos causados por el diferente calentamiento y enfriamiento de mar y tierra en ciclos diurnos. Este fenómeno se debe a que el océano tiene un calor específico más alto que la tierra, lo que implica que durante el día la tierra se calienta más que el océano, y por tanto el aire sobre él. El proceso se invierte durante la noche, cuando la tierra se enfría más que el océano. Esto da lugar a diferencias de presión tierra-mar que dan lugar a las brisas a lo largo de cerca de dos tercios de las costas de la Tierra (Simpson, 1994). Así tenemos el escenario en el que pueden tener lugar las brisas mar-tierra, es decir, a lo largo de las costas adyacentes a las grandes masas de agua: océanos, mares, lagos, ríos, ...

La descripción general de un evento de brisas mar-tierra puede comenzar con condiciones meteorológicas en calma donde las presiones superficiales sobre la tierra y el mar son inicialmente las mismas a lo largo de una costa recta. Después de la insolación durante todo el día, el aire de la tierra se calienta y comienza a expandirse. A continuación, una caída de la presión a niveles bajos en la atmósfera interior conduce a un gradiente de presión entre el aire sobre la tierra y el aire sobre el mar. Una vez que el gradiente de presión está actuando, se puede decir que la aparición de la brisa ha tenido lugar. Este gradiente de presión durante el día es la fuerza motriz de los vientos de superficie en tierra conocido como la brisa del mar.

Las figuras 8.1 y 8.2 muestran dos esquemas idealizados para un sistema de brisa. Estos esquemas detallan las brisas lago-tierra que actúan en los Grandes Lagos (América del Norte) sobre la base de valores documentados en la literatura (Moroz, 1967; Lyons, 1972; Lyons and Olsson, 1973; Keen and Lyons, 1978) y nos permiten explicar las principales dinámicas de las brisas mar-tierra. Sin embargo, aunque el espesor de la capa y los valores de velocidad se mantienen en números bastante similares, hay que hacer notar

8. SUMMARY OF THE THESIS IN SPANISH

que las escalas horizontales tienden a ser más largas en las áreas oceánicas en comparación con las de los sistemas de brisas lago-tierra (Simpson, 1994; Hyder et al., 2002; Rippeth et al., 2002; Simpson et al., 2002; Gille et al., 2003; Zhang et al., 2009; Hyder et al., 2011). Las escalas horizontales oceánicas pueden extenderse desde varias decenas a unos pocos cientos de kilómetros en paralelo a la costa, y a más de 100 km hacia el interior del océano (Simpson, 1994; Gille et al., 2003; Aparna et al., 2005; Gille et al., 2005; Zhang et al., 2009).

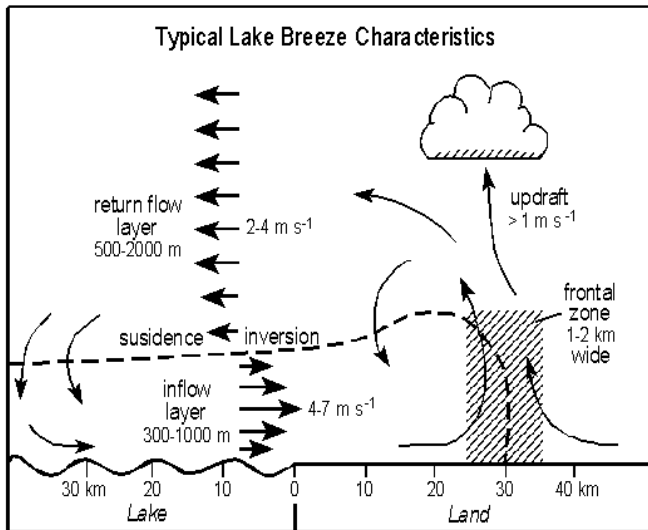


Figure 8.1: Diagrama de un régimen de brisas de lagos - Ilustración idealizada de una circulación de brisa típica en lago y su frente asociado. La línea discontinua representa el límite exterior de la capa de entrada. La zona frontal no se muestra a escala. [De Sills (1998)].

El espesor de la capa de brisa del mar puede llegar a una altura desde la superficie de entre 300 – 1000 m, dependiendo del sitio, con velocidades de viento típicos de alrededor de 4 – 7 m s⁻¹ (Figura 8.1). No obstante, también se ha descubierto que incluso puede superar los 10 m s⁻¹, en algunos casos (Pattiaratchi et al., 1997). Este aire frío y húmedo que fluye hacia el

8.1 Un Escenario Forzado por las Brisas

interior converge con el aire caliente y seco ascendente en la tierra caliente. El resultado es una zona frontal (1-2 km de ancho) en paralelo a la costa, donde tiende a formarse una línea de nubes tipo cúmulos. Esta formación de nubes es una evidencia del llamado ‘frente de brisa marina’. Por encima de las brisas marinas fluye hacia el interior un flujo de retorno menor de $2 - 4 \text{ m s}^{-1}$ que equilibra el sistema a una altura de $\sim 500 - 2000 \text{ m}$, y se hunde hacia las aguas costeras cerrando la célula de la brisa de mar.

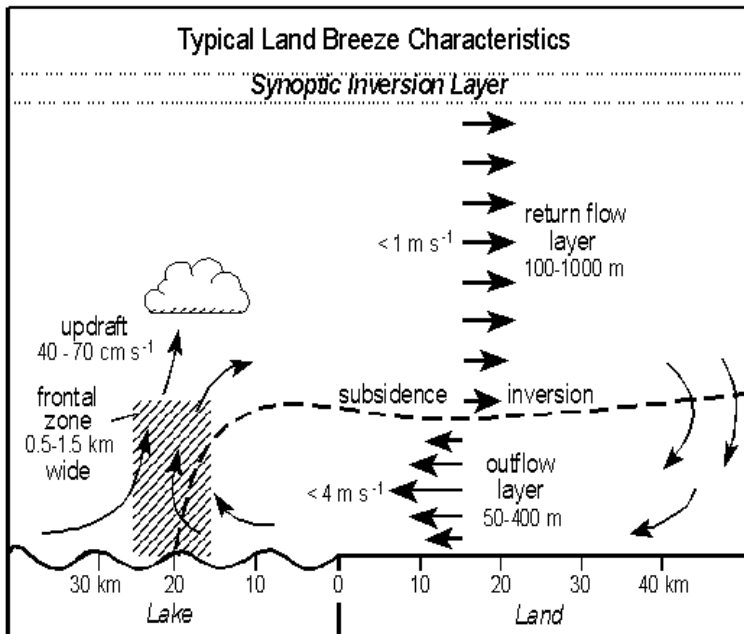


Figure 8.2: Diagrama de un régimen de brisa de tierra - Ilustración idealizada de una circulación de brisa de tierra típica y su frente asociado. La línea discontinua representa el límite exterior de la capa de salida. La zona frontal no se muestra a escala. [De Sills (1998)].

Durante la noche y la madrugada, la tierra se vuelve más fría que el mar y se revierte el proceso (Figura 8.2). A partir de ahí, el aire se contrae hacia el interior y desciende creando una zona de presión relativamente alta. El gradiente de presión consecuente entre tierra y mar impulsa la aparición de

8. SUMMARY OF THE THESIS IN SPANISH

los vientos hacia el mar conocidos como ‘brisas de tierra’ (Figura 8.2). El enfriamiento de la atmósfera sobre tierra se limita a una capa más superficial por la noche que la capa de calentamiento del aire durante el día. Esto hace que las brisas de tierra sean típicamente menos profundas y más débiles que las brisas de mar. Por lo tanto, el espesor de la capa de brisa de tierra presenta una menor altura que varía entre 50 – 400 m con velocidades de viento típicas de $<4 \text{ m s}^{-1}$. Estas brisas marinas se equilibran por un flujo de retorno ($<1 \text{ m s}^{-1}$) en dirección a la tierra, que se mueve a una altura de 100 – 1000 m y descende sobre la costa. En este caso, la zona de convergencia tiende a formar cúmulos sobre el mar, donde el aire fluye hacia arriba. Este límite se conoce como el ‘frente de brisa de tierra’.

Como era de esperar para los vientos inducidos térmicamente, la fuerza de los sistemas brisa mar-tierra es directamente proporcional al gradiente de temperatura entre el aire sobre la tierra y aire sobre el océano (Pielke and Segal, 1986). Por lo tanto, la frecuencia y la intensidad de los eventos brisa mar-tierra son más altos durante los períodos de fuerte calentamiento durante el día y tiempo de enfriamiento nocturno en ausencia de sistemas de viento a gran escala. En los climas tropicales y subtropicales, donde el gradiente de presión atmosférica entre la tierra y el mar tiende a ser estable a lo largo del año, se espera que los eventos de brisa ocurran en cualquier época del año. Por el contrario, en climas templados, las brisas mar-tierra a menudo han de superar vientos de diferentes direcciones impulsados por el paso de los ciclones y anticiclones que les afecta (Simpson, 1994). En estas latitudes, el sistema de brisas necesita una diferencia de temperatura entre la tierra y el mar que debe ser lo suficientemente grande como para conseguir promover la brisa en sistemas de viento a gran escala. Por lo tanto, se observa con mayor frecuencia durante los meses de primavera y verano, cuando las mayores diferencias de temperatura mar-tierra se acompañan de condiciones favorables sinópticas.

Un buen ejemplo de la variabilidad estacional de las brisas mar-tierra se muestra en Zhang et al. (2009) para la plataforma de Texas-Louisiana (Figura 8.3). Ellos utilizan un espectro de potencia wavelet de la compo-

8.1 Un Escenario Forzado por las Brisas

nente este-oeste del viento para evaluar la evolución temporal de la variación del viento en una ubicación en la plataforma desde diciembre de 1997 hasta abril de 2004. Como puede verse en el espectro, la magnitud de la variación diurna del viento, principalmente asociado con la brisa del mar, alcanza valores máximos en los meses de verano (junio-agosto) y es más débil durante los restantes meses (septiembre-mayo) (Zhang et al., 2009).

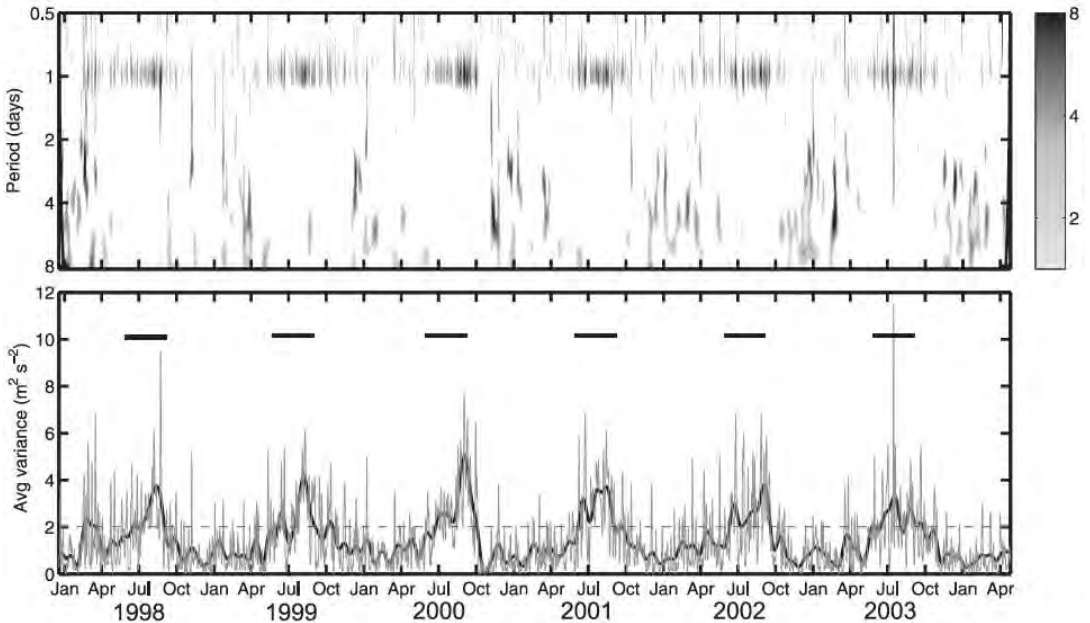


Figure 8.3: Variabilidad estacional de las brisas mar-tierra en la plataforma de Texas-Louisiana - (panel superior) Espectro de potencia Wavelet (sin unidades) de la componente del viento este-oeste a 10 m normalizada (el valor medio se extrae de la serie temporal y luego se normaliza por la desviación estándar) en la boya NDBC estación PTAT2 (27.838 °N, 97.058 °W). Sólo se representan valores significativos, que son $> 95\%$ de confianza para un proceso de ruido rojo con un coeficiente de retraso-1 de 0,72 (Torrence y Compo 1998). (panel inferior) La curva de trazo gris es la frecuencia (período) promediada de la serie temporal de varianza wavelet ($\text{m}^2 \text{s}^{-2}$) sobre la banda 0.83-1.17 cpd durante el período de observación. La curva de color negro sólido son los valores filtrados con paso de tres meses realizado sobre los valores de la curva gris. La línea horizontal gris punteada es el nivel de 95 % de confianza. Las barras negras indican los períodos de verano. [De Zhang et al. (2009) - Fig. 2].

8. SUMMARY OF THE THESIS IN SPANISH

A lo largo de una costa recta y sobre un terreno plano, la brisa del mar se extiende inicialmente hacia el mar así como hacia tierra en ángulo recto a la costa. A lo largo del día, la dirección de la brisa se desplaza unos pocos grados anticiclónicamente debido a la rotación de la Tierra y, después de un período de tiempo, puede aproximarse al balance geostrófico y fluye aproximadamente paralela a la costa si la circulación es suficientemente duradera (Lyons, 1972), particularmente mar adentro. El período de tiempo que la dirección de la brisa necesita para conseguir este cambio está relacionado con el parámetro de Coriolis y por lo tanto depende de la latitud. Las brisas de tierra, por el contrario, están normalmente menos desviadas, no más de $20 - 30^\circ$.

Sin embargo, la mayoría de las costas son irregulares, lo que induce a puntos de convergencia y divergencia en la brisa. Por lo tanto, dondequiera que la costa no sea recta, la forma de la línea de costa hace que el resultado sea más complicado y el flujo de brisas no sea uniforme. Simpson (1994) mostró en un diagrama simple (Figura 8.4) cómo la brisa del mar converge (las brisas de tierra divergen) en las costas convexas y, a la inversa, las brisas marinas divergen (las brisas de tierra convergen), cuando la costa es cóncava. En consecuencia, las zonas de convergencias que promueven fuertes brisas marinas durante el día (y brisas de tierra divergentes más débiles en la noche) se puede encontrar en los cabos, penínsulas, etc, y las brisas marinas divergentes (brisas terrestres convergentes) ocurren con más frecuencia en las bahías, golfos, etc.

Las desviaciones en el viento, además de las producidas por la rotación de la Tierra y por las irregularidades a lo largo de la costa, pueden producirse también por la presencia de la topografía costera. Este efecto tiende a cambiar la dirección de la brisa marina al final del día hacia la principal masa de tierra caliente en el interior. Todos estos factores juntos hacen que el comportamiento de un evento brisas mar-tierra no sea sencillo. El resultado puede ser tan sorprendente como que podemos encontrar vientos que giran en sentidos diferentes en áreas relativamente cercanas, oscilando incluso en contra de la rotación de la Tierra (Simpson, 1994).

El hecho de que los sistemas de brisas mar-tierra no están determinados

8.1 Un Escenario Forzado por las Brisas

únicamente por un aspecto, sino que dependen de la interacción de varios factores locales, presenta importantes consecuencias para forzar el océano costero. Como uno puede imaginar, un sistema de vientos con rotación en sentido anticiclónico no producirá la misma respuesta en el océano a una latitud dada que un viento ciclónico. Así, una metodología apropiada que nos permita caracterizar en el espacio de tiempo-frecuencia las propiedades de rotación de las brisas mar-tierra es crucial para explorar más a fondo la dinámica de las oscilaciones forzadas por las brisas en el océano. Sobre la base de estos argumentos, encontramos que el método wavelet rotatorio (*Apéndice A*) es una opción adecuada para este tipo de estudios, aunque a nuestro conocimiento no ha sido aplicada con anterioridad.

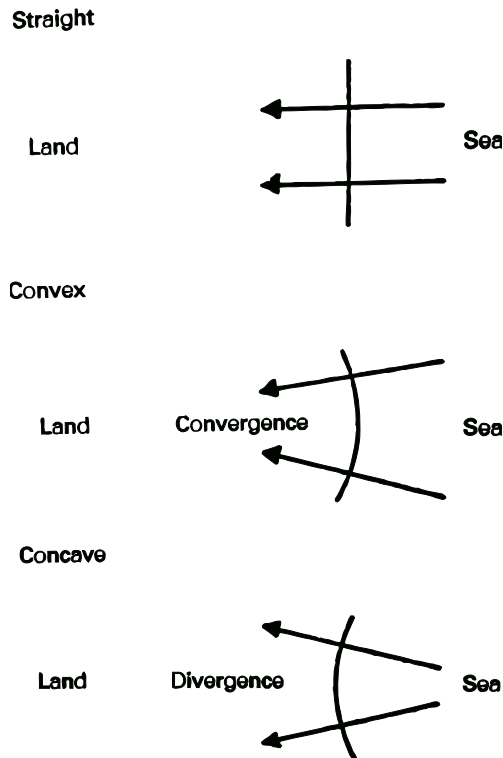


Figure 8.4: El efecto de la costa sobre las brisas [De Simpson (1994) - Fig. 7.1].

8. SUMMARY OF THE THESIS IN SPANISH

8.1.2 Oscilaciones Forzadas por las Brisas

En las zonas costeras, donde el viento dominante está conducido por un gradiente de presión entre el aire sobre la tierra y sobre el mar en ciclos diurnos ('brisas mar-tierra'), el océano puede ser forzado en respuesta a esta transferencia periódica de impulso. El movimiento que resulta de este forzamiento es conocido como 'oscilaciones forzadas por las brisas' (BFOs).

Estos movimientos forzados se caracterizan por una rotación anticiclónica en la frecuencia diurna y 180° de desfase entre las corrientes que fluyen por encima y por debajo de la piconclina. A los ojos del lector esta descripción perfectamente podría coincidir con la atribuida a movimientos inerciales 'libres' que actúan cerca de 30° N/S, donde los períodos de inercia y diurno están cerca el uno del otro. Sin embargo, a pesar de que las oscilaciones forzadas por las brisas son un tipo de movimientos casi inerciales, y de ahí su similitud, la presentan algunas características que las hacen diferente.

En términos generales, las oscilaciones casi inerciales (NIOs) surgen en respuesta a inyecciones impulsivas de momento, que pueden ser causadas por cambios en el vector de la tensión del viento (Pollard and Millard, 1970) o en la respuesta transitoria en un proceso de ajuste geostrófico (Gill, 1984). Los movimientos resultantes son impulsados por un equilibrio dinámico entre las aceleraciones geostróficas y radial, lo que los hace girar anticiclónicamente en la frecuencia local inercial f . Las oscilaciones generadas en la superficie tienen por consiguiente más energía en las capas superficiales, y se propagan hacia abajo a través de la columna de agua por la fricción interna (Qi et al., 1995). Por consiguiente, existe un aumento de la energía de retardo de fase y decaimiento en profundidad relativa a corrientes giratorias casi inerciales en aguas más superficiales. La estructura vertical se caracteriza, pues, por un modo baroclínico primero con un desfase de $\sim 180^\circ$ entre la superficie y las capas inferiores (Millot and Crepon, 1981; Orlić, 1987; Salat et al., 1992; Knight et al., 2002). Estos movimientos 'libres' pueden durar muchos ciclos oscilatorios, especialmente en regiones donde la amortiguación por fricción es

débil.

Por el contrario, las oscilaciones forzadas por las brisas son movimientos inerciales ‘periódicos’ en respuesta a un forzamiento más regular cerca de la frecuencia inercial (Hyder et al., 2011). Al principio, la respuesta del océano parece análoga a la mostrada por las oscilaciones casi-inerciales ‘libres’, corrientes anticiclónicas rotatorias en desfase por encima y por debajo de la piconclina. Sin embargo, estas oscilaciones generadas por el viento cerca de las zonas costeras difieren de las oscilaciones casi-inerciales puras en varios aspectos que describimos ahora, y que responden a la naturaleza de su fuerza motriz: las brisas mar-tierra.

En cuanto a su variabilidad en el tiempo, las oscilaciones forzadas por la brisa aparecen con mayor frecuencia e intensidad durante los meses de verano, de acuerdo con la variabilidad de su forzamiento. A lo largo de este periodo estacional, el gradiente de presión atmosférica debido a los ciclos de calentamiento y enfriamiento diurno promueve fuertes brisas con fase constante y, consecuentemente, la transferencia de energía al océano resulta en una banda diurna altamente enriquecida en el espectro cinético. Por ejemplo, Zhang et al. (2009) examinan la variabilidad de la oscilación forzada por las brisas en la plataforma de Texas-Louisiana (TLS), utilizando un análisis wavelet. Así, se presentan el espectro de potencias wavelet de las series temporales de corrientes norte-sur a 14 m con el fin de poner de manifiesto cómo las bandas inerciales diurnas (DIB) alcanzan valores máximos en verano en comparación con el resto del año (Figura 8.5). En su análisis también encontraron que, mientras que la estratificación ayuda a la mejora de la varianza de la corriente DIB, la profundización de la profundidad de la capa de mezcla parece debilitarla (Zhang et al., 2009).

8. SUMMARY OF THE THESIS IN SPANISH

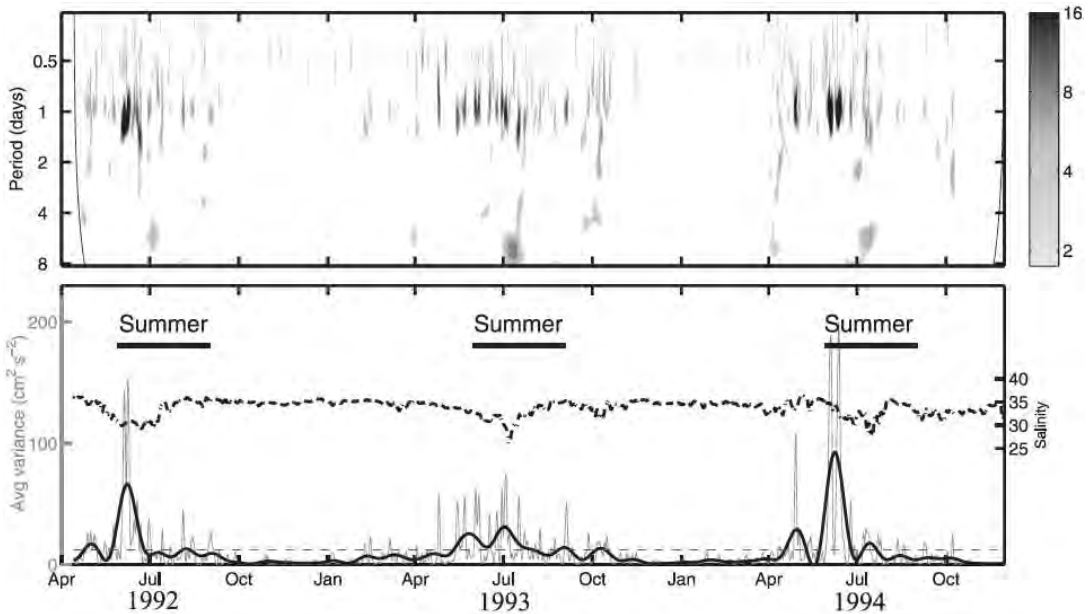


Figure 8.5: Variabilidad estacional de las oscilaciones forzadas por la brisa en la plataforma de Texas-Louisiana - (parte superior) Espectro de potencia Wavelet (sin unidades) para la serie horaria de corrientes norte-sur en los primeros 14 m del anclaje 21. Sólo se representan valores significativos, que son aquellos con confianza $>95\%$ para un proceso de ruido rojo con un coeficiente de retraso-1 de 0.72 (Torrence y Compo 1998). Las dos líneas grises en cualquiera de los extremos indican la zona de influencia, donde los efectos de borde se vuelven importantes. (inferior) La curva de trazo gris es la frecuencia-(período) promedio para la serie temporal de varianza wavelet ($\text{cm}^2 \text{s}^{-2}$) sobre la banda 0.83-1.17 cpd durante el período de observación. La curva en negro es el filtrado a 1-mes de los valores de la curva gris. La línea horizontal gris punteada es el nivel de confianza de 95% . La curva punto-ralla en negro es la serie de salinidad promediada a 2-días en el primer metro del anclaje 21. [De Zhang et al. (2009) - Fig. 4].

También es notable que las corrientes rotatorias de oscilaciones forzadas por las brisas son de magnitud similar en todas las profundidades a través de la plataforma y hasta el borde de la misma (por ejemplo, la Figura 8.6), aparentemente sin efectos de propagación de fase hacia abajo, tal como ocurre con las oscilaciones puramente inerciales.

Craig (1989b) propuso que la inversión del flujo en profundidad es forzada a

través de una pendiente de la superficie barotrópica impulsada por las brisas, y como resultado de la condición de ausencia de flujo normal en el límite costero (véase también Webster (1968); Chen and Xie (1997)). Así, las brisas serían capaces de transferir energía hacia el fondo a través de un gradiente de presión que es de una magnitud comparable al forzado en superficie pero con fase opuesta. Este mecanismo (que se detalla en la *Sección 1.2.1-1.2.2*) se ha modelado con éxito para explicar las corrientes energéticas en desfase observadas en las capas inferiores (Rippeth et al., 2002; Simpson et al., 2002).

Al contrario de lo que ocurre con los movimientos inerciales ‘libres’, que presentan una evolución de fase no-constante como resultado de las inyecciones impulsivas de momento, las oscilaciones forzadas por las brisas muestran una evolución de fase casi constante en el tiempo mientras se ven forzados por una frecuencia específica (la de la brisa del mar-tierra). A este respecto Simpson et al. (2002) muestran un ejemplo ilustrativo de un forzamiento por brisa que se interrumpe (después de 31 días en la Figura 8.7) y el movimiento resultante cambia a la frecuencia inercial de modo que, cuando se ve como un movimiento forzado diariamente, hay un aumento regular en el retardo de fase con el tiempo (Figura 8.7).

Así, la alternancia de las oscilaciones forzadas diariamente y las oscilaciones inerciales transitorias es una característica esperada de este tipo de fenómenos oceanográficos. Algunos autores (Hyder et al., 2002; Rippeth et al., 2002; Sobarzo et al., 2007; Hyder et al., 2011) han observado además en datos de series temporales que hay un periodo de ritmo de $\sim 2\pi/(\omega - f)$ en el que la fuerza de las componentes periódicas diurnas de la corriente (ω) oscilan en combinación con las componentes de corrientes inerciales de fase libre (f).

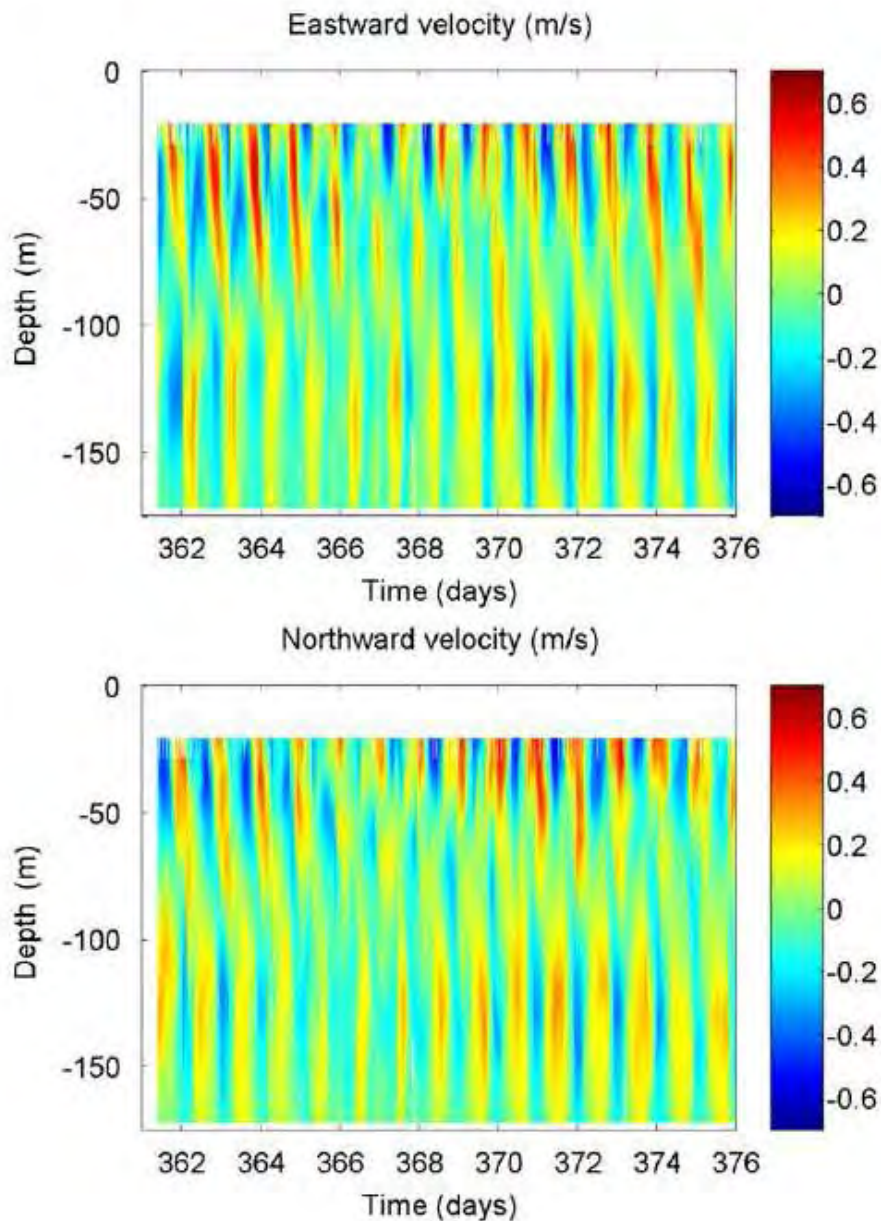


Figure 8.6: Oscilaciones forzadas por la brisa en la plataforma de Namibia - La estructura vertical observada de las corrientes hacia el este y hacia el norte en un periodo de quince días del 28 de diciembre de 1998 00:00 GMT al 12 de enero de 1999 00:00 GMT. Se ha eliminado a ambas componentes la media sobre el período de 15 días (no se ha aplicado filtrado alguno). [De Hyder et al. (2011) - Fig. 6].

8.1 Un Escenario Forzado por las Brisas

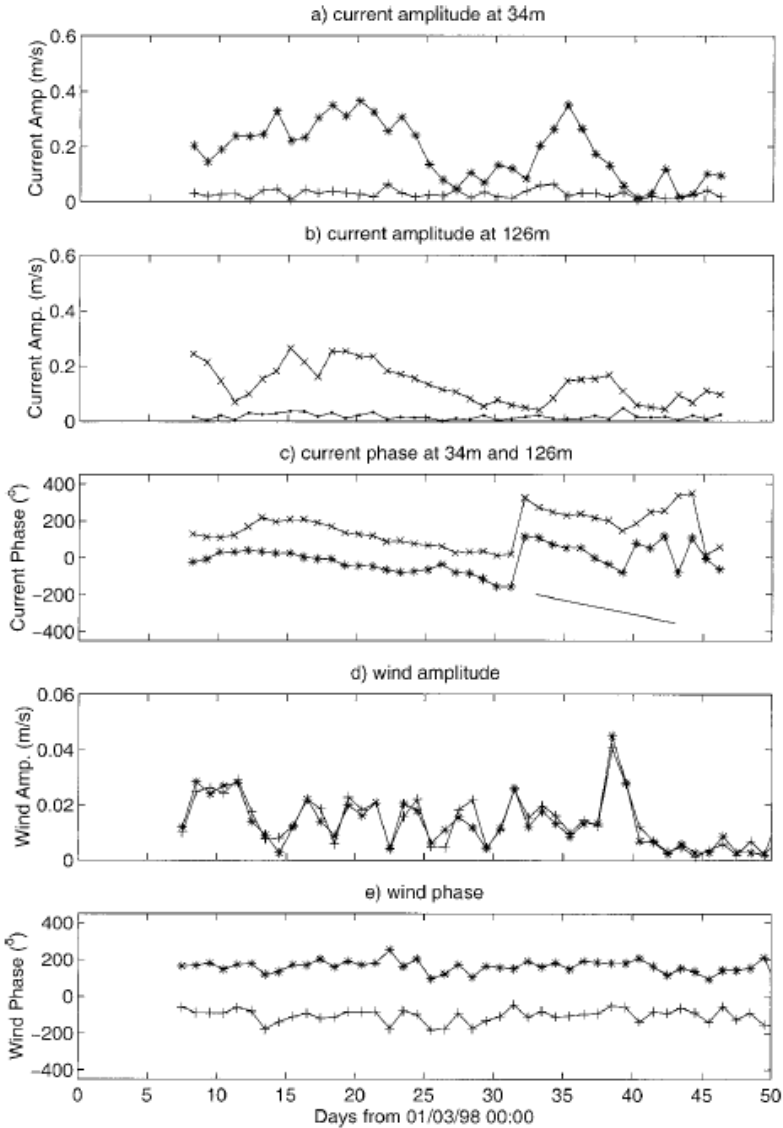


Figure 8.7: Evolución de la fase de oscilaciones forzadas por brisa y casi-inercial ‘libres’ - La amplitud y la fase del movimiento diario durante el período de registro. (a) Velocidad en 34-m en sentido antihorario (*) y horario (+), (b) la corriente a 126 m hacia la izquierda (x) y a la derecha (•), (c) la fase de la componente en sentido antihorario a 34 m (*) y 126 m (x), (d) Amplitud de componentes del viento en sentido antihorario (*) y horario (+), y (e) la fase de los componentes de viento (*) hacia la izquierda y hacia la derecha (+). La línea recta inclinada en (c) indica la tasa de cambio de fase de una oscilación inercial pura ($15.5^{\circ} \text{ d}^{-1}$). [De Simpson et al. (2002) - Fig. 7].

8. SUMMARY OF THE THESIS IN SPANISH

Geográficamente, las oscilaciones cercanas a la frecuencia inercial son una característica generalizada en el océano profundo y costero que pone en juego una importante fuente de energía disponible para la mezcla (Webster, 1968; Millot and Crepon, 1981; Salat et al., 1992; Font et al., 1995; van Haren et al., 1999; Knight et al., 2002; van Aken et al., 2005; Sobarzo et al., 2007; Chaigneau et al., 2008).

No obstante, los niveles de energía de la banda inercial no son uniformes en todas partes y son más variable que el resto del espectro (Fu, 1981; Garrett, 2001; Gerkema and Shrira, 2005). Las oscilaciones forzadas por las brisas contribuyen (entre otros fenómenos que no se abordan aquí) a las diferencias geográficas observadas en los niveles de energía casi inerciales. Esto se basa en el hecho de que en función de la latitud en la que el forzamiento por brisas está actuando, la respuesta del océano puede ser resonante. Cerca de 30° N/S, cuando los periodos inercial y diurno están cerca uno de otro, la transferencia de momento y energía a partir del forzamiento de las brisas a movimientos inerciales puede verse de este modo aumentado significativamente (Hyder et al., 2002; Rippeth et al., 2002; Simpson et al., 2002; Sobarzo et al., 2007).

Sobre la base de todas las diferencias mencionadas entre las oscilaciones forzadas por las brisas y las oscilaciones casi inerciales ‘libres’, en las últimas décadas se han hecho valiosos esfuerzos para desarrollar una base teórica y de modelaje de oscilaciones forzadas por las brisas (Craig, 1989b; Chen and Xie, 1997; Rippeth et al., 2002; Simpson et al., 2002; Hyder et al., 2002, 2011).

A continuación, revisamos los trabajos teóricos y modelos que se centran en el comportamiento observado del océano forzado por las brisas. Además, destacamos que los resultados de los modelos que predicen características interesantes no están aún confirmadas con observaciones y, por lo tanto, necesitan de mayor investigación. Esta revisión ofrece una visión más profunda de la física detrás de la generación y evolución de las oscilaciones forzadas por las brisas.

Forzamiento periódico y resonancia casi-inercial

Los avances teóricos y los modelos sobre la respuesta del océano producido por forzamiento periódico (las mareas y el viento) a una frecuencia particular, se han beneficiado en gran medida de los estudios de Battisti and Clarke (1982) y Craig (1989a,b). A continuación se describe la dinámica de las oscilaciones forzadas por brisa mediante la introducción de algunos trabajos recientes reveladores.

El mecanismo esencial y la variación latitudinal de los movimientos diurnos forzados por el viento se ilustran claramente en Simpson et al. (2002) con un modelo simple para una columna de agua de profundidad H verticalmente uniforme siendo la velocidad forzada por un esfuerzo del viento oscilante τ_s sin gradientes de presión horizontales (Figura 8.8). La amortiguación de fricción es lineal y se introduce a través de $(-ru, -rv)$, dejando las ecuaciones dinámicas de la velocidad compleja $w = u + iv$ como

$$\frac{\partial w}{\partial t} + if\omega = \frac{-rw + \tau_s}{\rho H} \quad (8.1)$$

Entonces, las amplitudes complejas para los forzamientos horarios (W_-) y antohorarios (W_+) en la frecuencia ω son

$$W_- = \frac{A_-}{i(f - \omega) + r'}; \quad W_+ = \frac{A_+}{i(f + \omega) + r'} \quad (8.2)$$

donde $\tau_s/(\rho H) = A_{\pm}e^{\pm i\omega t}$ y $r' = r/(\rho H)$. Como puede verse en la Figura 8.8 (arriba), la respuesta del océano es resonante ($W \rightarrow A/r'$) para el caso horario a la latitud crítica de 30°N donde $f = \omega$, y para el caso en sentido antihorario en la latitud crítica de 30° donde $f = -\omega$. En otras palabras, la respuesta del océano es resonante cuando se acercan los periodos diurnos y de inercia. Bajo estas circunstancias, la corriente y el forzamiento están en fase

8. SUMMARY OF THE THESIS IN SPANISH

y la transferencia de momento y la energía se mejoran significativamente.

También se muestra que la fase de la corriente cambia rápidamente entre valores límite de $+\pi/2$ y $-\pi/2$ al alejarnos de 30°N/S , y que este efecto es más agudo cuando se utiliza un coeficiente más elevado para la amortiguación por fricción.

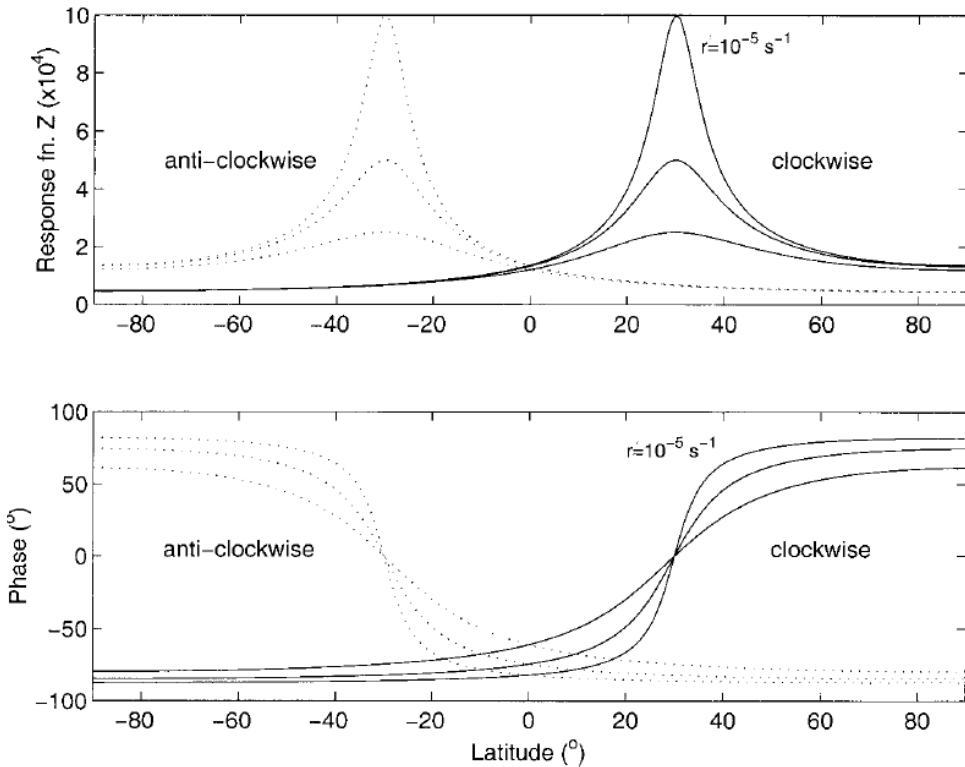


Figure 8.8: Modelo de oscilaciones forzadas - Variación de la función de respuesta $Z = W/A$ con la latitud para un modelo de sencillo de oscilaciones forzadas con $r' = 10^{-5}, 2 \cdot 10^{-5}, 410^{-5} \text{ s}^{-1}$. La amplitud (a) y la fase (b) se muestran a la derecha (línea continua) y a la izquierda (línea punteada). [De Simpson et al. (2002) - Figura 1].

Si ahora vamos un paso más allá, nos encontramos con el modelo de dos capas desarrollado por Simpson et al. (2002), que nos permite introducir la física detrás de las oscilaciones forzadas por brisa en las zonas costeras. Ellos

plantearon la hipótesis de una oscilación diurna del esfuerzo del viento que actúa directamente en la superficie del océano y en presencia de una costa. Esta condición produce una variación de la pendiente perpendicular a la costa, que impulsa la transferencia de momento a la columna de agua a través de un gradiente de presión de una magnitud comparable pero de fase opuesta al forzamiento superficial.

Desde este punto de partida, Simpson et al. (2002) utilizan un modelo analítico de dos capas sin fricción con la capa superior forzada por una fuerza del viento diurna y la pendiente de la superficie opuesta resultante de este forzamiento del viento; y, la capa inferior está forzada únicamente por el pendiente de la superficie. Este gradiente de presión externa fuerza a la capa inferior, lo que lleva a movimientos desplazados en fase con relativamente la misma amplitud que en la capa superior. El modelo reproduce satisfactoriamente las características clave de oscilaciones forzadas por brisa tal y como recoge la literatura: corrientes anticiclónicas girando $\sim 180^\circ$ fuera de fase por encima y por debajo de la piconocline con amplitudes energéticas de magnitud similar y fase casi constante dentro de cada capa (Chen et al., 1996; Rippeth et al., 2002; Simpson et al., 2002; Zhang et al., 2009; Hyder et al., 2011). En contraste con lo que se observa con movimientos casi-inerciales libres (Millot and Crepon, 1981; Orlić, 1987), que exhiben un aumento en el retardo de fase y corrientes menos energéticas en aguas más profundas debido a que el impulso se transfiere hacia abajo a través de la tensión de corte descrita por la teoría clásica de Ekman.

Simpson et al. (2002) configuraron su sencillo modelo de dos capas para tener en cuenta la respuesta del océano al forzamiento de viento diurno de la siguiente manera. Se considera el flujo en una región de la plataforma delimitada por la línea de costa que se extiende en la dirección y para $x = 0$ y con un perfil de profundidad $H(x)$. Las capas se suponen uniformes en densidad (ρ) y velocidad (u, v) , pero independientes una de otra por una interfaz de fricción. La profundidad de cada capa está dada por h_1 y h_2 , las capas superior e inferior, respectivamente. El movimiento es forzado por un esfuerzo

8. SUMMARY OF THE THESIS IN SPANISH

del viento oscilatorio (τ_x, τ_y) a la frecuencia diurna ω , que actúa directamente sólo en la capa superficial. Por lo tanto, se derivan las siguientes ecuaciones de movimiento para las capas superior (subíndice 1) e inferior (subíndice 2):

$$\begin{aligned} \frac{\partial u_1}{\partial t} - f v_1 &= \frac{\tau_x}{\rho h_1} - g \frac{\partial \eta}{\partial x}, \\ \frac{\partial v_1}{\partial t} + f u_1 &= \frac{\tau_y}{\rho h_1}; \end{aligned} \quad (8.3)$$

$$\begin{aligned} \frac{\partial u_2}{\partial t} - f v_2 &= -g \frac{\partial \eta}{\partial x}, \\ \frac{\partial v_2}{\partial t} + f u_2 &= 0; \end{aligned} \quad (8.4)$$

donde η es la elevación de la superficie, g es la aceleración gravitacional, y f es la frecuencia de Coriolis. El componente clave de este modelo entra en juego a través de la ‘aproximación Craig’ (Craig, 1989b) (ec. 8.5), que establece el papel de la frontera costera induciendo un gradiente de presión en respuesta al forzamiento del esfuerzo en superficie. La aproximación deriva de la solución de menor orden integrada verticalmente, después de asumir que la relación de la anchura de la plataforma L a la longitud de onda barotrópica $2\pi(gH)^{1/2}/\omega$ es pequeña. Este requisito de la ‘aproximación Craig’ implica que el tiempo de tránsito de la onda barotrópica a lo largo de la plataforma es pequeño en comparación con el período de inercia. Entonces, la pendiente de la superficie inducida por el estrés aplicado por el viento puede ser definido como

$$\frac{\partial \eta}{\partial x} = \frac{\tau_x + i(f/\omega)\tau_y}{\rho g H}. \quad (8.5)$$

Debido a la condición de ausencia de flujo normal a la costa, el esfuerzo del

viento diurno transversal a la pendiente τ_x genera una componente opuesta a la pendiente en superficie. En este sentido, el esfuerzo del viento diurno a lo largo de la costa τ_y induce una corriente paralela a la costa de profundidad uniforme $V = i\pi/(\omega gH)$ que, en equilibrio geostrófico, requiere una componente de inclinación de la superficie de amplitud $(f/\omega)\tau_y/(\rho gH)$.

A medida que el sistema se deriva, es evidente que el forzamiento por estrés del viento y la inclinación de la superficie contraria gobiernan la capa superior, mientras que en la capa inferior sólo opera la variación inducida por la superficie de la pendiente (el gradiente de presión asociado con la pendiente de la superficie actúa a lo largo de toda la columna de agua).

Definiendo la velocidad compleja como $w = u + iv = W e^{i\omega t}$, e introduciendo la ‘aproximación Craig’ en las ecuaciones de movimiento, ecuación (8.3) y ecuación (8.4), Simpson et al. (2002) describen la resonancia diurna inercial en el hemisferio sur a través de las soluciones regulares oscilatorios para el movimiento en sentido antihorario

$$W_1 = \frac{\gamma T_x + i(\gamma + f/\omega + 1)T_y}{i\rho H(f + \omega)}; \quad (8.6)$$

$$W_2 = \frac{-(T_x - if/\omega T_y)}{i\rho H(f + \omega)}. \quad (8.7)$$

con $\gamma = h_2/h_1$, ω positiva correspondiente al movimiento antihorario; T_x y T_y siendo las amplitudes complejas del esfuerzo del viento; y W_1 y W_2 las amplitudes complejas del movimiento en las capas superior e inferior, respectivamente. Por lo tanto, la respuesta del océano, ecuación (8.6) y ecuación (8.7), para el movimiento anticiclónico se verá reforzada en las latitudes próximas a 30° S donde entra en resonancia con $f \rightarrow -\omega$ tal que $f/\omega \rightarrow -1$ llevando a

8. SUMMARY OF THE THESIS IN SPANISH

$$W_1 \approx \frac{\gamma T_x + i(\gamma + iT_y)}{\rho H(f + \omega)} \approx W_2. \quad (8.8)$$

Esta solución particular para la respuesta en estado estacionario del océano cerca de latitudes críticas reproduce las principales características de las observaciones para oscilaciones forzadas por viento diurnas inerciales que pueden estar influidas por las fronteras terrestres (Chen et al. (1996); Rippeth et al. (2002); Simpson et al. (2002); Zhang et al. (2009); Hyder et al. (2011)). La fase del movimiento forzado oscilando dentro de la banda diurna-inercial se desplaza 180° entre las capas superior e inferior, y la amplitud de la velocidad es de una magnitud comparable en las dos capas cuando el factor γ , que es función de la profundidad de la piconclina, es del orden de la unidad, como ocurre en el área de estudio de Simpson et al. (2002). Se obtienen efectos análogos para las soluciones regulares oscilatorios de movimiento horario en el hemisferio norte (vea Rippeth et al. (2002)). La respuesta del océano es entonces reforzada en latitudes cercanas a 30°N donde $f \rightarrow \omega$ (hemisferio norte) y el movimiento es resonante. En ambos hemisferios, la respuesta del océano al forzamiento ciclónico a la frecuencia diurna es notablemente más débil en la relación $| (f + \omega) | / | (f - \omega) |$.

Cabe señalar que el modelo anterior (Simpson et al., 2002) ignora los efectos internos y de fricción en el mecanismo. Sin embargo, se ha profundizado en estos efectos de acoplamiento por fricción entre capas por Rippeth et al. (2002) mediante un modelo de fricción continua con base en la misma dinámica que el modelo de Simpson et al. (2002). Por lo tanto, el nuevo modelo incluye muchas capas y más esfuerzos cortantes especificados en términos de una viscosidad turbulenta. Este trabajo de modelado fue probado en cuatro casos diferentes (Figura 8.9): prueba A incluyendo una piconclina y la condición de frontera costera; prueba B incluyendo una piconclina pero no una condición de borde costero; prueba C no incluye piconclina, pero sí la condición de contorno costero, y prueba D sin incluir ni piconclina ni la condición de borde costero.

El objetivo fue evaluar si la condición de contorno costero o la existencia de picnoclina determinan la estructura vertical de los movimientos forzados por viento.

Los resultados de las pruebas sólo reproducen el cambio de fase característico y la penetración de la energía hasta cerca del fondo en los casos en los que se incluyó la condición de frontera costera (pruebas A y C en la Figura 8.9), mientras que en su ausencia (pruebas B y D) los movimientos forzados no exhiben estas características. Los autores también descubrieron que las tensiones internas de corte no modificaron demasiado la respuesta al forzamiento por fricción (pruebas A y C), y confirmaron que el flujo inverso en las capas inferiores es fundamentalmente el resultado de un gradiente de presión barotrópico ('aproximación de Craig'), creado por el esfuerzo del viento aplicado y la condición de flujo no-normal en el límite costero, que es la base del modelo.

Por consiguiente, estos resultados indican que las capas superior e inferior de los movimientos forzados por brisa se comportan de manera diferente que los de movimientos puramente inerciales, donde el desfase de capas no están impulsadas por un esfuerzo constante sino por los efectos de propagación de fase y también porque la picnoclina tiene un papel principal en la propagación.

Los resultados del modelado de Rippeth et al. (2002) también encuentran un ciclo de pulsos entre periodos diurnos y inercial, a pesar de usar un forzamiento diurno. En el caso de pruebas sin picnoclina (casos C y D), el pulso muere después de 4 días cuando la señal transitoria se amortigua, dejando una solución de estado estacionario de periodo diurno. Este comportamiento parece ser consistente con los periodos de pulsos antes mencionados que se encuentran en las observaciones (Hyder et al., 2002; Sobarzo et al., 2007; Hyder et al., 2011).

8. SUMMARY OF THE THESIS IN SPANISH

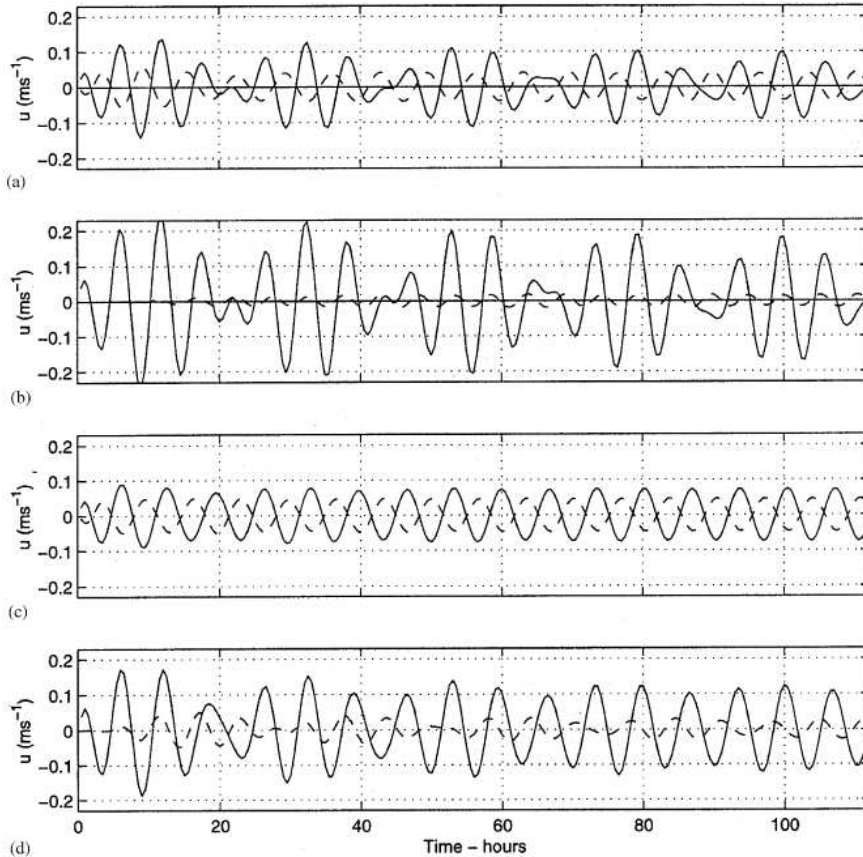


Figure 8.9: Modelo Continuo con fricción de oscilaciones forzadas - Los resultados del modelo continuo. Componentes predichas para la corriente cerca de la superficie (línea continua) y cerca del fondo (línea de puntos) a lo largo de la costa. (a) Prueba A: resultados de la ejecución del modelo, que incluye un piconclina y la condición de contorno costero. (b) Prueba B: resultados de la ejecución del modelo que incluye una piconclina, pero no incluye un límite costero. (c) Prueba C: resultados de la ejecución del modelo que incluye el límite costero pero sin piconclina. (d) Prueba D: resultados de la ejecución del modelo, sin límite costero ni piconclina. [De Rippeth et al. (2002) - Fig. 9].

Estratificación y Mezcla Vertical

Las oscilaciones casi-inerciales cerca de la latitud crítica para la resonancia

diurna inercial juegan un papel importante en los procesos de mezcla verticales, especialmente en las zonas costeras estratificadas con baja energía de las mareas (Rippeth et al., 2002; Simpson et al., 2002; Hyder et al., 2011). Como se destaca en Hyder et al. (2011), las sugerencias anteriores de que las NIOs ponen en juego alrededor de la mitad de la energía cinética en los océanos a escala global (Pollard and Millard, 1970; Pollard, 1980, 1970) ahora se confirma con nuevas observaciones. Por lo tanto, se puede encontrar en la literatura un flujo de energía estimado de $\sim 0.5 - 0.7$ TW, un valor comparable con el de las mareas internas de 0.9 TW (Park et al., 2005; Watanabe and Hibiya, 2002; Alford, 2003a,b; Munk and Wunsch, 1998) .

El primer modo baroclínico de las NIOs, con movimientos antifase entre las capas por encima y por debajo de la piconclina, conlleva importantes cizallas verticales que promueven la disipación y la mezcla vertical en las zonas estratificadas. Trabajos previos sobre fuertes oscilaciones inerciales (Knight et al., 2002; van Haren, 2000) estimaron el número de gradiente de Richardson, Ri , para evaluar las condiciones de mezcla promovidas por las NIOs. Este número no dimensional se calcula como

$$Ri = \frac{N^2}{S^2} , \quad (8.9)$$

donde N^2 es el cuadrado de la frecuencia de Brunt-Väisälä (frecuencia de flotabilidad al cuadrado), y S^2 es el cuadrado de la cizalladura vertical de la corriente aplicada a una parcela de fluido. La frecuencia al cuadrado de Brunt-Väisälä está dada por

$$N^2 = -\frac{g}{\rho_0} \frac{\Delta\rho}{\Delta z} , \quad (8.10)$$

donde ρ es la densidad potencial calculada a partir de datos de temperatura y conductividad, g es la constante de gravedad, ρ_0 es la densidad potencial promedio y Δz es la distancia vertical entre la parte superior e inferior de la

8. SUMMARY OF THE THESIS IN SPANISH

de la parcela de fluido. Finalmente, el esfuerzo cortante vertical al cuadrado está dada por

$$S^2 = \left(\frac{\Delta u}{\Delta z}\right)^2 + \left(\frac{\Delta v}{\Delta z}\right)^2, \quad (8.11)$$

donde Δu y Δv son las diferencias en las componentes este-oeste y norte-sur de la velocidad entre la parte superior e inferior de la parcela de fluido, respectivamente. Entonces, los valores típicos para $Ri < 1$ indican la generación de inestabilidades de Kelvin-Helmholtz provocadas por el corte vertical que desencadena la mezcla en un fluido estratificado (Miles, 1986; Van Gastel and Pelegrí, 2004). Por el contrario, si $Ri \gg 1$, la flotabilidad es dominante ya que no hay suficiente energía cinética para homogeneizar la columna de agua.

Knight et al. (2002) estimaron Ri utilizando datos de ADCP y CTD en el Mar del Norte y encontraron valores inferiores a 1 cuando las fuertes corrientes inerciales tenían un importante cizallamiento verticales a través de la termoclina, aunque nunca se acercó a los valores críticos de 0.25. También se hicieron mediciones de la disipación donde comprobaron que la mezcla dentro de la termoclina fue más intensa y se asoció a altos coeficientes promedio de difusión en la termoclina cuando actuaba un alto cizallamiento en la corriente inercial.

Los resultados del modelado y observaciones en el Mar del Norte (van Haren, 2000) también apoyan la importancia de la cizalladura de marea y de inercia a través de la estratificación para el intercambio vertical probablemente debido a la cizalla interna impulsada por las turbulencias.

Si ahora consideramos los movimientos de inercia que actúan alrededor de las latitudes críticas para la resonancia diurna inercial, se encuentra que la respuesta casi resonante al forzamiento por viento diurno implica una transferencia eficiente de la energía y el momento al mar con movimientos inerciales diurnos que dominan el espectro de energía cinética (Simpson et al., 2002).

Bajo estas condiciones, es razonable esperar que las oscilaciones forzadas

por la brisa representen la principal fuente de energía cinética turbulenta que produzca mezcla vertical, especialmente en ausencia de fricción resultante del movimiento de marea fuerte (Rippeth et al., 2002; Simpson et al., 2002; Hyder et al., 2011). Sin embargo, las observaciones de cizalladura en los flujos verticales no son en sí mismos una prueba de mezcla como ha señalado acertadamente Zhang et al. (2009). Hasta donde sabemos, ellos publicaron por primera vez un análisis de series de tiempo de los efectos observados de oscilaciones forzadas por la brisa en la mezcla vertical.

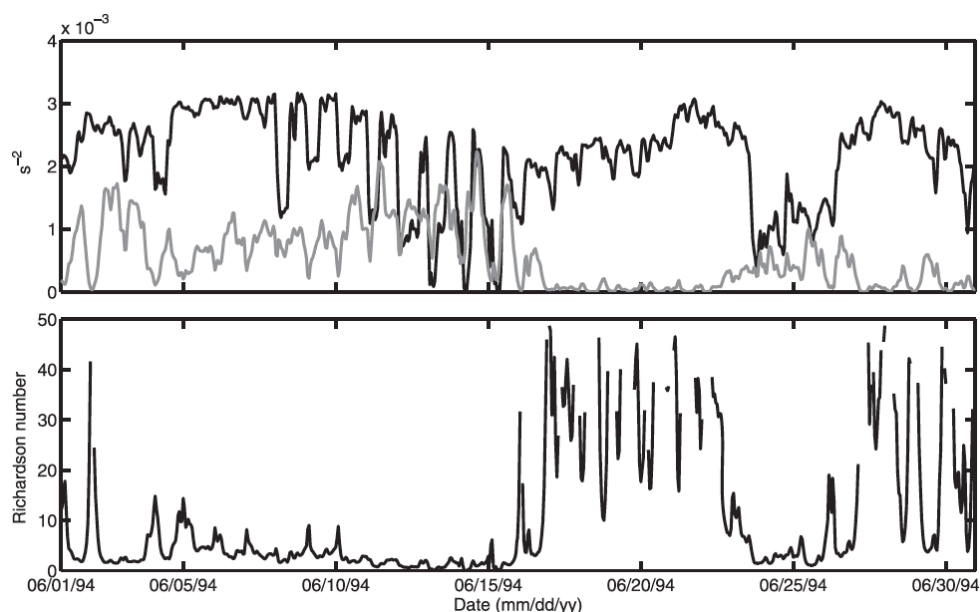


Figure 8.10: Efectos de las oscilaciones forzadas por brisa en la mezcla vertical - (top) Las curvas negras y grises son series temporales de frecuencia de Brunt-Väisälä y de cizallamiento al cuadrado calculado a partir de las mediciones de temperatura, conductividad y corriente en el anclaje 22, respectivamente. (inferior) Series temporales del número de Richardson calculado a partir de la frecuencia de Brunt-Väisälä y del cizallamiento al cuadrado (Ri_b). Por claridad, sólo se muestran los valores de Richardson inferiores a 50. [De Zhang et al. (2009) - Fig. 10].

Zhang et al. (2009) estimaron el número de Richardson en la plataforma de Texas-Louisiana (TLS) con mediciones a dos profundidades (3 y 23 m) en

8. SUMMARY OF THE THESIS IN SPANISH

el anclaje 22 (28.35°N, 93.96°W, ~ 50 m de profundidad), lo que les permitió explorar la estabilidad de la columna de agua durante eventos de corrientes forzadas por brisa, como parte del proyecto LATEX (Figura 8.10). De esta manera, se encontraron con que durante eventos fuertes de corrientes forzadas por brisa (~ 12 y 21-24 junio de 1994) el número de Richardson fue despreciable. La velocidad de cizallamiento aumentó de manera significativa durante estos periodos y también disminuyó la estratificación, haciendo pequeño el número de Richardson (del orden de 1 en ~ 12 junio de 1994). Y, por el contrario, se observó que el número de Richardson aumentó debido al aumento de la estratificación y la disminución significativa de la cizalladura de la velocidad cuando las corrientes forzadas por brisa desaparecieron después del paso de un frente meteorológico por el anclaje 22 el 16 de junio de 1994. Este análisis apoya que los eventos de corrientes fuertes forzadas por brisa podría aumentar significativamente la mezcla vertical a través de la columna de agua durante los períodos estivales en los TLS.

Aunque las brisas marinas han sido ampliamente descritas, se necesita más investigación para entender mejor la dinámica de corrientes forzadas por brisa en torno a latitudes críticas para la resonancia diurna inercial; y, posteriormente, para evaluar el impacto real de esta interacción atmósfera-océano en la mezcla vertical de aguas estratificadas.

8.1.3 Marco del Estudio, Objetivos y Metodología

Hyder et al. (2011) hicieron importantes contribuciones para representar en un mapa del mundo (Figura 8.11) las ubicaciones donde se han reportado corrientes superficiales rotatorias diurnas. Marcan las observaciones atribuidas al forzamiento por viento con $*$'s, mientras que con \bullet indican los candidatos que podrían ser movimientos forzados por el viento o que el re-análisis puede ayudar a determinar si son de hecho movimientos forzados por viento. Sin embargo, los autores son cautos y señalan que esta base de datos no es exhaustiva, y también que algunos casos de no incluidos podría ser enmascarado

8.1 Un Escenario Forzado por las Brisas

por, o ser atribuido a, forzamiento de mareas.

La Figura 8.11 también es utilizado por Hyder et al. (2011) para presentar las regiones esperados para resonancia diurna inercial basado en el límite hacia los polos de observaciones conocidas de corrientes superficiales rotatorias diurnas forzadas por el viento en el Egeo a 40° N (Hyder et al., 2002), donde $\omega/f \sim 0.77$ (periodo inercial ~ 18.7 h). Así, los autores dedujeron teóricamente que un límite hacia el Ecuador podría ser 23° S, donde encontramos una vez más que $\omega/f \sim 0.77$ (periodo inercial ~ 30.9 h).

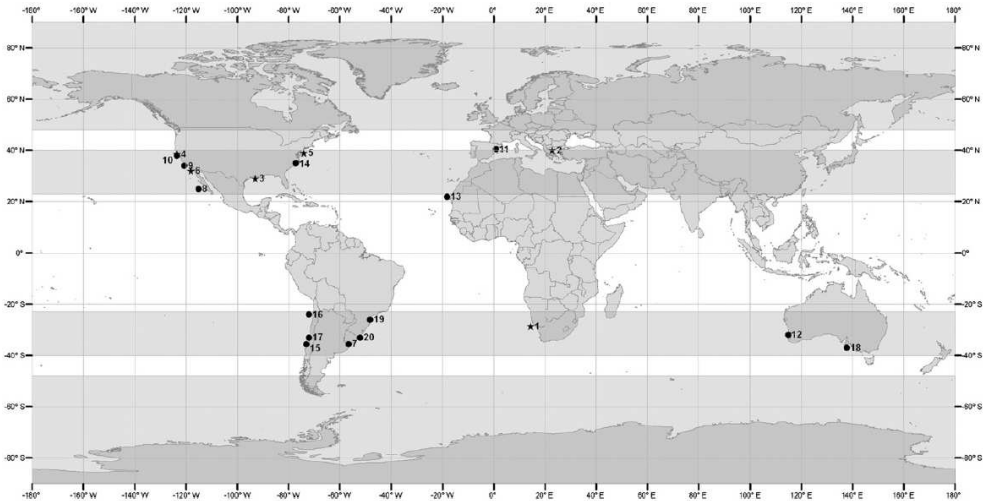


Figure 8.11: Regiones para resonancia diurna/semidiurna¹ - Las regiones hacia el ecuador donde se esperarían forzamientos por vientos o mareas para forzar corrientes energéticas diurnas rotatorias entre 23 y 40 N/S se muestran en gris. También se somborean las regiones correspondientes hacia el polo para resonancia inercial por forzamiento de marea semidiurno M_2 entre 48 y 90 N/S. [From Hyder et al. (2002) - Fig. 2].

Las regiones resonantes para el forzamiento de mareas se espera que actúen de manera similar (Maas and Van Haren, 1987; Furevik and Foldvik, 1996), y se muestran en la Figura 8.11 suponiendo los mismos límites de los períodos diurnos de marea ω/f . El resultado abarca en términos generales las mismas latitudes que para los movimientos forzados por viento. Análogamente, la

8. SUMMARY OF THE THESIS IN SPANISH

resonancia de marea semidiurna con el período de inercia (Furevik and Foldvik, 1996; Middleton and Denniss, 1993) se espera que esté entre 48° - 90° N/S para $M2$ (período 12.42 h) con resonancia en $\sim 75^{\circ}$ N/S, y entre 50° - 90° N/S para $S2$ (período de 12 h) con resonancia en el polo.

Además de los mecanismos de latitud crítica que mejoran la banda de energía casi inercial, también es interesante mencionar la inestabilidad sub-armónica paramétrica (PSI) (Simmons et al., 2004; MacKinnon and Winters, 2005; Van Haren, 2005; van Haren, 2007), que implica la transferencia de energía de las mareas semidiurnas hacia movimientos inerciales de alta frecuencia en las latitudes cerca de 28.8° N/S.

Sin embargo, aunque la respuesta dinámica de la pendiente periódica en superficie forzada por viento es similar a la del forzamiento de marea, es importante recordar que este último actúa a través de la columna de agua y, por lo tanto, se espera que sean más relevantes los efectos de amortiguamiento por fricción y de capa límite de fondo. Esta condición debe ser considerada, ya que puede reducir la extensión de las regiones para las mareas resonantes (Hyder et al., 2011).

En el contexto descrito para el tema ‘oscilaciones forzadas por las brisas’, el ámbito de aplicación de la presente tesis doctoral se centra en dos aspectos principales.

En primer lugar, la generación y evolución de resonancia en oscilaciones forzadas por brisa hacia el polo de la latitud crítica para la resonancia diurna inercial en el *Capítulo 2*. En este trabajo se utilizan datos de series temporales de dos regiones diferentes que pueden actuar como un generador de resonancia en oscilaciones forzadas por brisa hacia los polos a 30° N y cerca del límite para la resonancia diurna inercial: el Golfo de Cádiz y el Golfo de Valencia. Adicionalmente se utilizan datos de series temporales de una tercera región en la que no se espera que tenga lugar resonancia alguna. Esta región se coloca cerca, pero fuera de las latitudes críticas, y sirve como una prueba ‘en blanco’ para nuestro estudio: el área del Cabo Peñas. La metodología aplicada es la

Wavelet Rotatoria.

En segundo lugar, en el *Capítulo 3* se explora el papel de las oscilaciones forzadas por brisa en la promoción de procesos de mezcla diapicna. Esta investigación proporciona un nuevo conjunto de datos de oscilaciones forzadas por brisas en aguas estratificadas cerca de las latitudes críticas ($30^\circ \pm 10^\circ$ N/S) para la resonancia diurna inercial, que en gran medida puede contribuir a desencadenar mezcla diapicna.

8.2 Ondas Internas Solitarias en el Océano

Esta sección presenta observaciones y trabajos teóricos sobre las ondas solitarias en el océano. El objetivo es ofrecer al lector no especializado una breve reseña sobre el tema y centrar la atención en aquellos aspectos que rodean la generación y evolución de solitones de gran amplitud generados por la topografía.

Se describen las características principales que caracterizan las observaciones oceánicas de solitones: su dinámica y cinemática, escalas típicas, y los mecanismos de generación. Una vez se haya desarrollado la base sobre ondas solitarias en el océano, se discute la aproximación teórica al fenómeno. Se revisa la física matemática detrás de la teoría de onda solitaria, destacando aquellos trabajos de mayor relevancia para nuestro problema.

Por último, se discute en el marco de este estudio de doctorado dentro del contexto descrito.

8.2.1 Estudios Observacionales

Las ondas solitarias, también conocidas como solitones, son un fenómeno muy extendido en el océano, que son parte de la banda de alta frecuencia de las ondas internas.

Este término define un tipo de ondas que viajan en el interior de un fluido estratificado después de que una perturbación mueve las partículas de agua fuera de su posición de equilibrio. En un fluido en rotación a gran escala, como es el caso del océano, estas ondas internas se propagan en una gama de frecuencias entre la flotabilidad N y las frecuencias inerciales f , que establecen los límites máximo y mínimo de la frecuencia de la onda interna¹.

¹Este rango de frecuencias puede ser diferente cuando entran en juego ‘efectos no tradicionales’. Sin embargo, este no es el caso de nuestra investigación. Para más detalles sobre el ‘enfoque no tradicional’ ver (Gerkema and Shrira, 2005; Gerkema et al., 2008). Además, los efectos no lineales pueden ampliar este rango ligeramente.

Cuando la perturbación es causada por la interacción de flujo de marea barotrópico con la topografía, las ondas generadas de este modo son conocidas como ‘mareas internas’ (mareas baroclínicas), y por lo tanto se propagan con las frecuencias de marea.

Con mayor frecuencia, el origen de las ondas solitarias internas en el océano parecen estar relacionados con esta última, las mareas baroclínicas. Por lo tanto, se ha detectado la aparición de ondas solitarias, utilizando sensores remotos o *in situ*, especialmente en las proximidades de las regiones costeras. La generación ‘directa’ de ondas solitarias internas impulsados por un flujo de marea barotrópico sobre la topografía se asocia a zonas de borde de la plataforma y a topografías irregulares (dorsales, bancos, montes submarinos, ...).

El mecanismo de generación implica la liberación de la onda de la topografía de una onda interna de marea que se convierten en ondas más cortas (Maxworthy, 1979; Gerkema, 1994; Helfrich and Grimshaw, 2008). Los efectos no lineales en la corriente interna se equilibran por los no hidrostáticos y, en menor extensión, la dispersión de Coriolis que da lugar a un paquete de ondas solitarias de rango ordenado de unas pocas docenas de pulsos que se desplazan a sus propias velocidades individuales (Gerkema and Zimmerman, 1995; Gerkema, 1996; Apel, 2002).

Estas ondas no sinusoidales de alta frecuencia mantienen su forma (los efectos de no linealidad y dispersión se contrarrestan) y viajan con los más grandes, más rápidos y más largos solitones en la parte delantera de la secuencia. Por lo tanto, las ondas que avanzan en primer lugar presentan distancias más largas entre solitones sucesivos en comparación con los pulsos adyacentes en la parte trasera.

8. SUMMARY OF THE THESIS IN SPANISH

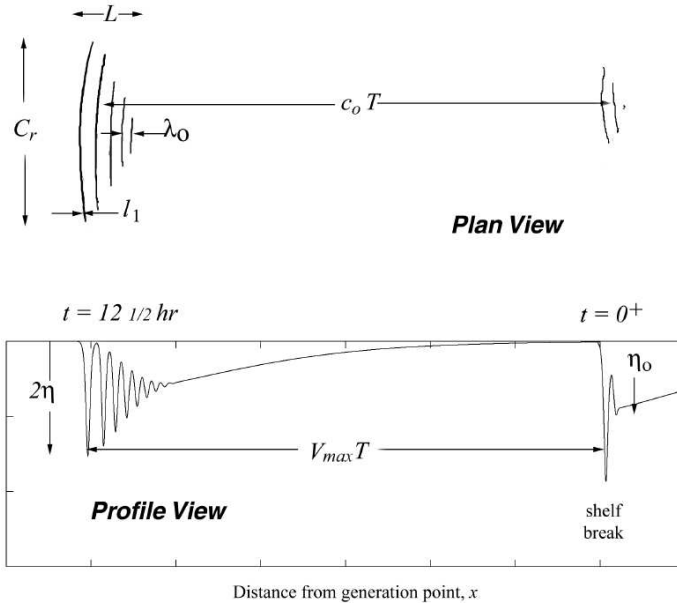


Figure 8.12: Esquema de paquetes de solitón canónico - Diagrama de paquetes de solitones que muestran la notación para las escalas de longitud (véase la tabla 4.1 para los valores típicos de los solitones de la plataforma continental). $V_{max}T$ es la longitud de onda interna; c_0T es la distancia entre los centroides de paquetes. [De Apel (2002) - Fig. 2].

Una idealización de un paquete de ondas solitarias generado sobre el talud continental se muestra en la Figura 8.12 de Apel (2002), detallando sus principales componentes. La vista superior de la Figura 8.12 presenta la evolución de dos paquetes de ondas solitarias formados durante dos ciclos sucesivos de marea (el paquete más a la izquierda se generan durante el ciclo de las mareas en primer lugar). Cada paquete se alarga y aumenta su número de solitones individuales en el tiempo. De forma complementaria, la vista de perfil de la Figura 8.12 muestra solitones como desplazamientos verticales de la interfaz que constituye dos paquetes diferentes que cambian su perfil cuando se propagan fuera de la zona de generación. La distancia observada entre los paquetes se denomina en este contexto como la longitud de onda ‘de la marea interna’. La velocidad teórica no lineal de los principales solitones V_{max} (Ver perfil en la

8.2 Ondas Internas Solitarias en el Océano

figura 8.12) se define para esa longitud de onda, la amplitud y el período de marea, T . Los valores típicos para solitones en la plataforma continental están dados por Apel (2002) como referencia (véase la Tabla 4.1), suponiendo que el mar en la plataforma está estratificado aproximadamente en una configuración de dos capas siendo h_1 la capa superior y h_2 la capa inferior.

Característica	Símbolo	Escala
Longitud del paquete	L (km)	1 - 10
Factor de amplitud	$2\eta_0$ (m)	-15
Profundidad de la capa superior	h_1 (m)	20 - 35
Profundidad de la capa inferior	h_2 (m)	30 - 200
Velocidad de onda larga	c_0 (m s ⁻¹)	0.5 - 1.0
Máxima longitud de onda	λ_{max} (m)	100 - 1000
Longitud de cresta	C_r (km)	0 - 30
Longitud de onda interna de marea	$D = VT$ (km)	15 - 40
Ancho característico del solitón	l_1 (m)	100

Table 8.1: Escalas típicas para solitones de plataforma - Valores típicos de solitones en plataformas continentales suponiendo que el mar en la plataforma está aproximadamente estratificado en dos capas siendo h_1 la superior y h_2 la inferior. [De Apel (2002) - Tabla 1.1].

Un ejemplo bien conocido de ondas solitarias en el océano se muestra en Stanton and Ostrovsky (1998) donde los solitones se propagan en las aguas poco profundas del norte de Oregon (Figura 8.13-izquierda). Las observaciones muestran claramente cómo la marea interna se inclina y desarrolla un borde no lineal. Las ondas resultantes se consideran altamente no lineales debido a grandes desplazamientos hacia abajo (de hasta 25 m) en comparación con la profundidad sin perturbaciones de la pycnoclina (~ 7 m).

8. SUMMARY OF THE THESIS IN SPANISH

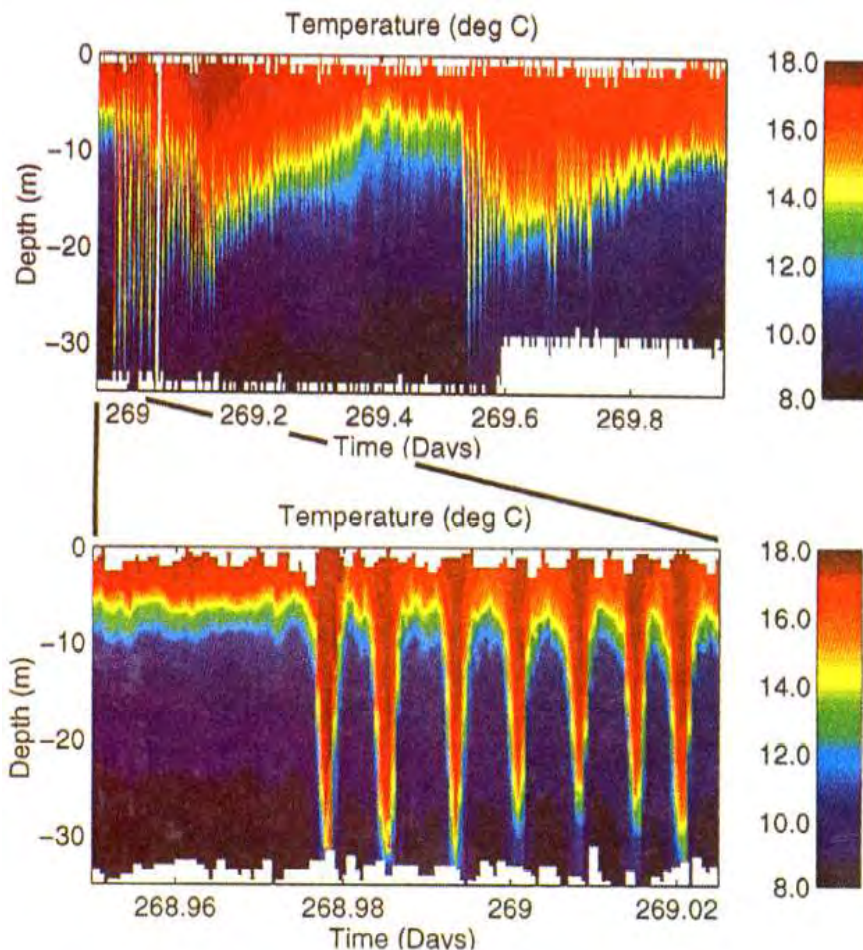


Figure 8.13: Ondas solitarias sobre la plataforma de Oregon - (a) Serie temporal de la temperatura de la superficie a 35 m de profundidad medida por el analizador de microestructura Loose-tethered (LMP) a lo largo un período de un día. La escala de 10°C se muestra a la derecha del panel. El desplazamiento de la marea interna semidiurna de baja frecuencia se puede ver claramente a lo largo de la isoterma en amarillo. (b) Serie temporal del perfil de las primeras 1.7 horas de la serie de tiempo que se muestra en (a). Las áreas blancas indican ausencia de datos. [De Stanton and Ostrovsky (1998) - Figura 1].

En tanto que la generación de solitones está vinculada a la actividad de marea interna, los paquetes de ondas solitarias exhibirán la misma variabilidad

que las mareas, y por lo tanto las propiedades de los solitones generados variará en ciclos semidiurnos, diurnos, quincenales y semestral. Por lo tanto se puede esperar, por ejemplo, solitones más grandes durante las mareas de primavera que durante las mareas muertas (Pingree and Mardell, 1985). Dependiendo del lugar y la hora, la generación de onda solitaria puede ser incluso posible sólo durante las mareas vivas, estando ausente en mareas muertas (Apel et al., 1985; Osborne and Burch, 1980).

Un caso ilustrativo de solitones de gran amplitud generados a partir de una dorsal se producen en el mar de Sulu (Apel et al., 1985; Liu et al., 1985). El área de estudio se muestra en la parte izquierda de la Figura 8.14.

El mecanismo consiste en la liberación de una marea interna en modo-bajo en la dorsal del Banco Pearl (Figura 8.14 - Lado derecho: a - b). Así, a medida que la marea interna se propaga, juegan su papel los efectos no lineales de inclinación y dispersión que llevan a la aparición de ondas solitarias distribuidas en paquetes separados por ciclos de mareas (Figura 8.14 - Lado derecho: c - d).

El mecanismo de generación sobre el talud continental y sobre un promontorio superficial (dorsales, bancos, montes submarinos, ...) es similar; sin embargo los solitones que se propagan hacia el océano evolucionan de manera diferente que los que viajan hacia la costa ya que los primeros están generalmente fuera de la zona controlada por la batimetría. Por lo tanto, la propagación de las ondas solitarias en la plataforma, donde baja la profundidad de la picnoclina y disminuye la profundidad del agua, está condicionada por los efectos de fricción del fondo. Esto conduce a la refracción de las ondas, impulsando el paquete de crestas a lo largo de las isóbatas y disminuyendo sus amplitudes, velocidades y longitudes de onda, independientemente de donde se generaron los solitones.

Un claro ejemplo de la refracción de ondas solitones debido a descensos en la profundidad del agua se puede encontrar en Zeng and Alpers (2004) para ondas solitarias que viajan hacia aguas poco profundas, de nuevo en el mar

8. SUMMARY OF THE THESIS IN SPANISH

de Sulu (Figura 8.15).

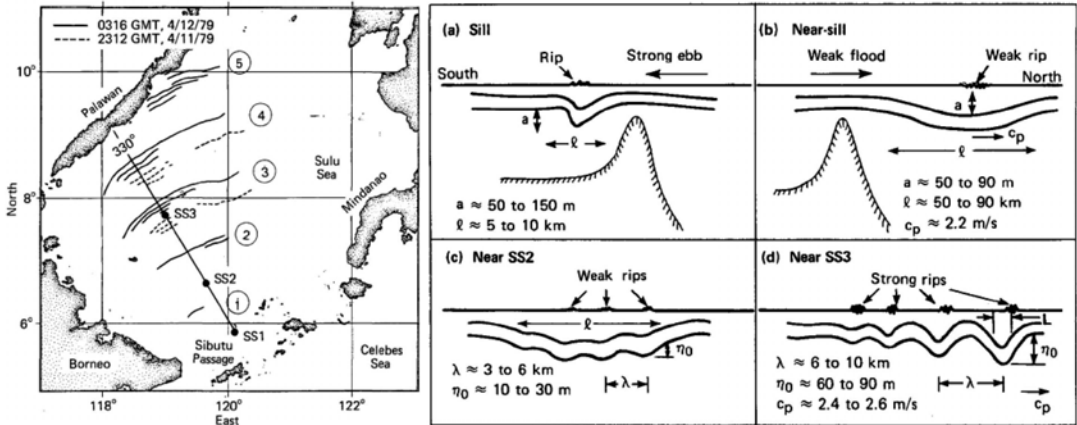


Figure 8.14: Evolución de un paquete de solitones en el Mar de Sulu - Composición de dos Figuras documentadas en Apel et al. (1985). Lado izquierdo: línea que muestra representaciones de DMSP (Programa de Defensa de meteorología por satélite), interpretando las estrías como la firma en superficie de paquetes de ondas internas solitarias. Varios solitones se producen en cada grupo, y hasta cinco paquetes son visibles en las imágenes. La distancia entre paquetes varía de 56 a 198 km, en función del azimut y la fase de marea quincenal. Las distancias entre solitones, que definen longitudes de onda, varían de 5 a 16 km. Dos imágenes diferentes de DMSP producen velocidades de aproximadamente 2.4 m s^{-1} . Lado derecho: Diagrama esquemático que resume la evolución de un paquete solitón en el Mar de Sulu: (a) En la región de la dorsal se produce un salto hidráulico interno por reflujo fuerte (hacia el sur) que fluye sobre la dorsal del Banco Pearl. (b) Dado que el flujo de mareas cambia a un flujo débil, una amplia depresión termoclina se mueve sobre la dorsal, propagándose hacia el norte. (c) Finalmente, las ondas solitarias comienzan a formarse en esta depresión, a medida que los efectos no lineales y dispersivos comienzan a equilibrarse. (d) Después de recorrer una distancia de aproximadamente 200 km el paquete solitón está bien desarrollado. Se muestran las escalas típicas. [De Apel et al. (1985): Lado derecho de la Fig. 13 y Fig. 25].

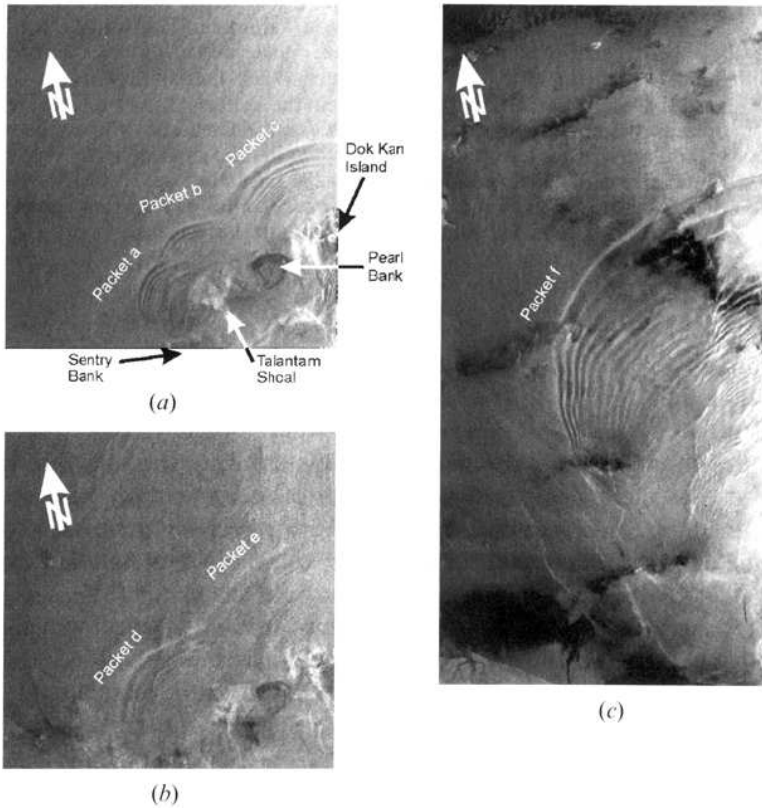


Figure 8.15: Imágenes de teledetección SAR (Synthetic Aperture Radar) de solitones en el Mar de Sulu - (a) Imagen SAR ERS-2 adquirida durante la órbita 14529 el 30 de enero de 1998, a las 02:24 UTC, que muestra las manifestaciones superficiales del mar de tres paquetes de ondas internas generadas en tres lugares diferentes, (b) Imagen ERS-2 SAR de la misma zona, pero adquirida durante su órbita 09018 el 10 de enero de 1997, a las 02:24 UTC, que se encontraba en una fase ligeramente posterior del ciclo de las mareas, (c) Imagen ERS-2 SAR adquirido durante la órbita 06284 el 3 de julio de 1996, a las 02:27 UTC mostrando fuerte refracción de ondas solitarias internas por la topografía del fondo. [De Zeng and Alpers (2004) - Figura 1].

Sin embargo, los paquetes de ondas solitarias se han observado también que viajan hacia el océano lejos de la plataforma y áreas con promontorios (por ejemplo, solitones en el Golfo de Vizcaya (Gerkema, 2001; New and da Silva, 2002)). Estos solitones responden a un mecanismo de generación diferente.

8. SUMMARY OF THE THESIS IN SPANISH

Entonces, debemos tener en cuenta que la energía de marea interna se puede irradiar tanto en distancia horizontal como ondas interfaciales en la termoclina (mecanismo explicado anteriormente y que se denomina ‘generación directa’) y/o verticalmente como ‘vigas’ hacia el continuo estratificado inferior (mecanismo conocido como ‘generación local’). Estas vigas emanan de topografías críticas en las que la pendiente del fondo coincide con la pendiente de las trayectorias de rayos y viajan en un ángulo respecto a la vertical en el océano profundo. Después de la reflexión desde el fondo del mar, la dispersión de estos haces en la base de la termoclina inducen la generación de ondas internas solitarias que se propagan a largas distancias desde el borde de la plataforma o promontorio que causó la viga inicial de energía interna mareas (New, 1990; Gerkema, 2001; Da Silva and New, 2009). Otro posible mecanismo de generación de solitones incluye la inestabilidad del flujo cortante justo corriente arriba de la dorsal (Farmer and Armi, 1999), aguas arriba del bloqueo (Lee and Beardsley, 1974), o de una generación transcítica (Grimshaw, 1986; Melville and Helfrich, 1987).

Como se puede imaginar, una mejor comprensión de los mecanismos dominantes por los que se generan solitones se beneficiarán de la evaluación de las áreas candidatas para la actividad de los solitones. Además, el interés de los solitones oceánicos se apoya por el impacto que estas ondas tienen sobre diversos aspectos: mezcla oceánica y productividad biológica (Sandstrom and Elliott, 1984; Pinkel, 2000; Sangrà et al., 2001; Moum et al., 2003; Macias et al., 2006), la acústica del agua (Tiemann et al., 2001), el transporte de sedimentos (Sandstrom and Elliott, 1984; Bogucki et al., 1997; Butman et al., 2006), plataformas petroleras (Osborne and Burch, 1980), etc. La incertidumbre acerca de la importancia relativa de cada mecanismo generador a escala global hace que los solitones oceánicos aún represente un trabajo de campo desafiante. Se pueden encontrar buenas revisiones de los trabajos empíricos y teóricos sobre solitones en Ostrovsky and Stepanyants (1989); Grimshaw et al. (1998); Apel (2002); Apel et al. (2006); Helfrich and Melville (2006).

El arranque para la siguiente sección está relacionada con el primer informe

científico que describe la manifestación superficial de una onda solitaria, que fue hecha por J. Scott Russell en 1838 en un montículo solitario en un canal escocés (Russell, 1838b,a). Medio siglo más tarde, Korteweg y de Vries proporcionaron por primera vez una explicación teórica de este fenómeno importante en el campo de la física matemática (Korteweg and de Vries, 1895). Este trabajo abre una línea de investigación en todo el estudio de las propiedades de solitones desde un punto de vista teórico cuyo interés persiste en el tiempo. A continuación nos centramos en la introducción de la teoría de la onda solitaria que es de principal interés para esta tesis doctoral.

8.2.2 Descripción Matemática de los Solitones

Para establecer el alcance de la presente tesis, primero discutimos la teoría de una onda solitón sobre la base de las aplicaciones de la ecuación cuadrática Korteweg-de Vries (KdV) y su versión ampliada cúbica (eKdV), que describen las características dominantes y la evolución de los solitones bajo condiciones débiles (KdV) y más fuertemente no lineales (eKdV), respectivamente, dado un perfil inicial. Los modelos teóricos tradicionalmente se construyen a partir de la situación más simplificada posible, que se vuelve más completa mediante la inclusión de nuevos elementos en la modelización del proceso a medida que se entiende el estado anterior. En la teoría de onda solitaria, no es de extrañar que los modelos de tipo KdV se hayan convertido en el enfoque clásico para describir las ondas no lineales dispersivas. Se han utilizado ampliamente en la literatura y muestran buen ajuste con las relaciones predominantes entre la velocidad de fase, amplitud y escalas de longitud de onda en comparación con las observaciones notificadas de los solitones oceánicos (Osborne and Burch, 1980; Pingree and Mardell, 1985; Ostrovsky and Stepanyants, 1989; Stanton and Ostrovsky, 1998; Xu and Yin, 2012). Además, permiten modelar el fenómeno de interés con un conjunto reducido de ecuaciones. Sin embargo, no todas las características cuantitativas están completamente bien captadas.

La ecuación Korteweg-de Vries (KdV) es un modelo cuadrático no lineal

8. SUMMARY OF THE THESIS IN SPANISH

que admite soluciones de onda solitaria conservando la forma en una dimensión y sobre la base de un equilibrio entre la no linealidad y los efectos dispersivos. Por simplicidad, aquí se discute la ecuación KdV en términos de un fluido de dos capas con una tapa rígida en la superficie, incluido el fondo y sin flujo medio (Djordjevic and Redekopp, 1978; Kakutani and Yamasaki, 1978), siguiendo

$$\frac{\partial \eta}{\partial t} + c_0 \frac{\partial \eta}{\partial x} + \alpha \eta \frac{\partial \eta}{\partial x} + \beta \frac{\partial^3 \eta}{\partial x^3} = 0 \quad (8.12)$$

donde t es el tiempo; x es la variable espacial en la dirección de propagación de la onda; h_1 (h_2) es el espesor de la capa superior (inferior); g es la aceleración gravitacional; $\eta(x, t)$ es el desplazamiento interfacial con respecto de su nivel de reposo, y α , β y c_0 son los llamados coeficientes ambientales del medio que describen la no linealidad, la dispersión y la larga longitud de onda de la velocidad de fase dados como

$$c_0^2 = \Lambda \rho g \frac{h_1 h_2}{h_1 + h_2}, \quad \alpha = \frac{3}{2} \frac{h_1 - h_2}{h_1 h_2} c_0, \quad \beta = \frac{1}{6} h_1 h_2 c_0, \quad (8.13)$$

con $\Lambda \rho = (\rho_2 - \rho_1)/\rho_2$. Además, las diferencias relativas en la densidad entre las dos capas ($\Lambda \rho$) se supone que es pequeña (aproximación de Boussinesq), lo que se obtiene en el océano con valores típicos del orden de 10^{-3} .

Esta ecuación KdV es aplicable en aguas poco profundas a los fluidos estratificados donde se supone que: 1) el desplazamiento interfacial es mucho menor (pero finito de amplitud) que la profundidad de cualquiera de las capas (es decir, no linealidad débil), y 2) las ondas son largas (pero de longitud finita) en comparación con la profundidad del fluido (es decir, la dispersión no hidrostática es débil). Por lo tanto, la ecuación KdV se escala por los parámetros pequeños $\alpha = a/H$ y $\beta = (H/l)^2$ de tal forma que ambos son

pequeños y de orden comparable ($\beta = O(\alpha) \ll 1$); tomando a como una medida de la amplitud de la onda, l como la escala de longitud de onda, y H como la escala vertical intrínseca. El límite en el que las ondas son infinitesimales ($\alpha \rightarrow 0$ conduce a la linealidad) y de longitud infinita ($\beta \rightarrow 0$ conduce a hidrostacia) se reduce a 8.12 para $\frac{\partial \eta}{\partial t} + c_0 \frac{\partial \eta}{\partial x}$, que se limita a describir las ondas que viajan hacia la derecha. Dondequiera que las ondas se supone que son pequeñas, pero de amplitud finita y de longitud de onda larga pero finita, los parámetros α y β toman valores diferentes a cero para incluir, respectivamente, efectos dispersivos no lineales y no hidrostáticos en la ecuación de evolución KdV.

La solución prototípica analítica a la ecuación KdV para un sólo solitón es el perfil secante hiperbólico, que dice

$$\eta(x, t) = \eta_0 \operatorname{sech}^2 \left(\frac{x - ct}{\lambda} \right) \quad (8.14)$$

donde c es la velocidad de fase no lineal derivada de la teoría KdV y relacionada con la velocidad de fase lineal c_0 y amplitud, y λ es la anchura característica del solitón, que está relacionada con la amplitud de desplazamiento de la η_0 y los coefficients ambientales:

$$c = c_0 + \frac{\alpha \eta_0}{3}, \quad \lambda^2 = \frac{12\beta}{\alpha \eta_0} \quad (8.15)$$

Como λ^2 debe ser positivo, para una delgada capa superior con $h_1 < h_2$ tenemos que $\alpha < 0$, lo que se traduce en desplazamientos hacia abajo de la interfaz entre las capas ($\eta < 0$). Por otro lado, si la capa inferior asciende, de tal manera que $h_2 < h_1$, entonces los solitones se revierten a desplazamientos hacia arriba ($\alpha < 0$, $\eta < 0$). En la configuración en la que $h_1 = h_2$, el coeficiente de no linealidad cuadrática α se desvanece y se debe incluir en

8. SUMMARY OF THE THESIS IN SPANISH

la ecuación KdV un coeficiente de no linealidad de orden superior (cúbico) (Djordjevic and Redekopp, 1978; Kakutani and Yamasaki, 1978), dando lugar a su versión ampliada (eKdV):

$$\frac{\partial \eta}{\partial t} + (c_0 + \alpha \eta + \alpha_1 \eta^2) \frac{\partial \eta}{\partial x} + \beta \frac{\partial^3 \eta}{\partial x^3} = 0 \quad (8.16)$$

donde el coeficiente α_1 , ausente en la ecuación KdV (8.12), es el mencionado coeficiente de no linealidad cúbica

$$\alpha_1 = \frac{3c_0}{(h_1 h_2)^2} \left[\frac{7}{8} (h_1 - h_2)^2 - \left(\frac{h_2^3 + h_1^3}{h_1 + h_2} \right) \right] \quad (8.17)$$

Se debe hacer notar que mientras que el signo de α depende de la profundidad de la capa, resulta que α_1 es siempre negativo. Como el término cúbico α_1 es $O(\alpha^2)$, el eKdV formalmente debe incluir también términos adicionales dispersivos y no lineales dispersivos de orden $O(\beta^2)$ y $O(\alpha\beta)$, respectivamente, para equilibrar los efectos no lineales y dispersivos en un orden más alto de la ecuación KdV (Koop and Butler, 1981; Lamb and Yan, 1996; Grimshaw et al., 2002). Sin embargo, si el coeficiente cuadrático no lineal α es del orden de $O(\alpha)$ (es decir, los efectos no lineales cuadráticos son pequeños), como ocurre cuando $|h_1 - h_2| / (h_1 h_2) \ll 1$, entonces el eKdV es asintóticamente consistente, pero exige el balance $\beta = O(\alpha^2)$ (Helfrich and Melville, 2006).

La ecuación modificada KdV (mKdV) aparece cuando la interfaz se encuentra en la relación de espesor crítico ($h_1 = h_2$) y el coeficiente cuadrático no lineal α es cero. Entonces la ecuación (8.16) se reduce a

$$\frac{\partial \eta}{\partial t} + (c_0 + \alpha_1 \eta^2) \frac{\partial \eta}{\partial x} + \beta \frac{\partial^3 \eta}{\partial x^3} = 0 \quad (8.18)$$

Kakutani and Yamasaki (1978) encontraron que la no linealidad de la ecuación cúbica mKdV gobierna las ondas largas de gravedad no lineales en la relación de espesor crítico, mientras que cerca de ésta la no linealidad se rige por la ecuación de una forma combinada de las ecuaciones KdV y KdV modificada.

El comportamiento de la ecuación de onda solitaria eKdV (Kakutani and Yamasaki, 1978; Ostrovsky and Stepanyants, 1989; Gerkema and Zimmerman, 2008) puede ser descrito por

$$\eta(x, t) = \frac{\eta_0}{b + (1 - b)\cosh^2\gamma(x - ct)}, \quad (8.19)$$

donde

$$c = c_0 + \frac{\eta_0}{3} \left(\alpha + \frac{1}{2} \alpha_1 \eta_0 \right), \quad \gamma^2 = \frac{\eta_0 \left(\alpha + \frac{1}{2} \alpha_1 \eta_0 \right)}{12\beta}, \quad (8.20)$$

$$b = \frac{-\eta_0 \alpha_1}{2\alpha + \alpha_1 \eta_0}, \quad Lw = \eta_0^{-1} \int_{-\infty}^{\infty} \eta dx \quad (8.21)$$

siendo η_0 una medida de la amplitud máxima del solitón; Lw es el ancho característico de la onda; c , la velocidad de fase no lineal derivada de la teoría eKdV; y b y γ son los parámetros que definen el sistema.

La Figura 8.16 muestra ondas solitarias eKdV próximas a su máxima amplitud y convirtiéndose planas en su parte superior, una ruptura radical con el clásico solitón KdV que no tiene límite matemático formal a su amplitud.

Como se señaló anteriormente, en el marco del modelo de dos capas, α_1 es siempre negativo (8.17). Sin embargo, para estratificaciones más generales

8. SUMMARY OF THE THESIS IN SPANISH

y flujo con cizalla de fondo el coeficiente no lineal cúbico puede ser negativo o positivo. En este último caso, las soluciones de solitón de ambas polaridades positivas y negativas pueden existir independientemente del signo de α (Grimshaw et al., 1997, 2004).

KdV cúbico, aunque incluye altas no linealidades, todavía se basa en una expansión de un parámetro pequeño ($\alpha = a/H$) y también lo es todavía sujeto a la suposición de linealidad débil. Un cambio radical útil y bien conocido del modelo KdV débilmente no lineal de dos capas fue derivado por Miyata (1985, 1988) y Choi and Camassa (1999). El resultado de su trabajo fue un conjunto equivalente de ecuaciones de ondas bi-direccionales con no linealidad *completa*, $\alpha = O(1)$ y efectos débiles dispersivos de primer orden, $\beta \ll 1$.

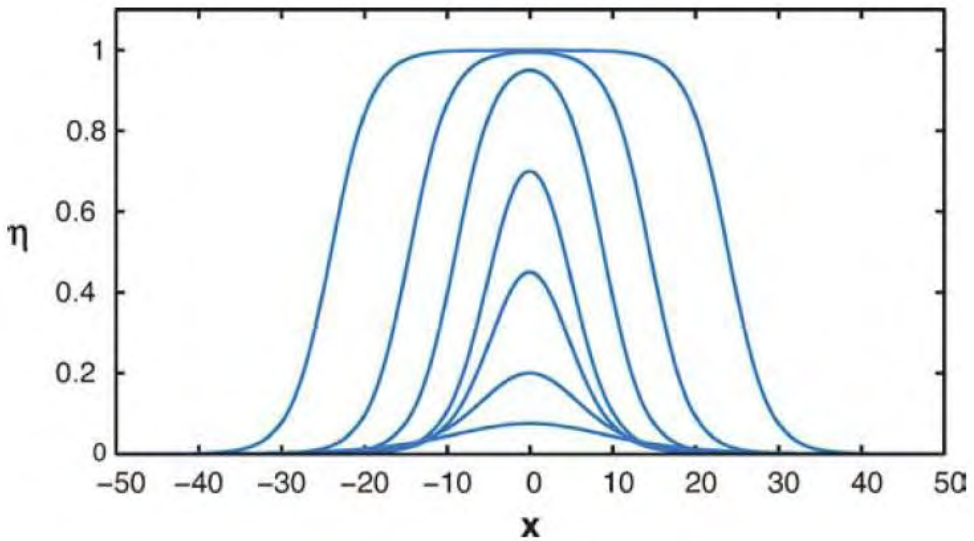


Figure 8.16: Soluciones de ondas solitarias de la ecuación eKdV - Ejemplos de soluciones de onda solitarias de la ecuación eKdV (Ecuación 6) para la elección arbitraria de los parámetros $\beta = \alpha = \alpha_1$. A medida que aumenta la amplitud máxima de las ondas, las ondas eventualmente amplian y desarrollan una cresta plana en la amplitud máxima de $\eta_{0,max} = 1$ [De Helfrich and Melville (2006) - Figura 4].

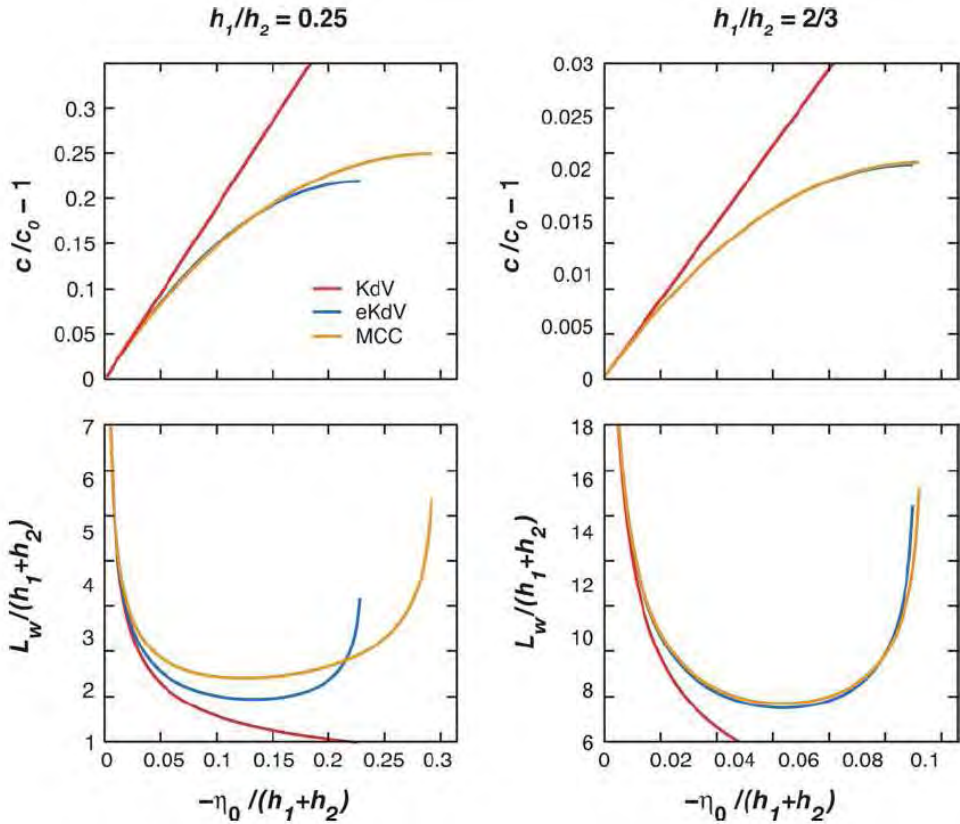


Figure 8.17: Comparativa de las teorías KdV y MCC - Comparación de las propiedades de ondas solitarias de las teorías KdV de dos capas (rojo), eKdV (azul), y MCC (naranja). La fila superior muestra la velocidad de la onda c vs amplitud η_0 , y la fila inferior muestra la longitud de onda (aquí se lee el ancho característico de la onda para el solitón) L_w vs η_0 . La comparación se hace con las dos estratificaciones $h_1/h_2 = 1/4$ (columna izquierda) y $h_1/h_2 = 2/3$ (columna derecha). Para las ondas eKdV y MCC la amplitud de onda máxima se corresponde con la salida de la curva de velocidad. [De Helfrich and Melville (2006) - Figura 5].

Helfrich and Melville (2006) destacaron con la Figura 4.6 la desviación entre los modelos débilmente no lineal KdV, el más fuertemente no lineal eKdV y el *completamente* no lineal Miyata-Choi-Camassa (MCC). La dependencia de la

8. SUMMARY OF THE THESIS IN SPANISH

amplitud con la velocidad de la onda c y el ancho de onda característico Lw ¹ para los tres modelos se muestra para dos capas de diferente espesor ($h_1/h_2 = 1/4$ y $h_1/h_2 = 2/3$) en un sistema de dos capas de fluidos.

Surgen diferencias notables al comparar el resultado de los modelos débilmente no lineal KdV y de los fuertemente no lineales eKdV y MCC, para ambas c y Lw , incluso para amplitudes relativamente pequeñas. Las soluciones de onda solitarias de la eKdV y las ecuaciones de MCC aumentan su velocidad de fase c con amplitud cada vez mayor hasta que comienzan a disminuir cuando se acercan a su máximo de η_{0max} (Figura 8.17 - fila superior). Por el contrario, las soluciones de KdV muestran velocidad de fase creciente linealmente con la amplitud. También cabe señalar que la amplitud de onda máxima tanto para el eKdV y para el MCC se corresponde con el final de las curvas de velocidad (lo que no ocurre con solitones KdV).

Como ya se ha mostrado en la Figura 8.16 para ondas solitarias eKdV, su ancho de onda característico se estrecha a medida que crecen (aumentando η_0) para ampliarse finalmente cuando se alcanza el límite superior (η_{0max}). Este comportamiento también es exhibido por la teoría MCC (Figura 8.17 - fila inferior), a diferencia de las ondas clásicas KdV solitarias cuyo ancho de onda se estrecha a medida que se hacen más grandes hasta su máxima amplitud.

En su conjunto, la comparación de las formas de onda y propiedades entre las teorías eKdV y MCC indica un buen ajuste para $0.4 < h_1/(h_1h_2+) < 0.6$, cuando los requisitos de escala de eKdV se alcanzan razonablemente (Helfrich and Melville, 2006). Fuera de este rango, las diferencias entre las dos teorías comienzan a crecer (ver Figura 8.17 - columna de la izquierda, fila inferior).

Como hemos descrito, la ecuación Korteweg-de Vries (KdV) y su versión ampliada (eKdV) sin términos de forzamiento incluidos, constituyen una herramienta apropiada para el estudio de la evolución de un determinado perfil inicial bajo condiciones débilmente no lineales (KdV y eKdV). Para ir a la configuración fuertemente no lineal, se deben utilizar ecuaciones del tipo MCC.

¹En las ondas solitarias KdV $Lw = 2\gamma^{-1}$.

Pero para estos no existe un modelo que incluya un mecanismo de forzamiento. El objetivo principal de los capítulos siguientes es ampliar el modelo MCC para incluir el mecanismo de forzamiento por las mareas barotrópicas sobre topografía.

A lo largo de la siguiente sección, se discuten la base y el alcance de la presente tesis.

8.2.3 Marco del estudio, Objetivos y Metodología

Ahora nos interesa incluir un elemento de forzamiento en el sistema para reproducir la generación y evolución de los solitones completamente no lineales débilmente no hidrostáticos en un océano rotando a través de la desintegración de una corriente interna de modo bajo liberada por la interacción con la topografía. Sin embargo, la interacción marea-topografía da lugar a ondas que se propagan en dos direcciones (hacia la izquierda y hacia la derecha del obstáculo topográfico) y la teoría KdV describe las ondas que viajan en una dirección única. Adicionalmente, se debe incluir la dispersión de Coriolis, que no se contabiliza en (e)KdV. Por lo tanto, los modelos de tipo KdV no son adecuados para ser generalizados para la inclusión de este mecanismo de forzamiento. Vamos a utilizar un punto de partida diferente al de la ecuación de Korteweg-de Vries. El marco de nuestro modelo de generación será la de Euler con ecuaciones de continuidad, que no se limita unidireccionalmente. A continuación se discuten las principales hipótesis y aproximaciones adoptadas en nuestro estudio, su validez y, por tanto, el alcance de la generación del modelo resultante. Sin embargo, para mayor claridad, vamos a recordar las hipótesis y aproximaciones de nuevo en el *Capítulo 5*.

Elegimos la configuración más simple posible, ampliamente utilizada en la literatura para modelos análogos: un sistema de dos capas de fluido en la que cada capa consta de un fluido homogéneo e incompresible y no viscoso. Esta configuración es compatible con nuestro estudio, ya que puede describir el primer modo de una marea interna (Gerkema, 1994), y estamos interesados

8. SUMMARY OF THE THESIS IN SPANISH

en la generación de ondas internas solitarias por la desintegración de la marea interna de modo bajo (aquí se descarta la generación de solitones por vigas internas de marea).

Se consideran las ondas que se propaguen en la dirección x . Con la rotación, se producirá el movimiento en la dirección transversal y ; sin embargo, una mayor simplificación consistirá en omitir las dependencias transversales (por lo tanto consideramos ondas planas). De lo contrario, la derivación del modelo tendría que enfrentarse con ecuaciones más complicadas que podrían no compensar la mejora en los resultados.

Las diferencias relativas de la densidad en el océano son extremadamente pequeñas (valores típicos son del orden de 10^{-3}), por lo que en términos de un sistema de dos capas podemos aplicar la aproximación de Boussinesq ($\Delta\rho = (\rho_2 - \rho_1)/\rho_2 \ll 1$). Además, se excluye cualquier movimiento en la superficie superior con una tapa rígida lo que nos permitirá reducir el conjunto de ecuaciones de evolución.

El forzamiento para la generación de la corriente interna consiste en una oscilación de fondo no plano que simula un flujo de marea barotrópico sobre topografía. Posteriormente, los solitones son generados por desintegración fuertemente no lineal del primer modo de la marea interna, con ondas adoptadas para ser larga en comparación con la profundidad total de fluido (ondas dispersivas débilmente no hidrostáticas).

La dispersión debida a la rotación de la Tierra no se puede despreciar, ya que la longitud de onda de las mareas internas son del orden del radio de Rossby 'interno de deformación' (c_0/f). Por lo tanto, incluimos estos efectos mediante el uso de la denominada aproximación en plano- f . Por lo tanto, en su conjunto, nuestro sistema incluye efectos dispersivos debido a la dispersión débilmente no hidrostática y de Coriolis.

Por lo tanto, nuestro enfoque teórico nos permite estudiar la generación y evolución de las ondas interfaciales no lineales en el límite de las ondas largas no lineales débilmente no hidrostáticas. Las fuertes no linealidades surgen a

través de la desintegración de una marea interna de bajo modo liberada por interacción con la topografía en un océano en rotación. Los efectos dispersivos incluyen la dispersión débil no hidrostática y de Coriolis (debido a la rotación de la Tierra). En ausencia de un mecanismo para la generación de la marea interna y despreciando los efectos de rotación de la Tierra, nuestro conjunto de ecuaciones se reduce a un equivalente Choi & Camassa.

La interpretación de un modelo matemático como el que nos ocupa aquí es siempre más fácil si las soluciones analíticas son viables; sin embargo, aun cuando la resolución del análisis es factible, a veces es complicado porque las ecuaciones se vuelven extremadamente complicadas y confunden la física detrás de este fenómeno. En nuestro caso, la resolución numérica representa un tratamiento más adecuado para explorar el modelo teórico y su comportamiento.

8.3 Conclusiones y Trabajo Futuro

Para finalizar, en esta sección se presentan las principales conclusiones y contribuciones de la presente tesis doctoral al ‘estado del arte’ en el estudio de los dos fenómenos oceanográficos objeto de este estudio de doctorado. Además, se sugieren aquellas líneas de investigación futuras que pueden beneficiar el conocimiento de dicho fenómenos.

I Oscilaciones forzadas por las brisas tierra-mar

- 1 La varianza de las corrientes diurno-inerciales en el Golfo de Cádiz y en el Golfo de Valencia muestran un patrón estacional con valores máximos en verano de hasta un orden de magnitud superiores a los estimados para invierno. Los resultados de nuestro análisis de wavelet rotatoria sugieren que las oscilaciones forzadas por las brisas son responsables de la generación y acumulación de dicha energía en las latitudes críticas para la resonancia diurno-inercial.
- 2 La varianza de las corrientes inerciales en el Cabo Peñas muestra un patrón estacional con valores máximos en verano; no obstante, su intensidad es menor que la observada en el Golfo de Cádiz y en el Golfo de Valencia. Los resultados de nuestro análisis de wavelet rotatoria sugieren que esto se debe a que Cabo Peñas se encuentra fuera de las latitudes críticas para la resonancia diurno-inercial.
- 3 Un análisis de los procesos de mezcla diapicna asociados a las oscilaciones forzadas por las brisas en latitudes críticas para la resonancia (Bahía de Setúbal), muestra evidencia de un aumento de energía diurno-inercial disponible para favorecer la mezcla vertical en flujos estratificados y con alta cizalla vertical con valores subcríticos de Ri . Esta investigación también sugiere que puede existir un control interno de la respuesta del océano a las brisas debido a la profundización y el

8. SUMMARY OF THE THESIS IN SPANISH

suavizado de la picnoclina impulsado por procesos de mezcla diapicna.

- 4 Trabajo Futuro: Obtener y analizar series de datos temporales (corrientes, temperatura y salinidad) que cubran la totalidad de la columna de agua en combinación con datos *in situ* simultáneos de viento para estudiar la evolución temporal y espacial de las oscilaciones forzadas por las brisas, con especial atención al papel que juegan los procesos de mezcla diapicnos en la estabilidad de la estructura vertical de estas corrientes forzadas. En este sentido, también encontramos que mediciones de la tasa de disipación de energía cinética turbulenta con una microperfilador de turbulencia costera ayudarán en la evaluación de los procesos de mezcla diapicna promovidos por las oscilaciones forzadas por las brisas.

II Ondas internas solitarias de origen mareal fuertemente no lineales

- 1 Se ha derivado con éxito un nuevo modelo para el estudio de ondas internas solitarias de origen mareal fuertemente no lineales.
- 2 Las simulaciones numéricas realizadas validan el modelo como una herramienta útil para el estudio de ondas internas solitarias de origen mareal fuertemente no lineales. Es importante destacar que el modelo reproduce, bajo condiciones críticas de fuerte no-linealidad, solitones en el límite de amplitud alcanzando la característica forma de meseta; así como la aparición de solitones en condiciones extremas como un sistema bicapa donde ambas capas tienen el mismo espesor.
- 3 Trabajo Futuro: Simulaciones numéricas que permitan comparaciones con datos observacionales en el océano.

Appendix A

Rotary Wavelet Method

The programs we use to apply the rotary wavelet method are based on modifications made by Hormazábal et al. (2004) to the original wavelet software (<http://paos.colorado.edu/research/wavelets/>) provided by Torrence and Compo (1998).

The content of this appendix is for the most part borrowed from *Appendix A* in Hormazábal et al. (2004) and Torrence and Compo (1998), though it has been summarized and adapted to be focused on the requirements of our research.

A.1 Rotary Wavelet Power Spectrum

The rotary wavelet power spectrum measures the time series variance of a vector at each period and each time for both the positive (counterclockwise) and negative (clockwise) rotation components. Starting from a complex discrete time series $x_n = u_n + iv_n$ with zero mean, constant time spacing δt , and time index $n = 0, \dots, N - 1$, the discrete Fourier transform develops as

$$\hat{x}(\omega_k) = \frac{1}{N} \sum_{n=0}^{N-1} x_n e^{-i\omega_k n \delta t} \quad k = 0, \dots, N - 1, \quad (\text{A.1})$$

A. ROTARY WAVELET METHOD

where N is the number of time steps in the time series, k is the frequency index, and ω_k is the angular frequency, which is defined as

$$\omega_k = \begin{cases} \frac{2\pi k}{N\delta t} & k \leq \frac{N}{2}, \\ -\frac{2\pi k}{N\delta t} & k > \frac{N}{2}. \end{cases} \quad (\text{A.2})$$

These positive ($+\omega_k$) and negative ($-\omega_k$) frequencies correspond to two dimensional vectors rotating counterclockwise (CCW) and clockwise (CW), respectively, at the frequency $|\omega_k|$ Gonella (1972). To separate both signals in time-frequency space, we need a wavelet function able to capture both the positive and negative oscillations of the time series as separate peaks in wavelet power. We use the derivative of a Gaussian (DOG) wavelet whose Fourier transform (of the normalized function) is

$$\hat{\Psi}(s\omega_k) = \left(\frac{2\pi s}{\delta t}\right)^{\frac{1}{2}} \frac{-i^m}{\sqrt{\Gamma(m+0.5)}} (s\omega_k)^m e^{-\frac{(s\omega_k)^2}{2}} \quad m = 6, \quad (\text{A.3})$$

where $\sqrt{2\pi s/\delta t}$ is the factor that normalizes the wavelets (what ensure a total energy of unity), Γ is the gamma function, m is the derivative of the DOG wavelet function, and s is the wavelet scale, which is related to Fourier period through the relation $\lambda = 2\pi s/\sqrt{m+0.5}$ (Table 1 in Torrence and Compo (1998)).

Next, in order to obtain the CCW and CW wavelet transform in Fourier space, we separate positive and negative frequencies. For a given scale s and time $n\delta t$ the continuous wavelet transform is defined as the inverse discrete Fourier transform of a product of Fourier transforms. Then, we have the CCW wavelet transform given by

$$W_n^+(s) = \sum_{k=0}^{N-1} \hat{x}(\omega_k) \hat{\Psi}^*(s\omega_k) e^{i\omega_k n\delta t} \quad \hat{\Psi}^*(s\omega_k) = 0 \quad \omega_k < 0, \quad (\text{A.4})$$

and, the CW wavelet transform given by

$$W_n^-(s) = \sum_{k=0}^{N-1} \hat{x}(\omega_k) \hat{\Psi}^*(s\omega_k) e^{i\omega_k n \delta t} \quad \hat{\Psi}(s\omega_k) = 0 \quad \omega_k > 0. \quad (\text{A.5})$$

where the asterisk indicates the complex conjugate. Then, the rotary wavelet power spectra of the counterclockwise and clockwise components are obtained by multiplying each wavelet transform by its corresponding complex conjugate

$$S_n^+(s) = W_n^+(s) W_n^{+*}(s) \quad \omega_k \geq 0, \quad (\text{A.6})$$

$$S_n^-(s) = W_n^-(s) W_n^{-*}(s) \quad \omega_k \leq 0. \quad (\text{A.7})$$

The total wavelet power spectrum is defines as $S_n(s) = S_n^+(s) + S_n^-(s)$.

A.2 Rotary Coefficient

The rotation finally exhibited by the vector (counterclockwise or clockwise) is determined by the component containing the largest magnitude for a given frequency and time. If both components have equal magnitude, then the motions are rectilinear. As for rotary spectral analysis, the rotary coefficient can be defined as

$$r_n(s) = \frac{S_n^+(s) - S_n^-(s)}{S_n^+(s) + S_n^-(s)} \quad (\text{A.8})$$

and ranges from $r_n(s) = +1$ for a CCW gyre to $r_n(s) = -1$ for a CW gyre, and over $r_n(s) = 0$ for unidirectional motion (Emery and Thomson, 1998).

A.3 Statistical Significance Test

The null hypothesis for the significance of a peak in the wavelet power spectrum is defined (Torrence and Compo, 1998) as follows. We assume that the time series has a mean power spectrum given by a red or white noise background spectrum associated with the wavelet power spectrum. Whether a peak in the wavelet power spectrum is significantly above this background spectrum, it can be assumed that peak is a true feature with a certain percent confidence. For clarity, the reader should notice that ‘significant at the 5% level’ is equivalent to the ‘95% confidence *level*’ and involves a test against a certain background level. And, the ‘95% confidence *interval*’ refers to the range of confidence about a given value.

We model the wavelet transform for each scale and all times as a lag-1 autoregressive process to develop a statistical significance test for the wavelet power spectrum (Torrence and Compo, 1998). A simple model for red noise is the univariate lag-1 autoregressive [AR(1), or Markov] process:

$$x_n = \alpha x_{n-1} + z_n, \quad (\text{A.9})$$

where α is the assumed lag-1 autocorrelation, $x_0 = 0$, and z_n is taken from Gaussian white noise. Application of Gilman et al. (1963) leads to the red or white noise background spectrum associated with the wavelet power spectrum at a given time and scale following

$$P_k = \frac{1 - \alpha^2}{1 + \alpha^2 - 2\alpha \cos(2\pi k/N)}, \quad (\text{A.10})$$

where $k = 0N/2$ is the frequency index; $\alpha = (\alpha_1 + \sqrt{\alpha_2})/2$; and, α_1 and α_2 are the lag-1 and lag-2 complex autocorrelations, respectively. Hence, by choosing an appropriate lag-1 autocorrelation, one can use eq. (A.10) to model either a red-noise spectrum, or a white noise spectrum if $\alpha = 0$. In our research, we use the red noise background spectrum.

Next, the wavelet power spectrum distribution at each time n and scale s is given by

$$\frac{S_n(s)}{\sigma^2} \sim \frac{1}{2} P_k \chi_2^2, \quad (\text{A.11})$$

where the wavelet power spectrum is chi-square distributed with 2 degrees of freedom.

A.4 Cross-Rotary Wavelet Power Spectrum

The rotary wavelet analysis implies a separation of the vector time series for a specified period (scale) and time into CCW- and CW-rotating components. Hence, application of this analysis to two different vector time series which were measured simultaneously allow us to determine the similarity between the two times series in terms of their CW and CCW components in time-frequency space.

Thus, the corotating cross-rotary wavelet spectrum provides an estimate of the joint energy contained by two time series for rotating components in the same direction (e.g., the CW component of x with the CW component of y). With this objective, we define a set of corotating functions which provide this estimate.

Given two complex time series x and y with rotary wavelet transform $W_n^{\pm x}$ and $W_n^{\pm y}$, where n is the time index, s is the scale, and \pm represents a positive (CCW) and negative (CW) component, respectively, the corotating cross-wavelet spectrum follows

$$S_n^{\pm xy}(s) = W_n^{\pm x} W_n^{\pm y*}. \quad (\text{A.12})$$

A.5 Rotary Wavelet Coherence Squared Spectrum

The corotating wavelet coherence measures the correlation between rotary components of two different vector time series which are rotating in the same direction as a function of period (scale) and time. The coherence takes positive

A. ROTARY WAVELET METHOD

values $0 \leq \pm\gamma_n^2(s) \leq 1$ whereby coherences near zero indicate a negligible relationship between corotating components, while coherences near unity indicate a high degree of similarity.

The corotating coherence squared, $\pm\gamma_n^2(s)$, between the rotary component of two different vector time series measured simultaneously, is given by

$$\pm\gamma_n^2(s) = \frac{|\langle s^{-1}S_n^{\pm xy}(s) \rangle|^2}{\langle s^{-1}S_n^{\pm x}(s) \rangle \langle s^{-1}S_n^{\pm y}(s) \rangle}, \quad (\text{A.13})$$

where $\langle \rangle$ indicates smoothing in time and scale, and the factor s^{-1} converts the wavelet power to energy density. The smoothing for the complex cross-wavelet spectrum is performed separately for the real and imaginary parts.

The wavelet function provides a natural width of the smoothing function (Torrence and Webster, 1999). For time smoothing, the filter is provided by a Gaussian function $\exp[-(n\delta t/s)^2/2]$, defined for each scale and normalized to have unit weight. For the scale smoothing, the filter width is given by the scale decorrelation length of the wavelet we are using. In our case we use DOG ($m = 6$), for which the scale is 0.97 (see Table 2 in Torrence and Compo (1998)). The scale smoothing is done using a triangle filter.

A.6 Rotary Wavelet Phase Spectrum

The corotating wavelet phase shows any lag or lead relationship between corotating components of two different vector time series measured simultaneously as a function of period and time. The corotating wavelet phase between positive (CCW) or negative (CW) components is defined as

$$\phi_n^\pm(s) = \tan^{-1} \frac{\mathbb{I}[\langle s^{-1}S_n^{\pm xy}(s) \rangle]}{\mathbb{R}[\langle s^{-1}S_n^{\pm xy}(s) \rangle]}, \quad (\text{A.14})$$

where \mathbb{R} is the real, and \mathbb{I} is the imaginary part of the smoothed, corotating

cross-wavelet spectrum ¹.

¹As for corotating cross-wavelet spectrum, we can define counterrotating functions for cross spectrum, coherence, and phase, which provide an estimate of the joint energy, correlation, and difference of phase between rotary components that are rotating in opposite directions (e.g., between the CW component of x and the CCW component of y). However, in this thesis, we only deal with corotating wavelet analysis.

Appendix B

Theorem for Derivatives of Integrals with Variable Boundaries

To differentiate with respect to x the following integral in z with both boundaries being variable as $A(x)$ and $B(x)$

$$\frac{\partial}{\partial x} \int_{A(x)}^{B(x)} f(x, z) dz, \quad (\text{B.1})$$

let us first consider $F(x, z, t)$ as the primitive of $f(x, z)$. Then, we can write

$$\int_{A(x)}^{B(x)} f(x, z) dz = F(x, z, t) \Big|_{A(x)}^{B(x)} = F(x, B(x)) - F(x, A(x)). \quad (\text{B.2})$$

Applying the derivative $\frac{\partial}{\partial x}$ to (B.2), it yields

B. THEOREM FOR DERIVATIVES OF INTEGRALS WITH VARIABLE BOUNDARIES

$$\begin{aligned} \frac{\partial}{\partial x} \int_{A(x)}^{B(x)} f(x, z) dz &= \frac{\partial F(x, B(x))}{\partial x} + \frac{\partial F(x, B(x))}{\partial z} \frac{\partial B(x)}{\partial x} \\ &\quad - \frac{\partial F(x, A(x))}{\partial x} - \frac{\partial F(x, A(x))}{\partial z} \frac{\partial A(x)}{\partial x}, \end{aligned} \tag{B.3}$$

where regrouping terms the derivative of the integral follows as

$$\begin{aligned} \frac{\partial}{\partial x} \int_{A(x)}^{B(x)} f(x, z) dz &= \frac{\partial F(x, z)}{\partial x} \Big|_{A(x)}^{B(x)} + f(x, B(x)) \frac{\partial B(x)}{\partial x} - \\ &\quad - f(x, A(x)) \frac{\partial A(x)}{\partial x}, \end{aligned} \tag{B.4}$$

$$\begin{aligned} \frac{\partial}{\partial x} \int_{A(x)}^{B(x)} f(x, z) dz &= \int_{A(x)}^{B(x)} \frac{\partial f(x, z)}{\partial x} dz + f(x, B(x)) \frac{\partial B(x)}{\partial x} - \\ &\quad - f(x, A(x)) \frac{\partial A(x)}{\partial x}. \end{aligned} \tag{B.5}$$

The last expression leads, in turn, to the Theorem for the Integral of a Derivative with Variable Boundaries as

$$\begin{aligned} \int_{A(x)}^{B(x)} \frac{\partial f(x, z)}{\partial x} dz &= \frac{\partial}{\partial x} \int_{A(x)}^{B(x)} f(x, z) dz + f(x, A(x)) \frac{\partial A(x)}{\partial x} - \\ &\quad - f(x, B(x)) \frac{\partial B(x)}{\partial x}. \end{aligned} \tag{B.6}$$

Appendix C

Derivation of Function $G_i(x, t)$

C.1 Upper Layer

From dimensionless continuity equation (5.19) we develop each derivative

$$\frac{\partial \eta_1}{\partial t} + \bar{u}_1 \frac{\partial \eta_1}{\partial x} + \eta_1 \frac{\partial \bar{u}_1}{\partial x} = 0,$$

and introduce $\eta_1 = h_1 - \zeta$

$$-\frac{\partial \zeta}{\partial t} - \bar{u}_1 \frac{\partial \zeta}{\partial x} - \eta_1 \frac{\partial \bar{u}_1}{\partial x} = 0,$$

which results in

$$\boxed{D_1 \zeta = \eta_1 \frac{\partial \bar{u}_1}{\partial x}} \tag{C.1}$$

with the operator D_i (material derivative) defined as

C. DERIVATION OF FUNCTION $G_I(X, T)$

$$D_i = \partial/\partial t + \bar{u}_i^{(0)}\partial/\partial x \quad (\text{C.2})$$

Now we apply the material derivative D_1 (C.2) to both sides of (C.1) as follows

$$D_1^2\zeta = D_1\left(\eta_1\frac{\partial\bar{u}_1}{\partial x}\right) \quad (\text{C.3})$$

$$\left(\frac{\partial}{\partial t} + \bar{u}_1\frac{\partial}{\partial x}\right)\left(\frac{\partial\zeta}{\partial t} + \bar{u}_1\frac{\partial\zeta}{\partial x}\right) = \left(\frac{\partial}{\partial t} + \bar{u}_1\frac{\partial}{\partial x}\right)\left(\eta_1\frac{\partial\bar{u}_1}{\partial x}\right)$$

$$\begin{aligned} \frac{\partial^2\zeta}{\partial t^2} + \frac{\partial\bar{u}_1}{\partial t}\frac{\partial\zeta}{\partial x} + \bar{u}_1\frac{\partial^2\zeta}{\partial x\partial t} + \bar{u}_1\frac{\partial^2\zeta}{\partial x\partial t} + \bar{u}_1\frac{\partial\bar{u}_1}{\partial x}\frac{\partial\zeta}{\partial x} + (\bar{u}_1)^2\frac{\partial^2\zeta}{\partial x^2} = \\ = \frac{\partial\eta_1}{\partial t}\frac{\partial\bar{u}_1}{\partial x} + \eta_1\frac{\partial^2\bar{u}_1}{\partial x\partial t} + \bar{u}_1\frac{\partial\eta_1}{\partial x}\frac{\partial\bar{u}_1}{\partial x} + \bar{u}_1\eta_1\frac{\partial^2\bar{u}_1}{\partial x^2} \end{aligned}$$

Finally by substituting the dimensionless continuity equation (5.19) in the right-hand side of the equation we have

$$\begin{aligned} \frac{\partial^2\zeta}{\partial t^2} + \frac{\partial\bar{u}_1}{\partial t}\frac{\partial\zeta}{\partial x} + 2\bar{u}_1\frac{\partial^2\zeta}{\partial x\partial t} + \bar{u}_1\frac{\partial\bar{u}_1}{\partial x}\frac{\partial\zeta}{\partial x} + (\bar{u}_1)^2\frac{\partial^2\zeta}{\partial x^2} = \\ = \left(-\bar{u}_1\frac{\partial\eta_1}{\partial x} - \eta_1\frac{\partial\bar{u}_1}{\partial x}\right)\frac{\partial\bar{u}_1}{\partial x} + \eta_1\frac{\partial^2\bar{u}_1}{\partial x\partial t} + \bar{u}_1\frac{\partial\eta_1}{\partial x}\frac{\partial\bar{u}_1}{\partial x} + \bar{u}_1\eta_1\frac{\partial^2\bar{u}_1}{\partial x^2} \end{aligned}$$

$$\begin{aligned} \frac{\partial^2\zeta}{\partial t^2} + \frac{\partial\bar{u}_1}{\partial t}\frac{\partial\zeta}{\partial x} + 2\bar{u}_1\frac{\partial^2\zeta}{\partial x\partial t} + \bar{u}_1\frac{\partial\bar{u}_1}{\partial x}\frac{\partial\zeta}{\partial x} + (\bar{u}_1)^2\frac{\partial^2\zeta}{\partial x^2} = \\ = -\bar{u}_1\frac{\partial\bar{u}_1}{\partial x}\frac{\partial\eta_1}{\partial x} - \eta_1\left(\frac{\partial\bar{u}_1}{\partial x}\right)^2 + \eta_1\frac{\partial^2\bar{u}_1}{\partial x\partial t} + \bar{u}_1\frac{\partial\eta_1}{\partial x}\frac{\partial\bar{u}_1}{\partial x} + \bar{u}_1\eta_1\frac{\partial^2\bar{u}_1}{\partial x^2} \end{aligned}$$

$$\begin{aligned} \frac{\partial^2 \zeta}{\partial t^2} + \frac{\partial \bar{u}_1}{\partial t} \frac{\partial \zeta}{\partial x} + 2\bar{u}_1 \frac{\partial^2 \zeta}{\partial x \partial t} + \bar{u}_1 \frac{\partial \bar{u}_1}{\partial x} \frac{\partial \zeta}{\partial x} + (\bar{u}_1)^2 \frac{\partial^2 \zeta}{\partial x^2} = \\ = \eta_1 \left[\frac{\partial^2 \bar{u}_1}{\partial x \partial t} + \bar{u}_1 \frac{\partial^2 \bar{u}_1}{\partial x^2} - \left(\frac{\partial \bar{u}_1}{\partial x} \right)^2 \right] \end{aligned}$$

whence we obtain the second material derivative of ζ in terms of the function $G_1(x, t)$

$$\frac{\partial^2 \zeta}{\partial t^2} + \frac{\partial \bar{u}_1}{\partial t} \frac{\partial \zeta}{\partial x} + 2\bar{u}_1 \frac{\partial^2 \zeta}{\partial x \partial t} + \bar{u}_1 \frac{\partial \bar{u}_1}{\partial x} \frac{\partial \zeta}{\partial x} + (\bar{u}_1)^2 \frac{\partial^2 \zeta}{\partial x^2} = \eta_1 G_1(x, t)$$

and hence

$$\boxed{D_1^2 \zeta = \eta_1 G_1(x, t)} \tag{C.4}$$

C.2 Lower Layer Over an Oscillating Topography

Now we introduce $\eta_2 = h_2 - h(x, t) + \zeta$ into the dimensionless continuity equation (5.22) and follow the same steps as previously. Derivation follows as

$$\frac{\partial \eta_2}{\partial t} + \bar{u}_2 \frac{\partial \eta_2}{\partial x} + \eta_2 \frac{\partial \bar{u}_2}{\partial x} = 0$$

$$\frac{\partial \zeta}{\partial t} - \frac{\partial h}{\partial t} + \bar{u}_2 \frac{\partial \zeta}{\partial x} - \bar{u}_2 \frac{\partial h}{\partial x} + \eta_2 \frac{\partial \bar{u}_2}{\partial x} = 0$$

which results in

C. DERIVATION OF FUNCTION $G_I(X, T)$

$$\boxed{D_2\zeta - D_2h(x, t) = -\eta_2 \frac{\partial \bar{u}_2}{\partial x}}$$

Now we apply the material derivative D_i (C.2) to both sides of (C.5) as follows

$$D_2^2\zeta - D_2^2h(x, t) = D_2\left(-\eta_2 \frac{\partial \bar{u}_2}{\partial x}\right)$$

$$\left(\frac{\partial}{\partial t} + \bar{u}_2 \frac{\partial}{\partial x}\right) \left(\frac{\partial \zeta}{\partial t} + \bar{u}_2 \frac{\partial \zeta}{\partial x}\right) - D_2^2h(x, t) = \left(\frac{\partial}{\partial t} + \bar{u}_2 \frac{\partial}{\partial x}\right) \left(-\eta_2 \frac{\partial \bar{u}_2}{\partial x}\right)$$

$$\begin{aligned} \frac{\partial^2 \zeta}{\partial t^2} + \frac{\partial \bar{u}_2}{\partial t} \frac{\partial \zeta}{\partial x} + \bar{u}_2 \frac{\partial^2 \zeta}{\partial x \partial t} + \bar{u}_2 \frac{\partial^2 \zeta}{\partial x \partial t} + \bar{u}_2 \frac{\partial \bar{u}_2}{\partial x} \frac{\partial \zeta}{\partial x} + (\bar{u}_2)^2 \frac{\partial^2 \zeta}{\partial x^2} - D_2^2h(x, t) = \\ = -\frac{\partial \eta_2}{\partial t} \frac{\partial \bar{u}_2}{\partial x} - \eta_2 \frac{\partial^2 \bar{u}_2}{\partial x \partial t} - \bar{u}_2 \frac{\partial \eta_2}{\partial x} \frac{\partial \bar{u}_2}{\partial x} - \bar{u}_2 \eta_2 \frac{\partial^2 \bar{u}_2}{\partial x^2} \end{aligned}$$

Finally, by substituting the dimensionless continuity equation (5.22) in the right-hand side we obtain

$$\begin{aligned} \frac{\partial^2 \zeta}{\partial t^2} + \frac{\partial \bar{u}_2}{\partial t} \frac{\partial \zeta}{\partial x} + 2\bar{u}_2 \frac{\partial^2 \zeta}{\partial x \partial t} + \bar{u}_2 \frac{\partial \bar{u}_2}{\partial x} \frac{\partial \zeta}{\partial x} + (\bar{u}_2)^2 \frac{\partial^2 \zeta}{\partial x^2} - D_2^2h(x, t) = \\ = \left(\frac{\partial \eta_2}{\bar{u}_2 \partial x} + \eta_2 \frac{\partial \bar{u}_2}{\partial x}\right) \frac{\partial \bar{u}_2}{\partial x} - \eta_2 \frac{\partial^2 \bar{u}_2}{\partial x \partial t} - \bar{u}_2 \frac{\partial \eta_2}{\partial x} \frac{\partial \bar{u}_2}{\partial x} - \bar{u}_2 \eta_2 \frac{\partial^2 \bar{u}_2}{\partial x^2} \end{aligned}$$

$$\begin{aligned} \frac{\partial^2 \zeta}{\partial t^2} + \frac{\partial \bar{u}_2}{\partial t} \frac{\partial \zeta}{\partial x} + 2\bar{u}_2 \frac{\partial^2 \zeta}{\partial x \partial t} + \bar{u}_2 \frac{\partial \bar{u}_2}{\partial x} \frac{\partial \zeta}{\partial x} + (\bar{u}_2)^2 \frac{\partial^2 \zeta}{\partial x^2} - D_2^2h(x, t) = \\ = \bar{u}_2 \frac{\partial \bar{u}_2}{\partial x} \frac{\partial \eta_2}{\partial x} + \eta_2 \left(\frac{\partial \bar{u}_2}{\partial x}\right)^2 - \eta_2 \frac{\partial^2 \bar{u}_2}{\partial x \partial t} - \bar{u}_2 \frac{\partial \eta_2}{\partial x} \frac{\partial \bar{u}_2}{\partial x} - \bar{u}_2 \eta_2 \frac{\partial^2 \bar{u}_2}{\partial x^2} \end{aligned}$$

C.2 Lower Layer Over an Oscillating Topography

$$\begin{aligned} \frac{\partial^2 \zeta}{\partial t^2} + \frac{\partial \bar{u}_2}{\partial t} \frac{\partial \zeta}{\partial x} + 2\bar{u}_2 \frac{\partial^2 \zeta}{\partial x \partial t} + \bar{u}_2 \frac{\partial \bar{u}_2}{\partial x} \frac{\partial \zeta}{\partial x} + (\bar{u}_2)^2 \frac{\partial^2 \zeta}{\partial x^2} - D_2^2 h(x, t) = \\ = -\eta_2 \left[\frac{\partial^2 \bar{u}_2}{\partial x \partial t} + \bar{u}_2 \frac{\partial^2 \bar{u}_2}{\partial x^2} - \left(\frac{\partial \bar{u}_2}{\partial x} \right)^2 \right] \end{aligned}$$

whence we obtain the second material derivative of ζ and $h(x, t)$ in terms of the function $G_2(x, t)$

$$\begin{aligned} \frac{\partial^2 \zeta}{\partial t^2} + \frac{\partial \bar{u}_2}{\partial t} \frac{\partial \zeta}{\partial x} + 2\bar{u}_2 \frac{\partial^2 \zeta}{\partial x \partial t} + \bar{u}_2 \frac{\partial \bar{u}_2}{\partial x} \frac{\partial \zeta}{\partial x} + (\bar{u}_2)^2 \frac{\partial^2 \zeta}{\partial x^2} - \\ - D_2^2 h(x, t) = -\eta_2 G_2(x, t) \end{aligned}$$

and hence

$$\boxed{D_2^2 \zeta = -\eta_2 G_2(x, t) + D_2^2 h(x, t)} \quad (\text{C.5})$$

C. DERIVATION OF FUNCTION $G_I(X, T)$

Appendix D

Derivation of $\overline{\left(\frac{\partial p_2'(1)}{\partial x}\right)}$

Starting from the initial expression

$$\begin{aligned}
 \overline{\left(\frac{\partial p_2'(1)}{\partial x}\right)} &= \left[(h_2 - h) \frac{\partial G_2}{\partial x} - \frac{\partial h}{\partial x} G_2 - \frac{\partial}{\partial x} (D_2^2 h) \right] \frac{1}{\eta_2} \int_{-h_2+h}^{\zeta} dz z \\
 &\quad + \frac{1}{2} \frac{\partial G_2}{\partial x} \frac{1}{\eta_2} \int_{-h_2+h}^{\zeta} dz z^2 + \frac{\partial h}{\partial x} \zeta G_2 - \eta_2 \frac{\partial \zeta}{\partial x} G_2 \\
 &\quad - ([h_2 - h] \zeta + \zeta^2/2) \frac{\partial G_2}{\partial x} + \frac{\partial \zeta}{\partial x} D_2^2 h + \zeta \frac{\partial}{\partial x} (D_2^2 h)
 \end{aligned} \tag{D.1}$$

we develop the integral and obtain

$$\begin{aligned}
 \overline{\left(\frac{\partial p_2'(1)}{\partial x}\right)} &= \left[(h_2 - h) \frac{\partial G_2}{\partial x} - \frac{\partial h}{\partial x} G_2 - \frac{\partial}{\partial x} (D_2^2 h) \right] \frac{1}{2\eta_2} (\zeta^2 - [-h_2 + h]^2) \\
 &\quad + \frac{\partial G_2}{\partial x} \frac{1}{6\eta_2} (\zeta^3 - [-h_2 + h]^3) \\
 &\quad + \frac{\partial h}{\partial x} \zeta G_2 - \eta_2 \frac{\partial \zeta}{\partial x} G_2 - ([h_2 - h] \zeta + \zeta^2/2) \frac{\partial G_2}{\partial x} + \frac{\partial \zeta}{\partial x} D_2^2 h \\
 &\quad + \zeta \frac{\partial}{\partial x} (D_2^2 h) \\
 &= \left[(h_2 - h) \frac{\partial G_2}{\partial x} - \frac{\partial h}{\partial x} G_2 - \frac{\partial}{\partial x} (D_2^2 h) \right] \frac{1}{2} (\zeta - h_2 + h) \\
 &\quad + \frac{\partial G_2}{\partial x} \frac{1}{6} (\zeta^2 + \zeta(-h_2 + h) + (-h_2 + h)^2) \\
 &\quad + \frac{\partial h}{\partial x} \zeta G_2 - \eta_2 \frac{\partial \zeta}{\partial x} G_2 - ([h_2 - h] \zeta + \zeta^2/2) \frac{\partial G_2}{\partial x} + \frac{\partial \zeta}{\partial x} D_2^2 h \\
 &\quad + \zeta \frac{\partial}{\partial x} (D_2^2 h)
 \end{aligned} \tag{D.2}$$

D. DERIVATION OF $\overline{\left(\frac{\partial P_2^{(1)}}{\partial X}\right)}$

$$\begin{aligned}
&= G_2 \left[-\frac{1}{2}(\zeta - h_2 + h) \frac{\partial h}{\partial x} + \zeta \frac{\partial h}{\partial x} - \eta_2 \frac{\partial \zeta}{\partial x} \right] \\
&\quad + \frac{\partial G_2}{\partial x} \left[\frac{1}{2}(h_2 - h)(\zeta - h_2 + h) + \frac{1}{6}(\zeta^2 + \zeta(-h_2 + h) + (-h_2 + h)^2) \right. \\
&\quad \quad \left. - ([h_2 - h]\zeta + \zeta^2/2) \right] \\
&\quad + \left[\zeta - \frac{1}{2}(\zeta - h_2 + h) \right] \frac{\partial}{\partial x}(D_2^2 h) + \frac{\partial \zeta}{\partial x} D_2^2 h \\
&= \eta_2 G_2 \left[\frac{1}{2} \frac{\partial h}{\partial x} - \frac{\partial \zeta}{\partial x} \right] - \frac{\eta_2^2}{3} \frac{\partial G_2}{\partial x} + \frac{\eta_2}{2} \frac{\partial}{\partial x}(D_2^2 h) + \frac{\partial \zeta}{\partial x} D_2^2 h \\
&= \frac{1}{\eta_2} \left(\eta_2^2 G_2 \left[-\frac{1}{2} \frac{\partial h}{\partial x} - \frac{\partial \eta_2}{\partial x} \right] - \frac{\eta_2^3}{3} \frac{\partial G_2}{\partial x} \right) + \frac{\eta_2}{2} \frac{\partial}{\partial x}(D_2^2 h) + \frac{\partial \zeta}{\partial x} D_2^2 h \\
&= \frac{1}{\eta_2} \left(-\eta_2^2 G_2 \frac{\partial \eta_2}{\partial x} - \frac{\eta_2^3}{3} \frac{\partial G_2}{\partial x} \right) - \frac{1}{2} \eta_2 G_2 \frac{\partial h}{\partial x} + \frac{\eta_2}{2} \frac{\partial}{\partial x}(D_2^2 h) + \frac{\partial \zeta}{\partial x} D_2^2 h
\end{aligned} \tag{D.3}$$

and, finally,

$$\overline{\left(\frac{\partial p_2^{(1)}}{\partial x}\right)} = -\frac{1}{3\eta_2} \frac{\partial}{\partial x}(\eta_2^3 G_2) - \frac{1}{2} \eta_2 G_2 \frac{\partial h}{\partial x} + \frac{\eta_2}{2} \frac{\partial}{\partial x}(D_2^2 h) + \frac{\partial \zeta}{\partial x} D_2^2 h \tag{D.4}$$

Appendix E

Substituting \bar{u}_2 in terms of \bar{u}_1

We need to substitute u_2 in terms of u_1 for the three terms involving u_2 in equation (5.94), which are

$$\frac{\partial \bar{u}_2}{\partial t}; \quad \frac{\partial^2 \bar{u}_2}{\partial x \partial t}; \quad \frac{\partial^3 \bar{u}_2}{\partial x^2 \partial t}$$

Then the first term, considering equality (5.60), works out as

$$\frac{\partial \bar{u}_2}{\partial t} = \frac{\partial}{\partial t} \left(\frac{Uh - (h_1 - \zeta)\bar{u}_1}{(h_2 - h + \zeta)} \right), \quad (\text{E.1})$$

$$\begin{aligned} \frac{\partial \bar{u}_2}{\partial t} = \frac{1}{(h_2 - h + \zeta)^2} & \left[(h_2 - h + \zeta) \left[h \frac{\partial U}{\partial t} + U^2 \frac{\partial h}{\partial x} + \bar{u}_1 \frac{\partial \zeta}{\partial t} - (h_1 - \zeta) \frac{\partial \bar{u}_1}{\partial t} \right] \right. \\ & \left. - (Uh - (h_1 - \zeta)\bar{u}_1) \left(-U \frac{\partial h}{\partial x} + \frac{\partial \zeta}{\partial t} \right) \right], \end{aligned}$$

$$\frac{\partial \bar{u}_2}{\partial t} = \frac{1}{(h_2 - h + \zeta)} \left[h \frac{\partial U}{\partial t} + U^2 \frac{\partial h}{\partial x} + \bar{u}_1 \frac{\partial \zeta}{\partial t} - (h_1 - \zeta) \frac{\partial \bar{u}_1}{\partial t} - \bar{u}_2 \left(-U \frac{\partial h}{\partial x} + \frac{\partial \zeta}{\partial t} \right) \right],$$

$$\frac{\partial \bar{u}_2}{\partial t} = \frac{1}{(h_2 - h + \zeta)} \left[h \frac{\partial U}{\partial t} + U^2 \frac{\partial h}{\partial x} + (\bar{u}_1 - \bar{u}_2) \frac{\partial \zeta}{\partial t} - (h_1 - \zeta) \frac{\partial \bar{u}_1}{\partial t} + \bar{u}_2 U \frac{\partial h}{\partial x} \right],$$

E. SUBSTITUTING \bar{U}_2 IN TERMS OF \bar{U}_1

At this point we introduce the continuity equation (5.38) to solve the time-derivative of ζ

$$\frac{\partial \bar{u}_2}{\partial t} = \frac{1}{\eta_2} \left[h \frac{\partial U}{\partial t} + U^2 \frac{\partial h}{\partial x} + (\bar{u}_1 - \bar{u}_2) \left(\eta_1 \frac{\partial \bar{u}_1}{\partial x} - \bar{u}_1 \frac{\partial \zeta}{\partial x} \right) - \eta_1 \frac{\partial \bar{u}_1}{\partial t} + \bar{u}_2 U \frac{\partial h}{\partial x} \right]$$

resulting the first term in (E.1) as

$$\frac{\partial \bar{u}_2}{\partial t} = -\frac{\eta_1}{\eta_2} \frac{\partial \bar{u}_1}{\partial t} + \frac{1}{\eta_2} \left[h \frac{\partial U}{\partial t} + U^2 \frac{\partial h}{\partial x} + (\bar{u}_1 - \bar{u}_2) \left(\eta_1 \frac{\partial \bar{u}_1}{\partial x} - \bar{u}_1 \frac{\partial \zeta}{\partial x} \right) + \bar{u}_2 U \frac{\partial h}{\partial x} \right] \quad \text{(E.2)}$$

For simplicity we define here the variable ϕ as

$$r = \frac{1}{\eta_2} \left[h \frac{\partial U}{\partial t} + U^2 \frac{\partial h}{\partial x} + (\bar{u}_1 - \bar{u}_2) \left(\eta_1 \frac{\partial \bar{u}_1}{\partial x} - \bar{u}_1 \frac{\partial \zeta}{\partial x} \right) + \bar{u}_2 U \frac{\partial h}{\partial x} \right] \quad \text{(E.3)}$$

leading to

$$\boxed{\frac{\partial \bar{u}_2}{\partial t} = -\frac{\eta_1}{\eta_2} \frac{\partial \bar{u}_1}{\partial t} + \phi} \quad \text{(E.4)}$$

and being ϕ a variable to be added on the right-hand side of equation (5.110) when substituting \bar{u}_2 in terms of \bar{u}_1 on its left-hand side.

Analogously, the second term in (E.1) involves

$$\frac{\partial^2 \bar{u}_2}{\partial x \partial t} = \frac{\partial^2}{\partial x \partial t} \left(\frac{Uh - (h_1 - \zeta)\bar{u}_1}{(h_2 - h + \zeta)} \right) \quad \text{(E.5)}$$

what is the same as applying $\frac{\partial}{\partial x}$ to (E.4) following

$$\boxed{\frac{\partial^2 \bar{u}_2}{\partial x \partial t} = -\frac{\eta_1}{\eta_2} \frac{\partial^2 \bar{u}_1}{\partial x \partial t} - \frac{\partial(\eta_1/\eta_2)}{\partial x} \frac{\partial \bar{u}_1}{\partial t} + \frac{\partial \phi}{\partial x}}$$

(E.6)

Analogously, the third term involves

$$\frac{\partial^3 \bar{u}_2}{\partial x^2 \partial t} = \frac{\partial^3}{\partial x^2 \partial t} \left(\frac{Uh - (h_1 - \zeta) \bar{u}_1}{(h_2 - h + \zeta)} \right) \quad (\text{E.7})$$

what is the same as applying $\frac{\partial}{\partial x}$ to (E.6) following

$$\frac{\partial^3 \bar{u}_2}{\partial x^2 \partial t} = -\frac{\partial(\eta_1/\eta_2)}{\partial x} \frac{\partial^2 \bar{u}_1}{\partial x \partial t} - \frac{\eta_1}{\eta_2} \frac{\partial^3 \bar{u}_1}{\partial x^2 \partial t} - \frac{\partial^2(\eta_1/\eta_2)}{\partial x^2} \frac{\partial \bar{u}_1}{\partial t} - \frac{\partial(\eta_1/\eta_2)}{\partial x} \frac{\partial^2 \bar{u}_1}{\partial x \partial t} + \frac{\partial^2 \phi}{\partial x^2} \quad (\text{E.8})$$

$$\boxed{\frac{\partial^3 \bar{u}_2}{\partial x^2 \partial t} = -2 \frac{\partial(\eta_1/\eta_2)}{\partial x} \frac{\partial^2 \bar{u}_1}{\partial x \partial t} - \frac{\eta_1}{\eta_2} \frac{\partial^3 \bar{u}_1}{\partial x^2 \partial t} - \frac{\partial^2(\eta_1/\eta_2)}{\partial x^2} \frac{\partial \bar{u}_1}{\partial t} + \frac{\partial^2 \phi}{\partial x^2}}$$

(E.9)

References

- Aguiar-González, B., Rodríguez-Santana, A., Cisneros-Aguirre, J., Martínez-Marrero, A., 2011. Diurnal-inertial motions and diapycnal mixing on the Portuguese shelf. *Cont. Shelf Res.* 31 (11), 1193–1201.
- Akylas, T., Grimshaw, R., Clarke, S., Tabaei, A., 2007. Reflecting tidal wave beams and local generation of solitary waves in the ocean thermocline. *J. Fluid Mech.* 593, 297–314.
- Alford, M., 2003a. Reply to comment by F. Feser et al. on Improved global maps and 54-year history of wind-work on ocean inertial motions. *Geophys. Res. Lett.* 30 (22), 2166.
- Alford, M. H., 2003b. Redistribution of energy available for ocean mixing by long-range propagation of internal waves. *Nature* 423, 159–162.
- Allard, R., Dykes, J., Hsu, Y. L., Kaihatu, J., Conley, D., 2008. A real-time nearshore wave and current prediction system. *J. Mar. Syst.* 69, 37–58.
- Aparna, M., Shetye, S., Shankar, D., Shenoi, S., Mehra, P., Desai, R., 2005. Estimating the seaward extent of sea breeze from QuikSCAT scatterometry. *Geophys. Res. Lett.* 32 (13), L13601.
- Apel, J., 2002. *An Atlas of Oceanic Internal Solitary Waves: Oceanic Internal Waves and Solitons.*
- Apel, J. R., Holbrook, J. R., Liu, A. K., Tsai, J. J., 1985. The Sulu Sea internal soliton experiment. *J. Phys. Oceanogr.* 15 (12), 1625–1651.
- Apel, J. R., Ostrovsky, L. A., Stepanyants, Y. A., Lynch, J. F., 2006. *Internal solitons in the ocean.* Tech. rep., Woods Hole Oceanographic Institution.
- Battisti, D., Clarke, A., 1982. A simple method for estimating barotropic tidal currents on continental margins with specific application to the M2 tide off the Atlantic and Pacific coasts of the United States. *J. Phys. Oceanogr.* 12, 8–16.

REFERENCES

- Bogucki, D., Dickey, T., Redekopp, L., 1997. Sediment resuspension and mixing by resonantly generated internal solitary waves. *J. Phys. Oceanogr.* 27 (7), 1181–1196.
- Butman, B., Alexander, P. S., Scotti, A., Beardsley, R. C., Anderson, S. P., 2006. Large internal waves in Massachusetts Bay transport sediments offshore. *Cont. Shelf Res.* 26 (17), 2029–2049.
- Chaigneau, A., Pizarro, O., Rojas, W., 2008. Global climatology of near-inertial current characteristics from Lagrangian observations. *Geophys. Res. Lett.* 35.
- Chen, C., Reid, R., Nowlin, W., 1996. Near-inertial oscillations over the Texas-Louisiana shelf. *J. Geophys. Res.* 101, 3509–3524.
- Chen, C., Xie, L., 1997. A numerical study of wind-induced, near-inertial oscillations over the Texas-Louisiana shelf. *J. Geophys. Res.* 102 (C7), 15583–15.
- Choi, W., Camassa, R., 1999. Fully nonlinear internal waves in a two-fluid system. *J. Fluid Mech.* 396 (1-36), 1–36.
- Coelho, E. F., Robinson, A. R., 2003. NATO tactical ocean modeling: the mini-HOPS strategy in the Maritime Rapid Environmental Assessment 2003 Sea Trial. In: MREP03 Proceedings, NATO Undersea Research Centre. pp. CP-47/CD-70.
- Craig, P., 1989a. A model of diurnally forced vertical current structure near 30 latitude. *Cont. Shelf Res.* 9 (11), 965–980.
- Craig, P., 1989b. Constant-eddy-viscosity models of vertical structure forced by periodic winds. *Cont. Shelf Res.* 9 (4), 343–358.
- Criado-Aldeanueva, F., García-Lafuente, J., Navarro, G., Ruiz, J., 2009. Seasonal and interannual variability of the surface circulation in the eastern Gulf of Cadiz (SW Iberia). *J. Geophys. Res.* 114 (C1).
- Da Silva, J., New, A.L. and Magalhaes, J., 2009. Internal solitary waves in the Mozambique Channel: Observations and interpretation. *J. Geophys. Res.* 114 (C5), C05001.
- da Silva, J. C., New, A., Azevedo, A., 2007. On the role of SAR for observing” local generation” of internal solitary waves off the Iberian Peninsula. *Can. J. Rem Sens.* 33 (5), 388–403.

-
- De Mesquita, A., Harari, J., 2003. On the harmonic constants of tides and tidal currents of the South-eastern Brazilian shelf. *Cont. Shelf Res.* 23 (11), 1227–1237.
- DiMarco, S., Howard, M., Reid, R., 2000. Seasonal variation of wind-driven diurnal current cycling on the Texas–Louisiana continental shelf. *Geophys. Res. Lett.* 27, 1017–1020.
- Djordjevic, V. D., Redekopp, L., 1978. The fission and disintegration of internal solitary waves moving over two-dimensional topography. *J. Phys. Oceanogr.* 8 (6), 1016–1024.
- Durrant, D., 1999. Numerical methods for wave equations in geophysical fluid dynamics. Vol. 32. Springer Verlag.
- Emery, W., Thomson, R., 1998. *Data Analysis Methods in Physical Oceanography*. Pergamon.
- Farmer, D., Armi, L., 1999. Stratified flow over topography: the role of small-scale entrainment and mixing in flow establishment. *Proceedings of the Royal Society of London. Series A: Mathematical, Physical and Engineering Sciences* 455 (1989), 3221–3258.
- Font, J., García-Ladona, E., Gorriz, E., 1995. The seasonality of mesoscale motion in the North Channel of the western Mediterranean: several years of evidence. *Oceanologica Acta* 18, 207–219.
- Fu, L. L., 1981. Observations and models of inertial waves in the deep ocean. *Rev. Geophys. Space Phys.* 19, 141–170.
- Furevik, T., Foldvik, A., 1996. Stability at M 2 critical latitude in the Barents Sea. *J. Geophys. Res.* 101, 8823–8837.
- Garret, C., 2001. What is the ‘Near-Inertial’ Band and Why Is It Different from the Rest of the Internal Wave Spectrum? *J. Phys. Oceanogr.* 31, 962–971.
- Gerkema, T., 1994. Nonlinear dispersive internal tides: generation models for a rotating ocean. Ph.D. thesis, Utrecht University.
- Gerkema, T., 1996. A unified model for the generation and fission of internal tides in a rotating ocean. *J. Mar. Res.* 54 (3), 421–450.

REFERENCES

- Gerkema, T., 2001. Internal and interfacial tides: beam scattering and local generation of solitary waves. *J. Mar. Res.* 59 (2), 227–255.
- Gerkema, T., Shrira, V. I., 2005. Near-inertial waves in the ocean: beyond the ‘traditional approximation’. *J. Fluid Mech.* 529, 195–219.
- Gerkema, T., Zimmerman, J., 1995. Generation of nonlinear internal tides and solitary waves. *J. Phys. Oceanogr.* 25 (6), 1081–1094.
- Gerkema, T., Zimmerman, J., 2008. An introduction to internal waves. Vol. 119.
- Gerkema, T., Zimmerman, J., Maas, L., van Haren, H., 2008. Geophysical and astrophysical fluid dynamics beyond the traditional approximation. *Rev. Geophys.* 46 (2).
- Gill, A., 1984. On the behavior of internal waves in the wakes of storms. *J. Phys. Oceanogr.* 14 (7), 1129–1151.
- Gille, S., Smith, S., Lee, S., 2003. Measuring the sea breeze from QuikSCAT Scatterometry. *Geophys. Res. Lett.* 30 (3), 1114.
- Gille, S., Smith, S., Statom, N., 2005. Global observations of the land breeze. *Geophys. Res. Lett.* 32 (5), L05605.
- Gilman, D., Fuglister, F., Mitchell Jr, J., 1963. On the power spectrum of red noise. *J. Atmos. Sci.* 20 (2), 182–184.
- Gonella, J., 1972. A rotary-component method for analyzing meteorological and oceanographic vector time series. *Deep-Sea Res.* 19, 833–846.
- Grimshaw, R.H.J. and Smyth, N., 1986. Resonant flow of a stratified fluid over topography. *J. Fluid Mech.* 169, 429–464.
- Grimshaw, R., Ostrovsky, L., Shrira, V., Stepanyants, Y. A., 1998. Long nonlinear surface and internal gravity waves in a rotating ocean. *Surv. Geophys.* 19 (4), 289–338.
- Grimshaw, R., Pelinovsky, E., Poloukhina, O., 2002. Higher-order Korteweg-de Vries models for internal solitary waves in a stratified shear flow with a free surface. *Nonlinear Proc. Geoph.* 9 (3/4), 221–235.

- Grimshaw, R., Pelinovsky, E., Talipova, T., 1997. The modified Korteweg-de Vries equation in the theory of large-amplitude internal waves. *Nonlinear Proc. Geoph.* 4 (4), 237–250.
- Grimshaw, R., Pelinovsky, E., Talipova, T., Kurkin, A., 2004. Simulation of the transformation of internal solitary waves on oceanic shelves. *J. Phys. Oceanogr.* 34 (12), 2774–2791.
- Haley, P., Lermusiaux, P., 2010. Multiscale two-way embedding schemes for free-surface primitive equations in the Multidisciplinary Simulation, Estimation and Assimilation System. *Oc. Dynam.* 60 (6), 1497–1537.
- Halpern, D., 1977. Description of wind and of upper ocean current and temperature variations on the continental shelf off northwest Africa during March and April 197. *J. Phys. Oceanogr.* 7, 422.
- Hayashi, Y., 1979. Space-Time Spectral Analysis of Rotary Vector Series. *J. Atmos. Sci.* 36 (5), 757–766.
- Helfrich, K., Grimshaw, R., 2008. Nonlinear disintegration of the internal tide. *J. Phys. Oceanogr.* 38 (3), 686–701.
- Helfrich, K. R., Melville, W. K., 2006. Long nonlinear internal waves. *Annu. Rev. Fluid Mech.* 38, 395–425.
- Hormazábal, S., Shaffer, G., Leth, O., 2004. Coastal transition zone off Chile. *J. Geophys. Res.* 109 (C01021).
- Hormazábal, S., Shaffer, G., Pizarro, O., 2002. Tropical Pacific control of intraseasonal oscillations off Chile by way of oceanic and atmospheric pathways. *Geophys. Res. Lett.* 29 (6), 1081.
- Hunter, E., Chant, R., Bowers, L., Glenn, S., Kohut, J., 2007. Spatial and temporal variability of diurnal wind forcing in the coastal ocean. *Geophys. Res. Lett.* 34 (3), L03607.
- Hyder, P., Simpson, J., Xing, J., Gille, S., 2011. Observations over an annual cycle and simulations of wind-forced oscillations near the critical latitude for diurnal-inertial resonance. *Cont. Shelf Res.*
- Hyder, P., Simpson, J. H., Christopoulos, S., 2002. Sea-breeze forced diurnal surface currents in the Thermaikos Gulf, North-west Aegean. *Cont. Shelf Res.* 22, 585–601.

REFERENCES

- Jarosz, E., Hallock, Z., Teague, W., 2007. Near-inertial currents in the DeSoto Canyon region. *Cont. Shelf Res.* 27 (19), 2407–2426.
- Jo, T.-C., Choi, W., 2002. Dynamics of strongly nonlinear internal solitary waves in shallow water. *Stud. Appl. Math.* 109 (3), 205–227.
- Kakutani, T., Yamasaki, N., 1978. Solitary waves on a two-layer fluid. *J. Phys. Soc. Japan* 45 (2), 674–679.
- Kaplan, D., Largier, J., Botsford, L., 2005. HF radar observations of surface circulation off Bodega Bay (northern California, USA). *J. Geophys. Res.* 110, C10020.
- Kaplan, D., Largier, J., Navarrete, S., Guíñez, R., Castilla, J., 2003. Large diurnal temperature fluctuations in the nearshore water column. *Estuar. Coast. Shelf Sci.* 57 (3), 385–398.
- Keen, C., Lyons, W., 1978. Lake/land breeze circulations on the western shore of Lake Michigan. *J. Appl. Meteor.* 17 (12), 1843–1855.
- Knight, P. J., Howarth, M. J., Rippeth, T. P., 2002. Inertial currents in the northern North sea. *J. Sea Res.* 47, 269–284.
- Ko, D., Martin, P., Rowley, C., Preller, R., 2008. A real-time coastal ocean prediction experiment for MREA04. *J. Mar. Syst.* 69 (1-2), 17–28.
- Koop, C. G., Butler, G., 1981. An investigation of internal solitary waves. *J. Fluid Mech.* 112, 225–251.
- Korteweg, D., de Vries, G., 1895. XLI. On the change of form of long waves advancing in a rectangular canal, and on a new type of long stationary waves. *The London, Edinburgh, and Dublin Philosophical Magazine and Journal of Science* 39 (240), 422–443.
- Kunze, E., 1985. Near-Inertial Wave Propagation in Geostrophic Shear. *J. Phys. Oceanogr.* 15, 544–565.
- Kunze, E., Boss, E., 1998. A Model for Vortex-Trapped Internal Waves. *J. Phys. Oceanogr.* 28, 2104–2115.
- Lam, F., Haley Jr, P., Janmaat, J., Lermusiaux, P., Leslie, W., Schouten, M., te Raa, L., Rixen, M., 2009. At-sea real-time coupled four-dimensional oceanographic and acoustic forecasts during battlespace preparation 2007. *J. Mar. Syst.* 78, S306–S320.

- Lamb, K. G., Yan, L., 1996. The evolution of internal wave undular bores: comparisons of a fully nonlinear numerical model with weakly nonlinear theory. *Journal of physical oceanography* 26 (12), 2712–2734.
- Lee, C., Beardsley, R., 1974. The generation of long nonlinear internal waves in a weakly stratified shear flow. *J. Geophys. Res.* 79 (3), 453–462.
- Lerczak, J., Hendershott, M., Winant, C., 2001. Observations and modeling of coastal internal waves driven by a diurnal sea breeze. *J. Geophys. Res.* 106 (19), 715–19.
- Lermusiaux, P., Xu, J., Chen, C., Jan, S., Chiu, L., Yang, Y., 2010. Coupled Ocean–Acoustic Prediction of Transmission Loss in a Continental Shelf-break Region: Predictive Skill, Uncertainty Quantification, and Dynamical Sensitivities. *IEEE Transactions, Journal of Oceanic Engineering* 35 (4), 895–916.
- Leslie, W.G. and Robinson, A., Haley, P.J. .and Logoutov, O., Moreno, P., Lermusiaux, P.F.J .and Coelho, E., 2008. Verification and training of real-time forecasting of multi-scale ocean dynamics for maritime rapid environmental assessment. *J. Mar. Syst.* 69 (1-2), 3–16.
- Liu, A. K., Holbrook, J. R., Apel, J., 1985. Nonlinear internal wave evolution in the Sulu Sea. *J. Phys. Oceanogr.* 15 (12), 1613–1624.
- Logan, J. D., 1987. *Applied mathematics: a contemporary approach.* Wiley.
- Lyons, W., 1972. The climatology and prediction of the Chicago lake breeze. *J. Appl. Meteor.* 11, 1259–1270.
- Lyons, W., Olsson, L., 1973. Detailed Mesometeorological Studies of Air Pollution Dispersion in the Chicago Lake Breeze. *Mon. Weather Rev.* 101 (5), 387–403.
- Maas, L., Van Haren, J., 1987. Observations on the vertical structure of tidal and inertial currents in the central North Sea. *J. Mar. Res.* 45 (2), 293–318.
- Maas, L., Zimmerman, J., 1989. Tide-topography interactions in a stratified shelf sea I. Basic equations for quasi-nonlinear internal tides. *Geophys. Astrophys. Fluid Dynam.* 45 (1-2), 1–35.

REFERENCES

- Macias, D., García, C. M., Echevarría Navas, F., Vázquez-López-Escobar, A., Bruno Mejías, M., 2006. Tidal induced variability of mixing processes on Camarinal Sill (Strait of Gibraltar): A pulsating event. *J. Mar. Syst.* 60 (1), 177–192.
- MacKinnon, J., Winters, K., 2005. Subtropical catastrophe: Significant loss of low-mode tidal energy at 28.9. *Geophys. Res. Lett.* 32 (15), L15605.
- Martínez-Marrero, A., Rodríguez-Santana, A., Hernández-Guerra, A., Fraile-Nuez, E., López-Laatzén, F., Vélez-Belchí, P., Parrilla, G., 2008. Distribution of water masses and diapycnal mixing in the Cape Verde Frontal Zone. *Geophys. Res. Lett.* 35 (7), L07609.
- Martins, F., Leitao, P., Neves, R., 2002. Simulating vertical water mixing in homogeneous estuaries: the SADO Estuary case. *Hydrobiologia* 475/476, 221–227.
- Maxworthy, T., 1979. A note on the internal solitary waves produced by tidal flow over a three-dimensional ridge. *J. Geophys. Res.* 84 (C1), 338–346.
- Melville, W., Helfrich, K., 1987. Transcritical two-layer flow over topography. *J. Fluid Mech.* 178, 31–52.
- Middleton, J., Denniss, T., 1993. The propagation of tides near the critical latitude. *Geophys. Astrophys. Fluid Dynam.* 68 (1-4), 1–13.
- Miles, J., 1986. Richardson's criterion for the stability of stratified shear flow. *Physics of Fluids* 29, 3470–3471.
- Millot, C., Crepon, M., 1981. Inertial Oscillations on the Continental Shelf of the Gulf of Lions - Observations and Theory. *J. Phys. Oceanogr.* 11, 639–657.
- Miyata, M., 1985. An internal solitary wave of large amplitude. *La Mer* 23, 43–48.
- Miyata, M., 1988. Long internal waves of large amplitude. In: K. Horikawa, H. M. (Ed.), *Nonlinear Water Waves, IUTAM Symp.*, Tokyo 1987. Berlin: Springer-Verlag, pp. 399–406.
- Moroz, W., 1967. A Lake Breeze on the Eastern Shore of Lake Michigan: Observations and Model. *J. Atmos. Sci.* 24, 337–355.

- Moum, J., Farmer, D., Smyth, W., Armi, L., Vagle, S., 2003. Structure and generation of turbulence at interfaces strained by internal solitary waves propagating shoreward over the continental shelf. *J. Phys. Oceanogr.* 33 (10), 2093–2112.
- Muench, R. D., Padman, L., Howard, S. L., Fahrbach, E., 2002. Upper ocean diapycnal mixing in the northwestern Weddell Sea. *Deep-Sea Res. II* 49, 4843–4861.
- Munk, W., Wunsch, C., 1998. Abyssal recipes II: energetics of tidal and wind mixing. *Deep-Sea Res. I* 45 (12), 1977–2010.
- New, A., 1988. Internal tidal mixing in the Bay of Biscay. *Deep-Sea Res.* 35 (5), 691–709.
- New, A., da Silva, J., 2002. Remote-sensing evidence for the local generation of internal soliton packets in the central Bay of Biscay. *Deep-Sea Res. I* 49 (5), 915–934.
- New, A., Pingree, R., 1992. Local generation of internal soliton packets in the central Bay of Biscay. *Deep-Sea Res.* 39 (9), 1521–1534.
- New, A.L. and Pingree, R., 1990. Large-amplitude internal soliton packets in the central Bay of Biscay. *Deep-Sea Res.* 37 (3), 513–524.
- O’Brien, J. J., Pillsbury, R. D., 1974. Rotary Wind Spectra in a Sea Breeze Regime. *J. Appl. Meteor.* 13 (7), 820–825.
- Orlić, M., 1987. Oscillations at the inertial period on the Adriatic Sea shelf. *Cont. Shelf Res.* 7, 577–598.
- Osborne, A., Burch, T., 1980. Internal solitons in the Andaman Sea. *Science* 208 (4443), 451–460.
- Ostrovsky, L., Stepanyants, Y. A., 1989. Do internal solitons exist in the ocean? *Rev. Geophys.* 27 (3), 293–310.
- Pacanowski, R. C., Philander, S. G. H., 1981. Parameterization of Vertical Mixing in Numerical Models of Tropical Oceans. *J. Phys. Oceanogr.* 11, 1443–1451.
- Park, J., Kim, K., King, B., 2005. Global statistics of inertial motions. *Geophys. Res. Lett.* 32 (14), L14612.

REFERENCES

- Pattiaratchi, C., Hegge, B., Gould, J., Eliot, I., 1997. Impact of sea-breeze activity on nearshore and foreshore processes in southwestern Australia. *Cont. Shelf Res.* 17, 1539–1560.
- Pawlowicz, R., Beardsley, B., Lentz, S., 2002. Classical tidal harmonic analysis including error estimates in MATLAB using T_TIDE. *Comput. Geosci.* 28 (8), 929–937.
- Pelegrí, J. L., Sangrà, P., 1998. A mechanism for layer formation in stratified geophysical flows. *J. Geophys. Res.* 103 (30), 679–693.
- Pidgeon, E., Winant, C., 2005. Diurnal variability in currents and temperature on the continental shelf between central and southern California. *J. Geophys. Res.* 110, C03024.
- Pielke, R., Segal, M., 1986. Mesoscale circulations forced by differential terrain heating. *Mesoscale Meteorology and Forecasting*, 516–548.
- Pingree, R., Mardell, G., 1985. Solitary internal waves in the Celtic Sea. *Prog. Oceanogr.* 14, 431–441.
- Pinkel, R., 2000. Internal solitary waves in the warm pool of the western equatorial Pacific. *J. Phys. Oceanogr.* 30 (11), 2906–2926.
- Piñones, A., Valle-Levinson, A., Narváez, D., Vargas, C., Navarrete, S., Yuras, G., Castilla, J., 2005. Wind-induced diurnal variability in river plume motion. *Estuar. Coast. Shelf Sci.* 65 (3), 513–525.
- Pollard, R., 1970. On the generation by winds of inertial waves in the ocean. *Deep-Sea Res.* 17 (4), 795–812.
- Pollard, R., 1980. Properties of near-surface inertial oscillations. *J. Phys. Oceanogr.* 10 (3), 385–398.
- Pollard, R. T., Millard, R. C., 1970. Comparison between observed and simulated wind-generated inertial oscillations. *Deep-Sea Res.* 17, 813–821.
- Poulain, P., 1990. Near-inertial and diurnal motions in the trajectories of mixed layer drifters. *J. Mar. Res.* 48 (4), 793–823.
- Qi, H., De Szoeke, R., Paulson, C., Eriksen, C., 1995. The structure of near-inertial waves during ocean storms. *Collections*.

- Reynolds-Fleming, J., Luettich Jr, R., 2004. Wind-driven lateral variability in a partially mixed estuary. *Estuar. Coast. Shelf Sci.* 60 (3), 395–407.
- Rippeth, T. P., Simpson, J. H., Player, R. J., Garcia, M., 2002. Current oscillations in the diurnal-inertial band on the Catalanian shelf in spring. *Cont. Shelf Res.* 22, 247–265.
- Rixen, M., Ferreira-Coelho, E., 2007. Operational surface drift prediction using linear and non-linear hyper-ensemble statistics on atmospheric and ocean models. *J. Mar. Syst.* 65, 105–121.
- Rodríguez-Santana, A., Pelegrí, J. L., Sangrà, P., Marrero-Díaz, A., 1999. Diapycnal mixing in Gulf Stream meanders. *J. Geophys. Res.* 104, 25891–25912.
- Rodríguez-Santana, A., Pelegrí, J. L., Sangrà, P., Marrero-Díaz, A., 2001. On the relevance of diapycnal mixing for the stability of frontal meanders. *Sci. Mar.* 65 (Suppl. 1), 259–267.
- Rosenfeld, L., 1988. Diurnal period wind stress and current fluctuations over the continental shelf off northern California. *J. Geophys. Res.* 93 (C3), 2257–2276.
- Russell, J., 1838a. Report on waves. In: Murray, J. (Ed.), Report of the 14th Meeting of British Association for the Advancement of Science. pp. 311–390.
- Russell, J., 1838b. Report to committee on waves. In: Murray, J. (Ed.), Report of the 7th Meeting of British Association for the Advancement of Science. pp. 417–496.
- Salat, J., Tintoré, J., Font, J., Wang, D.-P., Vieira, M., 1992. Near-Inertial Motion on the Shelf-Slope Front off Northeast Spain. *J. Geophys. Res.* 97 (C5), 7277–7281.
- Sandstrom, H., Elliott, J., 1984. Internal tide and solitons on the Scotian Shelf: A nutrient pump at work. *J. Geophys. Res.* 89 (C4), 6415–6426.
- Sangrà, P., Basterretxea, G., Pelegrí, J. L., Arístegui, J., 2001. Chlorophyll increase due to internal waves in the shelf-break of Gran Canaria Island (Canary Islands). *Sci. Mar.* 65 (Suppl. 1), 89–97.
- Schahinger, R. B., 1988. Near-inertial motions on the South Australian shelf. *J. Phys. Oceanogr.* 18, 492–504.

REFERENCES

- Sills, D., 1998. Lake and land breezes in southwestern Ontario: observations, analyses and numerical modelling. Ph.D. thesis, York University.
- Simionato, C., , Meccia, V., Dragani, W. Nuñez, M., 2005. Barotropic tide and baroclinic waves observations in the Río de la Plata Estuary. *J. Geophys. Res.* 110, C06008.
- Simmons, H., Hallberg, R., Arbic, B., 2004. Internal wave generation in a global baroclinic tide model. *Deep-Sea Res. II* 51, 3042–3068.
- Simpson, J. E., 1994. *Sea Breeze and Local Wind*. Cambridge University Press, New York.
- Simpson, J. H., Hyder, P., Rippeth, T. P., 2002. Forced Oscillations near the Critical Latitude for Diurnal-Inertial Response. *J. Phys. Oceanogr.* 32, 177–187.
- Sobarzo, M., Bravo, L., Moffat, C., 2010. Diurnal-period, wind-forced ocean variability on the inner shelf off Concepción, Chile. *Cont. Shelf Res.* 30 (20), 2043–2056.
- Sobarzo, M., Shearman, R. K., Lentz, S., 2007. Near-inertial motions over the continental shelf off Concepción, central Chile. *Prog. Oceanogr.* 75, 348–362.
- Stanton, T., Ostrovsky, L., 1998. Observations of highly nonlinear internal solitons over the continental shelf. *Geophys. Res. Lett.* 25 (14), 2695–2698.
- Tiemann, C., Worcester, P., Cornuelle, B. D., 2001. Acoustic scattering by internal solitary waves in the Strait of Gibraltar. *J. Acoust. Soc. Am.* 109, 143.
- Torrence, C., Compo, G., 1998. A practical guide to wavelet analysis. *B. Am. Meteorol. Soc.* 79 (1), 61–78.
- Torrence, C., Webster, P., 1999. Interdecadal changes in the ENSO-monsoon system. *Journal of Climate* 12 (8), 2679–2690.
- Ueckermann, M., Lermusiaux, P., 2010. High-order schemes for 2D unsteady biogeochemical ocean models. *Oc. Dynam.* 60 (6), 1415–1445.
- van Aken, H. M., Maas, L. R. M., van Haren, H., 2005. Observations of Inertial Wave Events near the Continental Slope off Goban Spur. *J. Phys. Oceanogr.* 35, 1329–1340.

- Van Gastel, P., Pelegrí, J. L., 2004. Estimates of gradient Richardson numbers from vertically smoothed data in the Gulf Stream region. *Scientia Marina* 68 (4), 459–482.
- van Haren, H., 2000. Properties of vertical current shear across stratification in the North Sea. *J. Mar. Res.* 58, 465–491.
- Van Haren, H., 2005. Tidal and near-inertial peak variations around the diurnal critical latitude. *Geophys. Res. Lett.* 32 (23), L23611.
- van Haren, H., 2007. Longitudinal and topographic variations in North Atlantic tidal and inertial energy around latitudes 30 ± 10 N. *J. Geophys. Res.* 112 (C10), C10020.
- van Haren, H., Maas, L., Zimmerman, J. T. F., Ridderinkhof, H., Malschaert, H., 1999. Strong inertial currents and marginal internal wave stability in the central North Sea. *Geophys. Res. Lett.* 26, 2993–2996.
- Wang, D., Lermusiaux, P., Haley, P., Eickstedt, D., Leslie, W., Schmidt, H., 2009. Acoustically focused adaptive sampling and on-board routing for marine rapid environmental assessment. *J. Mar. Syst.* 78, S393–S407.
- Watanabe, M., Hibiya, T., 2002. Global estimates of the wind-induced energy flux to inertial motions in the surface mixed layer. *Geophys. Res. Lett.* 29 (8), 1239.
- Webster, F., 1968. Observation of inertial period motions in the deep sea. *Rev. Geophys.* 6, 473–490.
- Xu, Z., Yin, B., 2012. Oceanography. InTech, Ch. Variability of Internal Solitary Waves in the Northwest South China Sea.
- Young, W. R., Ben Jelloul, M., 1997. Propagation of near-inertial oscillations through a geostrophic flow. *J. Mar. Res.* 55, 735–766.
- Zavialov, P., Möller Jr, O., Campos, E., 2002. First direct measurements of currents on the continental shelf of Southern Brazil. *Cont. Shelf Res.* 22 (14), 1975–1986.
- Zeng, K., Alpers, W., 2004. Generation of internal solitary waves in the Sulu Sea and their refraction by bottom topography studied by ERS SAR imagery and a numerical model. *Int. J. Remote Sens.* 25 (7-8), 1277–1281.

REFERENCES

- Zhang, X., DiMarco, S., Smith IV, D., Howard, M., Jochens, A., Hetland, R., 2009. Near-resonant ocean response to sea breeze on a stratified continental shelf. *J. Phys. Oceanogr.* 39 (9), 2137–2155.
- Zhang, X., Smith IV, D., DiMarco, S., Hetland, R., 2010. A numerical study of sea-breeze-driven ocean Poincaré wave propagation and mixing near the critical latitude. *J. Phys. Oceanogr.* 40 (1), 48–66.

Data Acknowledgements

It is not always needed to count with *new data* for making *new research*. One could think it may be straightforward to get success on presenting something *new* when one makes use of *untouched data*, but open public data and data recycled from previous projects (even when they were planned with different targets) are also a fruitful source of information always ready for refreshing insights and challenging research.

The first half of this PhD study has been developed following that *philosophy* with the support of Puertos del Estado (Spain), the Instituto Hidrográfico - Portugal and the NATO Undersea Research Centre (NURC), which allowed the use of the data we present.

Hence, I want to thank Puertos del Estado (Spain) for his efficient and kind service on providing the public data which are the base of the research in *Chapter 2*. Likewise, I thank Dr. Jesús Cisneros Aguirre and the NATO Undersea Research Centre (NURC) for permitting the use of the data collected during the MREA04 sea trial; as well as the Instituto Hidrográfico - Portugal for providing wind data from a land meteorological station at Sines. They form the core of the work reported in *Chapter 3*.

The second half of this PhD study was greatly benefited thanks to the kindness of Dr. Theo Gerkema, who provided me from the beginning with his numerical code for the generation of nonlinear dispersive interfacial tides and solitary waves on the f -plane (Gerkema, 1996). I cannot imagine a better starting point for the numerical code we developed in this thesis.



Agradecimientos

Este trabajo ha crecido bajo la mirada cómplice de personas muy especiales. Es el momento de darles las gracias. Algunos nombres se repetirán, diferentes son los motivos y los lugares, e incluso los idiomas. Intentaré mantener un orden, pero lo que ahora se presenta me voy a permitir el capricho de dejar que *fluya y oscile* con su período particular, el mío. Estoy convencido que lo entenderán...

La presente Tesis Doctoral ha sido dirigida por el Dr. Ángel Rodríguez Santana (Universidad de Las Palmas de Gran Canaria - ULPGC), el Dr. Theo Gerkema (Royal Netherlands Institute for Sea Research - NIOZ) y el Dr. Jesús Cisneros Aguirre (Universidad de Las Palmas de Gran Canaria - ULPGC), a quienes agradezco la confianza y dedicación que me han brindado durante estos años de mi etapa de formación como investigador. Aprecio enormemente el tiempo que habéis dedicado a guiar este trabajo con vuestra valiosa experiencia.

Me encuentro también agradecido al Dr. Samuel Hormazábal de la Universidad Católica de Valparaíso, cuyo contribución a mi trabajo de investigación ha sido muy importante. Gracias por tu dedicación y generosa hospitalidad. Este trabajo se ha nutrido también de la experiencia del Dr. Antonio Martínez Marrero, quien siempre mostró interés y encontró tiempo para atender mis dudas.

Dentro del Grupo de Investigación OFYGA, del cual he formado parte durante mi etapa como doctorando en la ULPGC, quiero también agradecer a la Dra. Ángeles Marrero Díaz su dedicación y atención conmigo, siempre disponible para ayudar. No podía ser de otro modo, dentro del Grupo OFYGA, agradezco muy especialmente a Ángel y a Jesús su continuado interés en mi formación, en mi presente y en mi futuro, siempre dispuestos a ofrecerme nuevas oportunidades, participación en campañas oceanográficas, contactos con otros centros de investigación, etc ... ¡Gracias!

Al Dr. Josep Lluís Pelegrí, al Dr. Pablo Sangrà Inciarte y al Dr. Miguel Bruno Mejías quisiera agradecer su confianza al permitirme la oportunidad de participar en varias campañas oceanográficas a su cargo. En todas ellas la experiencia vivida fue siempre enriquecedora.

Durante mis años de doctorado tuve la generosa oportunidad de colaborar con la Dra. May Gómez y el Dr. Ted Packard, gracias por contar conmigo en

Agradecimientos

vuestra investigación. Ted, investigar a tu lado es un placer, tu vitalidad es inspiradora, mil gracias por contagiarme tu entusiasmo por la ciencia.

Estos años de laboratorio no han podido contar con mejores compañeros de trabajo y amigos: Mónica, Francis, Carolina, Mireya, Sheila, Charles, Bego,... Compartir tiempo y espacio con ustedes ha sido un placer. No se me ocurre mejor escenario para trabajar y compartir vivencias durante el día.

Mis inicios en la programación con Matlab y escritura en L^AT_EX fueron mucho más amenos de lo que pudiera ser habitual al profano. Y eso fue gracias al tiempo que generosamente me dedicó el Dr. Francisco Machín. Esta tesis tiene mucho de lo que he aprendido de ti. Guardo especialmente en el recuerdo el tiempo compartido juntos en Barcelona.

Idaira, Aridane, Isis, Inma, Rosa,... están vinculados de manera especial a mis primeros años de curiosidad oceanográfica durante la carrera.

En lo que a problemas informáticos se refiere, gracias por tu ayuda Jorge, más de un disco duro se ha salvado gracias a ti. Mis inicios en la *oceanografía con Mac* tuvieron algún que otro contratiempo que rápidamente se resolvió gracias a la buena disposición y ayuda de David.

Desde que inicié la carrera en Ciencias del Mar (CCM) hasta el día de hoy he compartido mis vivencias oceanográficas con muchos amigos que vienen ahora a mi memoria ... es imposible nombrarlos a todos, pero no por ello dejo de decirles desde aquí: gracias por estar ahí.

Desde hace más de una década que cuento con vuestra amistad, cariño y apoyo... ¡menuda suerte!... Gracias Mónica, Ángela, Fedé.

En el *Centre Mediterrani D'Investigacions Marines i Ambientals* (CMIMA-CSIC) en Barcelona realicé mis cursos de Máster y Doctorado en Oceanografía a través del programa organizado por la ULPGC. Allà el Dr. Josep Lluís Pelegrí em va rebre amablement durant la meva estada, oferint-me totes les facilitats d'accés i ubicació al *Departament d'Oceanografia Física* per superar amb èxit la meva primera etapa investigadora. Moltes Gràcies Josep Lluís!

After my stay at the CMIMA-CSIC, I travelled to The Hague (The Netherlands) to collaborate with Dr. Frans-Peter A. Lam and Dr. Mathijs Schouten at the *Netherlands Organisation for Applied Scientific Research* (TNO). During this period I was introduced to HOPS numerical modeling. The time I spent at TNO is unforgettable, working with both of you is one of the gifts

I will always remember from my PhD time. There are not enough words to thank all I received from you. I appreciated very much your advices and careful guide. I also thank Prof. Dr. P. F. J. Lermusiaux (Massachusetts Institute of Technology, MIT) for his help, inputs and comments in the distance on modeling work for MREA exercises. From my period at TNO I cannot forget about Benoit and Jeroen for all their help at my arrival and for the joyful time we shared, as well as with Mathieu, Antonio, Jacqueline, Michael,...

My stays at NIOZ were possible thanks to Dr. Frans-Peter A. Lam, who firstly introduced me to Prof. Dr. L. R. M. Maas and Dr. T. Gerkema. The Netherlands always brings to me nice memories. My time there was special, and that was thanks to the people I met on my way. They made my stay to be great: joyful and fruitful at the same time.

I already mentioned people from The Hague at TNO, but I also met wonderful people I want to remember in these lines at Texel during my stays at NIOZ, specially Jenny, Femke, Carola, Anna and Andrea. I also want to thank the Physical Oceanography Department at NIOZ, which kindly hosted me during my PhD time there. In this regard, I am grateful to Prof. Dr. Leo Maas, who always shared his interest on my work with refreshing and inspiring questions. At this point, it may be obvious to the reader that I deeply feel this thesis is half spanish, half dutch. And the dutch side of this research was developed thanks to Dr. Theo Gerkema. I appreciate a lot your hospitality and all the time you have spent working with me and supervising my PhD study. I am also grateful for your continuous interest on helping me with future steps: ¡Muchas Gracias por todo Theo! He aprendido y disfrutado muchísimo trabajando a tu lado.

Ángela, gracias por estar ahí siempre, por los muchos años de amistad desde que nos conocemos, y por todos los que vendrán. Muchas gracias por tu apoyo en lo personal y en lo laboral. Nuestras conferencias Gran Canaria - Texel, y luego al revés, son inolvidables... el destino es curioso, pero contigo al lado además de curioso es siempre agradable.

Mónica, muchas son las horas que hemos compartido dentro y fuera del lab, dentro y fuera de 'la isla'. Muchos son los grandes momentos vividos en estos años de amistad (y los que vendrán): viajes sorpresa, excursiones aventura, videoconferencias en la distancia,... Los he disfrutado y disfruto muchísimo. Muchas gracias por tu apoyo en lo personal y en lo laboral, por tu compañía, por estar ahí siempre.

Agradecimientos

Goonie, gracias por tirar de mi pantalón y guiar cada uno de mis pasos aquella noche de Febrero, tuviste que tirar fuerte, y en varias ocasiones, pero nunca te faltó fuerza a pesar de tu pequeño tamaño. Estoy seguro que estás en el cielo de las pizzas y los churros.

Las primeras palabras de esta tesis van dedicadas a ellos, y de ellos es el honor de cerrarla: mis padres Mappi e Ignacio, y mi hermano Jose. Ustedes han hecho posible que haya llegado hasta aquí. Gracias por vuestra compañía y cariño. No tengo palabras para agradecerles que siempre pueda contar con ustedes. Gracias por todas vuestras visitas cuando estoy fuera de 'la isla', me hacen sentir pieza importante en vuestra vida y siempre suponen una inyección de alegría. Mappi, gracias por explicarme 'la teoría del sandwich', aplicable a todos los ámbitos de la vida. Si he terminado esta tesis es gracias a que la he aplicado una vez más. Gracias por ayudarme siempre a ver lo esencial y a encontrar mi camino. Ignacio, en momentos de estrés 'tus teorías de las ondas' me hicieron reír y ver alguna que otra luz, gracias por ambos efectos, llegaban siempre que hacían falta. Jose, gracias por tus ánimos, por alegrarte e interesarte siempre por lo que hago, por tu tiempo conmigo y por cuidar siempre de tu 'hermanito pequeño' (aunque ya no sea tan pequeñito aún te necesito). ¡Gracias mis pequeños, gracias por apoyarme, millones de gracias!

Curriculum Vitae

Borja Aguiar González was born in Las Palmas de Gran Canaria (Canary Islands, Spain) on September 29th1982. From his childhood, summertime and vacations were always linked to life in the coast, specially in Lanzarote and Fuerteventura, where he used to share maritime activities with his family and friends.

Thus, he became interested in all phenomena related to the sea, and decided to study the Bachelor of Marine Sciences in the fall of 2000 at the *Universidad de Las Palmas de Gran Canaria* (ULPGC). From the very beginning he was involved in numerous projects as a trainee, most of them related to coastal management. He spent the last years of his bachelor collaborating with the research group OFYGA (in the Department of Physics), which introduced him to physical oceanography. After finishing the bachelor, he decided to continue his education as a researcher with this research group.

In January 2007, he is awarded with the PhD grant which supports the realization of this thesis. He developed his research partially at ULPGC and the *Royal Netherlands Institute for Sea Research* (NIOZ). During his years as a PhD student, he had also the opportunity to work with outstanding professionals at the *Centre Mediterrani D'Investigacions Marines i Ambientals* (CMIMA-CSIC), the *Netherlands Organisation for Applied Scientific Research* (TNO) and the *Universidad de Concepción* (UdeC).

Working at sea he learns and enjoys the most the job as oceanographer. On-board the ships *B/O García del Cid*, *B/O Sarmiento de Gamboa*, *Hidrográfico Malaspina* and *BIO Hespérides* he has sailed along the north-western coast of Africa, from the Strait of Gibraltar to the Cape Verde Islands; and, from the Southern South America to the Antarctic Peninsula across the Drake Passage.

The focus of his PhD research activities have been the observational study of resonant breeze-forced oscillations^{1,2} and modeling of strongly nonlinear

¹Aguiar-González B., Rodríguez-Santana A., Cisneros-Aguirre J., Martínez-Marrero. 2011. Diurnal-inertial motions and diapycnal mixing on the Portuguese shelf. *Cont. Shelf Res.* 31, 1193–1201.

²Aguiar-González B., Hormazábal S., Rodríguez-Santana A., Cisneros-Aguirre J., Martínez-Marrero. Breeze-Forced Oscillations around The Poleward Limit for Diurnal-Inertial Resonance. *In Preparation to be Submitted to an International refereed Journal*

Curriculum Vitae

tide-generated internal solitons¹. During the PhD time he also worked on HOPS (Harvard Ocean Prediction System) modeling for the Maritime Rapid Environmental Assessment 2004 (MREA04). In the recent years, he has been working on the contribution of mesoscale activity to near-inertial energy variability with drifters, remote sensing images and altimetry data (research *in progress*); as well as on the dominant processes which control oceanic mixing around the South Shetland Islands in Antarctica (research *in progress*).

As a result of his multidisciplinary education and the interaction with other research groups, he has recently co-authored a paper on theoretical and experimental biochemistry².

¹Aguiar-González B., Gerkema T. A Model for the Generation of Strongly Nonlinear, Weakly Nonhydrostatic Interfacial Waves. *In Preparation to be Submitted to an International refereed Journal*

²Aguiar-González B., Packard T., Berdalet E., Roy S., Gómez M. 2012. Respiration predicted from an Enzyme Kinetic Model and the Metabolic Theory of Ecology in two species of marine bacteria. *J. Exp. Mar. Biol. Ecol.* 412, 1–12

